



**HAL**  
open science

# Modeling coupled water flow, reactive transport and heat transfer in porous media

Sara Tabrizinejadas

► **To cite this version:**

Sara Tabrizinejadas. Modeling coupled water flow, reactive transport and heat transfer in porous media. Earth Sciences. Université de Strasbourg, 2022. English. NNT: 2022STRAH015. tel-04520047

**HAL Id: tel-04520047**

**<https://theses.hal.science/tel-04520047v1>**

Submitted on 25 Mar 2024

**HAL** is a multi-disciplinary open access archive for the deposit and dissemination of scientific research documents, whether they are published or not. The documents may come from teaching and research institutions in France or abroad, or from public or private research centers.

L'archive ouverte pluridisciplinaire **HAL**, est destinée au dépôt et à la diffusion de documents scientifiques de niveau recherche, publiés ou non, émanant des établissements d'enseignement et de recherche français ou étrangers, des laboratoires publics ou privés.

# THÈSE

Présentée par :

**Sara Tabrizinejadas**

Soutenance prévue : le **21 septembre 2022**

Pour obtenir le grade de : **Docteur de l'Université de Strasbourg**

Discipline/ Spécialité : Sciences de l'environnement

## **Modeling coupled water flow, reactive transport and heat transfer in porous media**

### **THÈSE dirigée par :**

**Monsieur Jérôme Carrayrou** Maître de conférences – HDR, Université de Strasbourg

**Monsieur Fahs Marwan** Maître de conférences – HDR, ENGEES

### **RAPPORTEURS :**

**Monsieur Amaziane Brahim** Maître de Conférences, Université de Pau, France.

**Madame Choquet Catherine** Professeur, Université de La Rochelle, La Rochelle, France

### **AUTRES MEMBRES DU JURY :**

**Monsieur Saaltink Maarten** Professeur, Université de Catalogne, Barcelone, Espagne

**Monsieur Jourde Hervé** Professeur, Université de Montpellier, France

**Monsieur TOUSSAINT Renaud** Directeur de Recherche, CNRS, Université de Strasbourg



## Table of contents

List of figures .....	6
Acknowledgements .....	10
Chapter I: Introduction .....	11
1.1. Overview .....	11
1.2. Multicomponent reactive transport models for Electro-diffusion process in porous media.....	13
1.3. Thermohaline Convection in porous media .....	14
1.3.1 An overview of chapter III: A Fourier series solution for transient three-dimensional thermohaline convection in porous enclosures.....	14
1.3.2 An overview of chapter IV: Robust numerical model for reactive-thermohaline convection of CO <sub>2</sub> in brine saturated reservoir .....	15
1.4. Dissolution processes in discrete fracture networks.....	17
Chapitre I: Introduction .....	19
1.1. Prolégomènes .....	19
1.2. Modèles de transport réactif multicomposants pour le processus d'électrodifusion dans les milieux poreux.....	21
1.3. Convection thermohaline dans les milieux poreux.....	22
1.3.1 Aperçu du chapitre III : Solution en série de Fourier pour la convection thermohaline tridimensionnelle transitoire dans des enceintes poreuses.....	23
1.3.2 Aperçu du chapitre IV : Modèle numérique robuste pour la convection réactive-thermohaline du CO <sub>2</sub> dans un réservoir saturé en saumure .....	24
1.4. Processus de dissolution dans les réseaux de fractures discrètes .....	26
Chapter II: On the Validity of the Null Current Assumption for Modeling.....	29
Sorptive Reactive Transport and Electro-Diffusion in .....	29
Porous Media.....	29
2.1. Introduction .....	29
2.2. Mathematical and numerical models.....	31
2.2.1. General NPP model .....	31
2.2.2. Electro-neutrality and NC assumption .....	32
2.2.3. Equivalency of NPP systems and Null current assumption models .....	33
2.2.4. Numerical models.....	34
2.3. Verification.....	35
2.4. Effect of sorption reactions .....	38
2.4.1. Total concentration.....	38
2.4.2. Total electric current.....	42
2.4.3. Total charge.....	44

2.4.4. Electric field .....	46
2.5. Conclusion.....	48
Chapter III: A Fourier series solution for transient three-dimensional thermohaline convection in porous enclosures .....	49
3.1. Introduction .....	49
3.2. Problem and model statement .....	52
3.2.1. Problem description.....	52
3.2.2. Model assumptions, governing equations and boundary and initial conditions .....	54
3.3. The Fourier series solution .....	55
3.3.1 Vector potential formulation and non-dimensional system.....	56
3.3.3. The spectral system .....	58
3.3.4. Solving the spectral system .....	59
3.4. Results and discussion: Verification and benchmarking .....	61
3.4.1. Verifications .....	62
3.4.2. Benchmarking .....	68
3.5. Sensitivity to parameters for THC under crossed thermal and solute gradient .....	71
3.5.1 Effect of $Ra_T$ .....	71
3.5.2. Effect of $N_g$ .....	77
3.5.3. Effect of $Le$ .....	79
3.6. Understanding the effects of temperature and concentration gradients on heat and salinity fluxes .....	82
3.7. Conclusion.....	85
Chapter IV: Robust numerical model for reactive-thermohaline convection of CO <sub>2</sub> in brine saturated reservoir.....	87
4.1. Introduction .....	87
4.2. Conceptual model and method .....	90
4.2.1. The porous square benchmark: problem description.....	90
4.2.2. The mathematical model .....	91
4.2.3. Dimensionless analysis.....	93
4.2.4. A new numerical model for RTHC .....	95
4.3. Comparison TRACES vs. COMSOL .....	96
4.3.1. Verification.....	96
4.3.2. Advantages of the newly developed model (TRACES).....	101
4.4. Effect of temperature on the processes of convective-reactive CO <sub>2</sub> dissolution.....	104
4.4.1. The hypothetical benchmark of porous square cavity .....	105
4.4.2. Field study: The Viking field in the North Sea .....	110
4.5. Conclusion.....	118

Chapter V: Modelling dissolution processes in discrete fracture networks: an advanced numerical scheme.....	120
5.1. Introduction .....	120
5.2. The Mathematical model.....	122
5.3. The Numerical model.....	124
5.3.1. Spatial discretization of the flow .....	124
5.3.2. Spatial discretization of the transport .....	126
5.4. Numerical experiments.....	130
5.4.1. Verification: Tracer transport in a DFN with constant aperture (example 1).....	130
5.4.2. Verification: Coupled flow, transport and dissolution in variable aperture fracture (example 2).....	134
5.4.3. Advantages of developed DG model: numerical diffusion (example 3) .....	136
5.5. Effects of geochemical dissolutions .....	137
5.5.1. Dissolution processes in a single fracture.....	138
5.5.2. Dissolution processes in a DFN .....	143
5.6. Conclusion.....	148
Chapter VI: Conclusion and perspectives .....	150
6.1. General conclusion .....	150
6.2. Perspective.....	153
Chapitre VI: Conclusion et perspectives .....	155
6.1. Conclusion générale .....	155
6.2. Perspectives .....	159
References .....	161
Chapter I: Introduction .....	161
Chapter II: On the Validity of the Null Current Assumption for Modeling Sorptive Reactive Transport and Electro-Diffusion in Porous Media .....	163
Chapter III: A Fourier series solution for transient three-dimensional thermohaline convection in porous enclosures .....	165
Chapter IV: Robust numerical model for reactive-thermohaline convection of CO <sub>2</sub> in brine saturated reservoir.....	169
Chapter V: Modelling dissolution processes in discrete fracture networks: an advanced numerical scheme.....	175
Appendices .....	180
Appendix A: Explanations of benchmarks in Chapter II .....	180
1. Benchmark 1.....	180
2. Benchmark 2.....	180
2. Benchmark 3.....	181
Appendix B: Coefficients of the spectral system in Chapter III.....	182

## List of figures

**Figure 2.1.** Comparison concentration results of NPP, NC and ‘Crunch’ models for 1D simulations of three benchmarks ..... 37

**Figure 2.2.** Comparison of Concentration results of NPP (Colors), NC (solid black lines) and ‘Crunch’ (dashed red lines) models for 2D simulations of benchmark 3 ..... 38

**Figure 2.3.** Comparison of total concentration results of NPP and NC-models for 1D simulations of the three benchmarks in the case of sorption reactions. Test case 1 deals with low sorptivity while test case 2 deals with high sorptivity ..... 40

**Figure 2.4.** Comparison of total concentration results of NPP (Colors) and NC (Lines) models for simulation of benchmark 3-2D with sorption: low sorptivity (test case 1 -left), high sorptivity (test case 2 -right) ..... 41

**Figure 2.5.** Comparison of total concentration results of NPP and NC models for Benchmark 2 with linear initial condition for NC model ..... 42

**Figure 2.6.** Total electrical current for the 1D benchmarks with the NPP and NC-models ..... 43

**Figure 2.7.** The total electrical current for the 2D benchmark in the horizontal (left) and vertical directions (right). The NPP model is represented with colors and the NC model with lines ..... 44

**Figure 2.8.** The total charge for the 1D benchmarks with the NPP and NC-models ..... 45

**Figure 2.9.** The total charge for the 2D benchmark with the NC-model ..... 46

**Figure 2.10.** The electric field for the 1D benchmarks with the NPP and NC-models ..... 47

**Figure 2.11.** Left: The electric field with NPP-model for the case of no sorption (colors), low sorption (black lines) and high sorption (red dashed lines). Right: Electric field with the NC-model for the case of no sorption (colors), low sorption (black lines) and high sorption (red dashed lines) ..... 47

**Figure 3. 1.** a) The conceptual problem of a cubic porous box with horizontal-crossed gradients of temperature and concentration and b) a conceptual model for a geothermal reservoir dealing with horizontal-crossed gradients of temperature and salinity. .... 53

**Figure 3.2.** Comparison of the steady state semi-analytical solution (Flood map) and COMSOL (dashed lines): concentration contours (left) and isotherms (right) in two diagonal plans. .... 65

**Figure 3.3.** Comparison of the transient semi-analytical solution (Flood map) and COMSOL (dashed lines): concentration contours (left) and isotherms (right) in two diagonal plans ( $\tau$  is the non-dimensional time,  $\varepsilon = 0.1$  and  $\sigma = 0.46$  ). ..... 67

**Figure 3.4.** Time variation of the average Nusselt ( $\overline{Nu}$ ) and Sherwood ( $\overline{Sh}$ ) numbers: Comparison of the transient Fourier series solution (SA-transient) and COMSOL for ‘test case 1’ and ‘test case 2’. All parameters for both test cases are given in Table 3.1. .... 68

**Figure 3.5.** Comparison of the steady state semi-analytical (SA-steady) solution in flood map and COMSOL in dashed lines for ‘test case 3’: concentration contours (left) and isotherms (right) in two diagonal plans. COMSOL-v5.3 is used to denote a previous version of the software while

COMSOL is used for the newer release (v5.4). Parameters for ‘test case 3’ are given in Table 3.1. .... 69

**Figure 3.6.** Time variation of the average Nusselt ( $\overline{Nu}$ ) and Sherwood ( $\overline{Sh}$ ) numbers: Comparison of the transient semi-analytical (SA-transient) solution and COMSOL for ‘test case 3’. COMSOL-v5.3 is used to denote a previous version of the software while COMSOL is used for the newer release (v5.4). Parameters for ‘test case 3’ are given in Table 3.1. .... 70

**Figure 3.7.** Effect of Rayleigh number on the flow structure: Arrow surface plot of the steady state velocity field at small and large thermal Rayleigh number in the cases of thermally (TD) and solute (SD) dominated convective flow. .... 73

**Figure 3.8.** Components of the overall flow: The solute driven convective flow (SDC) and the thermally-driven convective flow (TDC). .... 73

**Figure 3.9.** Effect of Rayleigh number on the flow structure: Stream-tubes showing the behavior of the vortex within the domain in the cases of thermally (TD) and solute (SD) -dominated convective flow  $Ra_T = 100$ , at steady state. For the TD case the stream-tubes are highlighted with concentration while for the SD cases they are highlighted with temperature. .... 74

**Figure 3.10.** Steady state isosurfaces of the vector potential components ( $\Psi_x$ : left and  $\Psi_y$ : right) and velocity field (arrows) at small and large thermal Rayleigh numbers in the cases of thermally (TD) and solute (SD) dominated convective flow. .... 74

**Figure 3.11.** Effect of the Rayleigh number on the concentration and temperature distributions: Steady state concentration and temperature isosurfaces (0.25, 0.5 and 0.75) at small and large thermal Rayleigh numbers in the cases of thermally (TD) and solute (SD) dominated convective flow. .... 75

**Figure 3.12.** Effects of the thermal Rayleigh number on the average Sherwood and Nusselt numbers in the cases of thermally (TD) and solute (SD) dominated convective flow: Steady state regime (top) and transient regime (bottom). .... 76

**Figure 3.13.** Effects of the gravity number on the maximum velocity components, average Sherwood and Nusselt numbers for steady state (a and b) and transient (c-e) regimes. .... 78

**Figure 3.14.** Effect of the gravity number ( $N_g$ ) on the concentration and temperature distributions: Main temperature and concentration isosurfaces (0.25, 0.5 and 0.75) for different values of  $N_g$  in the cases of thermally (TD- left) and solute (SD- right) dominated convective flow. .... 79

**Figure 3.15.** Effects of Lewis number on the maximum velocity components, average Sherwood and Nusselt numbers for steady state (a and b) and transient (c-e) regimes. .... 81

**Figure 3.16.** Effect of the Lewis number on the concentration and temperature distributions: Steady state concentration and temperature isosurfaces (0.25, 0.5 and 0.75) at different values of Lewis numbers in the TD and SD cases. .... 82

**Figure 3.17.** Effect of temperature (resp. concentration) gradient on mass (resp. heat) flux the domain, as measured by the average Sherwood (resp. Nusselt) number: Steady state regime (a and c) and transient regime (b and d). .... 84

**Figure 4.1.** Illustration of the conceptual model for GCS as a RTHC problem in a porous box. . 91

**Figure 4.2.** ‘Test case 1-H’: Comparison between TRACES and COMSOL for (a) dimensionless  $CO_2$  concentrations, (b) dimensionless  $CaCO_3$  concentration, (c) dimensionless temperature distribution at  $\tau = 0.05$ , (d)  $\overline{Nu}$ , (e)  $\overline{Sh}$  and (f)  $TF^{diff}$  ..... 99

**Figure 4.3.** Comparison between TRACES and COMSOL for ‘Test case 1’V’: (a) dimensionless  $CO_2$  concentrations, (b) dimensionless  $CaCO_3$  concentration, (c) dimensionless temperature, all at  $\tau = 0.05$ . (d) time variation of  $\overline{Nu}$ , (e) time variation of  $\overline{Sh}$  and (f) time variation of  $TF$  ..... 101

<b>Figure 4.4.</b> Comparison between TRACES and std-FE for ‘Test case 2’: (a) dimensionless $\text{CO}_2$ concentration, (b) dimensionless $\text{CaCO}_3$ concentration, (c) dimensionless temperature, all at $\tau = 0.05$ .	103
<b>Figure 4.5.</b> Oscillations with the std-FE solution for ‘Test case 2’. Negative $\text{CO}_2$ concentration (a and d), $\text{CaCO}_3$ concentrations larger than one and (b and e) and negative $\text{CaCO}_3$ concentration (c and f). All the results are presented at $\tau = 0.05$ .	103
<b>Figure 4.6.</b> Variation of the Damköhler number as a function of dimensionless temperature in ‘test case 3’.	106
<b>Figure 4.7.</b> Dimensionless concentration of $\text{CO}_2$ (left) and $\text{CaCO}_3$ (middle) and dimensionless temperature (right) for ‘test case 3’ with the three models at $\tau = 0.01$ .	107
<b>Figure 4.8.</b> Time variations of the metrics characterizing $\text{CaCO}_3$ and $\text{CO}_2$ with the three models ‘Isothermal’, ‘Linear temperature’ and ‘RTHC’: (a) the total amount of $\text{CaCO}_3$ available in the domain ( $T_{\text{CaCO}_3}$ ), (b) the instantaneous total flux of $\text{CO}_2$ at the top surface ( $TF_{\text{CO}_2}$ ) and (c) The cumulative total flux of $\text{CO}_2$ ( $TF_{\text{CO}_2}^{\text{Cum}}$ ).	109
<b>Figure 4.9.</b> Geological structure of the Viking field, showing the porosity distribution and the location of a vertical cross-section.	110
<b>Figure 4.10.</b> Description of the site: (a) initial and boundary conditions (b) Porosity map, (c) permeability map	111
<b>Figure 4.11.</b> Results of the three models ‘Isothermal’, ‘Linear temperature’ and ‘RTHC’: Spatial distributions of $\text{CO}_2$ (left), $\text{CaCO}_3$ (middle), and temperature (right) after 100 years.	114
<b>Figure 4.12.</b> Comparison between models ‘Isothermal’, ‘Linear temperature’ and ‘RTHC’: (a) cumulative $\text{CO}_2$ flux and (b) total amount of $\text{CaCO}_3$ available in the domain.	115
<b>Figure 4.13.</b> Results of reaction parameters sensitivity analysis with ‘RTHC’ model: Spatial distributions of $\text{CO}_2$ .	116
<b>Figure 4.14.</b> Comparison between the results of cumulative $\text{CO}_2$ flux with low, moderate and high values of activation energy and pre-exponential factor in the Arrhenius law: (a) and (c): Activation energy sensitivity analysis, (b) and (d): pre-exponential factor sensitivity analysis.	117
<b>Figure 5.1.</b> Flow and transport notations in a fracture k	124
<b>Figure 5.2.</b> Problem description: (a) network of fractures and boundary conditions, (b) Highlighted observation points ( $O_1$ , $O_2$ ) and fracture ( $F_1$ )	131
<b>Figure 5.3.</b> ‘Example 1’: Dimensionless concentration contours with (a): DG, (b): FE and comparison between DG and FE for dimensionless concentration (c): at $O_1$ , (d): at $O_2$ and (e): along fracture $F_1$	133
<b>Figure 5.4.</b> Conceptual model for dissolution in a single fracture	134
<b>Figure 5.5.</b> Example 2: Comparison between the three numerical schemes for dissolution on a single fracture, (a) and (b): time variation of concentration and fracture aperture, (c): concentration along the fracture after 50 and 100 seconds and (d) opening through the fracture and 1 year	135
<b>Figure 5.6.</b> ‘Example 3’: Comparison between DG and FV schemes for dimensionless concentrations (a) at $O_1$ , (b) at $O_2$ and (c) along line $F_1$ at $t=200s$	137
<b>Figure 5.7.</b> Spatial distributions of fracture aperture (a-e) concentration (f,g) and flow velocity (h,i) after 1 year with the RC and TC models. High and low values of constant reaction rate and Sherwood number are used for RC and TC models, respectively.	140
<b>Figure 5.8.</b> Time evolution of concentration (a,b), fracture aperture (c,d) and water flow (e,f) obtained with the RC and TC models with high and low values of constant reaction rate (KC) and the Sherwood number (Sh), respectively. The results correspond to the case of single fracture and they are plotted near the inlet at $X=0.1$	142

**Figure 5.9.** Conceptual model for dissolution process in a DFN ..... 143

**Figure 5.10.** Comparison of spatial distributions of fracture aperture (a,b), water flow (c,d) and concentration (e,f) after 1 year between reaction and transport control formulations in a network of fractures ..... 145

**Figure 5.11.** Comparison of the temporal evolutions of concentration (a,b), fracture aperture (c,d) and water flow (e,f) between RC and TC models in a network of fractures near the inlet at the point P<sub>1</sub> ..... 147

## Acknowledgements

My first and foremost appreciation is dedicated to my supervisor, Dr. Marwan Fahs who has always been caring about my Ph.D. progress and who has helped me in any possible way to improve my work. I have learnt both science and ethics from him that will always stay with me. Also, I would like to express my deepest gratitude to Dr. Anis Younes who has offered me his generous help and support through all my research activities. I have learnt how to deeply enjoy science and my Ph.D. work from him and that will always help me through my professional life. My appreciation extends to Dr. Jerom Carrayrou, Dr. Francois Lehmann, Dr. Behzad Ataie-Ashtiani and Dr. Craig T. Simmons for their valuable comments and advice during my Ph.D. studies. I am also grateful to Dr. Hussein Hoteit for providing field data for this Ph.D. thesis. I would also like to thank the members of the defense committee for their time and effort.

I would like send my appreciation to my friends during my Ph.D. life since they eased the difficulties of the way and they will always stay a part of my life. I would like to thank my dear friend, Tetyana who has been a caring sister for me. Her kindness, empathy and wisdom always made our time spending together a pleasant time for me. I also deeply thank my dear friend Daniel. I highly admire his kindness and his care for his friends. With the warmth of his company, we have discovered many unknown places together and all these memories remain bright for me forever. I also thank my dear friend, Carmen. With her great sense of humor and kindness, I have always enjoyed the time spending with her. I would like to thank my dear friend, Lou, with her great and strong tendency to the kindness and humanity we have made great memories. Also, I thank my dear friend Oscar, that with his kindness and sympathy we have spent such great times together. I would also like to thank Tobias and Maria (Lulu) with whom I had the most refreshing coffee breaks in a cosy corner of the department. My appreciation extends to Mouna, Jessica, Adrien, Iman, Felix, Gil, David, Nicolas and Celine with whom I have made pleasant memories. I thank you all for making my Ph.D. experience a very bright part of my life.

Finally, I would like to take the opportunity and thank my beloved parents, Asghar and Zahra, who have been supporting and encouraging me all through my life. During my Ph.D. life, I have always been warmed up by their support and unconditional love. Also, I would like to thank my lovely brother, Mohamad, for his supports, kindness and his care about me.

# Chapter I: Introduction

## 1.1. Overview

The coupled processes of flow, reactive transport and heat transfer in natural porous media have a major effect on human life resources and it is central to a wide range of applications in the fields of geology, hydrogeology, engineering and environmental research. A few examples of such extent of applications are observed in groundwater resources management (Singh, 2014), groundwater pollution management (van der Lee et al., 2003), geological carbon sequestration (Class et al., 2009; Firoozabadi and Myint, 2010; Juanes and Class, 2013; Vilarrasa and Carrera, 2015), mine operation (Khalili et al., 2014), waste disposal and radioactive waste management (Zhang and Schwartz, 1995), sea-aquifers interaction (Werner et al., 2013), geothermal systems (Al-Khoury, 2011; Kim et al., 2012; Nield and Bejan, 2013; Erfani et al., 2019) and oil and gas production (Chen, 2007). The high impact level of these applications on human life resources has motivated scientists to perform their studies on relatively large time and spatial scales to provide a comprehensive understanding of the rules governing these coupled processes in the subsurface. However, with the involvement of large time and space scales, the study of coupled flow, reactive transport and heat transfer becomes overcomplicated and the conventional methods become inefficient, expensive and even impractical (Zhao et al., 2009).

Numerical modeling is an attractive tool to deal with the aforementioned applications in large-scale studies (Zhao et al., 2009; Díaz Viera et al., 2012; Miller et al., 2013; May, 2014; Helmig, 2015). Numerical models are essential for understanding the complex and dynamic nature of the natural environment. Furthermore, they can be used for designing hydrogeological systems, decision making, risk management and prediction studies. In general, numerical modeling consists of representing the physical processes by mathematical equations and then solving these equations numerically using computers. In the field of hydrogeology, this mathematical representation is based on the three fundamental conservation laws (conservation of mass, linear momentum and energy) along with geochemical/biogeochemical rules. Modeling based on the above-mentioned laws is known as mechanistic modeling and consists of some sets of Algebraic Equations (AEs), Ordinary Differential Equations (ODEs) and most commonly, Partial Differential Equations (PDEs). These equations which are usually coupled and highly non-linear could be written in a variety of geometrical domains and be subjected to different types of initial and boundary conditions. Analytical solutions of such a system of coupled equation can be only obtained in limited configuration with simplified geometry and boundary conditions. This highlights the importance of numerical models that provide a numerical approximation to the solution and are capable of handling more complicated problems in the field of hydrogeology.

During the last 50 years, with the fast improvements in computer technology, numerical modeling has benefited from the development of several numerical methods, techniques, algorithms and procedures. However, numerical modeling of flow, reactive transport and heat transfer in natural porous media reveals specific challenges that are not common in all engineering applications (Miller et al., 2013; Zhao, 2016). These challenges arise from the nature of porous media and the governing equations. Multiple physical, chemical and biological processes that are taking place in a wide range of spatial (few micrometers to kilometers) and temporal (seconds to centuries) scales, high level of heterogeneity and anisotropy of the domain, dense fracture networks, highly nonlinear and fully coupled equations containing hyperbolic property as their convective terms are just a few examples highlighting the level of sophistication of numerical modeling of flow, mass transport and heat transfer in the subsurface. Furthermore, with the involvement of geochemical reactions, the additional computational cost keeps the reactive numerical models away from field/catchment studies. In addition, geochemical reactions at the solid-fluid interface can often lead to alternations in hydrodynamic properties which increase the nonlinearity of the coupling between the equations (Ladd and Szymczak, 2021). Therefore, efficiency and accuracy are two essential components of models for reactive transport coupled with flow and heat transfer.

Taking the aforementioned challenges into account, the advances in the numerical modeling for flow, reactive transport and heat transfer in porous media require efforts from mathematics, physics and chemistry associated with hydrogeology and geoscience with the aim of improving physical, chemical and theoretical understanding of the key processes, establishing the equations that can comprehensively describe those processes and developing advanced numerical schemes to improve the efficiency and accuracy of the numerical models. Remarkable advancements in the development of sophisticated numerical models in this area have been achieved in the last 10 years. However, due to the broad nature and complexity of related problems, this topic is still at a developing stage (Zhao et al., 2009). The demand for more accurate and comprehensive formulations and faster and more efficient simulating tools is still growing and the development of newer and more robust modeling schemes in this field is still the focus. The main goal behind new models and numerical schemes development is to obtain a comprehensive insight into underlying processes and improve the capacity of models in simulating real cases at large time and space scales. In addition, in reactive transport modeling, as the interaction between solid and fluid interface generates a nonlinear feedback mechanism, accurate and robust numerical models for precisely modeling the nonlinear behavior are highly required.

This brought us to the main objective of our work; to consider some ongoing topics of interest and contribute our effort to improve the existing models and numerical techniques as well as

understanding flow, reactive transport and heat transfer in porous media. In this context, the main focus of this work is on three applications: (i) Reactive transport models for Electro-diffusion process in porous media, (ii) Thermohaline convection in porous media (iii) Flow and dissolution processes in discrete fracture networks.

## **1.2. Multicomponent reactive transport models for Electro-diffusion process in porous media**

The term reactive transport refers to the coupling of chemical reactions with mass transport. This topic is an area of growing interest due to its role in understanding the composition of natural water aquifers and the formation and dissolution of rocks and minerals in geologic formations (Abd and Abushaikha 2021). For studying reactive transport, recently, numerical and mathematical models have gained popularity due to their great ability to mimic realistic situations that help manage subsurface resources (Abd and Abushaikha, 2019). Many modern codes have extensive capabilities and have been used to simulate reactive transport in different applications and in particular, for problems of solute transport in saturated porous media.

It is well-known that among the reactive transport codes, the ones based on the classical Fick's law cannot fully describe the multicomponent electrolyte systems. In such systems, each ion diffuses differently according to its own ionic properties and Electro-diffusion takes place as an additional mass transport process to neutralize the charge imbalance created by the differences in the movement of each ionic species. Therefore, classical Fick's law which considers the movement of each particle merely based on the gradient of concentration fails to provide a representation of the problem and the system is described fully by the Nernst-Planck equation, a formulation that explicitly considers the electric coupling between species and ensures the conservation of charge.

The common approach for implementation of the Nernst-Planck equation in the reactive transport codes for the domains that are not subjected to an external electric field is to consider the null current assumption for those domains. This assumption makes the code implementations more convenient as it represents one of the unknowns (electric field) as a function of solute concentrations. Even though the null current assumption has been properly used in several reactive transport problems the validity of this assumption has not been assessed in general reactive transport cases. We evaluated the validity of this assumption in a reactive transport problem where both aqueous and dry phases of the reactive species were participating in the formation of Electro-diffusion phenomenon and in such a case we found the credibility of this assumption under question. Therefore, we introduced the valid and comprehensive formulation for Electro-diffusion in a general reactive transport problem. This topic is developed in chapter II. It has been the subject of a paper published in the journal of Water (Tabrizinejadas et al, 2021)

### **1.3. Thermohaline Convection in porous media**

Thermohaline convection in porous media takes place when the density of the fluid in the place is changing simultaneously by thermal and compositional changes. This phenomenon is observed in several environmental applications. Among them, geothermal reservoir and geological CO<sub>2</sub> sequestration are of great interest because they contribute in reducing the amount of existing CO<sub>2</sub> in the environment and mitigating the global warming and the climate change. Therefore, these applications are attracting the efforts of the researchers from different disciplines, and hence, obtaining a comprehensive understanding of the underlying processes in these applications is essential. We developed a 3D semi-analytical solution for thermohaline convection inspired by the boundary conditions in a coastal geothermal reservoir. We also perform our studies towards the second application by developing an advanced numerical model for geological CO<sub>2</sub> sequestration as a Reactive Thermohaline Convection (RTHC) problem in a square cavity and also in a field scale, in Viking field, North Sea. These contributions are discussed in the following sub-sections:

#### ***1.3.1 An overview of chapter III: A Fourier series solution for transient three-dimensional thermohaline convection in porous enclosures***

Despite the severity of numerical codes developed for thermohaline convection, analytical solutions are still of great interest. Analytical solutions serve as an alternative to deal with computation requirement of numerical solutions. As they are free of numerical errors, they are helpful to provide insight on the physical processes. Analytical solutions are also important for benchmarking numerical codes and for the assessment of numerical schemes. In addition, due to the accuracy and efficiency of analytical solutions, they can be used for sensitivity analysis and parameter estimation. However, analytical solutions are usually limited to specific boundary conditions and geometry and cannot be obtained without significant simplifications of the governing equations. Semi-analytical solutions combine the accuracy of analytical solutions with the flexibility of numerical solutions in solving the full mathematical models under complex and realistic boundary conditions. For Thermohaline Convection, analytical and semi-analytical solutions are limited to 2D (Shao et al., 2016; Kalla et al., 2001; Trevisan and Bejan, 1986; Masuda et al., 2013). In general, analytical and semi-analytical solutions for density-driven flow model are limited to steady-state conditions.

Our contribution in this context is to develop a new semi-analytical solution for a transient-3D thermohaline convection problem in a porous enclosure. We considered a stable configuration of density-driven flow. Such a configuration is more relevant for benchmarking than unstable cases which can suffer from solution multiplicity (i.e. bifurcation and oscillations). As our main objective is to investigate an effective 3D configuration that cannot be simplified to 2D, we imposed horizontal-crossed gradient of thermal and salinity on a porous box. With these boundary conditions

two circulation flows arise on two different planes and a 3D investigation becomes inevitable. Such a configuration can be found in several applications as in geothermal systems in coastal aquifers or in islands where sea/ocean can generate a salinity gradient and geothermal wells create a thermal gradient. We developed the semi-analytical solution based on the Fourier series for such a configuration. An efficient technique is developed to solve the flow, mass transport and heat transfer equations in the spectral space. The developed semi-analytical model shows high performance in compare with existing numerical codes and the results provide a better understanding of the 3D structure of the flow in thermohaline convection. The developed model can be used for benchmarking purposes or explaining the inter-relation of the parameters associated with the physics of the problem. This topic is developed in chapter III.

This work has been the subject of a paper published in the journal Water Resources Research (Tabrizinejadas et al., 2020).

### ***1.3.2 An overview of chapter IV: Robust numerical model for reactive-thermohaline convection of CO<sub>2</sub> in brine saturated reservoir***

Global warming remains one of the most important environmental issues and the main reason responsible for that is an excessive amount of greenhouse emissions to the environment, among which the most important is carbon dioxide (CO<sub>2</sub>). Despite the ongoing efforts on reducing the use of fossil fuels as the source of power plants and substituting renewable sources, currently, most of the worldwide power plants are based on fossil fuels (Whitley 2018). Therefore, the emission of CO<sub>2</sub> to the atmosphere is currently inevitable and until other inexpensive, clean, and plentiful technologies are available, a temporary possible way to deal with global warming is mitigating the existing CO<sub>2</sub> in the atmosphere. To this end, various approaches have been suggested and among them, geologic CO<sub>2</sub> sequestration (GCS) is the most recommended technology to mitigate large-scale CO<sub>2</sub> emissions in the atmosphere.

GCS consists of capturing emissions of CO<sub>2</sub> at the industrial combustion sources (mainly fossil fuel-based power plants), compressing it to form the supercritical state of CO<sub>2</sub>, transporting it and injecting the supercritical CO<sub>2</sub> into geologic formations such as saline aquifers or depleted oil or gas reservoirs for long-term storage. In the Paris agreement, this approach is introduced as one of the most promising solutions to global warming (UNFCCC 2015).

Understating the fate of CO<sub>2</sub> in the geological formation is essential for securing the sequestration and for predicting the impact of dissolved CO<sub>2</sub> on aquifers and reservoirs. When the supercritical state of CO<sub>2</sub> is injected into the reservoir, CO<sub>2</sub> dissolution in the brine takes place due to mixing processes and a CO<sub>2</sub>-laden brine is formed. The density of dissolved CO<sub>2</sub> is higher than that of underlying brine. This results in additional dissolution related to gravity-induced fingering, caused

by the convective flow. In addition, dissolved CO<sub>2</sub> reacts with the primary minerals in the rocks such as Ca<sup>2+</sup>, Mg<sup>2+</sup>, Fe<sup>2+</sup>, etc. These geochemical reactions accompanied by the transport equation lead to more dissolution of CO<sub>2</sub> into the brine. The combination of these processes is known as the convective-reactive process and it has been widely investigated in the literature with the application of GCS. A common assumption in the existing studies is assuming the isothermal condition for the reservoir. However, the temperature gradient naturally exists in the reservoir by increasing towards the depth or it is induced by the injection of CO<sub>2</sub>. Therefore, a temperature gradient exists in the domain and it affects the density and viscosity of the fluid, as well as the geochemical reaction rate. Our contribution in this regard was to develop an advanced numerical model that takes the effects of the temperature gradient on convection and reaction into account and keeps the efficiency for large length and time-scale modeling while maintaining the accuracy. To do so, since there are several physical processes involved in GCS and they are highly coupled nonlinearly, an advanced numerical scheme is required for the discretization of each physical process. The reaction term is implemented with a Sequential Non-Iterative Approach (SNIA) and the intrinsic numerical error due to the Operator Splitting (OS) is controlled by implementation of an adaptive time stepping approach. The accuracy, efficiency and robustness of the newly developed model is demonstrated by comparing the results with a standard Finite Element model in a square benchmark.

In the second step of the work we performed simulations to understand the effects of temperature on reaction rate and convective flow associated with density and viscosity. Our analysis was based on the comparison of three models with increasing levels of complexity and realism. The first model is the 'Isothermal' model which considers constant temperature in time and space and it imitates the models that are usually used in previous studies, which are based on isothermal assumptions. The second model is the 'Linear Temperature' model which considers a linear increase in temperature towards the depth of the domain but the temperature is constant in time. In this model, the effect of temperature gradient is considered on the geochemical reaction but it is neglected on the thermal convective process. The third model is the 'RTHC' model which considers the temperature variable in time and space. The comparisons between the models have been done firstly on a homogeneous, square benchmark. Then, they have been extended to a field simulation, in Viking field, North Sea to understand the effect of temperature gradient in accompany with heterogeneity and geometric complexity in large spatial and temporal scale of simulation with the disturbance of natural temperature gradient due to the injection of CO<sub>2</sub>.

Since several input parameters in GCS are uncertain it is essential to investigate the sensitivity of the results to uncertain parameters. As the main goal of our work was to investigate the effect of

temperature on dissolution processes on GCS, we limited the sensitivity analysis to the parameters governing the rate of the dissolution.

This work is developed in chapter IV and it has been the subject of a paper submitted to the journal of greenhouse gas control.

#### **1.4. Dissolution processes in discrete fracture networks**

Water flow in carbonate rocks is usually associated with the dissolution process and the transport of dissolved species. Naturally existing networks of fractures as well as dissolution-induced fractures can significantly affect the domain transmissivity that, in turn, affect flow, transport and dissolution processes. When the porosity and permeability of the rocks are low, such as in carbonate rocks the fractures act as preferential fluid pathways. Therefore, the fluid flow in the rock matrix can be neglected and the domain can be represented as a discrete fracture network (DFN).

Modeling dissolution processes in DFNs reveals specific challenges that are not present in unfractured media. This challenge arises from the dynamic evolution of the fractured domain due to the geochemical dissolution. The enlargement of fractures as a result of dissolution process continuously affects the fluid flow field. Flow, in turn, is affecting the dissolution process and the transport of dissolved species. Therefore, the processes are coupled and nonlinear. Furthermore, in DFNs, the whole flow is assigned to the fractures and the storage is ignored in the matrix, thus, the transport of dissolved species is an advection-dominant process. In such cases, standard numerical methods, such as standard finite element (FE) or finite volume (FV) methods can generate numerical diffusion that may underestimate the dissolutions processes. Standard numerical methods can also introduce non-physical oscillations that lead to convergence issues and limit the applicability of the models.

It is known that Discontinuous Galerkin finite element (DG) method is well-adapted to capture the sharp moving fronts in the case of an advection-dominant transport (Younes and Ackerer, 2008). The employment of DG scheme for discretization of the hyperbolic term of the transport equation has been largely reported in the literature. However, to the best of our knowledge, DG method has been never applied to dissolution processes in DFNs. Yet, there is a significant potential of such as an application, as DG method can, on the one hand, reduces numerical diffusion and better predicts the dissolution processes, and on the other hand, improves the stability of the solution and enhances convergence of nonlinear solvers.

Our contribution in this regard was to develop an advanced numerical model for the simulation of dissolution processes in DFNs and to investigate the effects of geochemical dissolution on fracture evolution, flow and transport processes, taking advantages of the newly developed model. The

numerical model is developed based on an upwind DG scheme for transport. In a DFN, within the fractures, the transport equation is similar to unfractured domains. The main challenge for this scheme is the application for intersecting fractures. In fact, the main idea of the DG scheme suggested in the literature (Younes et al., 2009) is to use the average value of the concentration over a computational cell as well as the components of the concentration gradient as primary variables. The Riemann solver is then used to evaluate the concentration at the nodes. A new formulation is developed in this work for the nodes where several fractures are intersecting. The upwind approximation in the intersections of fractures is obtained based on an averaging method with the weight of the upwind velocities. The chemical processes are coupled with the advection-dispersion processes and solved simultaneously in order to avoid operator-splitting errors. The flow is simulated with the Richards' equations. This allows for handling both saturated and unsaturated flows. The flow equation is discretized with the Mixed Finite Element (MFE) method. The mass lumping technique developed by (Koohbor et al., 2020) is employed for the discretization of the flow to avoid over and undershoots observed in transient simulations with small time steps.

For the temporal discretization, a higher-order method is used through the method of lines (MOL). MOL has been proven to be very efficient in solving highly nonlinear systems of equations. With MOL, the spatial derivatives are discretized while the time derivatives are kept in their continuous form. This allows for converting the partial derivative equations to a system of Ordinary differential equations. This system is solved using the adaptive, high order implicit solver.

The newly developed DG scheme is compared to a standard FE solution obtained using COMSOL Multiphysics and a FV solution obtained using an in-house code. The new DG scheme is then used to understand the effects of the reaction rate on dissolutions, flow and transport characteristics based on different physical processes controlling the dissolution rate. The effect of dissolution processes on flow and transport processes is investigated using different dissolution models depending on the regimes of the reaction rate and flow.

This topic is developed in chapter V. The results of this work have been submitted to journal of advances in water resources.

# Chapitre I: Introduction

## 1.1. Prolégomènes

Les processus couplés d'écoulement, de transport réactif et de transfert de chaleur dans les milieux poreux naturels ont un effet majeur sur les ressources de la vie humaine et sont au cœur d'un large éventail d'applications dans les domaines de la géologie, de l'hydrogéologie, de l'ingénierie et de la recherche environnementale. Quelques exemples de cette gamme d'applications peuvent être observés dans la gestion des ressources en eaux souterraines (Singh, 2014), la gestion de la pollution des eaux souterraines (van der Lee et al., 2003), la séquestration géologique du carbone (Class et al., 2009 ; Firoozabadi et Myint, 2010 ; Juanes et Class, 2013 ; Vilarrasa et Carrera, 2015), l'exploitation minière (Khalili et al., 2014), l'élimination des déchets et la gestion des déchets radioactifs (Zhang et Schwartz, 1995), l'interaction entre la mer et les aquifères (Werner et al., 2013), les systèmes géothermiques (Al-Khoury, 2011 ; Kim et al., 2012 ; Nield et Bejan, 2013 ; Erfani et al., 2019) et la production de pétrole et de gaz (Chen, 2007). Le niveau d'impact élevé de ces applications sur les ressources de la vie humaine a motivé les scientifiques à effectuer leurs études sur des échelles temporelles et spatiales relativement grandes afin de fournir une compréhension globale des règles régissant ces processus couplés dans la subsurface. Cependant, avec l'implication de grandes échelles de temps et d'espace, l'étude de l'écoulement couplé, du transport réactif et du transfert de chaleur devient trop compliquée et les méthodes conventionnelles deviennent inefficaces, coûteuses et même impraticables (Zhao et al., 2009).

La modélisation numérique est un outil intéressant pour traiter les applications susmentionnées dans les études à grande échelle (Zhao et al., 2009 ; Díaz Viera et al., 2012 ; Miller et al., 2013 ; May, 2014 ; Helmig, 2015). Les modèles numériques sont essentiels pour comprendre la nature complexe et dynamique de l'environnement naturel. En plus, ils peuvent être utilisés pour la conception de systèmes hydrogéologiques, la prise de décision, la gestion des risques et les études prévisionnelles. En général, la modélisation numérique consiste à représenter les processus physiques par des équations mathématiques, puis à résoudre ces équations numériquement à l'aide d'ordinateurs. Dans le domaine de l'hydrogéologie, cette représentation mathématique est basée sur les trois lois fondamentales de conservation (conservation de la masse, de la quantité de mouvement linéaire et de l'énergie) ainsi que sur les règles géochimiques/biogéochimiques. La modélisation basée sur les lois susmentionnées est connue sous le nom de modélisation mécaniste et consiste en un ensemble d'équations algébriques (AE), d'équations différentielles ordinaires (ODE) et, le plus souvent, d'équations différentielles

partielles (EDP). Ces équations, qui sont généralement couplées et fortement non linéaires, peuvent être écrites dans une variété de domaines géométriques et être soumises à différents types de conditions initiales et limites. Les solutions analytiques d'un tel système d'équations couplées ne peuvent être obtenues que dans une configuration limitée avec une géométrie et des conditions aux limites simplifiées. Cela souligne l'importance des modèles numériques qui fournissent une approximation numérique de la solution et sont capables de traiter des problèmes plus compliqués dans le domaine de l'hydrogéologie.

Pendant des 50 dernières années, avec les améliorations rapides de la technologie informatique, la modélisation numérique a bénéficié du développement de plusieurs méthodes, techniques, algorithmes et procédures numériques. Cependant, la modélisation numérique de l'écoulement, du transport réactif et du transfert de chaleur dans les milieux poreux naturels révèle des défis spécifiques qui ne sont pas communs à toutes les applications d'ingénierie (Miller et al., 2013 ; Zhao, 2016). Ces défis découlent de la nature des milieux poreux et des équations qui les régissent. Les multiples processus physiques, chimiques et biologiques qui se déroulent dans une large gamme d'échelles spatiales (de quelques micromètres à des kilomètres) et temporelles (de quelques secondes à des siècles), le niveau élevé d'hétérogénéité et d'anisotropie du domaine, les réseaux de fractures denses, les équations hautement non linéaires et entièrement couplées contenant des propriétés hyperboliques comme termes convectifs ne sont que quelques exemples mettant en évidence le niveau de sophistication de la modélisation numérique de l'écoulement, du transport de masse et du transfert de chaleur dans la subsurface. De plus, avec l'implication des réactions géochimiques, le coût de calcul supplémentaire éloigne les modèles numériques réactifs des études sur le terrain/les bassins versants. En outre, les réactions géochimiques à l'interface solide-fluide peuvent souvent entraîner des variations des propriétés hydrodynamiques qui augmentent la non-linéarité du couplage entre les équations (Ladd et Szymczak, 2021). Par conséquent, l'efficacité et la précision sont deux composantes essentielles des modèles de transport réactif couplés à l'écoulement et au transfert de chaleur.

Compte tenu des défis susmentionnés, les progrès de la modélisation numérique de l'écoulement, du transport réactif et du transfert de chaleur dans les milieux poreux nécessitent des efforts de la part des mathématiques, de la physique et de la chimie associées à l'hydrogéologie et aux géosciences dans le but d'améliorer la compréhension physique, chimique et théorique des processus clés, d'établir les équations qui peuvent décrire ces processus de manière exhaustive et de développer des schémas numériques avancés pour améliorer l'efficacité et la précision des modèles numériques. Des progrès remarquables dans

le développement de modèles numériques sophistiqués dans ce domaine ont été réalisés au cours des dix dernières années. Cependant, en raison de la nature générale et de la complexité des problèmes connexes, ce sujet est encore en phase de développement (Zhao et al., 2009). La demande de formulations plus précises et plus complètes et d'outils de simulation plus rapides et plus efficaces ne cesse de croître et le développement de nouveaux schémas de modélisation plus robustes dans ce domaine est toujours d'actualité. L'objectif principal du développement de nouveaux modèles et schémas numériques est d'obtenir une vision globale des processus sous-jacents et d'améliorer la capacité des modèles à simuler des cas réels à de grandes échelles de temps et d'espace. En outre, dans la modélisation du transport réactif, étant donné que l'interaction entre l'interface solide et fluide génère un mécanisme de rétroaction non linéaire, des modèles numériques précis et robustes pour modéliser avec précision le comportement non linéaire sont très importants.

Ceci nous a amené à l'objectif principal de notre travail : considérer certains sujets d'intérêt en cours et contribuer à l'amélioration des modèles et des techniques numériques existants ainsi qu'à la compréhension de l'écoulement, du transport réactif et du transfert de chaleur dans les milieux poreux. Dans ce contexte, ce travail se concentre sur trois applications : (i) les modèles de transport réactif pour les processus d'électro-diffusion dans les milieux poreux, (ii) la convection thermohaline dans les milieux poreux (iii) les processus d'écoulement et de dissolution dans les réseaux de fractures discrètes.

## **1.2. Modèles de transport réactif multicomposants pour le processus d'électrodifusion dans les milieux poreux**

Le terme de transport réactif fait référence au couplage des réactions chimiques avec le transport de masse. Ce sujet suscite un intérêt croissant en raison de son rôle dans la compréhension de la composition des aquifères naturels et de la formation et de la dissolution des roches et des minéraux dans les formations géologiques (Abd et Abushaikha 2021). Pour étudier le transport réactif, les modèles numériques et mathématiques ont récemment gagné en popularité en raison de leur grande capacité à imiter des situations réalistes qui aident à gérer les ressources souterraines (Abd et Abushaikha, 2019). De nombreux codes modernes ont des capacités étendues et ont été utilisés pour simuler le transport réactif dans différentes applications et, en particulier, pour les problèmes de transport de solutés dans les milieux poreux saturés.

Il est bien connu que parmi les codes de transport réactif, ceux qui sont basés sur la loi de Fick classique ne peuvent pas décrire complètement les systèmes électrolytiques multicomposants. Dans ces systèmes, chaque ion diffuse différemment en fonction de ses propres propriétés

ioniques et l'électrodifffusion intervient comme un processus de transport de masse supplémentaire pour neutraliser le déséquilibre de charge créé par les différences de mouvement de chaque espèce ionique. Par conséquent, la loi de Fick classique, qui considère le mouvement de chaque particule simplement en fonction du gradient de concentration, ne fournit pas une représentation du problème et le système est entièrement décrit par l'équation de Nernst-Planck, une formulation qui prend explicitement en compte le couplage électrique entre les espèces et assure la conservation de la charge.

L'approche commune pour la mise en œuvre de l'équation de Nernst-Planck dans les codes de transport réactif pour les domaines qui ne sont pas soumis à un champ électrique externe consiste à considérer l'hypothèse de courant nul pour ces domaines. Cette hypothèse rend l'implémentation du code plus pratique car elle représente l'une des inconnues (le champ électrique) comme une fonction des concentrations de soluté. Bien que l'hypothèse de courant nul ait été correctement utilisée dans plusieurs problèmes de transport réactif, la validité de cette hypothèse n'a pas été évaluée dans des cas généraux de transport réactif. Nous avons évalué la validité de cette hypothèse dans un problème de transport réactif où les phases aqueuses et sèches de l'espèce réactive participaient à la formation du phénomène d'électrodifffusion et, dans ce cas, nous avons remis en question la crédibilité de cette hypothèse. Par conséquent, nous avons introduit une formulation valide et complète pour l'électrodifffusion dans un problème général de transport réactif. Ce sujet est développé au chapitre II. Il a fait l'objet d'un article publié dans la revue *Water* (Tabrizinejadas et al, 2021).

### **1.3. Convection thermohaline dans les milieux poreux**

La convection thermohaline dans les milieux poreux a lieu lorsque la densité du fluide dans le milieu change simultanément en raison de changements thermiques et de composition. Ce phénomène est observé dans plusieurs applications environnementales. Parmi celles-ci, les réservoirs géothermiques et la séquestration géologique du CO<sub>2</sub> sont d'un grand intérêt car ils contribuent à réduire la quantité de CO<sub>2</sub> existant dans l'environnement et à atténuer le réchauffement de la planète et le changement climatique. Par conséquent, ces applications attirent les efforts des chercheurs de différentes disciplines, et il est donc essentiel d'obtenir une compréhension globale des processus sous-jacents à ces applications. Nous avons développé une solution semi-analytique 3D pour la convection thermohaline inspirée par les conditions limites d'un réservoir géothermique côtier. Nous avons également réalisé nos études pour la deuxième application en développant un modèle numérique avancé pour la séquestration géologique du CO<sub>2</sub> en tant que problème de convection thermohaline réactive (RTHC) dans

une cavité carrée et également à l'échelle d'un champ, dans le champ de Viking, en mer du Nord. Ces contributions sont discutées dans les sous-sections suivantes :

### ***1.3.1 Aperçu du chapitre III : Solution en série de Fourier pour la convection thermohaline tridimensionnelle transitoire dans des enceintes poreuses***

Malgré la sévérité des codes numériques développés pour la convection thermohaline, les solutions analytiques restent d'un grand intérêt. Les solutions analytiques servent d'alternative pour faire face aux exigences de calcul des solutions numériques. Comme elles sont exemptes d'erreurs numériques, elles permettent de mieux comprendre les processus physiques. Les solutions analytiques sont également importantes pour l'étalonnage des codes numériques et pour l'évaluation des schémas numériques. En outre, en raison de leur précision et de leur efficacité, les solutions analytiques peuvent être utilisées pour l'analyse de sensibilité et l'estimation des paramètres. Cependant, les solutions analytiques sont généralement limitées à des conditions aux limites et à une géométrie spécifiques et ne peuvent être obtenues sans simplifier considérablement les équations de base. Les solutions semi-analytiques combinent la précision des solutions analytiques avec la flexibilité des solutions numériques pour résoudre les modèles mathématiques complets dans des conditions aux limites complexes et réalistes. Pour la convection thermohaline, les solutions analytiques et semi-analytiques sont limitées à la 2D (Shao et al., 2016 ; Kalla et al., 2001 ; Trevisan et Bejan, 1986 ; Masuda et al., 2013). En général, les solutions analytiques et semi-analytiques pour le modèle d'écoulement induit par la densité sont limitées aux conditions d'équilibre.

Notre contribution dans ce contexte est de développer une nouvelle solution semi-analytique pour un problème de convection thermohaline transitoire 3D dans une enceinte poreuse. Nous avons considéré une configuration stable d'un écoulement entraîné par la densité. Une telle configuration est plus pertinente pour l'évaluation comparative que les cas instables qui peuvent souffrir de la multiplicité des solutions (c'est-à-dire bifurcation et oscillations). Notre principal objectif étant d'étudier une configuration 3D efficace qui ne peut être simplifiée en 2D, nous avons imposé un gradient horizontal croisé de température et de salinité sur une boîte poreuse. Avec ces conditions aux limites, deux flux de circulation apparaissent sur deux plans différents et une étude en 3D devient inévitable. Une telle configuration peut être trouvée dans plusieurs applications comme dans les systèmes géothermiques dans les aquifères côtiers ou dans les îles où la mer/océan peut générer un gradient de salinité et les puits géothermiques créent un gradient thermique. Nous avons développé une solution semi-analytique basée sur la série de Fourier pour une telle configuration. Une technique efficace est développée pour résoudre les

équations d'écoulement, de transport de masse et de transfert de chaleur dans l'espace spectral. Le modèle semi-analytique développé montre une haute performance en comparaison avec les codes numériques existants et les résultats fournissent une meilleure compréhension de la structure 3D de l'écoulement dans la convection thermohaline. Le modèle développé peut être utilisé à des fins de benchmarking ou pour expliquer l'interrelation des paramètres associés à la physique du problème. Ce sujet est développé dans le chapitre III.

Ce travail a fait l'objet d'un article publié dans la revue *Water Resources Research* (Tabrizinejadas et al., 2020).

### ***1.3.2 Aperçu du chapitre IV : Modèle numérique robuste pour la convection réactive-thermohaline du CO<sub>2</sub> dans un réservoir saturé en saumure***

Le réchauffement climatique reste l'un des problèmes environnementaux les plus importants et la principale raison en est une quantité excessive d'émissions de gaz à effet de serre dans l'environnement, dont le plus important est le dioxyde de carbone (CO<sub>2</sub>). Malgré les efforts déployés pour réduire l'utilisation des combustibles fossiles dans les centrales électriques et les remplacer par des sources renouvelables, la plupart des centrales électriques dans le monde sont actuellement alimentées par des combustibles fossiles (Whitley 2018). Par conséquent, l'émission de CO<sub>2</sub> dans l'atmosphère est actuellement inévitable et jusqu'à ce que d'autres technologies peu coûteuses, propres et abondantes soient disponibles, un moyen temporaire possible de faire face au réchauffement climatique est d'atténuer le CO<sub>2</sub> existant dans l'atmosphère. À cette fin, plusieurs approches ont été proposées et, parmi elles, la séquestration géologique du CO<sub>2</sub> (SCG) est la technologie la plus recommandée pour atténuer les émissions de CO<sub>2</sub> à grande échelle dans l'atmosphère.

La séquestration géologique du CO<sub>2</sub> consiste à capturer les émissions de CO<sub>2</sub> au niveau des sources de combustion industrielles (principalement les centrales électriques utilisant des combustibles fossiles), à les comprimer pour former l'état supercritique du CO<sub>2</sub>, à les transporter et à injecter le CO<sub>2</sub> supercritique dans des formations géologiques telles que des aquifères salins ou des réservoirs de pétrole ou de gaz épuisés, en vue d'un stockage à long terme. Dans l'accord de Paris, cette approche est présentée comme l'une des solutions les plus prometteuses au réchauffement climatique (CCNUCC 2015).

Il est essentiel de comprendre le devenir du CO<sub>2</sub> dans la formation géologique pour garantir la séquestration et prévoir l'impact du CO<sub>2</sub> dissous sur les aquifères et les réservoirs. Lorsque l'état supercritique du CO<sub>2</sub> est injecté dans le réservoir, la dissolution du CO<sub>2</sub> dans la saumure

a lieu en raison des processus de mélange et une saumure chargée en CO<sub>2</sub> est formée. La densité du CO<sub>2</sub> dissous est plus élevée que celle de la saumure sous-jacente. Il en résulte une dissolution supplémentaire liée au fingering induit par la gravité, causé par le flux convectif. En outre, le CO<sub>2</sub> dissous réagit avec les minéraux primaires des roches tels que Ca<sup>2+</sup>, Mg<sup>2+</sup>, Fe<sup>2+</sup>, etc. Ces réactions géochimiques, accompagnées de l'équation de transport, entraînent une plus grande dissolution du CO<sub>2</sub> dans la saumure. La combinaison de ces processus est connue sous le nom de processus convectif-réactif et a été largement étudiée dans la littérature avec l'application des GCS. Une hypothèse courante dans les études existantes consiste à supposer que le réservoir est isotherme. Cependant, le gradient de température existe naturellement dans le réservoir en augmentant vers la profondeur ou il est induit par l'injection de CO<sub>2</sub>. Par conséquent, un gradient de température existe dans le domaine et affecte la densité et la viscosité du fluide, ainsi que le taux de réaction géochimique. Notre contribution à cet égard a été de développer un modèle numérique avancé qui prend en compte les effets du gradient de température sur la convection et la réaction et conserve l'efficacité pour la modélisation à grande échelle de longueur et de temps tout en maintenant la précision. Pour ce faire, étant donné que plusieurs processus physiques sont impliqués dans les GCS et qu'ils sont fortement couplés de manière non linéaire, un schéma numérique avancé est nécessaire pour la discrétisation de chaque processus physique. Le terme de réaction est implémenté avec une approche non itérative séquentielle (SNIA) et l'erreur numérique intrinsèque due au fractionnement de l'opérateur (OS) est contrôlée par l'implémentation d'une approche adaptative de pas de temps. La précision, l'efficacité et la robustesse du nouveau modèle développé sont démontrées en comparant les résultats avec un modèle d'éléments finis standard dans un benchmark carré.

Dans la deuxième étape du travail, nous avons effectué des simulations pour comprendre les effets de la température sur la vitesse de réaction et le flux convectif associé à la densité et à la viscosité. Notre analyse s'est basée sur la comparaison de trois modèles avec des niveaux croissants de complexité et de réalisme. Le premier modèle est le modèle "isotherme" qui considère une température constante dans le temps et l'espace et qui imite les modèles habituellement utilisés dans les études précédentes, qui sont basés sur des hypothèses isothermes. Le second modèle est le modèle de "température linéaire" qui considère une augmentation linéaire de la température vers la profondeur du domaine, mais la température est constante dans le temps. Dans ce modèle, l'effet du gradient de température est pris en compte pour la réaction géochimique, mais il est négligé pour le processus de convection thermique. Le troisième modèle est le modèle 'RTHC' qui considère la température variable dans le temps

et l'espace. Les comparaisons entre les modèles ont d'abord été effectuées sur une référence carrée homogène. Ensuite, elles ont été étendues à une simulation sur le terrain, dans le champ de Viking, en mer du Nord, pour comprendre l'effet du gradient de température en accompagnement de l'hétérogénéité et de la complexité géométrique à grande échelle spatiale et temporelle de la simulation avec la perturbation du gradient de température naturel due à l'injection de CO<sub>2</sub>.

Étant donné que plusieurs paramètres d'entrée dans les GCS sont incertains, il est essentiel d'étudier la sensibilité des résultats aux paramètres incertains. L'objectif principal de notre travail étant d'étudier l'effet de la température sur les processus de dissolution dans les SCG, nous avons limité l'analyse de sensibilité aux paramètres régissant la vitesse de dissolution.

Ce travail est développé dans le chapitre IV et a fait l'objet d'un article soumis au journal of greenhouse gas control.

#### **1.4. Processus de dissolution dans les réseaux de fractures discrètes**

L'écoulement de l'eau dans les roches carbonatées est généralement associé au processus de dissolution et au transport des espèces dissoutes. Les réseaux de fractures existant naturellement ainsi que les fractures induites par la dissolution peuvent affecter de manière significative la transmissivité du domaine qui, à son tour, affecte les processus d'écoulement, de transport et de dissolution. Lorsque la porosité et la perméabilité des roches sont faibles, comme dans les roches carbonatées, les fractures agissent comme des voies préférentielles pour les fluides. Par conséquent, l'écoulement des fluides dans la matrice rocheuse peut être négligé et le domaine peut être représenté comme un réseau de fractures discrètes (DFN).

La modélisation des processus de dissolution dans les DFN révèle des défis spécifiques qui ne sont pas présents dans les milieux non fracturés. Ce défi provient de l'évolution dynamique du domaine fracturé en raison de la dissolution géochimique. L'élargissement des fractures résultant du processus de dissolution affecte continuellement le champ d'écoulement des fluides. L'écoulement, à son tour, affecte le processus de dissolution et le transport des espèces dissoutes. Les processus sont donc couplés et non linéaires. En outre, dans les DFN, l'ensemble de l'écoulement est affecté aux fractures et le stockage est ignoré dans la matrice, de sorte que le transport des espèces dissoutes est un processus dominé par l'advection. Dans de tels cas, les méthodes numériques standard, telles que les méthodes d'éléments finis (FE) ou de volumes finis (FV), peuvent générer une diffusion numérique susceptible de sous-estimer les processus de dissolution. Les méthodes numériques standard peuvent également introduire des

oscillations non physiques qui entraînent des problèmes de convergence et limitent l'applicabilité des modèles.

On sait que la méthode des éléments finis de Galerkin discontinu (DG) est bien adaptée pour capturer les fronts mobiles aigus dans le cas d'un transport dominé par l'advection (Younes et Ackerer, 2008). L'utilisation du schéma DG pour la discrétisation du terme hyperbolique de l'équation de transport a été largement rapportée dans la littérature. Cependant, à notre connaissance, la méthode DG n'a jamais été appliquée aux processus de dissolution dans les DFN. Pourtant, il existe un potentiel important pour une telle application, car la méthode DG peut, d'une part, réduire la diffusion numérique et mieux prédire les processus de dissolution, et d'autre part, améliorer la stabilité de la solution et améliorer la convergence des solveurs non linéaires.

Notre contribution à cet égard a consisté à développer un modèle numérique avancé pour la simulation des processus de dissolution dans les DFN et à étudier les effets de la dissolution géochimique sur l'évolution des fractures et les processus d'écoulement et de transport, en tirant parti du nouveau modèle développé. Le modèle numérique est développé sur la base d'un schéma DG au vent pour le transport. Dans une DFN, à l'intérieur des fractures, l'équation de transport est similaire à celle des domaines non fracturés. Le principal défi pour ce schéma est l'application aux fractures entrecroisées. En fait, l'idée principale du schéma DG proposé dans la littérature (Younes et al., 2009) est d'utiliser la valeur moyenne de la concentration sur une cellule de calcul ainsi que les composantes du gradient de concentration comme variables primaires. Le solveur de Riemann est ensuite utilisé pour évaluer la concentration aux nœuds. Une nouvelle formulation est développée dans ce travail pour les nœuds où plusieurs fractures se croisent. L'approximation du vent ascendant dans les intersections de fractures est obtenue sur la base d'une méthode de calcul de la moyenne avec le poids des vitesses du vent ascendant. Les processus chimiques sont couplés aux processus d'advection-dispersion et résolus simultanément afin d'éviter les erreurs de séparation des opérateurs. L'écoulement est simulé à l'aide des équations de Richards. Cela permet de traiter les écoulements saturés et non saturés. L'équation de l'écoulement est discrétisée à l'aide de la méthode des éléments finis mixtes (MFE). La technique d'agrégation de masse développée par (Koohbor et al., 2020) est employée pour la discrétisation de l'écoulement afin d'éviter les dépassements et les sous-déplacements observés dans les simulations transitoires avec de petits pas de temps.

Pour la discrétisation temporelle, une méthode d'ordre supérieur est utilisée à travers la méthode des lignes (MOL). La MOL s'est avérée très efficace pour résoudre des systèmes d'équations

hautement non linéaires. Avec la MOL, les dérivées spatiales sont discrétisées tandis que les dérivées temporelles sont conservées sous leur forme continue. Cela permet de convertir les équations aux dérivées partielles en un système d'équations différentielles ordinaires. Ce système est résolu à l'aide d'un solveur implicite adaptatif d'ordre élevé.

Le nouveau schéma DG est comparé à une solution FE standard obtenue à l'aide de COMSOL Multiphysics et à une solution FV obtenue à l'aide d'un code interne. Le nouveau schéma DG est ensuite utilisé pour comprendre les effets de la vitesse de réaction sur les dissolutions, l'écoulement et les caractéristiques de transport basées sur différents processus physiques contrôlant la vitesse de dissolution. L'effet des processus de dissolution sur les processus d'écoulement et de transport est étudié à l'aide de différents modèles de dissolution en fonction des régimes du taux de réaction et de l'écoulement.

Ce sujet est développé dans le chapitre V. Les résultats de ce travail ont été soumis au journal of advances in water resources.

## **Chapter II: On the Validity of the Null Current Assumption for Modeling**

### **Sorptive Reactive Transport and Electro-Diffusion in**

#### **Porous Media**

##### **2.1. Introduction**

Mass transfer accompanied by chemical reactions, or reactive transport (RT), in porous media is central to a wide range of applications in the fields of geology, hydrogeology, engineering and environmental research. For instance, RT processes are encountered in geological carbon dioxide sequestration (Babaei and Islam, 2018; Islam et al., 2014), geothermal systems (Kim et al., 2015; Erfani et al., 2019), groundwater pollution (van der Lee et al., 2002) and nuclear waste disposals (Spycher et al., 2003).

Several applications involving RT processes reveal the necessity of the development of new models to better describe the chemical processes. Many modern codes have extensive capabilities and have been used to simulate RT in different applications. In particular, for problems of solute transport in saturated porous media, CrunchFlow (Steefel and Lasaga, 1994), Phreeqc (“User’s Guide to PHREEQC (Version 2), 1999), TOUGHREACT (Xu et al., 2004), MIN3P (Mayer et al., 2002), PHT3D (Prommer et al., 2003; Post and Prommer, 2007) and PHAST (Parkhurst et al., 2004) exemplify the RT simulators established in previous years. In recent years, significant advances have been achieved in the development of RT codes due to the increase of capability in coupling transport simulators with geochemical reactive codes. For instance, modules have been developed that couple Phreeqc, a widely used geochemical package (Charlton and Parkhurst, 2011; Parkhurst and Wissmeier, 2015), to other simulators (Kazemi Nia et al., 2013; Muniruzzaman and Rolle, 2016).

Most of the RT codes, mentioned above, neglect the coulombic interactions between the charged particles, as they are based on the classical Fick’s law. However, it is well known that electro-diffusion processes cannot be simulated with Fick’s law that assumes a constant diffusion coefficient for each dissolved species. This classical view assumes that the movements of each dissolved species in a system are merely based on concentration gradients. However, in a multicomponent electrolyte solution, each individual dissolved species migrates differently according to its ionic properties such as charge, ionic size or ionic mobility (Cussler and Cussler, 2009). Therefore, the features of a multicomponent electrolyte system cannot be fully represented by Fick’s law, and including electrochemical migration to a multicomponent reactive transport

model requires a departure from Fick's law by the use of the Nernst-Planck equation. This equation takes the ionic interactions into account by including the electric field generated by such interactions. Among the previous studies on electrochemical migration, more attention is given to the electro-diffusion process where the diffusion of charged particles is combined with their migration in a self-consistent electric field (Rubinstein, 1990). Several studies such as (Ben-Yaakov, 1972), (Katz and Ben-Yaakov, 1980), (Lasaga, 1979) and (Boudreau et al., 2004) exemplify electro-diffusion process with the diffusive flux as the only flux presented in the domain. The common assumption in these studies is that no electric current is passing through the domain. This is known as the null current (NC) assumption. It leads to an explicit determination of electric field in terms of species concentration and known parameters of the multicomponent electrolyte system. The advantage of the NC assumption is that it reduces the number of unknowns and simplifies the implementation of the problem into existing numerical codes. The electro-diffusion processes are represented as in Fick's law, but with specific diffusion coefficients that depend on concentrations. In recent years the NC assumption-based models have been used to solve problems with higher levels of sophistication and non-linearity. For instance, three benchmarks are presented in Rasouli et al., 2015 with the NC assumption and accurate analyses on the role of electrochemical migration in the mass transport process. A 2D multicomponent reactive transport model is developed in Muniruzzaman and Rolle, 2016 takes the electrostatic interactions during transport of charged ions in physically and chemically heterogeneous porous media into account. In Rolle et al., 2018, a multi-dimensional modeling approach is proposed, illustrating the importance of coulombic coupling in diffusive-dispersive Nernst-Planck based fluxes in one, two and three-dimensional porous media domains.

Despite the popularity of the NC assumption and its major contribution in simulation and understanding the electrostatic processes, this assumption is not able to describe a domain subjected to an external field. In this case, the total electric field represented by the Nernst-Planck equation is affected by both internal interactions of ions (liquid junction potential) and an externally applied electric field (Frizon et al., 2003; Mainault et al., 2005). In addition, the elimination of the electric field from the transport equation makes the description of electro-diffusion processes independent of the permittivity of the medium and dielectric properties of the porous media. Moreover, the NC assumption is not physically valid when the charged species participating in the mass fluxes are not the total charged species existing in the domain (Birgersson and Karnland, 2009). The aforementioned challenges of the NC assumption can be avoided by using a more general approach that couples the Nernst-Planck equation with the Poisson equation (NPP). In the Poisson equation, the electric field is linked to the total ionic concentration of species in the system and the dielectric

property of the medium. This approach is rarely used in reactive transport models because it cannot be easily coupled with existing codes.

Despite the common use of the NC assumption in models dealing with reactive transport and electro-diffusion, the validity of this assumption is questionable. Thus, the main goal of this work is to evaluate the validity of the NC assumption by comparing it to a full model based on the NPP equations. To the best of our knowledge, this topic has never been investigated in the past. Thus, we first presented a comprehensive formulation of the NPP equations. We also developed a (1D/2D) finite element model to solve these equations, using the mathematical module of COMSOL Multiphysics. With the same module, we also developed a (1D/2D) finite element model based on the NC assumption. We validated the developed models based on common benchmarks and we compared them in different configurations of RT in order to evaluate the validity of the NC assumption.

## 2.2. Mathematical and numerical models

### 2.2.1. General NPP model

The Nernst-Planck equation in corporation with the conservation of mass equation is used to describe the migration of interacting species. It accounts for molecular diffusion, electro-diffusion and advection:

$$\frac{\partial C_{total_i}}{\partial t} + \nabla \cdot \mathbf{J}_i = 0; \quad \mathbf{J}_i = -D_i \left( \nabla C_{D_i} + \frac{c_i F}{RT} z_i \nabla \psi \right) + C_{D_i} \mathbf{q} \quad (2.1)$$

where  $C_{total_i} [mol / m^3]$  is the total concentration of  $i^{th}$  species,  $t [s]$  is the time,  $\mathbf{J}_i [mol/m^2.s]$  is the total mass flux,  $D_i [m^2/s]$  is the species-dependent diffusion coefficient,  $C_{D_i} [mol/m^3]$  is the dissolved concentration of  $i^{th}$  species,  $F = 96485 [C/mol]$  is the Faraday constant,  $R = 8.341 [J/K.mol]$  is the gas constant,  $T [K]$  is the absolute temperature,  $z_i [-]$  is the charge number,  $\psi [V \text{ or } J/C]$  is the electric potential and  $\mathbf{q} [m/s]$  is the Darcy's velocity.

The Poisson equation, giving the electrical potential as function of electrical charges, is as follows:

$$\varepsilon_M \nabla^2 \psi = -F \sum_i z_i C_{total_i} \quad (2.2)$$

where  $\varepsilon_M [F/m]$  is the permittivity of the porous medium.

The permittivity of the domain depends on the soil porosity and permittivity of the solid grains. According to the averaging method (Brovelli and Cassiani, 2008), the bulk permittivity, representing the porous medium is given as follows:

$$\varepsilon_M = \phi \times (\varepsilon_r)_w \varepsilon_0 + (1 - \phi) \times (\varepsilon_r)_s \varepsilon_0 \quad (2.3)$$

where  $\phi [-]$  is the porosity of the porous medium,  $(\varepsilon_r)_w [-]$  and  $(\varepsilon_r)_s [-]$  are the relative permittivity of water and solid grains, respectively and  $\varepsilon_0 (= 8.85 \times 10^{-12} [F/m])$  is the vacuum permittivity. The permittivity of water is higher than that of solid grains. Thus, in a saturated porous media, the increase of porosity leads to the increase in the average permittivity of porous media. We neglect the effect of sorption on the permittivity of the solid grains.

The NC assumption could be invalid in the case of sorption processes that occurs with the cations dissolved in multicomponent electrolyte systems due to the negatively charged surfaces of clay soils (Birgersson and Karnland, 2009). The model used for simulating reactive transport is given here. For the sake of simplicity, the linear isotherms have been considered in this study. The sorbed concentration at each time step is therefore defined as a constant ratio of the total concentration of each species. The total concentration for the species having sorption is detailed as follows:

$$C_{total_i} = \phi C_{D_i} + (1 - \phi) \times \rho_b C_{B_i} \quad (2.4)$$

where,  $C_{D_i} [mol/m^3]$  and  $C_{B_i} [mol/kg]$  are the dissolved and sorbed concentration of the  $i^{th}$  species, respectively.  $\rho_b = 2200 [kg/m^3]$  is the bulk density of the medium

As common in the literature, we assume that the porosity is not affected by the sorption processes and consequently, the permittivity used in NPP models is not affected by the sorption. Therefore, the continuity equation of each species is as follows:

$$\phi \frac{\partial C_{D_i}}{\partial t} + (1 - \phi) \times \rho_b \times \frac{\partial C_{B_i}}{\partial t} + \nabla \cdot J_i = 0 \quad (2.5)$$

Using the sorption capacity,  $(\partial C_{B_i} / \partial C_{D_i})$ , the above equation can be rewritten as follows:

$$\left( \phi + (1 - \phi) \times \rho_b \times \frac{\partial C_{B_i}}{\partial C_{D_i}} \right) \frac{\partial C_{D_i}}{\partial t} + \nabla \cdot J_i = 0 \quad (2.6)$$

### 2.2.2. Electro-neutrality and NC assumption

Two physical requirements of the electro-neutrality are: (i) the total charge should be zero at every point of the domain and (ii) no electric current should pass through the domain. The following equations satisfy these two conditions, respectively:

$$\sum_i z_i C_{total_i} = 0 \quad (2.7)$$

$$\sum_i z_i J_i = 0 \quad (2.8)$$

Different views of electro-neutrality have been discussed in the literature. Electro-neutrality has been defined as equation (2.7) in (Lasaga, 1979). However, equation (2.8) is introduced as the only requirement of electro-neutrality in (Ben-Yaakov, 1972). These assumptions are investigated in (Boudreau et al., 2004) and it has been shown that both are strictly equivalent and lead to the same formulation as long as there is no initial electric charge and no electric current imposed to the domain.

In this work, the considered benchmarks deal with no initial charge and no external electric field in the domain. Thus, both approaches of the NC assumption are equivalent and we employ equation (2.8). We substitute the Nernst-Planck flux from equation (2.1) in this equation. The following expression for the electric field can be obtained:

$$\nabla \psi = \frac{RT}{F} \times \frac{q \sum_j^{N_{aq}} z_j C_{D_j} - \sum_k^{N_{aq}} D_k z_k \nabla C_{D_k}}{\sum_l^{N_{aq}} D_l z_l^2 C_{D_l}} \quad (2.9)$$

where  $N_{aq}$  is the total number of dissolved species.

If one assumes local electro-neutrality of the solution, equation (2.9) can be simplified to:

$$\nabla \psi = -\frac{RT}{F} \times \frac{\sum_k^{N_{aq}} D_k z_k \nabla C_{D_k}}{\sum_l^{N_{aq}} D_l z_l^2 C_{D_l}} \quad (2.10)$$

Equation (2.10) represents the classical form of the electro-diffusion model. It is substituted into the electro-diffusion term of the Nernst-Planck model (equation (2.1)). Therefore, electric potential doesn't appear as an unknown in the final system of equations. This means that only dissolved species concentrations should be calculated. This simplifies the implementation of coulombic effects into existing RT codes. However, the validity of the expression linking the electric potential to the dissolved species concentrations cannot be valid in general. Validity of this expression, which is in other word the validity of the NC assumption, will be discussed in the next sections.

### 2.2.3. Equivalency of NPP systems and Null current assumption models

It has been proven that local electro-neutrality and null-current assumption are equivalent. We show here that NPP approach can be reduced to both previous approaches for some conditions. Rearranging Poisson equation gives:

$$\frac{\varepsilon}{F} \nabla^2 \psi = -\sum_i z_i C_{total_i} \quad (2.11)$$

This equation shows that if  $\varepsilon \nabla^2 \psi \ll F$ , then  $\sum_i z_i C_{total_i} \approx 0$ . This means that, in a media with low dielectric permittivity and/or with a smooth distribution of electrical potential, the Poisson formulation leads to the local electro-neutrality assumption. Considering the value of  $F = 96485 [C / mol]$  and that of permittivity used in this work ( $\varepsilon = 7.08 \times 10^{-10} F/m, 5.75 \times 10^{-10} F/m$ ), makes this assumption more reliable.

#### 2.2.4. Numerical models

Two numerical models (1D and 2D) have been developed based on the NPP equations and the NC assumption, respectively. The model base on the NPP equations is denoted by NPP-model, while the model based on the NC assumption is called NC-model. Both models have been developed using the framework of the finite element with COMSOL Multiphysics. COMSOL is a software that can be used to simulate problems involving multi-physical processes. It has two options to implement a model. The first option, called ‘wizard model’, in which a model can be developed by selecting physics available in COMSOL. In the second option, called “blank model”, a model can be developed by specifying the governing mathematical equation. In this case, COMSOL can be seen as an advanced finite element library for solving coupled partial differential equations. Electro-diffusion physics is not included in COMSOL. The implementation of the NPP and NC-models, with the ‘wizard model’ option is not an easy task. The NC model can be developed using the physics of the module ‘Transport of Diluted Species in Porous media - tds’, by assuming a variable molecular diffusion, which is a function of the concentrations. The NPP model, can be developed by coupling physics from the modules ‘Transport of Diluted Species in Porous media –tds’ and ‘Electric Currents - ec’. However, coupling these modules in COMSOL does not allow for considering the electro-diffusion processes. To do that, the electro diffusion term should be defined as a source term in the mass transport equation. However, this implementation with the ‘wizard model’ can only work for examples dealing with Dirichlet boundary conditions. In the case of Neumann boundary condition (i.e., a constant total mass flux), the electro-diffusive flux cannot be counted in the total mass flux as it is calculated as source term. Thus, due to this limitation, the NPP-model has been developed with the mathematic modules in COMSOL (‘blank model’). For mathematical consistency, we also developed the NC-model in the same way. For the NPP model, we choose the ‘General PDE form–g’ from the PDE interfaces in mathematic modules to implement the mass conservation equation. We define all terms separately, with the total species concentrations as dependent variables. The ‘General PDE form–g’ is coupled with the ‘Poisson’s equation–poeq’

module in the classical PDEs group of mathematic modules. In the ‘poeq’ module, the electric potential is defined as the dependent variable and it appears directly in the mass flux defined in the mass balance equation. Therefore, there is the possibility of formulating a complete definition of the mass flux consisting of all the Nernst-Planck equation terms. For the classical NC-model, the only requirement is a mass balance equation given in the ‘General PDE form–g’ module. The electric potential can be expressed as a function of dissolved species concentrations as shown before.

### 2.3. Verification

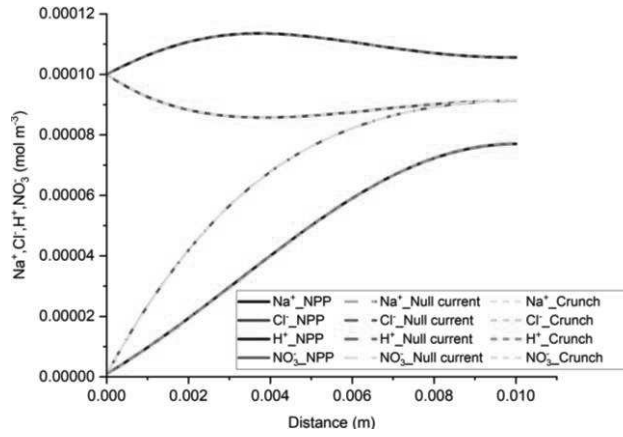
To gain confidence in the correctness of the NPP and NC models developed with COMSOL, we compare these models with the results of three benchmarks presented in Rasouli et al., 2015. These comparisons also allow for investigating the validity of the NC assumption. In that paper, these three benchmarks have been simulated based on the NC assumption with three reactive transport codes: CrunchFlow, MIN3P and PHREEQC. Since the results for these three simulators agreed well with each other, here we compare the results of our COMSOL models only with CrunchFlow. Beside electro-diffusion, benchmarks 1 and 2 deal with pure diffusion processes, while benchmark 3 deals with advection and molecular diffusion. Benchmarks 1 and 2 are in 1D while benchmark 3 is a 2D problem. The chemical systems of these benchmarks as well as a summary of the physical processes are presented in Table 2.1. The detailed explanations of three benchmarks (i.e. boundary conditions, initial conditions and physical parameters) are given in Appendix A. For the three benchmarks, the relative permittivity of water  $(\epsilon_r)_w$  and soil  $(\epsilon_r)_s$  to vacuum permittivity are considered to be equal to 80 [-] and 52 [-] at the temperature of 20° C. Benchmark 1 deals with pure water (Porosity = 1). Thus, the equivalent to the absolute permittivity is equal to that of water. For benchmarks 2 and 3 the porosity is set to 0.5. The bulk permittivity is calculated with the weighted averaging method as in equation (2.3).

**Table 2.1.** Summary of the three multicomponent reactive benchmarks

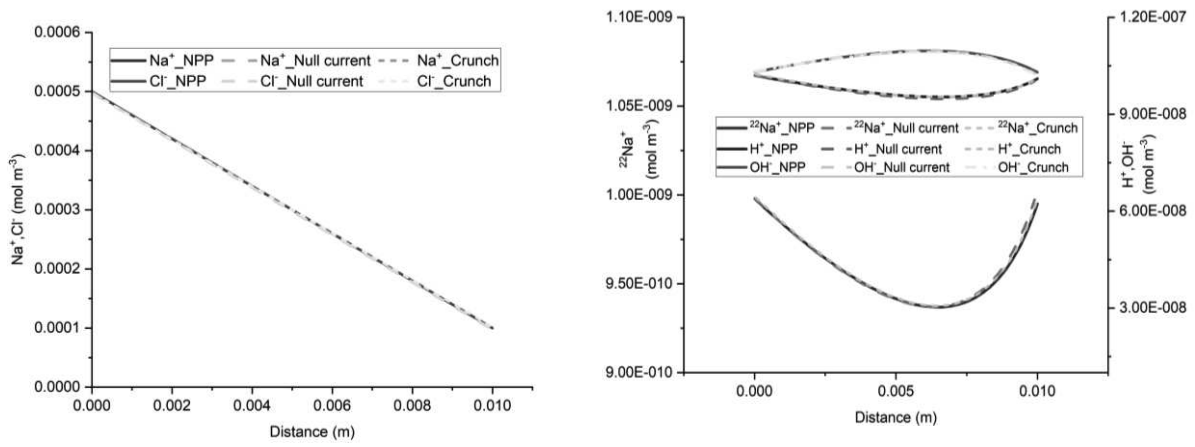
<b>Benchmark</b>	<b>Primary Components</b>	<b>Process</b>	<b>Dimension</b>
1	$H^+, NO_3^-, Na^+, Cl^-$	(Molecular/electro) Diffusion	1D
2	$Na^+, Cl^-, {}^{22}Na^+, H^+, OH^-$	(Molecular/electro) Diffusion	1D
3	$K^+, Cl^-, Mg^{++}$	(Molecular/electro) Diffusion/ Advection	1D/2D

<sup>1</sup>  ${}^{22}Na^+$  is another isotope of  $Na^+$  which is treated as a distinct component

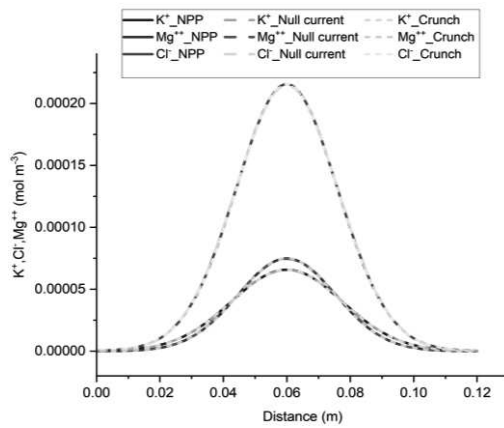
The results of the developed NPP and NC-models, for the 1D benchmarks, are presented in Figure 2.1. Similarly, the results of the 2D benchmarks are presented in Figure 2.2. The figures show also the solutions obtained with CrunchFlow in (Rasouli et al., 2015). Figures 2.1 and 2.2 show that the three solutions are indistinguishable. This confirms, on the one hand, the correctness of the implementation of the NPP and NC-models in COMSOL, and on the other hand, the equivalency between the NPP and NC-models. These results confirm the validity of the NC assumption for cases dealing with aqueous transport processes. In such cases, the total concentrations of charges are the ones participating in the mass flux. Therefore, the electric field calculated with the NC assumption on the mass flux is equivalent to a general case where the electric field is calculated from the total charges existing in the domain, which is the same approach used in the NPP model. This similarity between NPP and NC approaches for calculation of electric field as the origin of electrochemical migration through the domain leads to the same results for both NPP and NC models.



Benchmark1



Benchmark2



Benchmark3-1D

**Figure 2.1.** Comparison concentration results of NPP, NC and ‘Crunch’ models for 1D simulations of three benchmarks

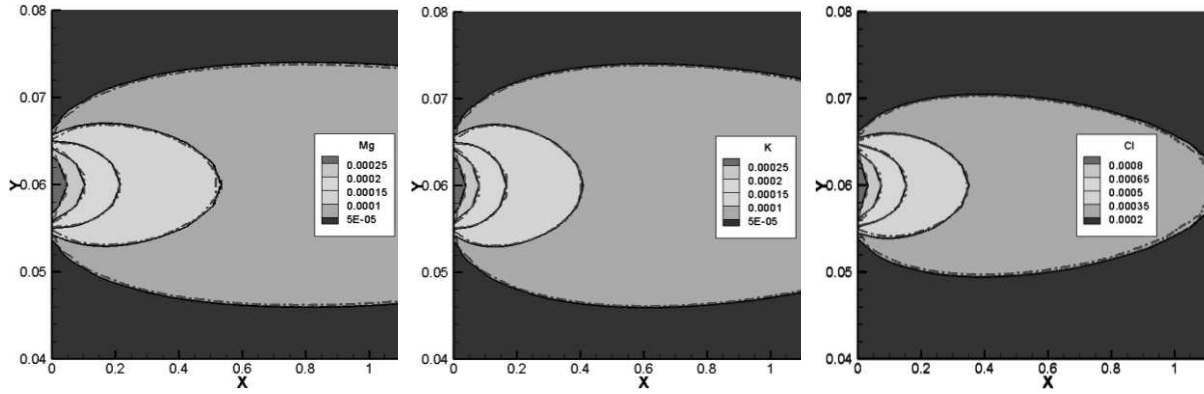


**Figure 2.2.** Comparison of Concentration results of NPP (Colors), NC (solid black lines) and ‘Crunch’ (dashed red lines) models for 2D simulations of benchmark 3

## 2.4. Effect of sorption reactions

The results of the previous section confirm the validity of the NC assumption in the case of reactive transport of aqueous species. However, it is well-known that transport processes are usually affected by sorption processes, due to the charge difference between the dissolved electrolyte systems and the surfaces of clay soils. When sorption processes occur, the charged species involved in the mass fluxes becomes different from the total charged species existing in the domain. In this case the NC assumption could become invalid. Thus, the main goal of this section is to investigate the validity of the NC assumption in the case of sorption reactions.

To do so we consider sorption processes in the three benchmarks presented in the previous section. In order to observe the sorption effects, the porosity of all benchmarks is set to be 0.5. In this study, we have considered a linear sorption model with a constant sorption capacity for each test case (equation (2.6)). In order to quantify and analyze the effects of sorption, we used two test cases, defined as ‘test case 1’ and ‘test case 2’ with low and high sorption capacity, respectively. For low and high sorption capacity, sorption capacities of  $5 \times 10^{-5}$  and  $10^{-4} [m^3 / kg]$  are considered, respectively. The domain is initially set to be at zero charges. All the other parameters, boundary, and initial conditions are kept the same as in the previous section. The same COMSOL models used in the previous section are modified to include sorption reactions and then used in the simulation of the different test cases in this section. The results are discussed in the next sections, in terms of total concentration, total charge, total current and electrical currents, respectively.

### 2.4.1. Total concentration

The total concentration results of NPP and NC-models for the three benchmarks defined with sorption are shown in Figures 2.3 and 2.4. As we can see, the results of the two approaches are different and the differences are more significant in test case 2 for each benchmark, due to the higher

sorption capacity considered for this test case. Some jumps appear in the results of the total concentration of the NC-model which also implies jumps in the results of dissolved and sorbed concentration. A mesh sensitivity analysis has been performed to obtain mesh-independent solutions and to ensure that these differences are not related to numerical artifacts. The jumps are mostly happening in the areas where the imposed initial concentration changes. For instance, in benchmark 1, jumps take place on the left, where the initial species concentration changes, in order to preserve higher and lower amounts for positive and negative charges, respectively. This can be explained by the underestimation of positive charges in the formulation of the electric field by the NC-model. In benchmark 2, the jumps take place in the middle of the domain, where the initial conditions for total species concentration change. Since benchmark 2 is a steady-state problem, the initial condition doesn't affect the final results. Figure 2.5 compares the results of the total concentration of the NPP and NC models with the linear initial condition for the species concentrations in the NC-model. There are no jumps in the total concentration results of the NC-model with linear initial conditions in this benchmark. However, the total concentrations of the species with electro-diffusion as the driving force which are  $^{22}\text{Na}^+$ ,  $\text{H}^+$  and  $\text{OH}^-$  (no initial gradient of concentration is imposed for these species) are different in the NPP and NC-models, with lower amounts of cations and higher amounts of anions in NC, because this approach does not consider the total amounts of cations in the formulation of electric field.

In benchmark 3(1D), the jumps can be seen for the NC-model around the 1cm middle source that has been applied to the domain as an initial injection of ions to assure the electrolyte solution. This is because the jumps in the NC-model preserve lower concentration for cations and higher concentrations for anions. For the 2D case the same trend of preservation for cations and anions is seen in parallel to the inlet Dirichlet boundary.

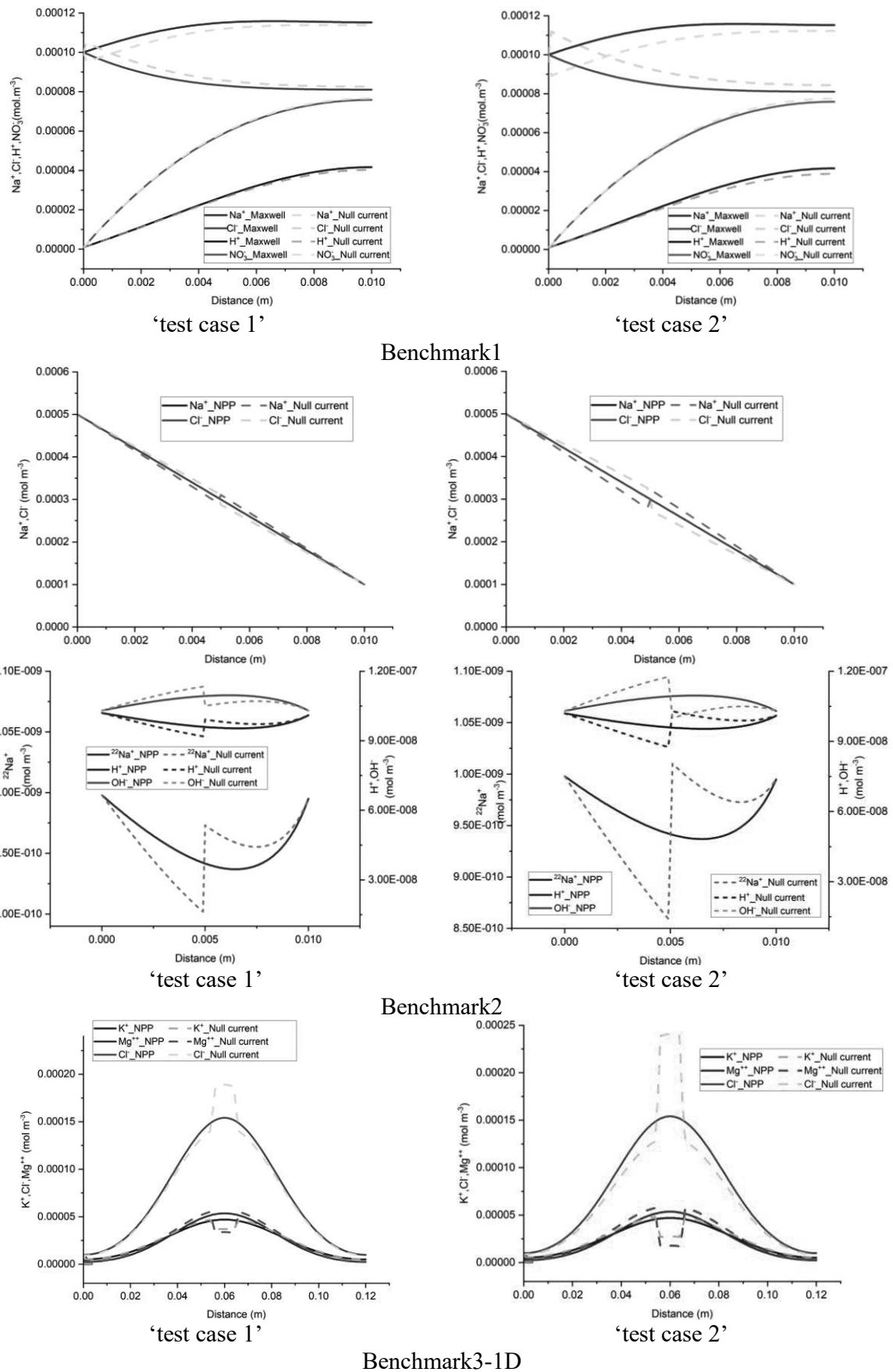
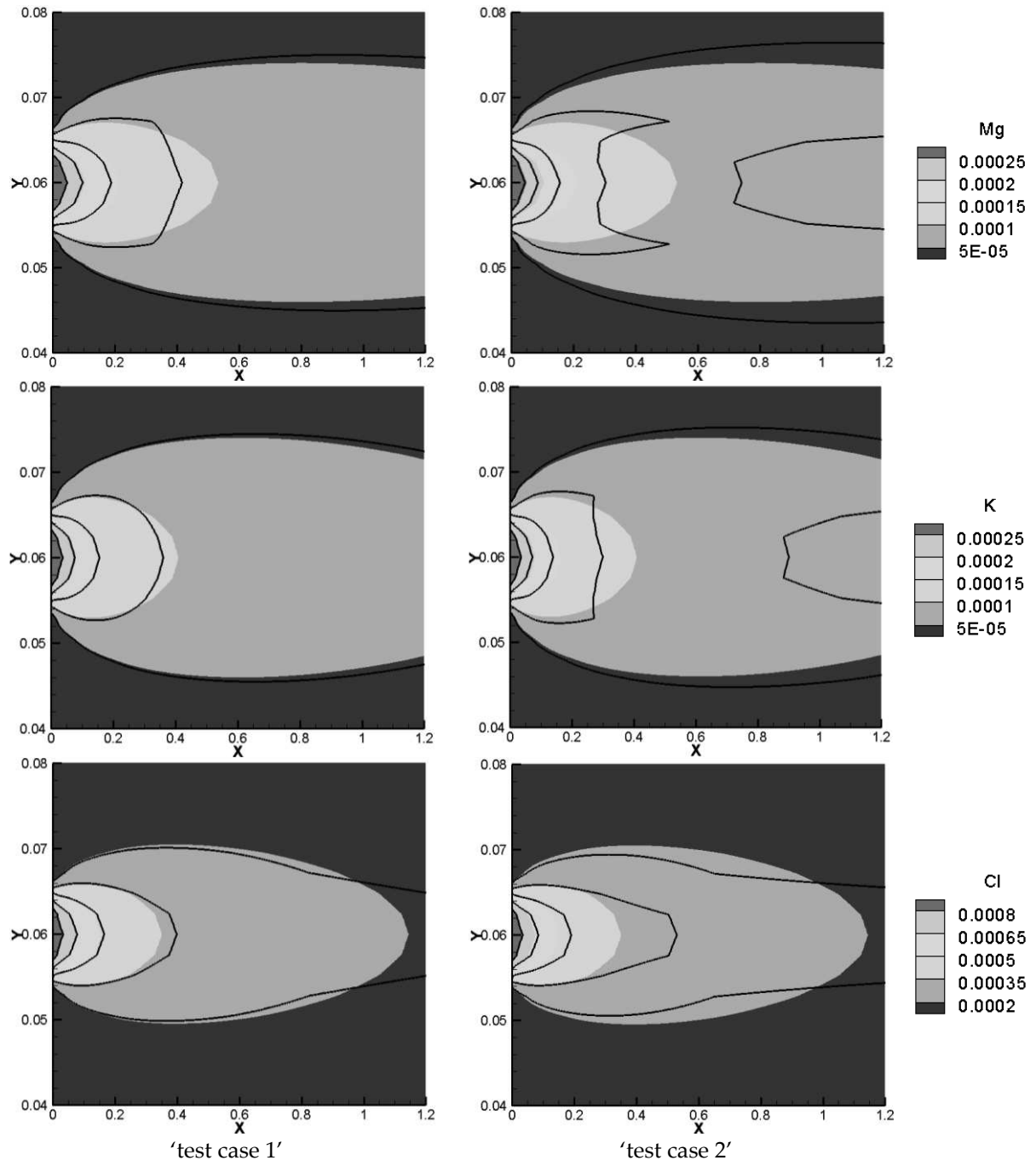


**Figure 2.3.** Comparison of total concentration results of NPP and NC-models for 1D simulations of the three benchmarks in the case of sorption reactions. Test case 1 deals with low sorptivity while test case 2 deals with high sorptivity.



Benchmark3-2D

**Figure 2.4.** Comparison of total concentration results of NPP (Colors) and NC (Lines) models for simulation of benchmark 3-2D with sorption: low sorptivity (test case 1 - left), high sorptivity (test case 2 -right)

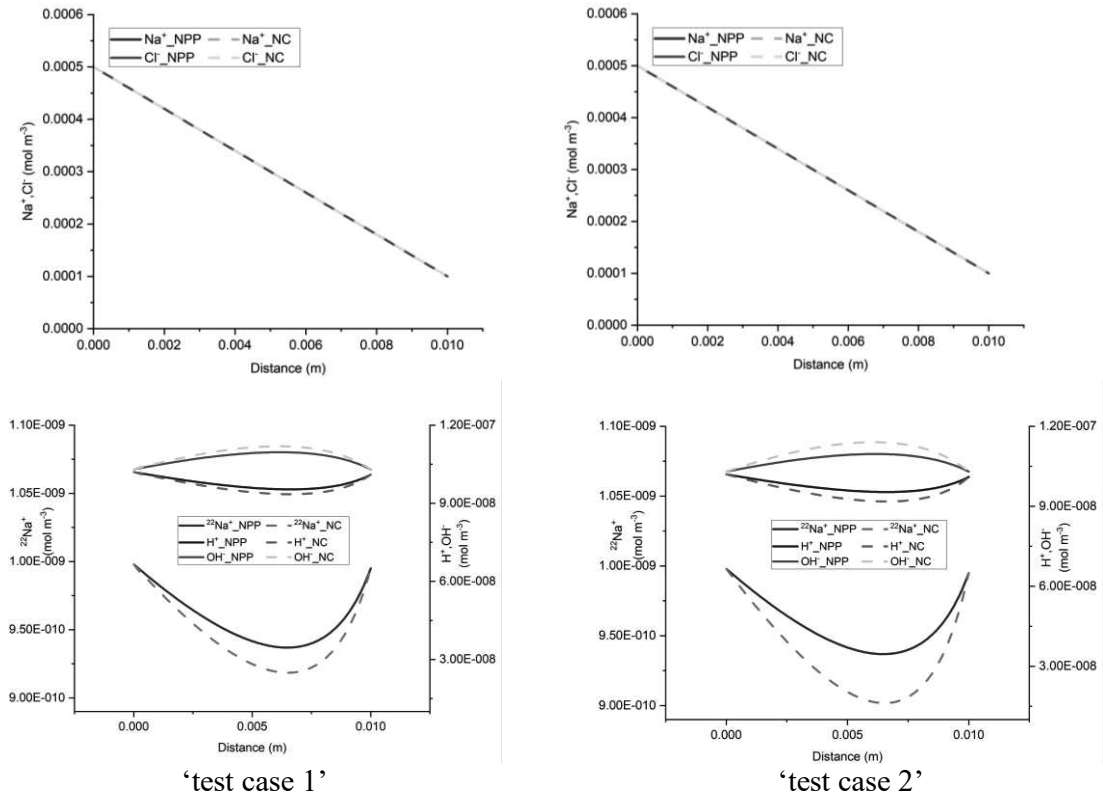


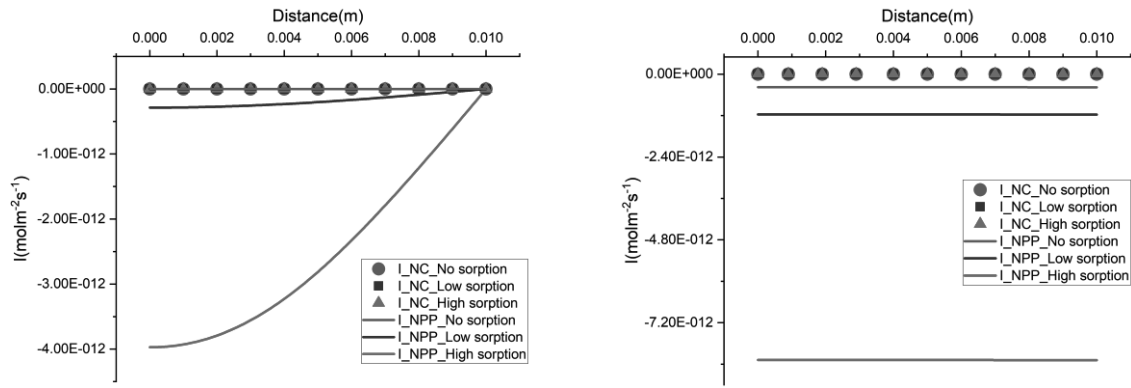
**Figure 2.5.** Comparison of total concentration results of NPP and NC models for Benchmark 2 with linear initial condition for NC model

In the three benchmarks, we can see that the total positive charge is underestimated in the NC-model and consequently, the total negative charge is overestimated. Although currently there is no experimental evidence for the full-validation of these results, the NPP-model with taking both sorbed and dissolved ionic species into account for the calculation of electric field is theoretically more reliable. Therefore, in the applications of solute transport, especially clay soils, the NPP model can be more representative of the physical processes than the classical NC-model.

#### 2.4.2. Total electric current

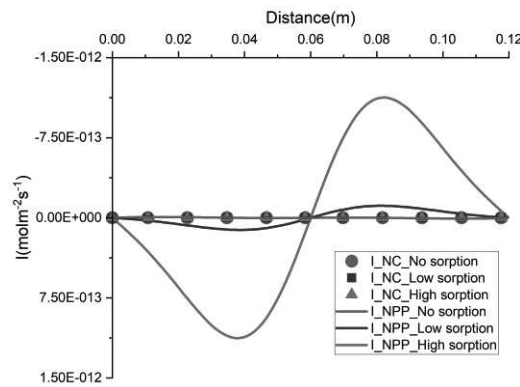
For the better understanding of the difference between the NPP and NC models, we investigate the total electrical current. In this section we plot the total electrical current through the domain calculated as  $I = \sum_i z_i \mathbf{J}_i$  which has been assumed to be equal to zero in the NC assumption. Figure

2.6 shows the total electrical current for 1D simulations. Obviously, total electrical current for the NC-model is zero in all 1D test cases. For the NPP model, however, the total electrical current deviates from zero when considering sorption and this value increases by increasing the sorption capacity in the model.



Benchmark1

Benchmark2



Benchmark3

**Figure 2.6.** Total electrical current for the 1D benchmarks with the NPP and NC-models

The total electrical currents of the 2D benchmark calculated with horizontal and vertical fluxes are shown in Figure 2.7. Fluxes in the horizontal and vertical direction are denoted ‘Ix’ and ‘Iy’, respectively. For the case without sorption, the values for Ix and Iy for both models are too small and they are considered to be zero in the numerical simulations and are not shown. By introducing sorption to the model and increasing it, the total electrical current in both directions increases in the NPP model. In the NC models, since the electro-diffusion is considered only in the vertical direction, the total electrical current for the vertical direction is equal to zero and is not shown. For the horizontal direction, the only considered flux is the advective flux. Therefore, in this direction, the electrical current in both approaches receives a value. The results for the total electrical current in the horizontal direction for NC and NPP-models are in the same order of magnitude. However, they are not exactly the same due to the differences in the total concentration results which brings the differences in dissolved concentration results.

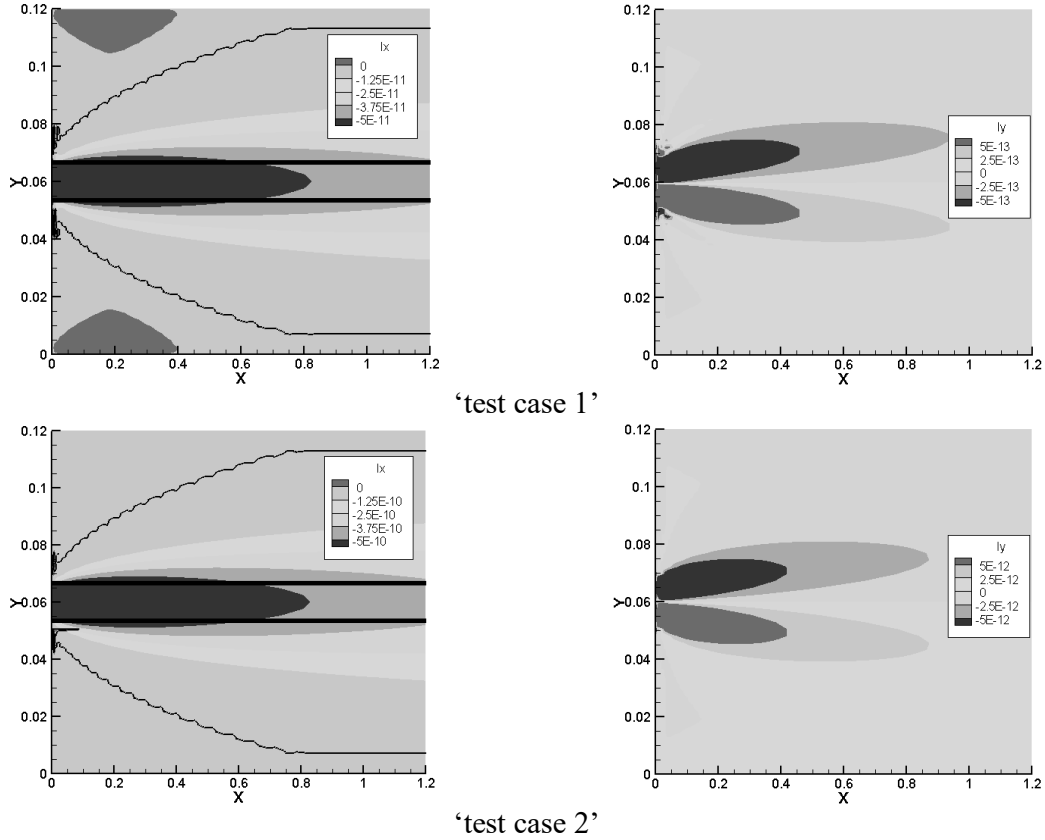


**Figure 2.7.** The total electrical current for the 2D benchmark in the horizontal (left) and vertical directions (right). The NPP model is represented with colors and the NC model with lines

### 2.4.3. Total charge

For a better understanding of the NPP and NC-models, we investigate in this section the total charge in the domain as, which is defined as:  $Z = \sum_i z_i C_{total_i}$ . Total charges for the 1D benchmarks are plotted in Figure 2.8. The results show that, for the NPP-model, the total charge in the domain tends to stay equal to zero. Therefore, in the areas with Dirichlet boundary conditions in benchmark 1 and benchmark 2, there are some jumps in the results of the total charge for the NPP-model because the non-zero total charge only exists at the Dirichlet boundary of the domain. However, for the NC-model we see that the amount of total charge increases with increasing sorption capacity. There are also some jumps in the results of the NC model in benchmark 3, in the area with a significant change in the initial concentration. Therefore, for the NC-model, despite the assumption of initial electro-neutrality in total concentration for all the test cases, the whole domain deviates from electro-neutrality as we introduce sorption to the model and increase it.

Figure 2.9 shows the total charge for the 2D benchmark, calculated by the NC-model. For the NPP models, the total charge for all the test cases (with or without) sorption is very small and in

numerical modeling, they are considered as zero. It is the same for the case without sorption in the NC-model. Therefore, in 2D, the total charge calculated with NPP approach for all test cases and the total charge calculated with NC approach for the case without sorption is not shown here.

The results are consistent with Boudreau et al., 2004, proving that for no sorption involvement in electro-diffusion process, NC and no Charges assumptions are equivalent. For the cases with sorption, as is shown in Figure 2.9, the NC-model shows the total charge to increase with increasing sorption capacity resulting in non-electroneutrality. Indeed, the NC-model maintains null current (or no charge according to Boudreau et al., 2004) for the water phase but allows charge accumulation on the solid phase. Thus, Figure 2.9 exhibits the sorbed charges in the case of the NC-model.

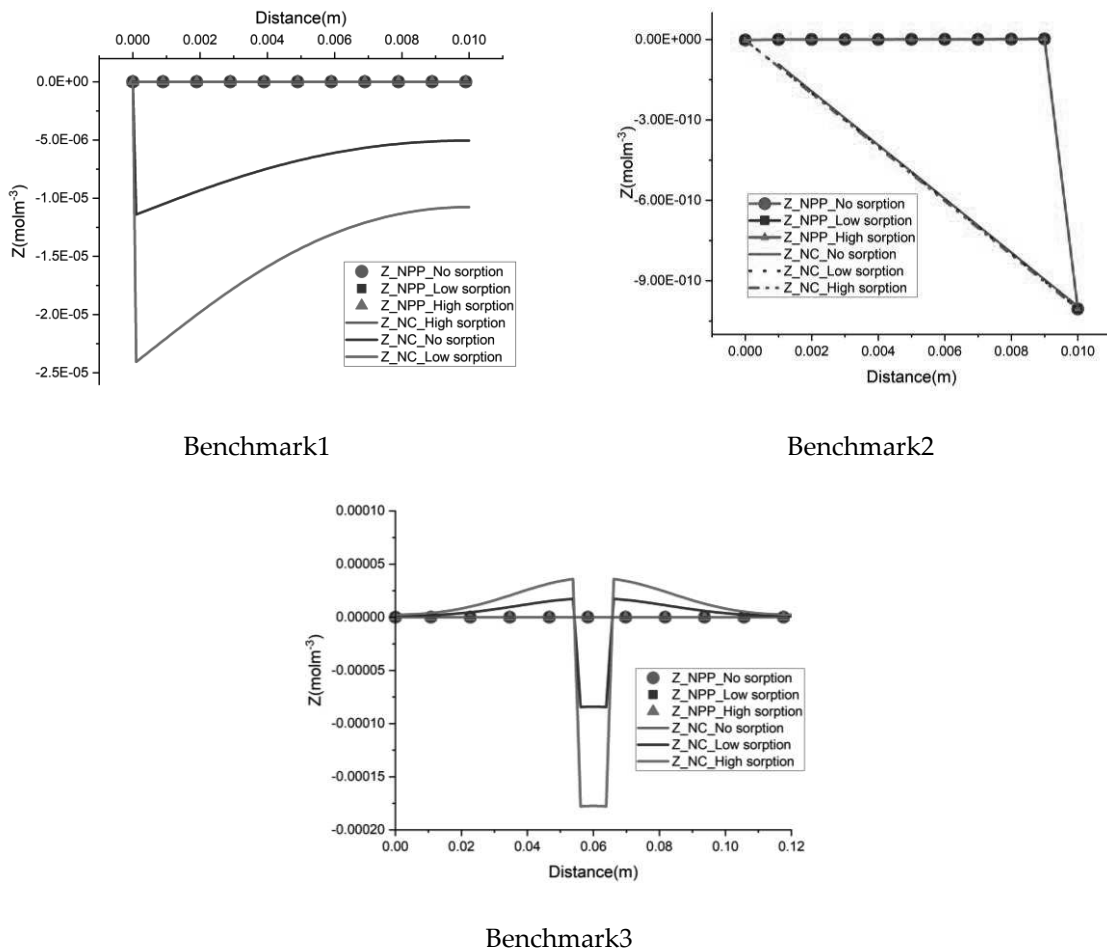


**Figure 2.8.** The total charge for the 1D benchmarks with the NPP and NC-models

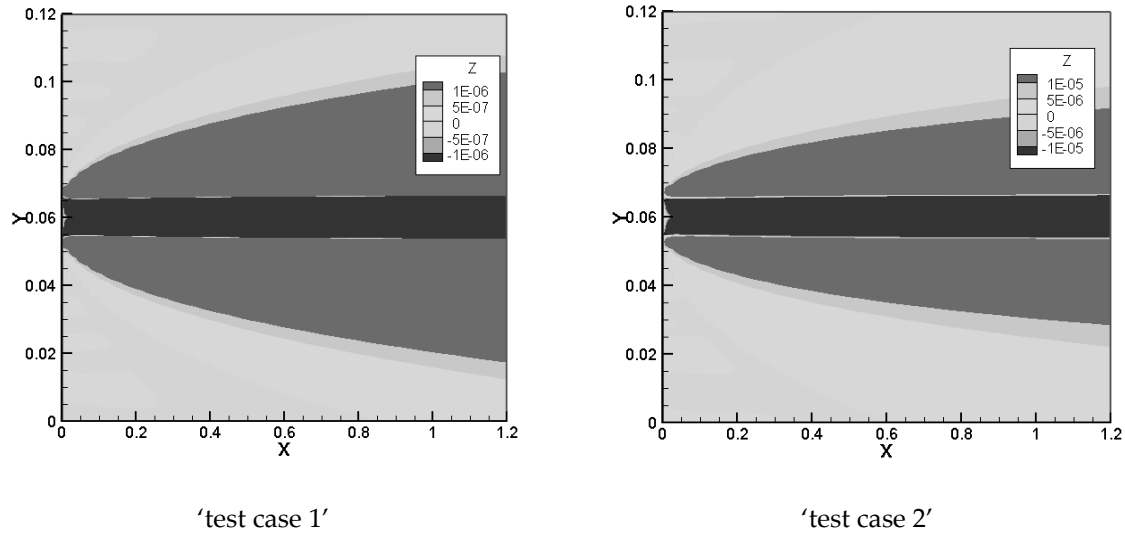
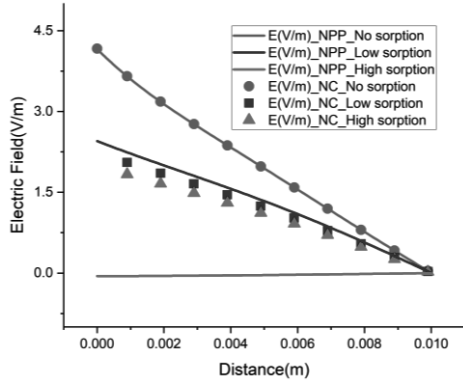


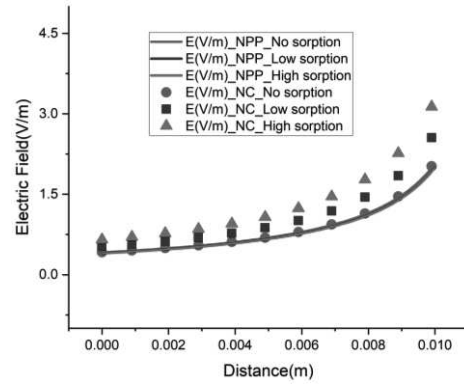
**Figure 2.9.** The total charge for the 2D benchmark with the NC-model

#### 2.4.4. Electric field

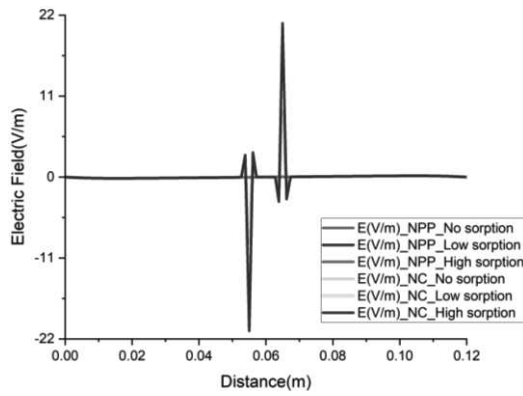
We also investigate the electrical field, for a deep understanding of the difference between the NC and NPP-models. In the NC models, the electric field is represented as a function of dissolved concentrations (equation 2.9). For the NPP models, however, it is calculated from the derivative of electric potential as  $E = -\nabla\psi$  which is linked to the total concentrations. The results of the electric field for the 1D benchmarks are plotted in Figure 2.10. For the cases without sorption, the NC and NPP models for the three 1D benchmarks agree well. By increasing the sorption capacity in benchmarks 1 and 2, the results of the two approaches become different and in benchmark 3, some jumps appear in the areas of a high concentration gradient. The electric fields for the 2D case of benchmark 3 calculated by the NPP and NC-models are shown in Figures 2.11(a) and (b), respectively. As we can see, for the NPP-model, in benchmark 3, either 1D or 2D, the electric field does not depend on sorption capacity. As shown in Figure 2.11(b), there are some oscillations in the electric field obtained from the NC assumption because of the dependence of the electric field on the concentration gradient, which may require a finer mesh. These oscillations increase with increasing sorption capacity for the NC-model.



Benchmark1

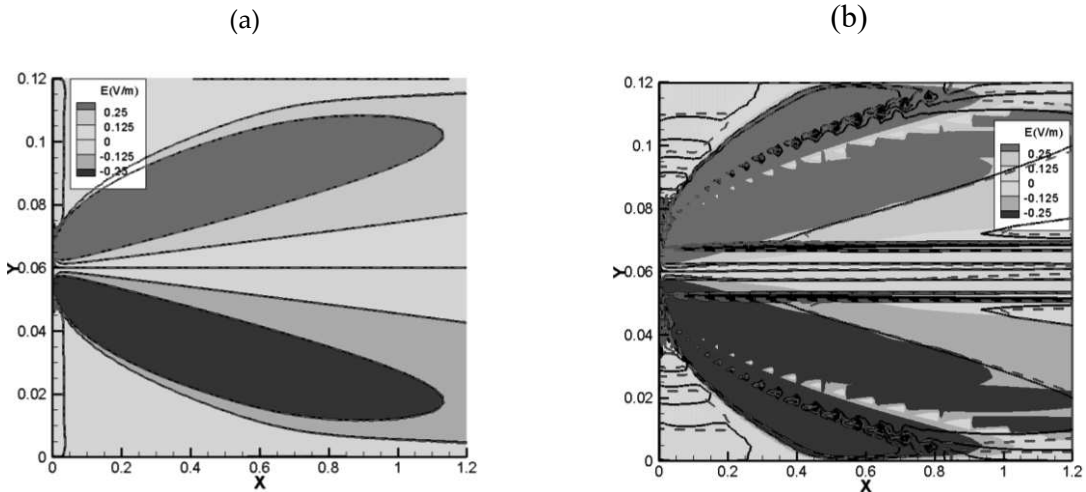


Benchmark2



Benchmark3

Figure 2.10. The electric field for the 1D benchmarks with the NPP and NC-models



Benchmark3-2D

Figure 2.11. Left: The electric field with NPP-model for the case of no sorption (colors), low sorption (black lines) and high sorption (red dashed lines). Right: Electric field with the NC-model for the case of no sorption (colors), low sorption (black lines) and high sorption (red dashed lines)

## 2.5. Conclusion

The problem of electro-diffusion is well-formulated by the Nernst-Planck equation containing advective and diffusive fluxes accompanied by an electro diffusion flux which considers an electric potential term. Existing studies of electro-diffusion in a domain without an external electric field are limited because of their assumption of null current on the Nernst-Planck equation. In this work, we propose a new approach based on the Nernst-Planck Poisson equation without any assumption of null current or charge. We show that this new approach leads to similar results as the usual NC approach if the electrical charge is only considered for the water phase. In such cases we show that NPP formulation leads to null current and charge in the domain without any assumption. However, this work proved that important differences between both approaches occur when also other than dissolved species create electric flow. For these cases, another system of equations has to be used which solves the Nernst-Planck equation containing advective, diffusive, and reactive fluxes accompanied by an electro-diffusion flux that considers an electric potential term. This electric potential is linked to the total ionic concentration in the Poisson equation and these two equations are solved together. The results we obtain from this system of equations for cases containing sorption are different from the results of the classical null current assumption. Since the dissolved ionic concentration in the system is only partly responsible for creating the electric potential term in the Nernst-Planck equation, a more valid model calculates the electric potential based on total ionic concentration. The NPP system is introduced as a more reliable solving approach in the cases with the inclusion of sorption. This new approach by the NPP system seems then to present some promising advantages that will be addressed in further works, such as, the existence of an external electric field, more flexibility for describing sorption processes, and electromigration through media with heterogeneities on dielectric permittivity. The existing benchmarks for electro-diffusion are based on the NC assumption. The results presented in this paper can be used as a new benchmark without this assumption.

The current work is based on numerical simulations. A full analysis has been performed to ensure numerical consistency of the solutions, but better confidence in the results can be obtained by confronting numerical simulation to laboratory experiments. The work shows, based on a case of sorption processes, the limitation of the NC assumption. However, this limitation could be not limited to sorption processes. Further studies with more generic analysis can be performed to fully understand the validity of the NC assumption. In the current model, we assume the permittivity of solid grains is constant. However, this permittivity can be affected by the sorption processes. The effect of sorption on permittivity could be an important topic for further investigations.

## **Chapter III: A Fourier series solution for transient three-dimensional thermohaline convection in porous enclosures**

### **3.1. Introduction**

Thermal and solute variations through porous media are the main causes of density changes of fluid and may give rise to density-driven flow. This phenomenon is usually called thermohaline or thermosolutal convection (THC). When the flow is driven by the concentration gradient of two different solutes the problem is called double diffusive convection (DDC). This phenomenon can be observed in several applications such as in geological carbon dioxide sequestration (Babaei and Islam, 2018; Islam et al., 2014), geothermal systems (Bao and Liu, 2019; Le Lous et al., 2015; van Lopik et al., 2015), underground thermal energy storage (Cabeza et al., 2015), salt mining (Zechner et al., 2019), salt domes (Jamshidzadeh et al., 2015; Evans et al., 2015), groundwater management (love et al., 2007), soil contamination (Neild et al., 2008) and waste disposal and seawater intrusion (Langevin et al., 2010; Thorne et al., 2006).

THC studies in real systems at field scale are increasingly reported in the literature. For instance, Yilmaz and Simsek, (2017) performed THC simulations of the Sorgun hydrothermal reservoir (Turkey). (Jamshidzadeh et al., 2015) investigated THC near salt dome at Napoleonville Dome (USA). Sheldon et al., (2012) assessed the potential for thermal convection to occur in the Perth Basin in Australia. Schilling et al., (2013) used THC simulations to provide insight into the subsurface thermal regime of the same basin. Magri et al., (2012) investigated fault-induced seawater intrusion in a geothermal system. However, in most theoretical and academic research and in several engineering applications, THC is often investigated using the problem of a porous enclosure. This problem is widely used to understand the THC physical processes and as a common benchmark for numerical models and schemes. Unstable configurations of this problem, in which the fluid density decreases with depth (vertical thermal and solute gradients either opposing or cooperating each other), have been extensively studied for different purposes. For instance, Cooper et al., (2001) performed an experimental study to evaluate the effect of buoyancy ratio on the development of double-diffusive finger convection in a Hele-Shaw cell. Based on a rectangular porous enclosure, Islam et al., (2013) investigated double diffusive convection of CO<sub>2</sub> in a brine saturated geothermal reservoir. Islam et al., (2014) extended their previous study to heterogeneous domains. Jamshidzadeh et al., (2013) used the modified thermohaline Elder problem to evaluate the effect of fluid dispersion on THC. Fingering phenomenon due to DDC has been investigated in Hughes et al., (2005) and Musuuza et al., (2012). A square porous enclosure is considered in Babaei

and Islam, (2018) to study convective-reactive CO<sub>2</sub> dissolution in aquifers and in Mansour et al., (2006) and Khadiri et al., (2010) to evaluate the Soret effect on THC. Several works on unstable THC are concerned with the onset of convective flow, based on linear or nonlinear stability analysis (e.g. Jafari Raad et al., 2019; Nield and Kuznetsov, 2013; Javaheri et al., 2010). Stable configurations (horizontal thermal and solute gradients) of the problem of THC in a porous enclosure have also been widely investigated in the literature as they are important in several applications. In this context, several previous works performed parameter sensitivity analysis to understand the effect of governing parameters on the flow, heat, and mass processes and on the overall rate of heat and mass transfer (e.g. Trevisan and Bejan, 1986; Alavyoon, 1993). Chamkha et al., (2002) studied THC in a rectangular porous enclosure with cooperating gradients and evaluate the effects of heat generation or absorption. Bennacer et al., (2001) investigated the effect of anisotropy on the average Nusselt and Sherwood numbers. The effect of anomalous fluid density was investigated in Sivasankaran et al., (2008). Mchirgui et al., (2012) studied entropy generation due to THC. The influence of a local non-equilibrium state on THC has been developed in Bera et al., (2014). Shao et al., (2016) developed a benchmark reference solution and investigated the effect of heterogeneity on THC. Most studies dealt with horizontal thermal and solute gradients either cooperating or opposing each other. Few studies investigated cases with crossed (vertical-horizontal) heat and mass gradients (Kalla et al., 2001; Mohamad and Bennacer, 2001; 2002; Mansour et al., 2006).

Despite the fact that THC processes are three-dimensional in nature, due to boundary conditions and/or domain heterogeneity, all of the works described above are limited by the assumption of two-dimensional flow. The 2D assumption is widely adopted to deal with computational complexity (computational cost, memory requirement, unphysical oscillations and convergence issues), as THC simulations require simultaneously solving the coupled nonlinear equations of flow, solute transport and heat transfer under variable fluid density. Studies that consider three-dimensional configurations of THC are limited. The most studied configuration is the case of horizontal thermal and solute gradients. Based on numerical simulations and laboratory experiments, Sezai and Mohamad, (1999) found that, for a certain range of parameters (Lewis and Rayleigh numbers), the convective flow is strictly three-dimensional. Stajnko et al., (2017) developed a 3D solution based on the boundary element method and investigated the effect of governing parameters on convective flow and rate of heat and mass transfer. Zhu et al., (2017) studied the influence of heterogeneity on entropy generation associated to THC. Hadidi and Bennacer, (2018) studied THC in a bi-layered porous domain. Mohamad and Bennacer, (2001) investigated THC in a 3D porous enclosure subjected to vertical solute and horizontal heat gradients. They indicated that, even though the convective flow has a three-dimensional structure, the difference between three-and two-

dimensional rate of mass and heat transfer is not significant. Our careful literature review shows that few studies are concerned with three-dimensional THC in a porous enclosure and, in general, the precise mechanisms of THC in 3D are still poorly understood. The cases considered in the literature deal with specific boundary conditions for which the problem can be simplified to 2D. While most engineering applications and real-world problem of THC are unsteady or transient in nature, the existing works are limited to steady-state conditions. Furthermore, due to computational limitations, the simulations in the existing 3D studies are limited to low Rayleigh numbers. As accurate simulation of three-dimensional THC is beyond the ability of current numerical models, there is a need for new efficient and accurate methods to investigate effective 3D cases under transient conditions with higher Rayleigh numbers, to understand three-dimensional THC processes.

Analytical solutions serve as an alternative to deal with computation requirement of numerical solutions. They are helpful to provide insight on the physical processes as they are free of numerical errors. Analytical solutions are also important for benchmarking numerical codes and for the assessment of numerical schemes such as in the convergence analysis. However, analytical solutions are usually limited to specific boundary conditions and geometry and cannot be obtained without significant simplifications of the governing equations. Semi-analytical solutions combine the accuracy of analytical solutions with the flexibility of numerical solutions in solving the full mathematical models under complex and realistic boundary conditions. For THC, analytical solutions are scarce. Kalla et al., (2001) developed a 2D analytical solution based on the parallel flow approximation. Analytical solutions for 2D cases have been obtained in Trevisan and Bejan (1986) and Masuda et al., (2013) using the boundary layer approximation. Shao et al., (2015) developed a 2D semi-analytical solution for the full mathematical model (without any approximation), based on the Fourier series method (FS). The existing analytical or semi-analytical solutions are limited to 2D cases. In general, analytical and semi-analytical solutions for density-driven flow model are limited to steady-state conditions.

Thus, in view of the scarcity of studies on three-dimensional transient THC and in the absence of analytical or semi-analytical solutions, the main goal of this study is to develop a 3D-transient semi-analytical solution for the problem of THC in a porous enclosure. Our main objective is to investigate an effective 3D configuration that cannot be simplified to 2D. The motivations are i) to provide a reference solution that could be helpful for code benchmarking and ii) to understand the physical processes of THC in such a configuration (3D-transient). The semi-analytical solution is obtained using the FS method applied to the vector potential formulation of the governing equation, as in Shao et al., (2018). Here, we show how this method can be extended to solve the governing

equations under transient conditions. The extension to transient solutions represents an important technical feature of this work, as the applications of the FS method to density-driven problems have to date been limited to steady-state conditions.

## **3.2. Problem and model statement**

### ***3.2.1. Problem description***

The problem under investigation is a saturated porous box which is commonly used as a benchmark for density-driven flow in porous media (Voss et al., 2010; Shao et al., 2018). The domain is cubic box of size  $H$ , as shown in Figure 3.1a. All walls are assumed to be impermeable and adiabatic. Heat and mass fluxes only arise in the direction of imposed gradients of temperature and concentration. We consider stable configuration of density-driven flow. Such a configuration is important in several applications and it is more relevant for benchmarking than unstable cases which can suffer for solution multiplicity. As our goal is to investigate an effective 3D case, we impose horizontal-crossed thermal and solute gradients. Thus, we have a horizontal thermal gradient parallel to  $x$ -direction and a horizontal solute gradient parallel to  $y$ -direction (Figure 3.1a). Constant temperatures are applied to the back and front walls of the domain and left and right walls are imposed to the constant salinity concentrations. With these boundary conditions two circulation flows arise on two different planes and a 3D investigation become inevitable. Such a configuration can be found in several applications as in geothermal systems in coastal aquifers or in islands (e.g. GEOTREF project: <https://geotref.com>; van Lopik et al., 2015; Navelot et al., 2018; De Giorgio et al., 2018) where sea/ocean can generate a salinity gradient and geothermal wells create a thermal gradient (Figure 3.1b). It is also important in applications involving variable density flow related to two different compositions (DDC) in which the solute gradient can be horizontal and crossed.

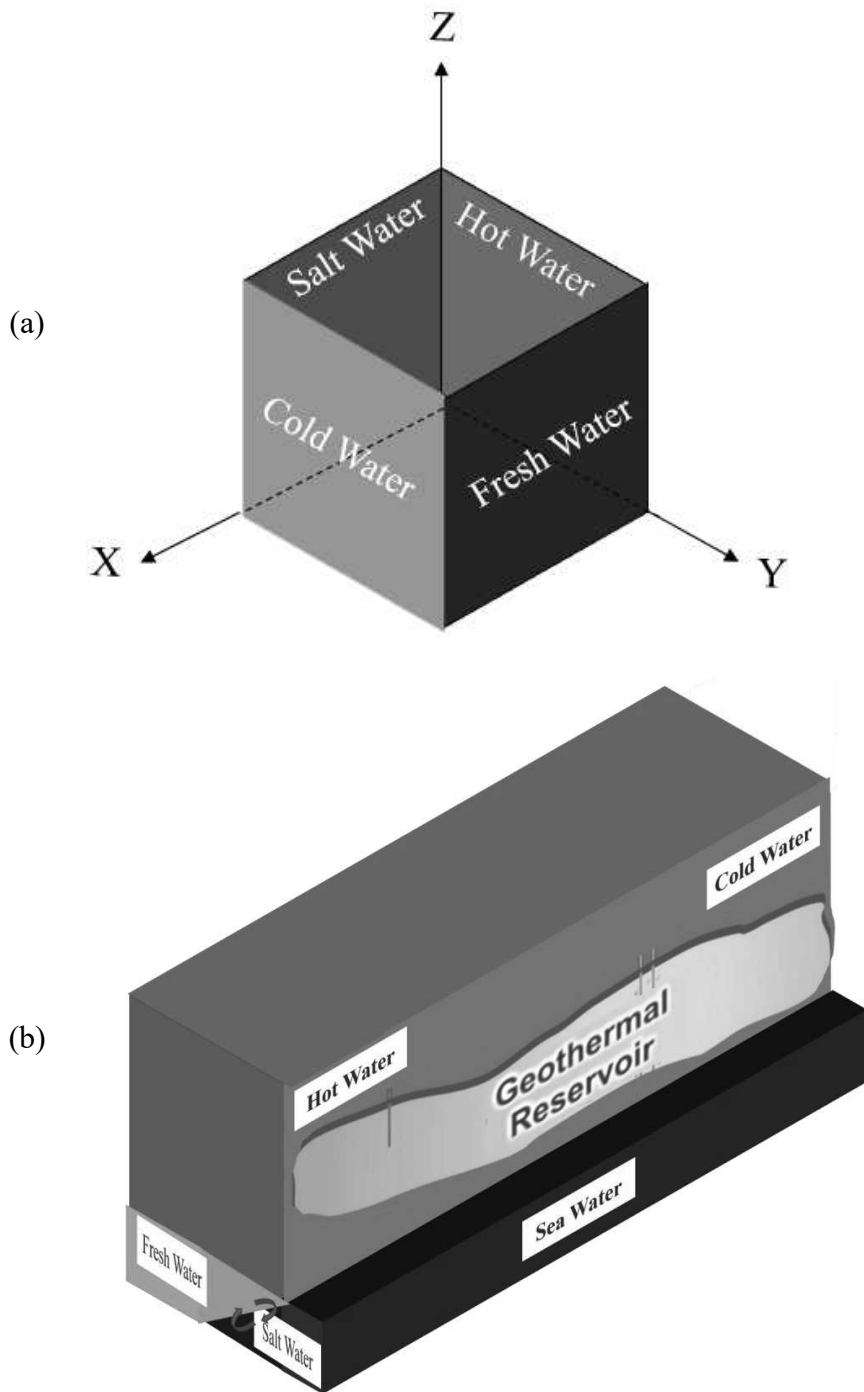


**Figure 3. 1.** a) The conceptual problem of a cubic porous box with horizontal-crossed gradients of temperature and concentration and b) a conceptual model for a geothermal reservoir dealing with horizontal-crossed gradients of temperature and salinity.

### 3.2.2. Model assumptions, governing equations and boundary and initial conditions

We consider an isotropic and homogenous porous media and we assume local thermal equilibrium between the solid and liquid phases. The Soret and Dufour effects are neglected. The only process contributes to mixing is the molecular diffusion for solute transport and thermal conduction for heat transfer. Hydrodynamic dispersion processes are neglected. The viscosity dependence to the temperature is also neglected. Such an approximation could be valid for small range of temperature change. For the porous media the assumption of incompressibility leads to elimination of specific storage from the continuity equation. The flow, mass transport and heat transport equations have been written in the transient mode. Boussinesq approximation is considered. Thus, fluid density is assumed to be constant in all terms of the governing equations, except the buoyancy term. Under the above assumptions, the fluid flow equations consist of continuity equation and generalized Darcy's law in terms of equivalent fresh-water head:

$$\nabla \cdot \mathbf{q} = 0 \quad (3.1)$$

$$\mathbf{q} = -\frac{\rho_0 g k}{\mu} \left( \nabla h + \frac{\rho - \rho_0}{\rho_0} \mathbf{e}_z \right) \quad (3.2)$$

where  $\mathbf{q} [m.s^{-1}]$  is Darcy's velocity,  $\rho_0 [kg.m^{-3}]$  is fresh-water density at the reference temperature,  $g [m.s^{-2}]$  is the gravity acceleration,  $k [m^2]$  is the permeability of the porous media,  $\mu [kg.m^{-1}.s^{-1}]$  is the water viscosity,  $h [m]$  is equivalent fresh-water head,  $\rho [kg.m^{-3}]$  is the density of salt water at a given temperature and  $\mathbf{e}_z$  is the vertical unit vector.

The governing equation for the saline mass transport is as follows:

$$\varepsilon \frac{\partial c}{\partial t} + \mathbf{q} \nabla c - D_m \nabla \cdot \nabla c = 0 \quad (3.3)$$

where  $\varepsilon [-]$  is porosity,  $c [-]$  is relative dimensionless concentration,  $D_m [m^2.s^{-1}]$  is the diffusion coefficient.

The heat transfer is governed by the equation of conservation of energy:

$$\sigma \frac{\partial T}{\partial t} + \mathbf{q} \nabla T - \alpha \nabla \cdot \nabla T = 0 \quad (3.4)$$

where,  $\sigma [-]$  is the ratio of heat capacity,  $T [^{\circ}C]$  is the temperature,  $\alpha [m^2.s^{-1}]$  is the thermal diffusivity.

The flow and heat and mass transfer equations are coupled via the following linear mixture density equation:

$$\rho = \rho_0 (1 + \beta_C (c - c_0) - \beta_T (T - T_0)) \quad (3.5)$$

where,  $\beta_C[-]$  and  $\beta_T[^\circ C^{-1}]$  are, respectively, the solute and thermal expansions,  $c_0[-]$  is the reference relative salt concentration and  $T_0[^\circ C]$  is the reference temperature.

The boundary conditions are as follows:

$$\begin{aligned} x = 0 &\rightarrow q_x = 0; T = T_H; \partial c / \partial x = 0 \\ x = H &\rightarrow q_x = 0; T = T_C; \partial c / \partial x = 0 \\ y = 0 &\rightarrow q_y = 0; c = c_S; \partial T / \partial y = 0 \\ y = H &\rightarrow q_y = 0; c = c_F; \partial T / \partial y = 0 \\ z = 0; z = H &\rightarrow q_z = 0; \partial c / \partial z = 0; \partial T / \partial z = 0 \end{aligned} \quad (3.6)$$

where  $T_H[^\circ C]$  and  $T_C[^\circ C]$  are the hot and cold temperatures,  $c_F[-]$  is the relative salinity concentration of freshwater which is equal to zero and  $c_S[-]$  is the relative salinity concentration of saltwater which is equal to one. For the transient cases, we assume that the initial temperature and concentration varies linearly with respect to x and y, respectively.

### 3.3. The Fourier series solution

The 3D semi-analytical solution is developed using the FS method also called Fourier-Galerkin method (Peyret, 2013). This method has been used to obtain semi-analytical solutions for several 2D density-driven flow problems (Henry, 1964; Segol, 1994, Simpson and Clement, 2003; 2004; Van Reeuwijk et al., 2009; Zidane et al., 2012, Younes and Fahs, 2014; 2015; Fahs et al., 2014; 2015; 2016; Shao et al., 2015; 2016; Koohbor et al., 2018). Shao et al., (2018) extended the FS method to solve a three-dimensional solute density-driven flow problem. In all the aforementioned works the FS method implementations have been limited to steady-state cases. This method has never been used to obtain transient solutions. In this work, we extend the steady-state FS method developed by Shao et al., (2018) to THC by including heat transfer processes and we develop a new implementation of this method to obtain transient solutions. In both cases (steady-state and transient), the solutions have been obtained using the vector potential formulation of the governing equations. This formulation simplifies the resolution procedure by i) eliminating the pressure head which acts as source term in the linear momentum conservation equation and may be at the origin of slower convergence of the Fourier series, ii) honoring the continuity equation and iii) ensuring

homogenous boundary conditions required for the FS method. The main steps of the FS method are listed below:

### 3.3.1 Vector potential formulation and non-dimensional system

The continuity equation implies the existence of the vector potential ( $\boldsymbol{\Psi} [m^2.s^{-1}]$ ) which is defined by (Guerrero-Martínez et al., 2017):

$$\nabla \times \boldsymbol{\Psi} = \mathbf{q} \quad (3.7)$$

The vector potential formulation of the governing equations can be obtained by applying the curl operator to the Darcy's law and by substituting equation (3.7) into equations (3.3) and (3.4). The non-dimensional form of the equations can be obtained using the following dimensionless variables:

$$X = \frac{x}{H}; Y = \frac{y}{H}; Z = \frac{z}{H}; \boldsymbol{\Psi} = \frac{\boldsymbol{\Psi}}{\alpha}; \tau = \frac{t\alpha}{H^2}; \theta = \frac{T - T_C}{T_H - T_C} \quad (3.8)$$

Thus, by using the dimensionless variables and the vector potential and by assuming that the reference temperature is  $T_C$  ( $T_0 = T_C$ ) and the reference concentration is  $c_F$  ( $c_0 = c_F$ ), the governing equations become (more details can be found in Shao et al. 2018):

$$\nabla^2 \Psi_x - Ra_T \left( N_g \frac{\partial c}{\partial Y} - \frac{\partial \theta}{\partial Y} \right) = 0 \quad (3.9)$$

$$\nabla^2 \Psi_y + Ra_T \left( N_g \frac{\partial c}{\partial X} - \frac{\partial \theta}{\partial X} \right) = 0 \quad (3.10)$$

$$\nabla^2 \Psi_z = 0 \quad (3.11)$$

$$\varepsilon \frac{\partial c}{\partial \tau} + (\nabla \times \boldsymbol{\Psi}) \nabla c - \frac{1}{Le} \nabla^2 c = 0 \quad (3.12)$$

$$\sigma \frac{\partial \theta}{\partial \tau} + (\nabla \times \boldsymbol{\Psi}) \nabla \theta - \nabla^2 \theta = 0 \quad (3.13)$$

where  $\Psi_x, \Psi_y, \Psi_z$  are the components of the vector potential  $\boldsymbol{\Psi}$ ,  $Ra_T = \frac{\rho_0 g k H \beta_T (T_H - T_C)}{\mu \alpha}$

is the thermal Rayleigh number representing the ratio between thermal buoyancy to thermal

diffusivity,  $N_g = \frac{\beta_C (c_S - c_F)}{\beta_T (T_H - T_C)}$  is the Gravity number which is the ratio of mass buoyancy to

thermal buoyancy and  $Le = \frac{\alpha}{D_m}$  is the Lewis number expressing the ratio of thermal diffusivity to

mass diffusivity.

### 3.3.2. Homogenous boundary conditions

The FS method requires homogenous boundary conditions to ensure periodicity. For the vector potential, the impermeable boundary conditions can be expressed as follows (for more details readers can refer to Shao et al. 2018):

$$\begin{aligned} \partial\Psi_x/\partial X = \Psi_y = \Psi_z = 0, \quad \text{at } X = 0,1 \\ \partial\Psi_y/\partial Y = \Psi_x = \Psi_z = 0, \quad \text{at } Y = 0,1 \\ \partial\Psi_z/\partial Z = \Psi_x = \Psi_y = 0, \quad \text{at } Z = 0,1 \end{aligned} \quad (3.34)$$

Thus, the flow boundary conditions are homogenous. The thermal and solute boundary conditions are homogenous except in the x and y directions, respectively. To get homogenous boundary conditions, we use the following shifted concentration and temperature:

$$C = c + (Y - 1) \quad (3.15)$$

$$\Theta = \theta + (X - 1) \quad (3.16)$$

The final system of equations become:

$$\nabla^2\Psi_x - Ra_T \left( N_g \frac{\partial C}{\partial Y} - N_g - \frac{\partial\Theta}{\partial Y} \right) = 0 \quad (3.17)$$

$$\nabla^2\Psi_y + Ra_T \left( N_g \frac{\partial C}{\partial X} - \frac{\partial\Theta}{\partial X} + 1 \right) = 0 \quad (3.18)$$

$$\nabla^2\Psi_z = 0 \quad (3.19)$$

$$\varepsilon \frac{\partial C}{\partial \tau} - \frac{\partial\Psi_y}{\partial Z} \frac{\partial C}{\partial X} + \frac{\partial\Psi_x}{\partial Z} \frac{\partial C}{\partial Y} + \left( \frac{\partial\Psi_y}{\partial X} - \frac{\partial\Psi_x}{\partial Y} \right) \frac{\partial C}{\partial Z} - \frac{1}{Le} \left( \frac{\partial^2 C}{\partial X^2} + \frac{\partial^2 C}{\partial Y^2} + \frac{\partial^2 C}{\partial Z^2} \right) - \frac{\partial\Psi_x}{\partial Z} = 0 \quad (3.20)$$

$$\sigma \frac{\partial \Theta}{\partial \tau} - \frac{\partial \Psi_y}{\partial Z} \frac{\partial \Theta}{\partial X} + \frac{\partial \Psi_x}{\partial Z} \frac{\partial \Theta}{\partial Y} + \left( \frac{\partial \Psi_y}{\partial X} - \frac{\partial \Psi_x}{\partial Y} \right) \frac{\partial \Theta}{\partial Z} - \left( \frac{\partial^2 \Theta}{\partial X^2} + \frac{\partial^2 \Theta}{\partial Y^2} + \frac{\partial^2 \Theta}{\partial Z^2} \right) + \frac{\partial \Psi_y}{\partial Z} = 0 \quad (3.21)$$

The third component of the flow system (equation (3.19)) associated to the boundary conditions leads to  $\Psi_z = 0$ . Thus, equation (3.19) and  $\Psi_z$  can be eliminated from the final system.

### 3.3.3. The spectral system

As boundary conditions are homogenous, the components of the vector potential ( $\Psi_x, \Psi_y$ ), shifted concentration ( $C$ ) and shifted temperature ( $\Theta$ ) can be expressed as Fourier series in the spectral space. The Fourier series that satisfy the boundary conditions are as follows:

$$\Psi_x(X, Y, Z) = \sum_{i=0}^{Ni} \sum_{j=1}^{Nj} \sum_{k=1}^{Nk} A_{i,j,k} \cos(i\pi X) \sin(j\pi Y) \sin(k\pi Z) \quad (3.22)$$

$$\Psi_y(X, Y, Z) = \sum_{l=1}^{Nl} \sum_{m=0}^{Nm} \sum_{n=1}^{Nn} B_{l,m,n} \sin(l\pi X) \cos(m\pi Y) \sin(n\pi Z) \quad (3.23)$$

$$C(X, Y, Z) = \sum_{u=0}^{Nu} \sum_{v=1}^{Nv} \sum_{w=0}^{Nw} E_{u,v,w} \cos(u\pi X) \sin(v\pi Y) \cos(w\pi Z) \quad (3.24)$$

$$\Theta(X, Y, Z) = \sum_{s=1}^{Ns} \sum_{p=0}^{Np} \sum_{t=0}^{Nt} G_{s,p,t} \sin(s\pi X) \cos(p\pi Y) \cos(t\pi Z) \quad (3.25)$$

where  $A_{i,j,k}$ ,  $B_{l,m,n}$ ,  $E_{u,v,w}$  and a  $G_{s,p,t}$  are the Fourier series coefficients,  $Ni$ ,  $Nj$ ,  $Nk$ ,  $Nl$ ,  $Nm$ ,  $Nn$ ,  $Nu$ ,  $Nv$ ,  $Nw$ ,  $Ns$ ,  $Np$ ,  $Nt$  are the truncation order of the Fourier series in the space directions.

The Fourier series coefficient can be calculated by substituting the Fourier series into equations (3.17) -(3.18) -(3.20) and (3.21) and by projecting the resulting equation into the spectral space using the Fourier modes as trial function. The final spectral system can be written as follows:

$$\begin{aligned} RFX_{I,J,K} = & -\pi^2 (I^2 + \alpha_I J^2 + \alpha_I K^2) A_{I,J,K} - \frac{N_g Ra_T \alpha_I}{\pi} \sum_{v=1}^{Nv} \sum_{w=0}^{Nw} v E'_{I,v,w} \Gamma_{J,v} \Gamma_{K,w} \\ & + \frac{2N_g Ra_T}{\pi^2} \Gamma_{J,0} \Gamma_{K,0} \delta_{I,0} - \frac{Ra_T J}{\pi} \sum_{s=1}^{Ns} \sum_{t=0}^{Nt} G'_{s,J,t} \Gamma_{s,I} \Gamma_{K,t} \end{aligned} \quad (3.26)$$

$(I = 0, \dots, Ni; J = 1, \dots, Nj; K = 1, \dots, Nk)$

$$\begin{aligned}
RFY_{L,M,N} = & -\pi^2(\alpha_M L^2 + M^2 + \alpha_M N^2)B_{L,M,N} - \frac{LN_g Ra_T}{\pi} \sum_{v=1}^{Nv} \sum_{w=0}^{Nw} E'_{L,v,w} \Gamma_{v,M} \Gamma_{N,w} \\
& - \frac{Ra_T \alpha_M}{\pi} \sum_{s=1}^{Ns} \sum_{t=0}^{Nt} s G'_{s,M,t} \Gamma_{L,s} \Gamma_{N,t} + \frac{2Ra_T}{\pi^2} \Gamma_{L,0} \Gamma_{N,0} \delta_{M,0} \\
& (L = 1, \dots, Nl; M = 0, \dots, Nm; N = 1, \dots, Nn)
\end{aligned} \tag{3.27}$$

$$\begin{aligned}
RT_{U,V,W} = & \varepsilon \alpha_U \alpha_W \frac{dE_{\tau,U,V,W}}{d\tau} \\
& + \frac{\pi^2}{8} \sum_{u=0}^{Nu} \sum_{v=1}^{Nv} \sum_{w=0}^{Nw} E_{u,v,w} \left[ \sum_{i=0}^{Ni} \sum_{j=1}^{Nj} \sum_{k=1}^{Nk} A_{i,j,k} \xi_{S,i,s} (kv\gamma_{V,j,v} \eta_{W,k,w} + jw\kappa_{V,j,v} \zeta_{W,k,w}) \right. \\
& \quad \left. + \sum_{l=1}^{Nl} \sum_{m=0}^{Nm} \sum_{n=1}^{Nn} B_{l,m,n} \kappa_{V,j,v} (nu\zeta_{U,l,u} \eta_{W,n,w} - wl\eta_{U,l,u} \zeta_{W,n,w}) \right] \\
& + \frac{\pi^2}{Le} (U^2 \alpha_W + V^2 \alpha_U \alpha_W + W^2 \alpha_U) E_{U,V,W} - \pi W \alpha_U A'_{U,V,W} \\
& (U = 0, \dots, Nu; V = 1, \dots, Nv; W = 0, \dots, Nw)
\end{aligned} \tag{3.28}$$

$$\begin{aligned}
RE_{S,P,T} = & \sigma \alpha_P \alpha_T \frac{dG_{\tau,S,P,T}}{d\tau} \\
& + \frac{\pi^2}{8} \sum_{s=1}^{Ns} \sum_{p=0}^{Np} \sum_{t=0}^{Nt} G_{s,p,t} \left[ \sum_{i=0}^{Ni} \sum_{j=1}^{Nj} \sum_{k=1}^{Nk} A_{i,j,k} \kappa_{S,i,s} (jt\eta_{P,j,p} \zeta_{T,k,t} - kp\zeta_{P,p,j} \eta_{T,k,t}) \right. \\
& \quad \left. - \sum_{l=1}^{Nl} \sum_{m=0}^{Nm} \sum_{n=1}^{Nn} B_{l,m,n} \eta_{P,m,p} (lt\kappa_{S,l,s} \zeta_{T,n,t} + ns\gamma_{S,l,s} \eta_{T,n,t}) \right] \\
& + \pi^2 (S^2 \alpha_P \alpha_T + P^2 \alpha_T + T^2 \alpha_P) G_{S,P,T} + \pi T \alpha_P B'_{S,P,T} \\
& (S = 1, \dots, Ns; P = 0, \dots, Np; T = 0, \dots, Nt)
\end{aligned} \tag{3.29}$$

where,  $RFX$ ,  $RFY$ ,  $RT$  and  $RE$  are the residuals corresponding to the flow and mass and heat transport equations, respectively. The coefficients of equations (3.25)-(3.29) are given in Appendix B.

The spectral system (equations (3.25)-(3.29)) is a system of differential algebraic equations that contains a set of ordinary differential equations (mass and heat transport residuals) and algebraic nonlinear equations (residuals of the x and y-components of the flow equations). The steady state spectral system can be obtained by dropping out the transient terms (first terms) in equations (3.28) and (29) which yields an algebraic nonlinear system.

### 3.3.4. Solving the spectral system

Solving the spectral system (equations (3.25)-(3.29)) is a crucial step to obtain the Fourier coefficients and in consequence the semi-analytical solution. For both transient and steady state configurations, the performance of the FS method depends on the way in which the spectral system

is solved. This is a challenging task as, for sharp solutions (i.e. high Rayleigh or Lewis numbers), the FS method requires large number of Fourier modes to avoid the Gibbs phenomenon (Peyert, 2002) for which the solution could become impractical due to the computational cost and nonlinearity. This would undermine the first advantage of the semi-analytical solution regarding its practicality when compared against numerical solutions. Furthermore, for transient configurations, the accuracy of the solution depends on the numerical technique used for time integration. Here, we present the numerical implementations used to ease these challenges and to obtain accurate solutions in approachable CPU time.

#### *- Transient solution*

As shown in the previous section, in the spectral space, the problem of THC in a porous cubic box is modeled as a system of differential algebraic equations (DAEs) that contains a set of ordinary differential equations (ODEs) (equations 3.28 and 3.29) and algebraic nonlinear constraints (equations 3.26 and 3.27). The unknowns are the Fourier series coefficients ( $A$ ,  $B$ ,  $E$  and  $G$ ). To obtain an accurate and efficient solution, we convert the DAEs system into an ODEs system. To do so, we use equations (3.26) and (3.27) to analytically express the coefficients  $A$  and  $B$  as function of ( $E$ ) and ( $G$ ) (see Appendix C). We then substitute the analytical expressions of  $A$  and  $B$  into equations (3.28) and (3.29). This procedure reduces, in one hand, the number of unknowns as the new system can be solved with only the Fourier series coefficients of the concentration and temperature as primary unknowns (i.e.  $E$  and  $G$ ), and on the other hand, simplifies and improves the resolution procedure as it is well-known that ODEs systems are more stable than DEAs systems. For stable and accurate time integration of the resulting ODEs system with strong non-linearity, we use the sophisticated and mature time integration solver DASPK (<https://techtransfer.universityofcalifornia.edu/NCD/10326.html>). This solver provides high accuracy as it is based on the Backward Difference Formulas (BDF) which is an implicit high order integration technique (Li and Petzold, 1999). The solver adapts both time step size and time integration order (up to fifth order) in order to reach high accuracy and stable solutions. Higher order time integration method also improves the efficiency of the integration procedure as it allows for large time step size. The Fixed Leading Coefficient Backward Difference Formulas (FLCBDF) is used in DASPK to deal with variable time step size and integration order. With this method the system is converted, at each time step, to a system of nonlinear algebraic equations. In DASPK, this system is solved using the modified Newton's method (Brown et al., 1994). The Jacobian matrix can be evaluated numerically (i.e. using finite difference approximation) or provided by the user. The assembly of the numerical Jacobian is computationally consuming, as the system is fully-dense. Thus, in our implementation, we provide the Jacobian matrix analytically in order to improve the

solution performance. The resulting linear system can be solved using either direct or iterative methods. We choose the iterative method (Krylov method) to gain computational efficiency owing to the highly dense nature of the matrices involved and to the system high-dimensionality in 3D (Brown et al., 1994). Our choice for iterative method is also justified by the memory limitation with direct methods for large linear systems. The relative and absolute local error tolerances are prescribed to  $10^{-8}$ .

#### *- Steady-state solution*

The spectral steady-state system can be obtained by dropping out the transient terms (first terms) in equations (28) and (29). This yields an algebraic nonlinear system with the Fourier coefficients as unknowns. To solve this system, we extend the implementation developed by Shao et al., (2018) to deal with THC. Thus, we first reduce the number of unknowns by expressing the coefficients A and B as function of (E) and (G), as in the transient solution (see appendix C). The resulting nonlinear system is then solved using the nonlinear solver of the IMSL library (<http://www.roguewave.com/products-services/imsl-numerical-libraries>). To improve the solver performance, we provide the analytical Jacobian matrix.

In both transient and steady state solutions, the nonlinear solvers require the evaluation of the residual vector. The evaluation of this vector involves six nested summations in the convection terms. Thus, when large number of Fourier coefficients should be used to avoid the Gibbs phenomenon, the solution becomes computationally impractical. As in Shao et al., (2018), we use the properties of the Kronecker delta function to reduce the number of nested summations to three.

### **3.4. Results and discussion: Verification and benchmarking**

Three targets are discussed in this section: i) as two numerical codes have been developed to solve the steady-state and transient spectral systems, we verify the correctness of these codes by comparison with finite elements solutions obtained using a commercial code (COMSOL Multiphysics®), ii) comparison against standard finite element solutions, for complex cases involving sharp concentration and/or temperature distributions, are also used to examine the worthiness of the developed semi-analytical solution in benchmarking numerical codes and iii) we use the developed solution to provide new physical insights on the three-dimensional THC processes in the case of crossed-horizontal gradients, under both steady-state and transient conditions. In our analysis, as common in the literature, we use the average Nusselt ( $\overline{Nu}$ ) and Sherwood ( $\overline{Sh}$ ) numbers to characterize the rates of heat and mass transfer to the domain, respectively. Both steady state values and time-variations of these numbers are investigated to

assess steady state and transient solutions, respectively.  $\overline{Nu}$  and  $\overline{Sh}$  are calculated using the Fourier series as follows:

$$\overline{Sh} = \int_0^1 \int_0^1 \frac{\partial c}{\partial Y} \Big|_{Y=0} dXdZ = \pi \sum_{v=1}^{N_v} v E_{0,v,0} - 1 \quad (3.30)$$

$$\overline{Nu} = \int_0^1 \int_0^1 \frac{\partial \theta}{\partial X} \Big|_{X=0} dYdZ = \pi \sum_{s=1}^{N_s} s G_{s,0,0} - 1 \quad (3.31)$$

### 3.4.1. Verifications

To gain confidence on the correctness of the codes developed to solve the steady state and transient spectral systems of the semi-analytical solution, we compare their results with a finite element solution (FE) obtained using COMSOL Multiphysics®. The steady state semi-analytical solution is denoted by ‘SA-steady’ and the transient solution is termed as ‘SA-transient’. To avoid numerical artifacts in the finite element solution, that could lead to discrepancy with the semi-analytical solution, we consider relatively simple cases dealing with smooth temperature and concentration distributions (low convective flow regime). Thus, we examine two cases dealing with  $Ra_T = 10$ ,  $N_g = 1.5$  and  $Le = 2$  (denoted by ‘test case 1’) and  $Ra_T = 100$ ,  $N_g = 1$  and  $Le = 0.5$  (denoted by ‘test case 2’), respectively. In ‘test case 1’ the conduction-diffusion regime is dominating (low thermal Rayleigh number), the mass transport is less diffusive than heat transfer ( $Le > 1$ ) and the convective flow is solute-dominated ( $N_g > 1$ ). In the ‘test case 2’, the convective flow is more pronounced than ‘test case 1’ (higher thermal Rayleigh number), molecular diffusion is more intense than thermal conduction ( $Le < 1$ ) and thermal and solute convective flows occur in equal proportions ( $N_g = 1$ ).  $Le < 1$  is not common in THC because heat is more diffusive than mass transfer, but such a configuration can be found in DDC. For the transient solutions, in both test cases, we consider  $\varepsilon = 0.1$  (porosity) and  $\sigma = 0.46$  (specific heat ratio).

The FS method could suffer from Gibbs oscillations around discontinuities. Thus, appropriate number of Fourier modes should be used to obtain stable solutions. To do so, we use the technique developed by Fahs et al. (2014) that proceeds by increasing progressively the number of Fourier modes until reaching stable value of  $\overline{Nu}$  and  $\overline{Sh}$ . In each space direction, we use the same number of Fourier modes for all variables ( $\Psi_x$ ,  $\Psi_y$ ,  $c$  and  $\Theta$ ). Thus, we have  $NX = Ni = Nl = Nu = Ns$ ,  $NY = Nj = Nm = Nv = Np$  and  $NZ = Nk = Nn = Nw = Nt$ . For the ‘test case 1’, stable solutions (both SA-steady and SA-transient) have been obtained with  $NX = 3$ ,  $NY = 12$  and  $NZ = 6$ . In ‘test case 2’ the temperature and concentration distributions are sharper than ‘test case 1’. Thus,

more Fourier modes are required to get a stable solution which is obtained with  $NX = 3$ ,  $NY = 24$  and  $NZ = 20$ . It should be mentioned that stable isotherms and concentration contours can be obtained with smaller number of Fourier modes, but these numbers were required to get stable  $\overline{Nu}$  and  $\overline{Sh}$ .

The COMSOL model has been built by coupling three modules: ‘Darcy’s Law  $-dl$ ’, ‘Heat Transfer in Porous Media  $-ht$ ’ and ‘Transport of Diluted Species in Porous media  $-tds$ ’. The density is assumed to be a function of temperature and concentration as in equation (3.5). The Boussinesq approximation is implemented in COMSOL by assuming constant density in the three modules ( $-dl$ ,  $-ht$  and  $-tds$ ) and including variable density in the gravity term. The physical parameters used in COMSOL to simulate ‘test case 1’ and ‘test case 2’ are given in Table 3.1. Transient simulations are performed in COMSOL. This is useful to avoid convergence issues usually encountered with steady-state solutions. It is also helpful for the comparison against the SA-transient solutions. Steady state solutions are obtained with COMSOL by letting the transient solutions evolve until permanent regime. For each case, a grid convergence analysis is performed to obtain a mesh-independent solution.  $\overline{Nu}$  and  $\overline{Sh}$  are used as metrics for the convergence analysis. 3D triangular grids, generated by the COMSOL meshing tool (physical controlled mesh), are used for the space domain discretization. For ‘test case 1’ and ‘test case 2’, mesh-independent solutions are obtained using grids consisting of about 35K and 100K elements, respectively.

**Table 3.1.** Non-dimensional parameters used in the semi-analytical solutions and physical parameters used in COMSOL for different test cases.

Non-dimensional parameters used in the semi-analytical solutions					
	$Ra_T$	$N_g$	$Le$	* $\varepsilon$	* $\sigma$
'test case 1'	10	1.5	2.0	0.1	0.46
'test case 2'	100	1.0	0.5	0.1	0.46
'test case 3'	100	1.5	2.0	0.1	0.46
Invariable physical parameters used in COMSOL					
Porous box side	$H = 1.0$ m				
Porosity	$e = 0.1$				
Freshwater density	$\rho_0 = 1000$ kg.m <sup>-3</sup>				
Solid phase density	$\rho_s = 2000$ kg.m <sup>-3</sup>				
Gravity	$g = 9.8$ m.s <sup>-2</sup>				
Viscosity	$\mu = 10^{-3}$ kg.m <sup>-1</sup> .s <sup>-1</sup>				
Cold temperature	$T_C = 273.15$ K				
Hot temperature	$T_H = 274.15$ K				
Concentration of saltwater	$c_S = 1$ mol.m <sup>-3</sup>				
Concentration of freshwater	$c_F = 0$ mol.m <sup>-3</sup>				
Thermal expansion coefficient of water	$\beta_T = 10^{-2}$ K <sup>-1</sup>				
Thermal capacity of Water	$cp_f = 4200$ J.kg <sup>-1</sup> .K <sup>-1</sup>				
Thermal capacity of soil	$cp_s = 850$ J.kg <sup>-1</sup> .K <sup>-1</sup>				
Thermal Conductivity of Water	$\lambda_f = 0.65$ W.m <sup>-1</sup> .K <sup>-1</sup>				
Thermal Conductivity of Soil	$\lambda_s = 1.59$ W.m <sup>-1</sup> .K <sup>-1</sup>				
Variable physical parameters used in COMSOL					
	Permeability $K(m^2)$	Molecular Diffusion $D_m(m^2.s^{-1})$	Mass Expansion $\beta_C(m^3.mol^{-1})$		
'test case 1'	$3.634 \times 10^{-11}$	$1.78 \times 10^{-7}$	$1.5 \times 10^{-2}$		
'test case 2'	$3.634 \times 10^{-10}$	$7.12 \times 10^{-7}$	$10^{-2}$		
'test case 3'	$3.634 \times 10^{-10}$	$1.78 \times 10^{-7}$	$1.5 \times 10^{-2}$		

\*  $\varepsilon$  and  $\sigma$  are only used for transient solutions.

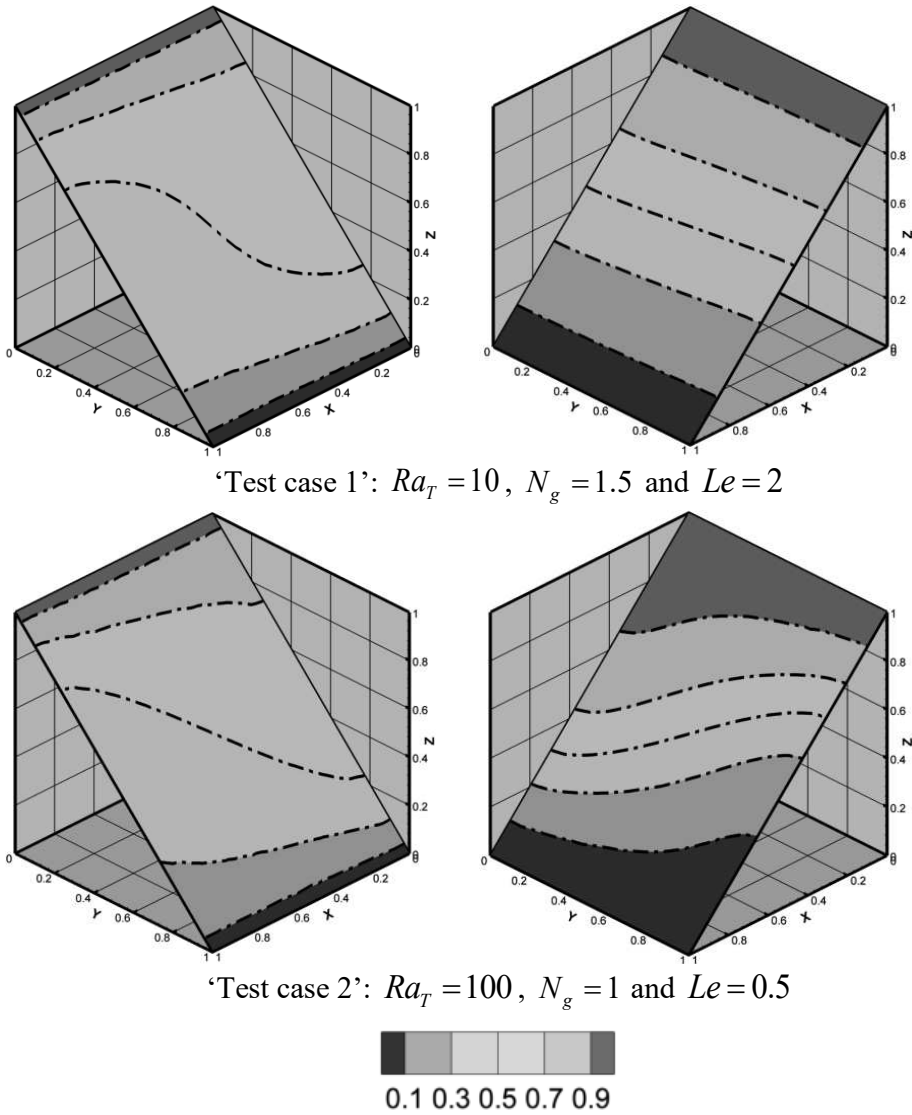


**Figure 3.2.** Comparison of the steady state semi-analytical solution (Flood map) and COMSOL (dashed lines): concentration contours (left) and isotherms (right) in two diagonal plans.

Figure 3.2 exemplifies results of the comparison between the ‘SA-steady’ solution against COMSOL. It shows the main concentration contours and isotherms on the diagonal planes along the solute and thermal gradients, respectively. These planes are helpful to understand the effects of thermal and solute gradients on concentration and temperature distributions. For ‘test case 1’, the figure shows a clear three-dimensional structure of the concentration distribution while the temperature field is almost two-dimensional because conduction regime is dominating (low  $Ra_T$  and  $Le > 1$ ). For higher thermal Rayleigh number, as in ‘test case 2’, both concentration distribution and temperature field have three-dimensional structures. Similar plots are made in Figure 3.3 for the comparison between the ‘SA-transient’ solution and COMSOL, at  $\tau = 0.005$  for ‘test case 1’

and  $\tau = 0.001$  for ‘test case 2’. At  $\tau = 0.005$ , the concentration contours and isotherms are almost linear in ‘test case 1’. Thus, the convective flow is relatively weak. The convective flow is more pronounced at earlier time in ‘test case 2’. We also compare the ‘SA-steady’ solutions and COMSOL based on  $\overline{Nu}$  and  $\overline{Sh}$ . The corresponding values are given in Table 3.2. For the SA-transient solutions, We plot, in Figure 3.4, the time variation of  $\overline{Nu}$  and  $\overline{Sh}$ . This figure indicates that, for ‘test case 1’, mass transfer to the domain increases with time while the heat transfer flux is almost constant. For ‘test case 2’, two variation regimes can be distinguished. Both  $\overline{Nu}$  and  $\overline{Sh}$  increase with time at the beginning until reaching their maximal values. After a critical time, they decrease and reach asymptotic values. Figures 3.2, 3.3 and 3.4 and Table 3.2 show excellent agreement between the results of the semi-analytical solutions and COMSOL. Moreover, the asymptotic values of transient  $\overline{Nu}$  and  $\overline{Sh}$  are equal to the corresponding steady state values, as in Table 3.2. These results provide compelling confidence in confirming the correctness of the codes developed to solve the steady state and transient spectral systems in the semi-analytical solution, respectively. It should be mentioned that relatively fine levels of grids have been used to obtain independent-mesh values of  $\overline{Nu}$  and  $\overline{Sh}$ , but in general, stable isotherms and concentration contours can be obtained with coarser grids.

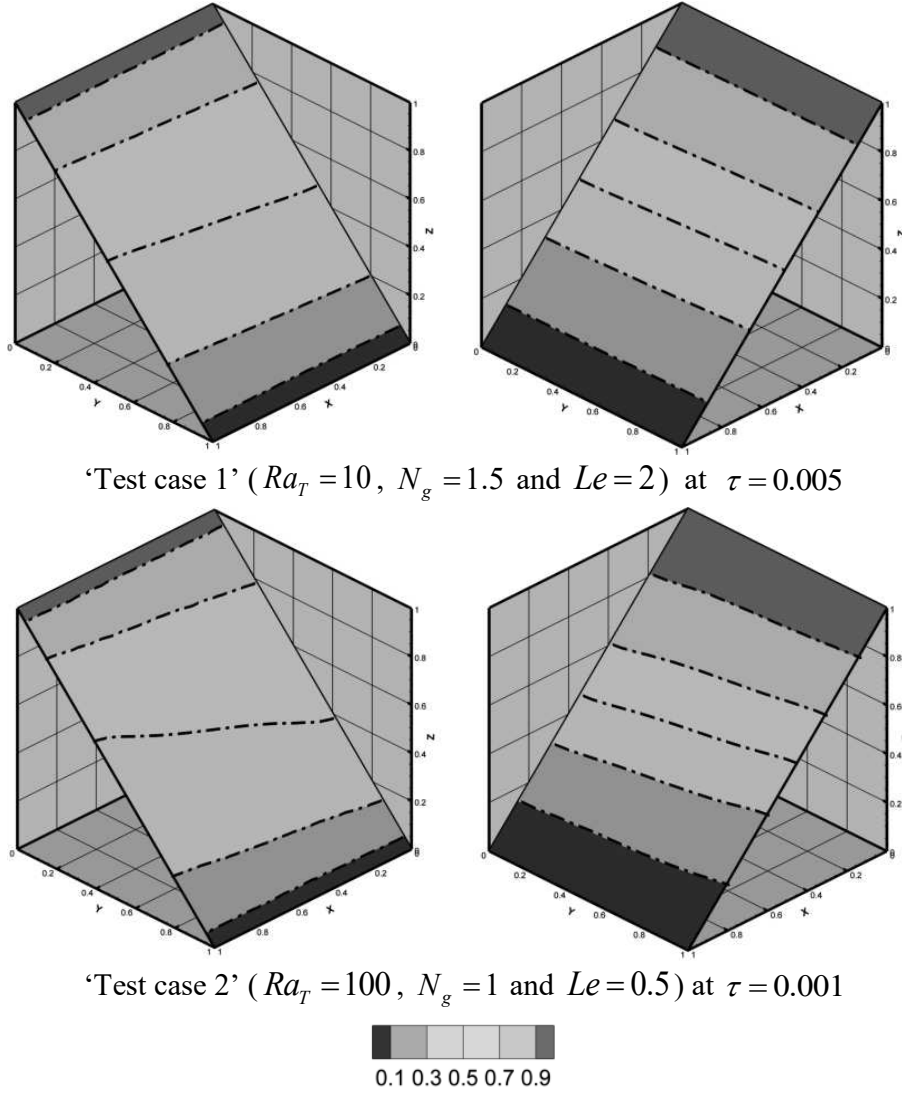


**Figure 3.3.** Comparison of the transient semi-analytical solution (Flood map) and COMSOL (dashed lines): concentration contours (left) and isotherms (right) in two diagonal planes ( $\tau$  is the non-dimensional time,  $\varepsilon = 0.1$  and  $\sigma = 0.46$  ).

**Table 3.2.** Average Nusselt ( $\overline{Nu}$ ) and Sherwood ( $\overline{Sh}$ ) numbers for different test cases obtained using the steady state semi-analytical solution (SA-steady) and COMSOL. COMSOL-v5.3 is used to denote a previous version of the software while COMSOL is used for the newer release (v5.4). All parameters for the three test cases are given in Table 3.1.

Test case	Method	$\overline{Sh}$	$\overline{Nu}$
‘Test case 1’	SA-steady	1.44	1.04
	COMSOL	1.42	1.04
‘Test case 2’	SA-steady	1.37	2.19
	COMSOL	1.37	2.16
‘Test case 3’	SA-steady	5.17	1.25
	COMSOL	5.01	1.25
	COMSOL-v5.3	1.97	1.17

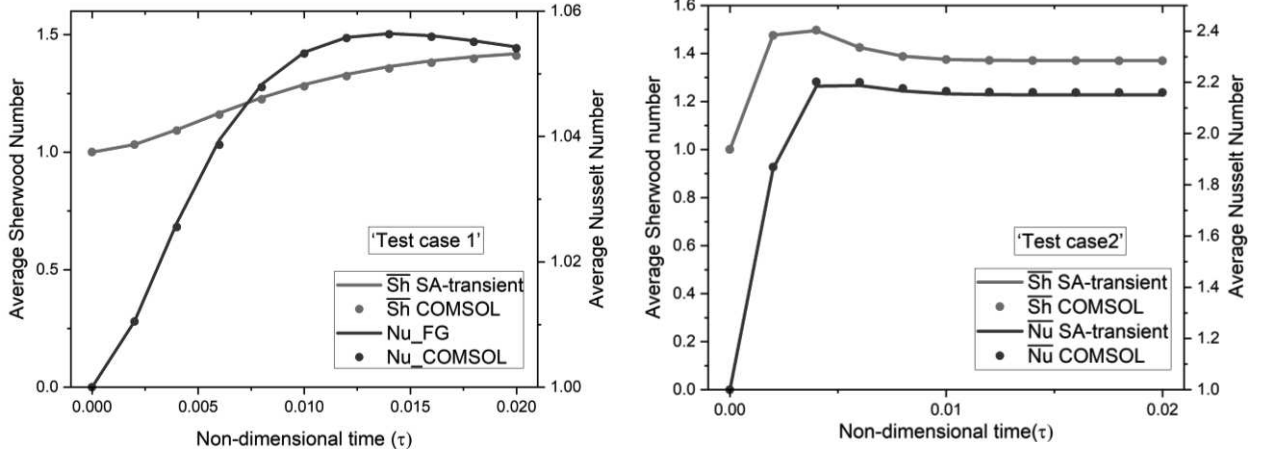


**Figure 3.4.** Time variation of the average Nusselt ( $\overline{Nu}$ ) and Sherwood ( $\overline{Sh}$ ) numbers: Comparison of the transient Fourier series solution (SA-transient) and COMSOL for ‘test case 1’ and ‘test case 2’. All parameters for both test cases are given in Table 3.1.

### 3.4.2. Benchmarking

We consider a complex case dealing with sharper temperature and concentration distributions than the previous test cases. To do so, we assume high values for  $Ra_t (=100)$ ,  $N_g (=1.5)$  and  $Le (=2)$ . The new test case is called ‘test case 3’. Its non-dimensional and physical parameters are given in Table 3.1. The semi-analytical solution is obtained with:  $NX = 17$ ,  $NY = 18$  and  $NZ = 15$ . Our first simulations have been performed using COMSOL version (5.3). The simulations are performed using a grid of about 100K elements, as in ‘Test case 2’. COMSOL is bound to run into convergence difficulties and cannot reach the permanent regime. Incoherent results can be observed with negative temperatures and concentrations and larger values beyond physics. Convergence issue and unphysical values of concentration and temperature are related to spurious oscillations because ‘test case 3’ is a convection-dominated problem for which the finite element method, used in COMSOL, can lead to instabilities. It has been proved that these oscillations can be removed by using a grid respecting a Péclet number less than 1 in the whole computational domain. In 3D, this requires a very fine grids with several million elements which is computationally highly expensive. When finer grid (about 400K elements) is used, COMSOL runs for the entire simulation duration until the steady-state solution. The numerical oscillations can be significantly reduced but they do not completely disappear. The COMSOL results and the SA-steady solution are plotted in Figure 3.5. It can be clearly seen that the solutions are useless. Oscillations are spread over the whole domain. As mass transfer is more convective than heat ( $N_g > 1$ ), oscillations are more pronounced for concentration contours than isotherms. The steady state Nusselt and Sherwood numbers obtained using the semi-analytical solution and COMSOL (v5.3) are given in Table 3.2 which

shows significant discrepancy between the results, especially for  $\overline{Sh}$ . This is coherent with the results presented in Figure 3.5.

For the comparison between the SA-transient solution and COMSOL, we only investigate time variation of  $\overline{Nu}$  and  $\overline{Sh}$ . For the sake of brevity, we do not present isotherms and concentration contours. The time variations of  $\overline{Nu}$  and  $\overline{Sh}$  are given in Figure 3.6. This figure indicates huge discrepancy between the semi-analytical solution and COMSOL-v5.3. The latter produces unphysical results as both  $\overline{Nu}$  and  $\overline{Sh}$  are decreasing with time. The origin of this behavior is the spurious oscillations that appear during entire simulation.

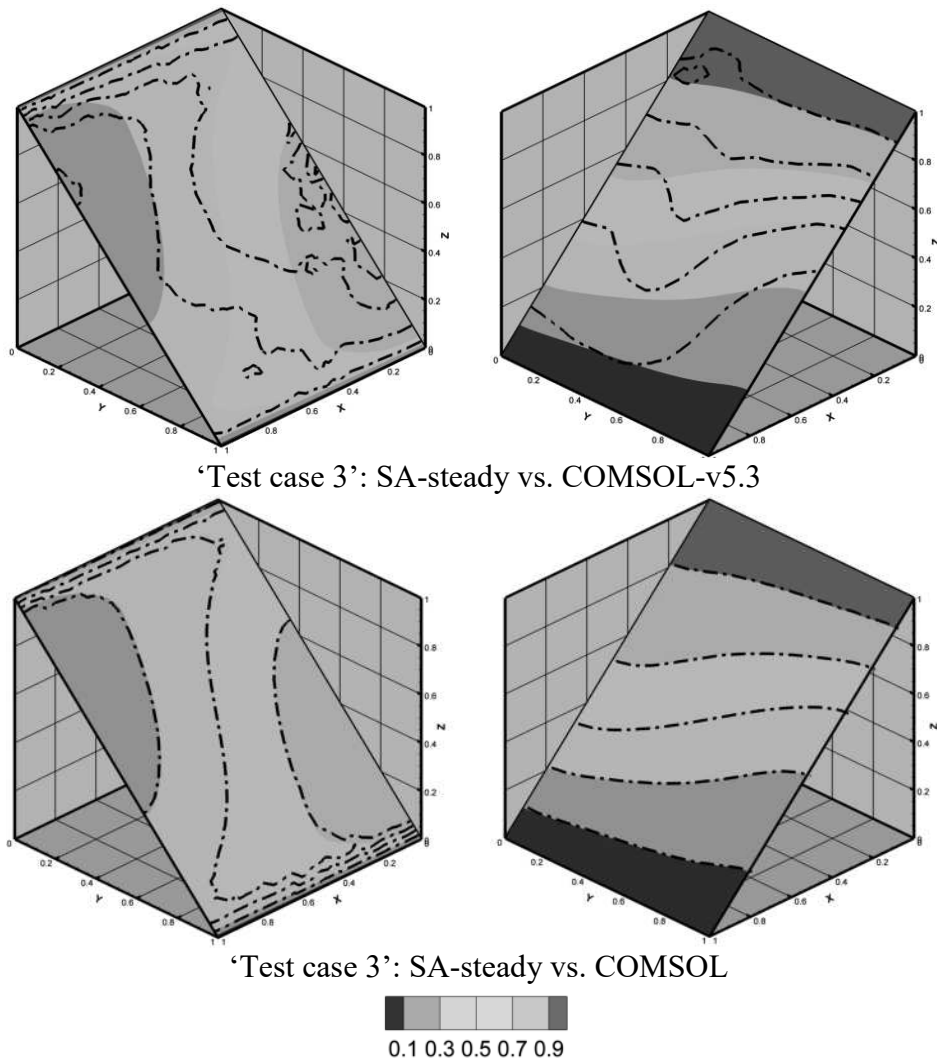


**Figure 3.5.** Comparison of the steady state semi-analytical (SA-steady) solution in flood map and COMSOL in dashed lines for ‘test case 3’: concentration contours (left) and isotherms (right) in two diagonal plans. COMSOL-v5.3 is used to denote a previous version of the software while COMSOL is used for the newer release (v5.4). Parameters for ‘test case 3’ are given in Table 3.1.

We also simulate ‘test case 3’ using the new release of COMSOL (version 5.4) with a grid consisting of about 400K elements. The resulting isotherms and concentration contours are plotted in Figure

3.5. This Figure shows good agreement with the semi-analytical solution. It confirms that a new numerical technique is implemented in the new version of COMSOL to reduce the unphysical oscillations. But this technique cannot remove the oscillations completely, as some instabilities are still visible on the concentration contours (see Figure 3.5). Good agreement is also found between the SA-steady solution and COMSOL (version 5.4) regarding  $\overline{Nu}$  and  $\overline{Sh}$ , as given in Table 3.2. The time variation of  $\overline{Nu}$  and  $\overline{Sh}$  with the new version of COMSOL are plotted in Figure 3.6. Excellent agreement can be observed with the SA-transient solution regarding  $\overline{Nu}$ , while small discrepancy can be noted for  $\overline{Sh}$  which is underestimated in COMSOL. This means that the numerical scheme used in COMSOL overestimates the molecular diffusion. This phenomenon is known as numerical diffusion. It affects only  $\overline{Sh}$  because concentration distribution is sharper than temperature ( $N_g > 1$ ).

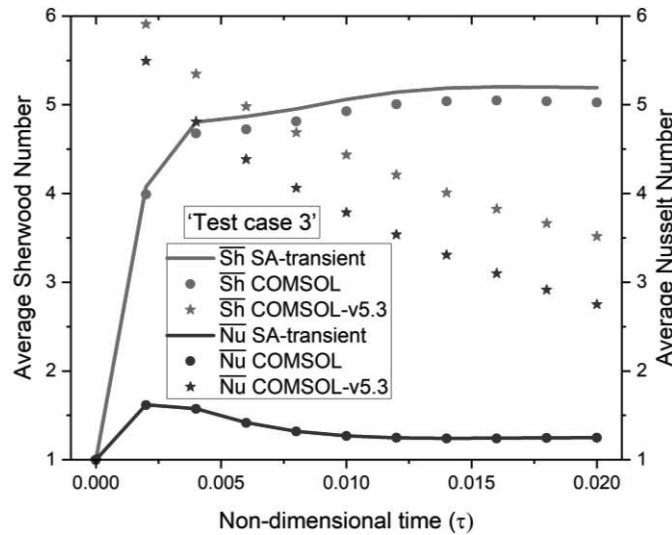


**Figure 3.6.** Time variation of the average Nusselt ( $\overline{Nu}$ ) and Sherwood ( $\overline{Sh}$ ) numbers: Comparison of the transient semi-analytical (SA-transient) solution and COMSOL for ‘test case 3’. COMSOL-v5.3 is used to denote a previous version of the software while COMSOL is used for the newer release (v5.4). Parameters for ‘test case 3’ are given in Table 3.1.

Both versions of COMSOL (5.3) and (5.4) give similar results for ‘test case 1’ and ‘test case 2’. Thus, contrary to the previous test cases, the numerical solution of ‘test case 3’ is sensitive to the numerical scheme used to solve the governing equations. This is an important property for a good benchmark that can be useful for the verification of numerical codes and to assess the robustness of numerical schemes for solving the equations of THC. ‘Test case 3’ is also helpful in comparing performance of numerical codes. To highlight this property, we perform several simulations of ‘Test case 3’ using different strategies of time integration in COMSOL. The results show that the

performance of the numerical solution (CPU time) is more sensitive to the time integration scheme than the first test cases.

The comparison between the semi-analytical solution and COMSOL, particularly for ‘test case 3’, points out the high performance of the former. In fact, while a grid involving about 400K elements (370K nodes), leading to a system with 740K degrees of freedom, is required to obtain an accurate numerical solution, the semi-analytical solution is obtained with only 14K degrees of freedom. This leads to a huge gain in computational time. This gain is more significant for convection-dominated cases. Moreover, we should mention that the problem of unphysical oscillations has been reported in purely compositional or thermal natural convection in porous media for higher Rayleigh (Shao et al., 2018). The results here show that THC simulation is more challenging than purely compositional or thermal natural convection because numerical instabilities could appear at relatively small values of Rayleigh number.

### 3.5. Sensitivity to parameters for THC under crossed thermal and solute gradient

At steady state, the THC in the porous box is controlled by three parameters:  $Ra_T$ ,  $N_g$  and  $Le$ . Two additional parameters ( $\varepsilon$  and  $\sigma$ ) are involved in transient solutions. The developed semi-analytical solution deals with three-dimensional THC in the case of crossed horizontal salinity and temperature gradients. The effects of the parameters controlling THC on heat and mass transfer processes in such a case have been never investigated in the literature because it requires 3D simulations which are computationally expensive. In this section, taking advantage of the efficiency and robustness of the developed semi-analytical solution, we perform a detailed parameters sensitivity analysis. The effects of  $\varepsilon$  and  $\sigma$  on convective flow and heat and mass transfer are predictable as they affect mainly on the time required to reach the steady state regime. Thus, in our analysis we consider the sensitivity to  $Ra_T$ ,  $N_g$  and  $Le$ . For the transient simulations, we assume  $\varepsilon = 0.1$  and  $\sigma = 0.46$ .

#### 3.5.1 Effect of $Ra_T$

We assume moderate value of  $Le$  ( $= 2$ ) to confine the discussion. This value is physically plausible as heat transfer is more diffusive than mass transfer. We vary  $Ra_T$  from 10 to 200 and we consider two cases dealing with thermally ( $N_g = 0.5$ ) and solute ( $N_g = 1.5$ ) -dominated convective flow, respectively. The cases dealing with thermally-dominated convective flow are denoted by ‘TD’ while the cases involving solute-dominated convective flow are denoted by ‘SD’. The effect of  $Ra_T$  on the structure of the steady-state velocity field is investigated using the arrow-surface representation as in Figure 3.7. This figure is helpful in understanding the 3D structure of the main

flow which is the superposition of the two components. The first component is related to the solute-driven convective flow (SDC) while the second one is the thermally-driven convective flow (TDC). The SDC flow component is two-dimensional and occurs in the vertical planes orthogonal to the x-axis. The TDC flow component is also planar and takes place in the vertical planes orthogonal to y-axis. The superposition of these flow components (SDC and TDC) results in a three-dimensional overall flow with the structures represented in Figure 3.8. Different structures are reported for the TD and SD cases. For the TD case, the primary flow is the TDC flow component, which is two-dimensional. The three-dimensional structure of the overall flow is created by the crossing SDC flow component that leads to vortex formation at the vertical plane  $Y=1$ . The inviscid evolution of this vortex within the domain is represented using stream-tubes in Figure 3.9. For the TD case, the vortex structure is an association of two hourglass shaped vortices oriented diagonally from the plane  $Y=1$  to the plane  $Y=0$ . For the SD case, the primary flow is analogue to the SDC flow component and three-dimensional structure are attributed to the TDC flow component. Crossing-flows leads to a central vortex which has the same shape as in the SD case, but with different orientation from the plane  $X=1$  to  $X=0$ . Figure 3.10 shows the iso-surfaces of the steady-state vector potential. This figure indicates that distribution of  $\Psi_x$  is attributed to the SDC flow. This is coherent with equation (3.17) which confirms that variation of  $\Psi_x$  is mainly related to the y-component of the concentration gradient. The variation of  $\Psi_y$  is linked with the TDC which is consistent with the mathematical formulation in equation (3.18). For low Rayleigh number, the vector potential isosurfaces have regular form, indicating almost two-dimensional conditions. Irregular shapes can be observed at high Rayleigh, indicating three-dimensional flow. For the TD case,  $\Delta\Psi_x$  ( $= 0.09$ ) is smaller than  $\Delta\Psi_y$  ( $= 0.18$ ). Thus, the TDC flow is dominating. The opposite is true for the SD case. Vector potential isosurfaces indicate that the strength of the convective flow increases with increasing Rayleigh (both  $\Delta\Psi_x$  and  $\Delta\Psi_y$  increase with  $Ra_T$ ).

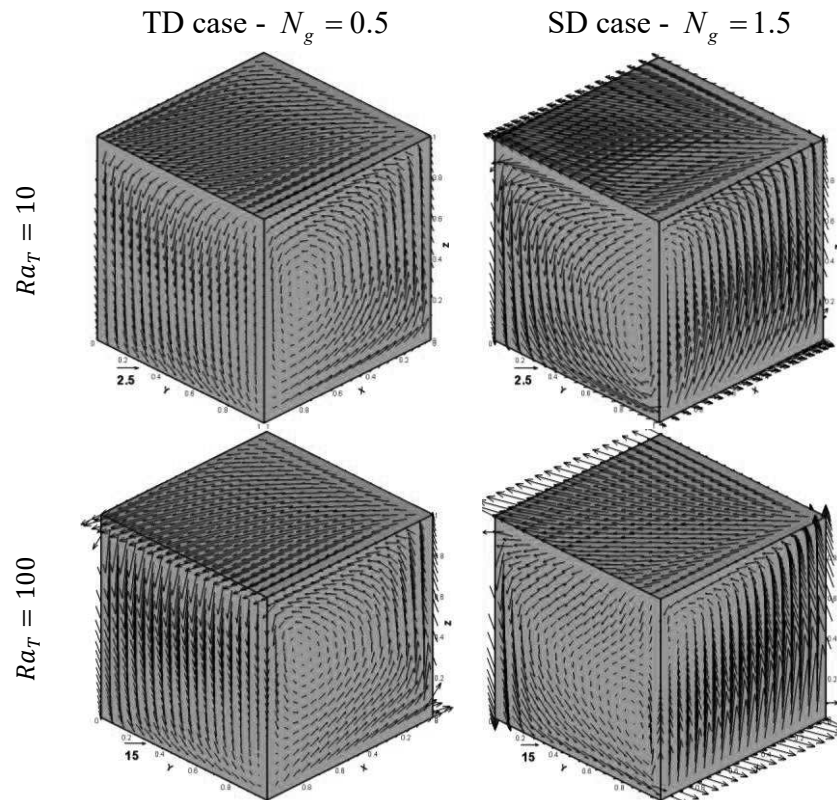


**Figure 3.7.** Effect of Rayleigh number on the flow structure: Arrow surface plot of the steady state velocity field at small and large thermal Rayleigh number in the cases of thermally (TD) and solute (SD) dominated convective flow.

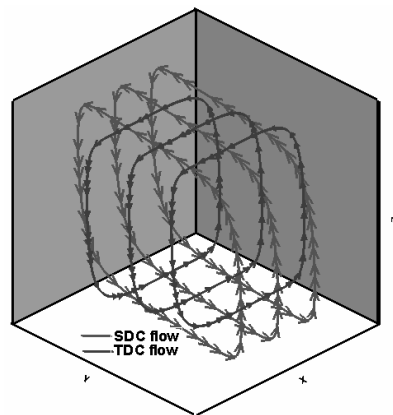


**Figure 3.8.** Components of the overall flow: The solute driven convective flow (SDC) and the thermally-driven convective flow (TDC).

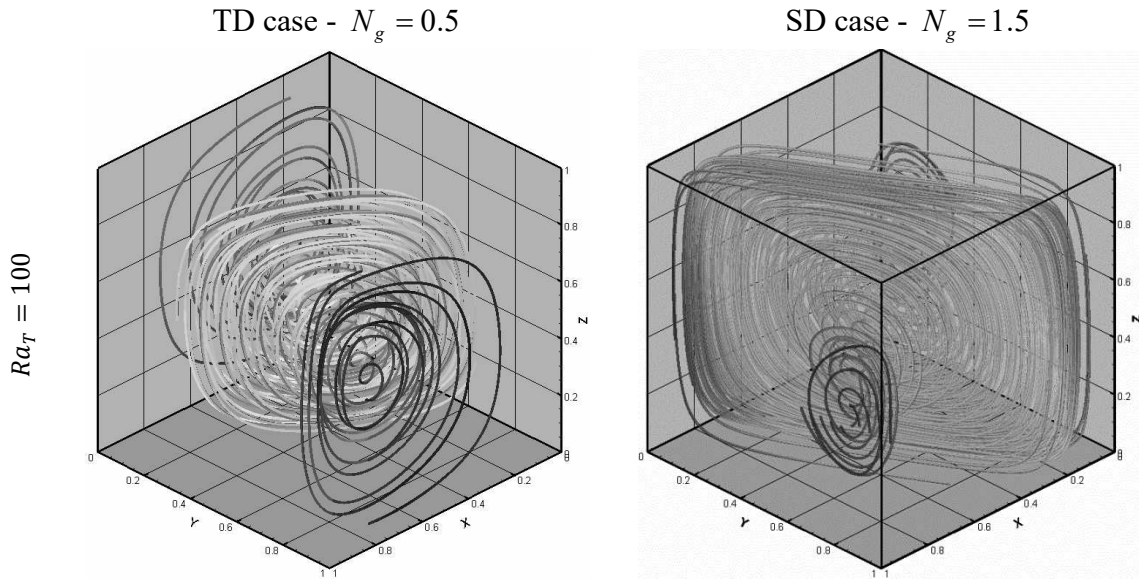


**Figure 3.9.** Effect of Rayleigh number on the flow structure: Stream-tubes showing the behavior of the vortex within the domain in the cases of thermally (TD) and solute (SD) -dominated convective flow  $Ra_T = 100$ , at steady state. For the TD case the stream-tubes are highlighted with concentration while for the SD cases they are highlighted with temperature.

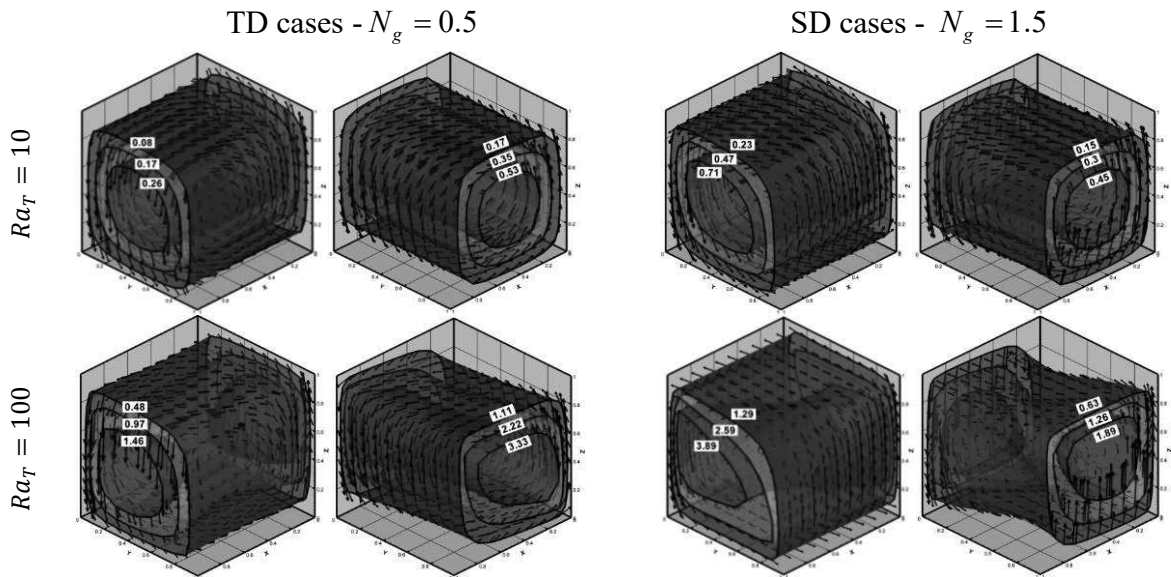


**Figure 3.10.** Steady state isosurfaces of the vector potential components ( $\Psi_x$ : left and  $\Psi_y$ : right) and velocity field (arrows) at small and large thermal Rayleigh numbers in the cases of thermally (TD) and solute (SD) dominated convective flow.

Figure 3.11 shows the effect of  $Ra_T$  on the concentration and temperature distributions. These figures indicate that concentration distribution is sensitive to  $Ra_T$  in the SD case while temperature field is affected by  $Ra_T$  in the TD case. At low  $Ra_T$ , in the TD case, the concentration isosurfaces are almost planar and vertical because the main flow occurs in the planes orthogonal to the

concentration gradient. This is also the case for temperature isosurfaces at low  $Ra_T$  in the SD case. At high  $Ra_T$ , in the TD case, both temperature and concentration isosurfaces follow the flow structure. The three-dimensional variation of the concentration is confined to limited zones at the top and bottom surfaces of the domain. However, the temperature isosurfaces are fully three-dimensional. The opposite is true for the SD case at high thermal Rayleigh number.

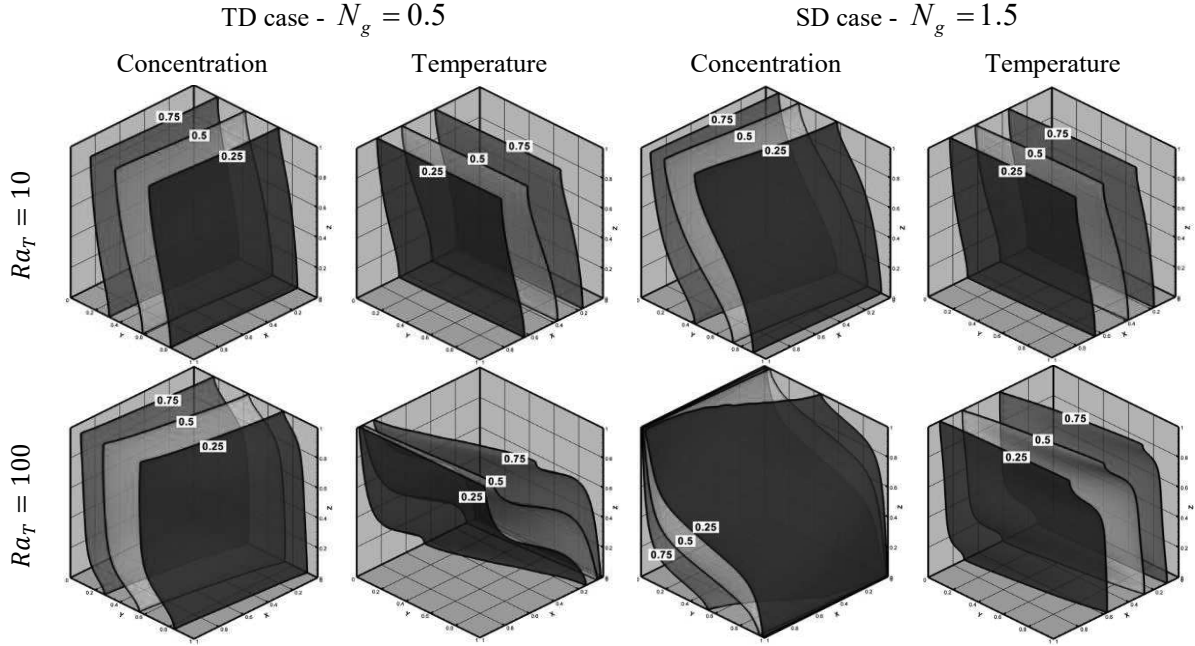


**Figure 3.11.** Effect of the Rayleigh number on the concentration and temperature distributions: Steady state concentration and temperature isosurfaces (0.25, 0.5 and 0.75) at small and large thermal Rayleigh numbers in the cases of thermally (TD) and solute (SD) dominated convective flow.

The effects of  $Ra_T$  on  $\overline{Nu}$  and  $\overline{Sh}$  (both steady state and transient) are depicted in Figure 3.12, for both TD and SD cases. Figures 3.12a and 3.12b confirm that the steady state values of both  $\overline{Nu}$  and  $\overline{Sh}$  increase with  $Ra_T$ . The increase of Rayleigh leads to flow intensification which narrow the solute and thermal boundary layers and enhance heat and mass transfer to the domain. However, the effect of  $Ra_T$  on heat ( $\overline{Nu}$ ) and mass ( $\overline{Sh}$ ) transfer fluxes are not equally distributed. In the TD case,  $Ra_T$  has slight effect on  $\overline{Sh}$  and significant impact on  $\overline{Nu}$ . The opposite is true for the SD case. This means that in the TD cases, the increase of  $Ra_T$  enhance significantly the heat transfer flux, while for the SD cases,  $Ra_T$  has more impact on the mass transfer flux.

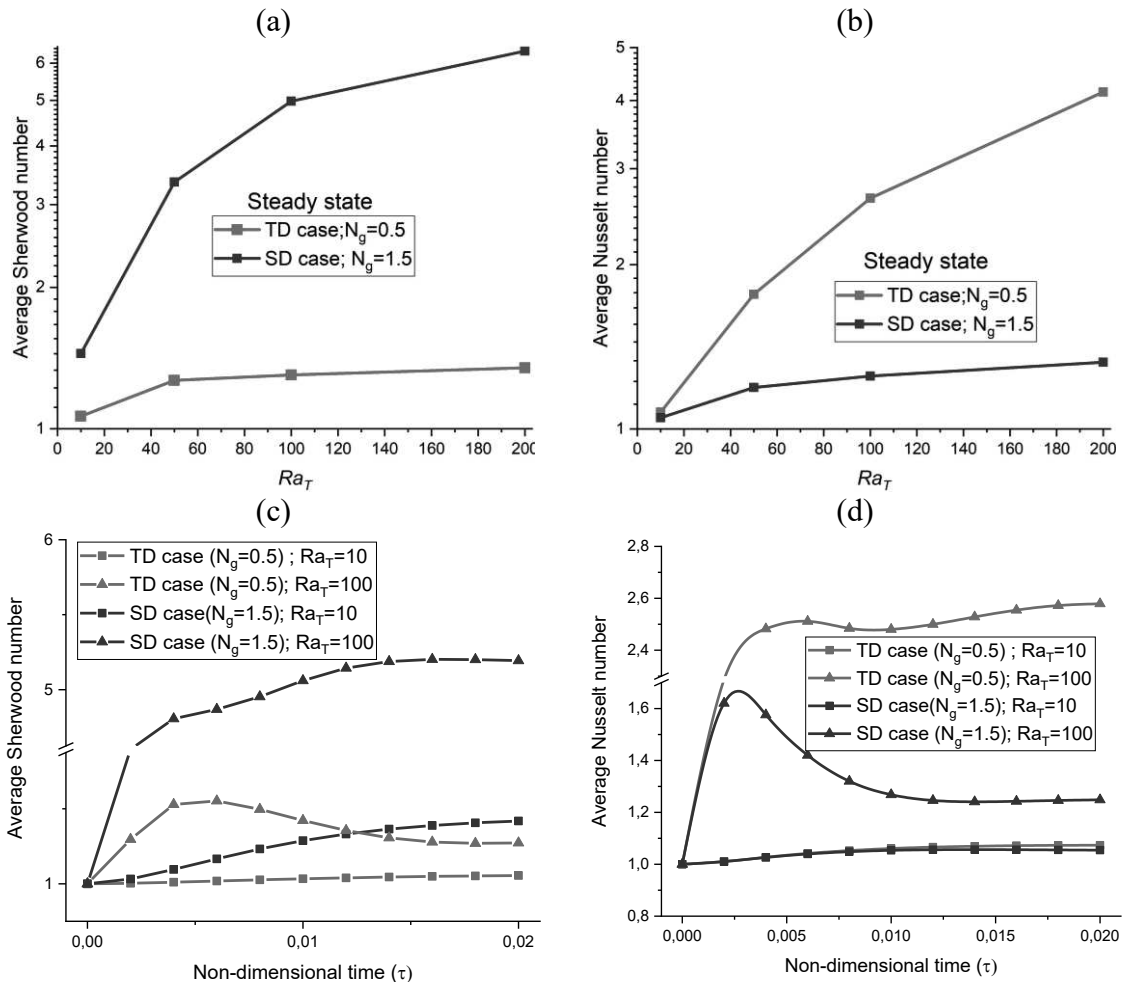


**Figure 3.12.** Effects of the thermal Rayleigh number on the average Sherwood and Nusselt numbers in the cases of thermally (TD) and solute (SD) dominated convective flow: Steady state regime (top) and transient regime (bottom).

Figures 3.12c and 3.12d show the time variations of  $\overline{Sh}$  and  $\overline{Nu}$  at low and high values of  $Ra_T$ , for TD and SD cases. The general behavior is that both  $\overline{Sh}$  and  $\overline{Nu}$  start from 1 at  $t=0$  and evolve until reaching asymptotic values indicating the steady state regime. The initial value of one is related to the initial conditions that is the linear distribution for concentration and temperature. The time required to reach the steady state regime decreases with increasing  $Ra_T$ . While in general, the mass flux to the cavity increases with time, Figure 3.12c shows particular variation of  $\overline{Sh}$  in the TD case and at high Rayleigh. This figure shows that, in such a case, the time variation of the mass flux (as measured by  $\overline{Sh}$ ) exhibits two regimes. Thus, it increases first to reach a maximum value at a transition time after which it decreases asymptotically toward the steady state value. Similar behavior can be observed for  $\overline{Nu}$  but in the SD case and at high Rayleigh.

### 3.5.2. Effect of $N_g$

As in the previous section, we assume  $Le = 2$ . And since  $N_g$  affects mainly the buoyancy forces, we consider high convective cases by assuming  $Ra_T = 100$ . The effect of  $N_g$  on the flow structure is investigated in the previous section. Thus, we investigate its effect on the maximum velocity components ( $Q_X^{\max}$ ,  $Q_Y^{\max}$  and  $Q_Z^{\max}$ )  $\mathbf{Q} = \left( \mathbf{q} \times \frac{H}{\alpha} \right)$  is the non-dimensional velocity field. The steady state results (Figure 3.13a) show that the maximum velocity component is in the vertical direction ( $Q_Z^{\max}$ ). There is an enhancement in the vertical flow when  $N_g$  is increased. In the TD cases, the  $x$ -component decreases with  $N_g$  while the  $y$ -component increases. Both components increase with  $N_g$  in the SD cases. For the TD cases, the flow in the  $x$ -direction is higher than in the  $y$ -direction. The opposite is true in the SD cases. The average Nusselt number decreases with  $N_g$  while the average Sherwood increases (Figure 3.13b). This indicates that the increase of  $N_g$  leads to the improvement of the mass flux to the domain and to the diminishment of the heat flux. The transient solutions confirm that the increase of  $N_g$  leads to the enhancement of the flow in the  $y$ -,  $z$ -components, whatever the time (Figure 3.13c). It is also true for the  $x$ -component in the SD cases and TD cases, but in TD cases, just for a short time at the beginning of the transient regime. After this short time and until the steady state regime,  $Q_X^{\max}$  decreases with the increase of  $N_g$ . In general, these results are coherent with the flow behavior at steady-state regime. Figure 3.13c shows that  $Q_Z^{\max}$  increases with time and reaches the steady state regime faster than the other velocity components.  $Q_Y^{\max}$  is almost increasing with time, but less time variability can be observed in the TD cases. Variation of  $Q_X^{\max}$  in time is highly sensitive to  $N_g$ . We can observe in Figure 3.13c that, in the TD case,  $Q_X^{\max}$  increases with time for  $N_g = 0.25$  while it decreases when  $N_g$  increased to 0.75. For the SD cases with  $N_g = 1.25$ ,  $Q_X^{\max}$  exhibits two regimes for time variation as it increases for a short time at the beginning of the simulation and then it decreases to reach the steady state value. Still for the SD cases but with  $N_g = 1.75$ ,  $Q_X^{\max}$  becomes decreasing with time. The time variations of the average Sherwood and Nusselt numbers are given in Figures. 3.13d and 3.13e, respectively. It is clear that, whatever the time,  $\overline{Sh}$  increases with the increase of  $N_g$ , while  $\overline{Nu}$  is decreasing. In the TD cases,  $\overline{Sh}$  follows two regimes of time variation. It increases with time at the beginning of the transient regime and then decreases until reaching its steady state value. Similar

behavior is observed for  $\overline{Nu}$  (Figure 3.13e), except for the TD case at small gravity number ( $N_g = 0.25$ ).

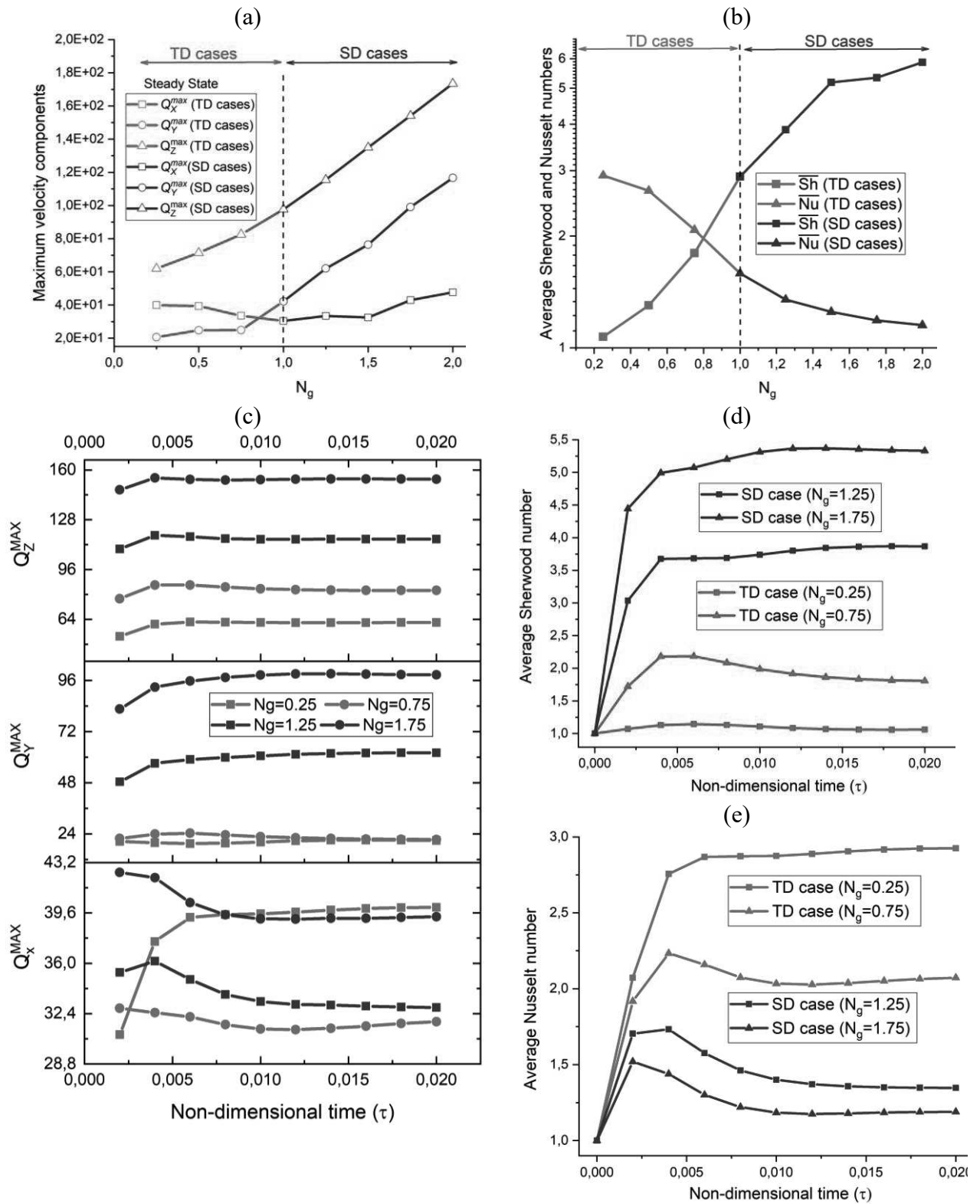


**Figure 3.13.** Effects of the gravity number on the maximum velocity components, average Sherwood and Nusselt numbers for steady state (a and b) and transient (c-e) regimes.

The effects of  $N_g$  on concentration and temperature distributions are investigated in Figure 3.14. For the TD cases, at constant  $Ra_T$ , the increase of  $N_g$  can be interpreted as an increase of the concentration gradient. This enhances the convective flow in the vertical planes parallel to YOZ and reduces the flow component in the vertical planes parallel to XOZ (related to the thermal gradient). This explains why the concentration isosurfaces become deformed when  $N_g$  is increased while the opposite is true for the temperature isosurfaces. Similar behavior is observed for the SD cases.

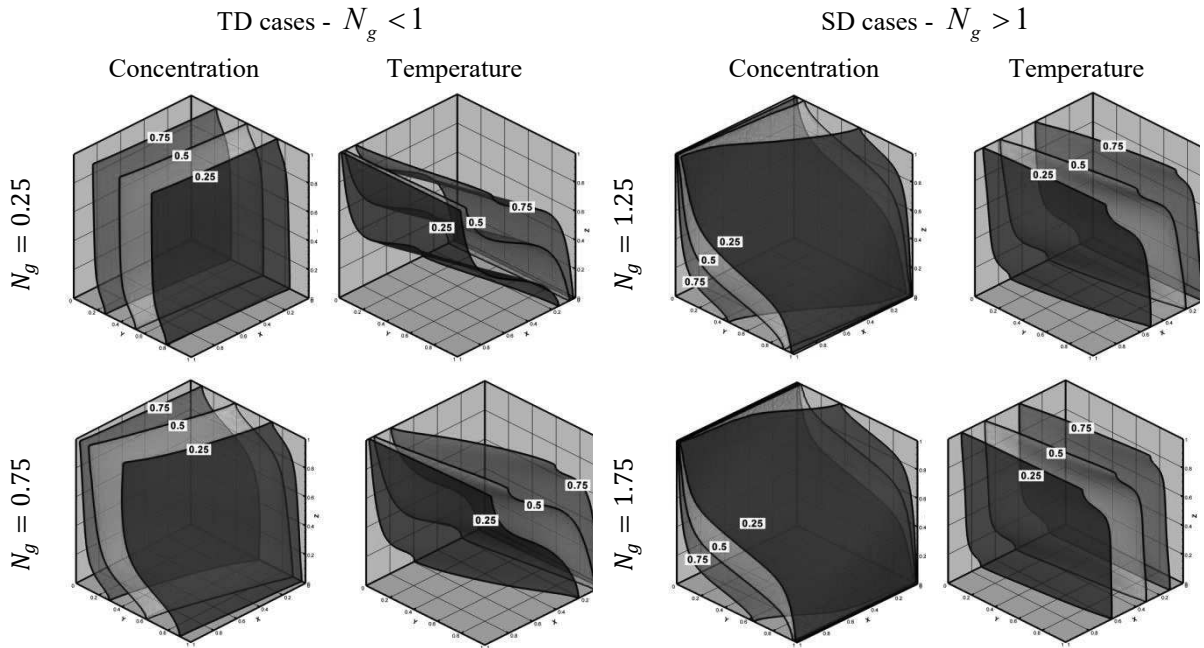


**Figure 3.14.** Effect of the gravity number ( $N_g$ ) on the concentration and temperature distributions: Main temperature and concentration isosurfaces (0.25, 0.5 and 0.75) for different values of  $N_g$  in the cases of thermally (TD- left) and solute (SD- right) dominated convective flow.

### 3.5.3. Effect of $Le$

The effect of  $Le$  is investigated in both TD ( $N_g = 0.5$ ) and SD ( $N_g = 1.5$ ) cases. We assume  $Ra_T = 100$ . The effects of  $Le$  on the steady state maximum velocity components is given in Figure 3.15a. It can be seen that the velocity field is slightly sensitive to  $Le$  in the TD cases. At constant thermal Rayleigh number, the increase of  $Le$  can be interpreted as a decrease of the molecular diffusion coefficient. The later can lead to sharper concentration distribution and in consequence a higher solute gradient. However, as in TD cases the convection flow is mainly caused by thermal gradient, the increase of the solute gradient cannot affect the velocity field. For the SD case, where convective flow is mainly related to concentration gradient, the velocity field becomes sensitive to

$Le$ , in particular  $Q_Y^{\max}$  and  $Q_Z^{\max}$ .  $Q_X^{\max}$  remains slightly sensitive to  $Le$ , which is logical as this component of the flow is caused by the temperature gradient. Figure 3.15a shows and intensifies convection rotating flow with the increase of  $Le$ . Time variations of the maximum velocity components are given in Figure 3.15c. This figure confirms that, in the TD cases, the transient convective flow is slightly sensitive to  $Le$ .  $Q_X^{\max}$  increases with time to reach its steady-state value while  $Q_Z^{\max}$  and  $Q_Y^{\max}$  have critical time for the transition between increasing and decreasing variations. For the ‘SD’ case, as for the steady state regime, the transient maximum velocity components increase with the increase of  $Le$ . It can be observed that  $Q_Y^{\max}$  and  $Q_Z^{\max}$  increase with time until reaching the steady state values, while  $Q_X^{\max}$  has different behavior as it is decreasing. In the SD case, both mass and heat fluxes to the domain are sensitive to  $Le$  (Figure 3.15b). As expected the mass flux to the domain is enhanced with the increase of  $Le$ . This is attributed to the increase of the solute gradient. However, the heat flux to the domain is reduced. In the TD case,  $\overline{Nu}$  is slightly sensitive to  $Le$  while expected  $\overline{Sh}$  increases with the increase of  $Le$ . The time variations of  $\overline{Sh}$  and  $\overline{Nu}$  are given in Figures 3.15d and 3.15e, respectively. Similar to the steady state condition, the transient mass flux in the domain increases with the increase of  $Le$  while the transient heat flux decreases. In the SD case,  $\overline{Sh}$  increases with the time until reaching the steady state regime while in the TD case it evolves to the steady state value by following increasing and decreasing periods. The opposite is true for  $\overline{Nu}$ . It is relevant to mention that, while steady state heat flux has been found to be insensitive to  $Le$ , the transient behavior of the  $\overline{Nu}$  shows some sensitivity to this parameter. Figures 3.15d and 3.15e show that both  $\overline{Sh}$  and  $\overline{Nu}$  reach the steady state regime in the SD case faster than the TD case.

The effects of  $Le$  on the temperature and concentration isosurfaces are investigated in Figure 3.16. It is clear from this figure that, for the considered range of variations, in both SD and TD cases, the temperature and concentration fields are slightly sensitive to  $Le$ . More sensitivity can be observed for concentration than temperature.

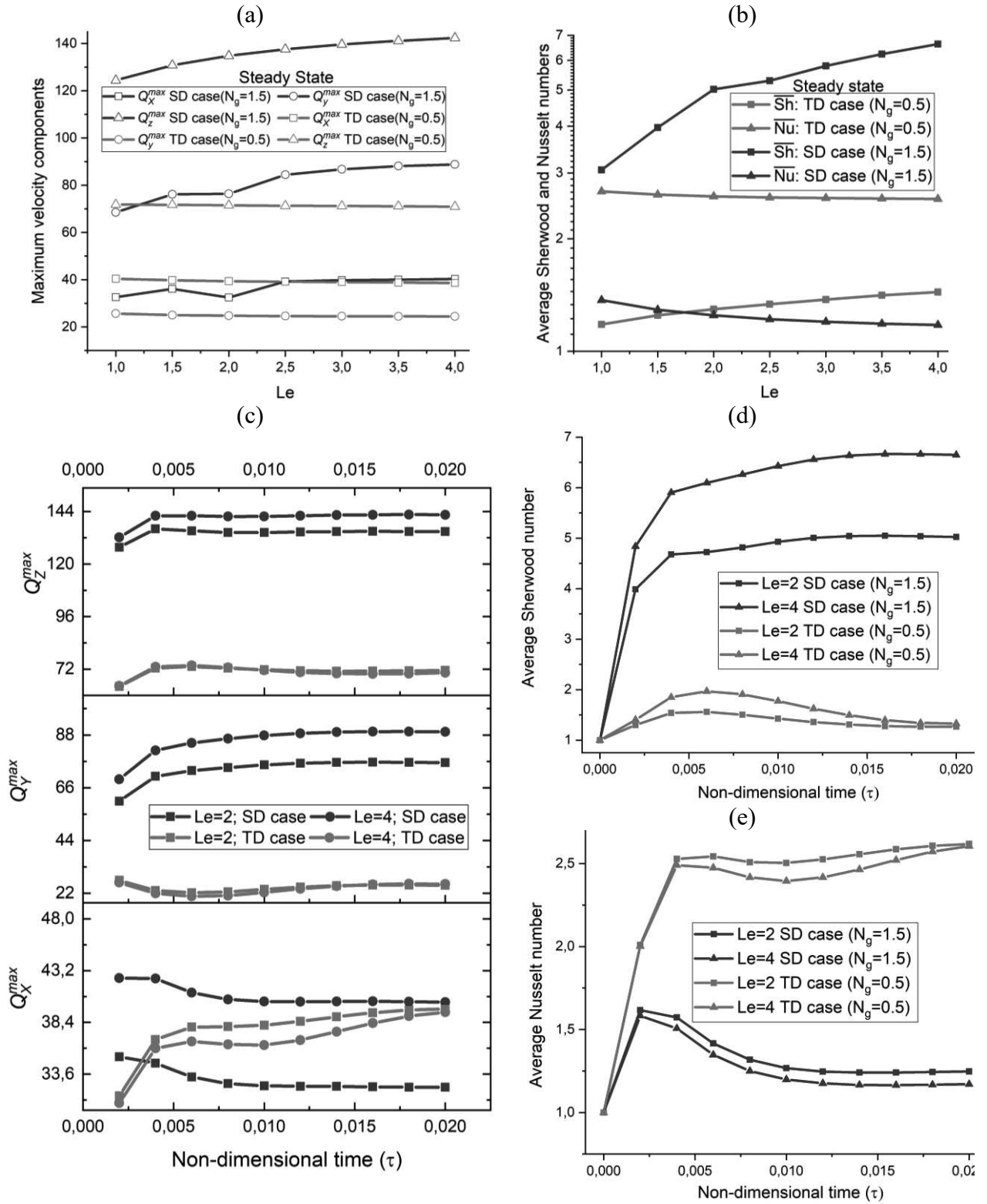


**Figure 3.15.** Effects of Lewis number on the maximum velocity components, average Sherwood and Nusselt numbers for steady state (a and b) and transient (c-e) regimes.

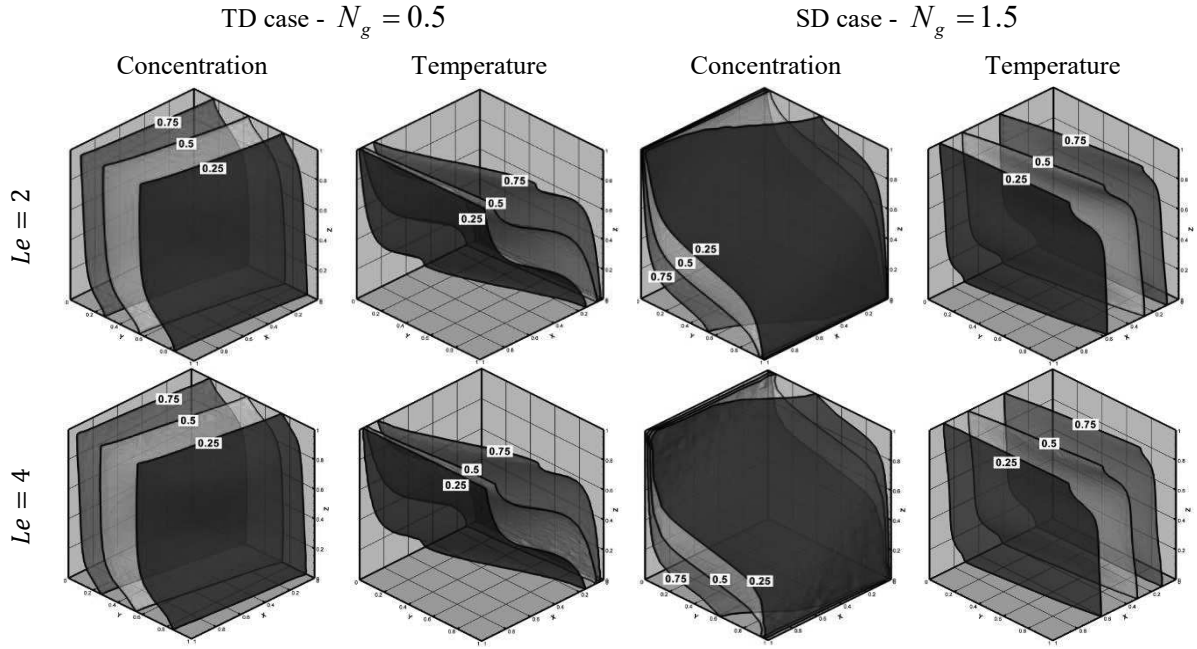


**Figure 3.16.** Effect of the Lewis number on the concentration and temperature distributions: Steady state concentration and temperature isosurfaces (0.25, 0.5 and 0.75) at different values of Lewis numbers in the TD and SD cases.

### 3.6. Understanding the effects of temperature and concentration gradients on heat and salinity fluxes

Several applications involve THC processes under different configurations of heat and salinity gradients. For instance, in applications involving injection of hot fluids inside wells (i.e geothermal, gas and oil wells) and in steam injection, there are significant heat losses that create a temperature gradient in the aquifers. In salinized aquifers, this creates an interaction with the existing salinity gradient (van Lopik et al., 2015). Thus, in such a case it is important to understand the effect of temperature gradient on mass flux entering the domain and the impact of salinity gradient on heat flux, which is the main objective of this section. This is useful to investigate the heat losses caused by the salinity gradient and/or the salinization induced by the heat gradient. Several previous studies addressed this question but under 2D assumption (van Lopik et al., 2015), which is not valid in the case of crossed-horizontal temperature and salinity gradients that needs 3D simulations. We address this question taking advantage of the developed semi-analytical solution. Thus, we first assume variable temperature gradient  $\Delta T = T_H - T_C$  and we investigate the effect of  $\Delta T$  on mass flux, as measured by the average Sherwood number. All other parameters related to fluid and porous domain properties are assumed to be invariable. The analysis is based on the parameters of test case 3, described in Table 1. However, to investigate both TD ( $N_g < 1$ ) and SD ( $N_g > 1$ ) cases, we consider  $N_g = 5$  for  $\Delta T = 1$ , We then increase  $\Delta T$  from 1 to 11, progressively. This corresponds to the

decrease of  $N_g$  from 5 to 0.45. The variation of the steady state average Sherwood number with respect to  $\Delta T$  is depicted in Figure 3.17a. As it can be seen, the increase of ( $\Delta T$ ) reduces the salinity flux in both ‘TD’ and ‘SD’ cases. In fact, the increase of ( $\Delta T$ ) is associated with the enhancement of the convective flow caused by the thermal gradient which occurs in the vertical planes parallel to the salinized wall. This leads to the decrease of the flow component perpendicular to the salinized wall and, in consequence, reduces the salinity flux. Figure 3.17a shows that the salinity flux is more sensitive to the temperature gradient in the SD cases than the TD cases. The effect  $\Delta T$  on the transient behavior of the salinity flux is depicted in Figure 3.17b. For small temperature gradient, the salinity flux reaches the steady state value faster than high temperature gradient where two-time variation regimes (increasing/decreasing) can be observed. As for steady state, the transient behavior of the salinity flux is slightly sensitive to  $\Delta T$  in the TD cases. We also investigate the effect of concentration gradient ( $\Delta c = c_s - c_f$ ) on heat flux, as measured by the average Nusselt number. Thus, as for the effect of  $\Delta T$ , we keep all parameters constant and we increase  $\Delta c$  from 1 to 11. We use the same parameters as Test case 3 in Table 1, but we assume that  $N_g = 0.2$  for  $\Delta c = 1$ . Thus,  $N_g$  varies from 0.2 to 2.2. Figure 3.17c shows that the steady state heat flux to the domain decreases with the increase of  $\Delta c$ . The explanation of this behavior is analogue to the variation of the salinity flux with temperature gradient. The heat flux is more sensitive to  $\Delta c$  in the TD cases. Figure 3.17d indicates that, in the SD cases, the transient heat flux reaches the steady state regime faster than the TD cases. In opposite to the salinity flux, similar behavior of heat flux with respect to time can be observed, whatever the concentration gradient.

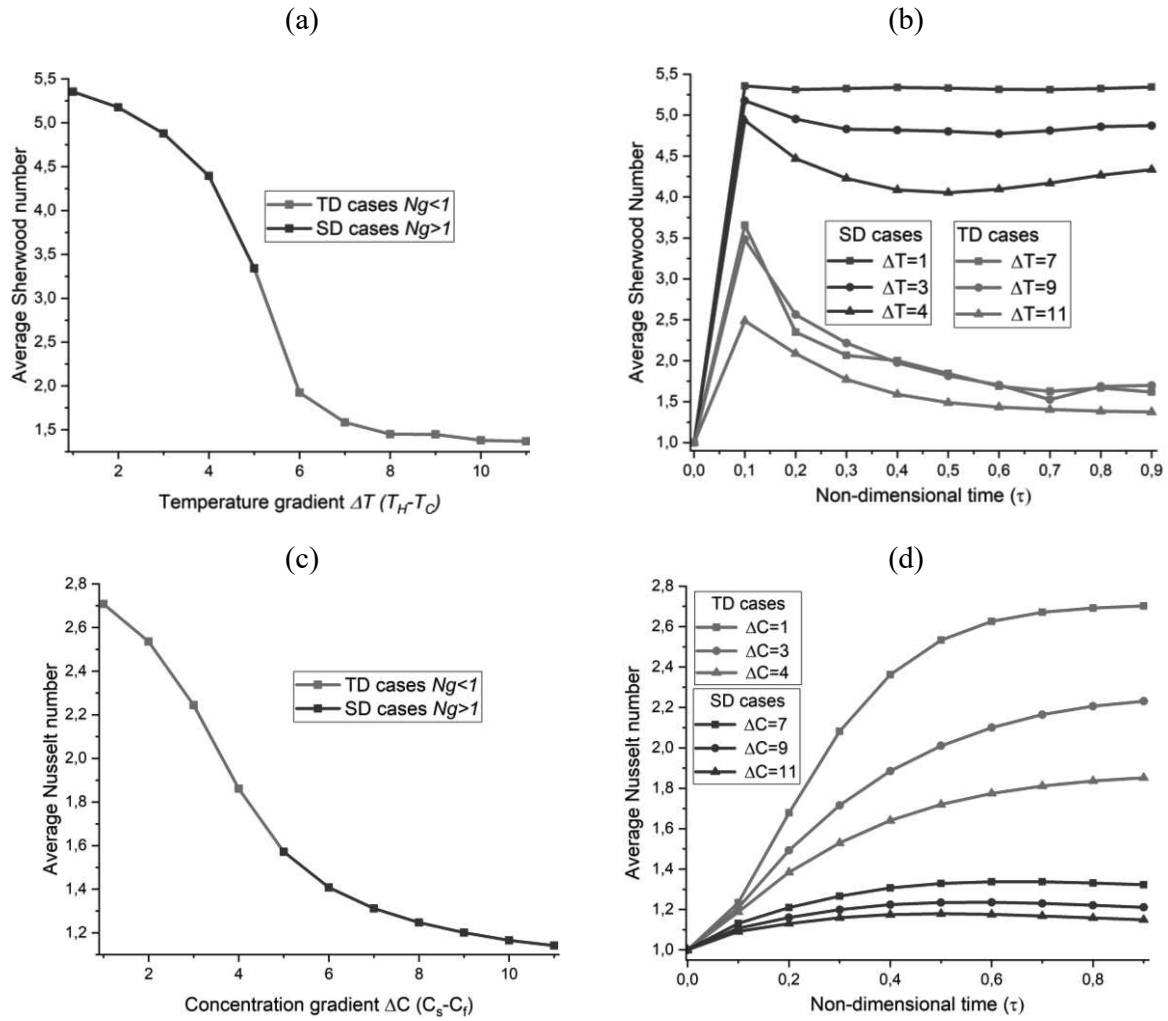


**Figure 3.17.** Effect of temperature (resp. concentration) gradient on mass (resp. heat) flux the domain, as measured by the average Sherwood (resp. Nusselt) number: Steady state regime (a and c) and transient regime (b and d)

### 3.7. Conclusion

Existing studies of thermohaline convection (THC) in porous enclosure are limited to 2D assumption under steady state conditions. In this work, we investigated three-dimensional THC in porous box under both transient and steady state regimes. We consider the case of crossed-horizontal temperature and concentration gradients for which the 2D assumption is not valid. Accurate 3D simulations of THC are computationally expensive as they require dense computational grids. We develop a meshless semi-analytical solution based on the Fourier series method (FS), applied to the vector potential form of the governing equations. The steady state semi-analytical solution is an extension of the solution developed by Shao et al [2018] for solute density driven flow. The FS method has been exclusively used to obtain semi-analytical solutions for density driven flow problems under steady state condition. From theoretical and technical point of view, the main contribution and novelty of this work is the new implementation of the FS method for solving transient problem.

The semi-analytical solution is verified against a finite element solution obtained with COMSOL. Excellent agreement between these solutions has been observed for cases involving small Rayleigh number. Numerical experiments with high Rayleigh number show high sensitivity of the finite element solution to the computational mesh and the numerical technique used in space discretization and time integration. This highlights the worthiness of the developed semi-analytical solution as benchmark for the assessment of new developed numerical methods and schemes. We provide high quality data, based on quantitative metrics, which can be used for codes benchmarking.

Effect of governing parameters on THC has been deeply investigated in the literature for different configurations of temperature and concentration gradients. Most of these studies deal with steady-state condition. Transient processes of THC are not well-understood. Despite its importance in several applications, the case of crossed-horizontal gradients has been never investigated because it requires 3D simulations. Taking advantage of the developed semi-analytical solution, we performed a complete parameters sensitivity analysis to address these gaps. In our analysis we distinguish between the cases of thermally-dominated convective flow (TD) and solute-dominated convective flow (SD). In both cases we observed the formation of single vortex convective flow which cannot be captured in 2D cases. The orientation of the vortex flow depends on the gravity number ( $N_g$ ) while its intensity is also sensitive to the thermal Rayleigh number ( $Ra_T$ ). As it is well known in problems involving density driven flow, the increase of  $Ra_T$  intensifies the convective flow and leads to the increase of both steady state Nusselt ( $\overline{Nu}$ ) and Sherwood ( $\overline{Sh}$ ) numbers. In the TD cases, two regimes (increasing then decreasing) of transient behavior are

observed for  $\overline{Sh}$ . Similar transient evolution is observed for  $\overline{Nu}$  in the SD cases. The increase of the gravity number can be interpreted as an increase of the solute Rayleigh number which is accompanied by convective flow intensification. The flow acceleration occurs in the plane parallel to the concentration gradient. This leads to the enhancement of the steady state salinity flux entering the domain (i.e.  $\overline{Sh}$ ) and reduction of the heat flux (i.e.  $\overline{Nu}$ ). Transient evolutions of  $\overline{Nu}$  and  $\overline{Sh}$  are sensitive to  $N_g$ . Either monotonous increasing variation or two regimes of variation can be observed, depending on  $N_g$ . The convective flow is slightly sensitive to the Lewis number ( $Le$ ). But in general, the vertical component increases with  $Le$ . The steady state heat flux to the domain is also slightly sensitive to  $Le$ , especially in the TD cases. However, the transient evolution of the heat flux is sensitive to  $Le$ .

We also investigate the effect of thermal gradient on the salinity flux and the effect of concentration gradient on heat flux. This is important in real applications involving heat gradient in salinized aquifers to understand heat losses due to salinity gradient or salinization induced by thermal gradient. The results show that, in the case of crossed gradients, the increase of heat gradient decreases the salinity flux to the domain, especially in the SD cases. The increase of salinity gradient decreases the heat losses from the hot source.

# Chapter IV: Robust numerical model for reactive-thermohaline convection of CO<sub>2</sub> in brine saturated reservoir

## 4.1. Introduction

Global warming is a crucial aspect of climate change, causing a wide range of consequences such as an increase in the frequency and severity of adverse weather events (Chen et al., 2021; Collins et al., 2013; Shi et al., 2020), an increase in global temperature at 1.5° C above the preindustrial level (Masson-Delmotte et al., 2018), ramifications in ecosystems such as desertification in arid and semi-arid regions (Chen et al., 2021; Wang et al., 2009) and reduction in bio-diversity (“IPCC. (2019).,” n.d.). Global warming is mainly related to anthropogenic greenhouse gas emissions. Burning fossil fuels (coal, oil, and gas), as primary energy sources, and large-scale deforestation have led to an accumulation of large amounts of greenhouse gases in the atmosphere, of which the most important is carbon dioxide (CO<sub>2</sub>). Despite the ongoing efforts on reducing the use of fossil fuels as the source of energy and substituting renewable sources, currently, most of the worldwide power plants are based on fossil fuels (Whitley, 2018). Therefore, the emission of CO<sub>2</sub> to the atmosphere is currently inevitable and until other inexpensive, clean, and plentiful technologies are available, a temporary possible way to deal with global warming is mitigating the existing CO<sub>2</sub> in the atmosphere. To this end, various approaches have been suggested including geologic CO<sub>2</sub> sequestration (GCS), which is the most effective technology to mitigate large-scale CO<sub>2</sub> emissions in the atmosphere (Zhang and Huisinigh, 2017). In the Paris agreement, this approach is introduced as one of the most promising solutions to address the global warming challenge (UNFCCC, 2015).

GCS consists of capturing CO<sub>2</sub> emissions at the industrial combustion sources (mainly fossil fuel-based power plants), compressing it to its supercritical state, transporting it, and injecting the supercritical CO<sub>2</sub> into deep saline aquifers or depleted oil or gas reservoirs for long-term storage. GCS involves a complex series of technologies based on the knowledge of geology, in-situ fluid chemistry, geochemistry, hydrology, and environmental science. Despite the reliability and richness of the injection techniques (Hoteit et al., 2019), the long-term geological storage capacity of CO<sub>2</sub> is not fully understood.

Understating the fate of CO<sub>2</sub> in the geological formation is essential for securing the sequestration and predicting the impact of dissolved CO<sub>2</sub> on host formation. In this context, numerical modeling has become an essential tool that is widely used for several field applications such as understanding physical processes, predicting the storage capacity, evaluating leakage risks, and designing storage systems (Emami-Meybodi et al., 2015; Jiang, 2011; Nordbotten and Celia, 2011). Despite the significant effort made in recent years on numerical modeling of GCS, some challenges are yet to

be resolved. For instance, the robustness, reliability, accuracy, and large-scale applicability of these numerical models are not fully understood. Research on the development of new numerical models is indispensable to improve the capacity of current simulators and to include further functionalities related to new applications.

The injected CO<sub>2</sub> can be trapped through various physical and chemical mechanisms. This covers stratigraphic, residual, solubility, and mineral trappings (Kim et al., 2019). Physical or stratigraphic trapping is a crucial mechanism to ensure long-term entrapment of CO<sub>2</sub>. Due to the low density of CO<sub>2</sub> compared to the brine in saline aquifers, injected CO<sub>2</sub> migrates upward in the formation until reaching an impermeable cap rock where it is physically entrapped, forming a gas cap. CO<sub>2</sub> continues to dissolve in brine, leading to solubility trapping. For large time scales, CO<sub>2</sub> can also chemically interact with rock formation. The dissolution of CO<sub>2</sub> in water increases its acidity, causing several primary minerals of the host rocks to dissolve into the formation water. As a result, the concentration of some cations such as Ca<sup>2+</sup>, Mg<sup>2+</sup>, and Fe<sup>2+</sup> increases. Reactions between these cations and carbonic acid can form carbonate minerals such as CaCO<sub>3</sub>, MgCO<sub>3</sub>, and FeCO<sub>3</sub>. This interaction is defined as mineral trapping (Zhang and Song, 2014), (Soltanian et al., 2019). In this work, we focus on solubility and mineral trappings which are crucial trapping processes due to their highly secure storage characteristics (Soltanian et al., 2017). In the following sections, we discuss two main shortcomings of the current numerical models and existing modeling-based studies.

The first challenge of numerical models is their capacity to reproduce the multi-physical processes at the interface between the structurally trapped CO<sub>2</sub> and the brine. Indeed, at this interface, CO<sub>2</sub> dissolution in the brine occurs due to mixing processes, where a CO<sub>2</sub>-laden brine is formed whose density is higher than the underlying brine. This results in additional dissolution related to gravity-induced fingering, caused by the convective flow (Lu et al., 2009). The effect of convective flow on CO<sub>2</sub> dissolution at the field scale has been discussed by Sathaye et al., (2014) and Ahmadiania et al., (2020) (Ahmadiania et al., 2020; Sathaye et al., 2014). Several modeling-based studies investigated the solubility trapping of CO<sub>2</sub> with the variable-density flow model coupling groundwater flow and mass transport under variable fluid density conditions. Depending on the objective of the study, different assumptions have been considered regarding the various physical processes. Several studies addressed the non-reactive convective flow (Farajzadeh et al., 2011; Hamann et al., 2015; Hewitt et al., 2014; Hidalgo and Carrera, 2009; Riaz et al., 2006; Singh and Islam, 2018). Convective-reactive CO<sub>2</sub> dissolution is extensively investigated in the literature (e.g., (Andres and Cardoso, 2011; Emami-Meybodi et al., 2015; Ghesmat et al., 2011; Ghoshal et al., 2017; Hidalgo et al., 2015; Kim et al., 2019; Shafabakhsh et al., 2021). For instance, Babaei and Islam, (2018) investigated convective-reactive CO<sub>2</sub> dissolution in aquifers with an immobile water

zone, while Erfani et al., (2020) studied the effect of geochemical reactions on CO<sub>2</sub> dissolution in sandstone aquifers. Most previous works assume isothermal conditions. However, it is well-known that temperature gradient, naturally in a reservoir or artificially introduced by CO<sub>2</sub> injection, can affect gravitational instability, fluid properties (notably viscosity), and dissolution processes (Ahmadinia et al., 2020; Emami-Meybodi et al., 2015). The coupled thermal and solute convection is usually called double diffusion convection or thermohaline convection (THC). Specific interests in THC of CO<sub>2</sub> appeared recently due to new applications involving coupled carbon storage and geothermal extraction (Wu and Li, 2020). Islam et al., (2013; 2014a), investigated THC of CO<sub>2</sub> in a brine-saturated geothermal reservoir. However, reactive THC (RTHC) of CO<sub>2</sub> is not well investigated in the literature (Islam et al., 2014b), and the effect of temperature on convective-reactive CO<sub>2</sub> dissolution are still poorly understood (Boudreau et al., 2020; Sjöberg and Rickard, 1984).

While broad interest has been paid to the numerical solutions of the equations governing reactive processes, the equations describing transport and flow processes are usually solved based on standard finite element (FE) or finite volume methods. For instance, Babaei and Islam, (2018) solved the stream function form of the governing equations using finite difference methods. The standard FE method is used in Kim et al., (2019). The finite volume method is used in Farajzadeh et al., (2011). A survey review on the numerical schemes used in the simulations of convective dissolution of CO<sub>2</sub> is reported in Emami-Meybodi et al., (2015). The standard numerical schemes used in the existing codes limit the applicability and reliability of these codes for the simulation of GCS at large space and time scales. Several works have shown that numerical simulations of variable-density flow problems are highly sensitive to the numerical scheme used in the approximation of the governing equations (Prasad and Simmons, 2005; van Reeuwijk et al., 2009; Voss et al., 2010). Standard FE or finite volume methods may generate unphysical oscillations that can affect the solutions' accuracy and convergence of the nonlinear solvers (Koohbor et al., 2020; Miller et al., 2013). Upwind schemes are usually implemented to avoid spurious oscillations ((Miller et al., 2013) and references therein). These schemes can reduce the numerical instability but at the expense of introducing numerical diffusion that can overestimate the mixing processes of CO<sub>2</sub>. Numerical diffusion can also overestimate the dissolution processes (Batlle et al., 2002). This can affect the predictions of domain clogging due to chemical reactions (Xu et al., 2017). In addition, in existing codes, reactive processes are usually included via the operator splitting approach. For kinetic reactions, this approach introduces intrinsic splitting errors that are proportional to the time step used in the numerical solution (Fahs et al., 2009). These numerical artifacts can be avoided by using dense computational grids with small time steps, which increase the computational requirements and the CPU time of simulations. This limits the applicability of

numerical models, especially in GCS applications that involve large time simulations for tens to hundreds of years at a large spatial scale. However, in the last years, advanced numerical methods (e.g., Mixed Hybrid finite elements (MHFE), Discontinuous Galerkin finite element (DGFE), Multipoints flux approximation approach (MPFA), error control based time stepping) have been developed for solving groundwater flow and transport equations in porous media. A detailed review of these numerical methods can be found in Miller et al., (2013). These advanced numerical techniques allow for enhancing model applicability by improving the computational time while maintaining high accuracy. They have been applied to a wide range of problems involving groundwater flow, and transport processes (e.g., (Hirthe and Graf, 2012; Hoteit and Firoozabadi, 2018; 2008; Koohbor et al., 2020; Moortgat, 2017; Moortgat et al., 2016), but their applications to problems dealing with variable-density flow models are limited (Raeisi Isa-Abadi et al., 2020; Younes et al., 2009). To the best of our knowledge, none of these numerical methods have been yet applied to RTHC problems.

The objective of this paper is to address the above-discussed shortcomings of numerical simulations of reactive-convection of CO<sub>2</sub> in geological formations by i) developing a new robust numerical model based on advanced numerical techniques, and ii) investigating the effect of temperature on the processes of convective-reactive CO<sub>2</sub> dissolution. The numerical model is developed based on the combination of the MHFE method (Younes et al., 2010) for groundwater flow and the DGFE method (Miller et al., 2013; Raeisi Isa-Abadi et al., 2020) for mass and heat transfer. The combination of these methods has shown several advantages in generating accurate and efficient numerical solutions of the variable-density flow problems (Younes et al., 2009), but it has never been applied to RTHC processes. Flow, mass transport, heat transfer, and chemical dissolution are solved sequentially. An adaptive time-stepping procedure, based on error control, is implemented to avoid operator splitting errors. The advantages of this scheme in the time integration of variable-density flow problems is highlighted in (Hirthe and Graf, 2012; Younes and Ackerer, 2010). This approach is extended in this work to model reactive processes. The numerical model is compared to the commercial FE software COMSOL Multiphysics. The new model is used to understand the effect of temperature on the processes of convective-reactive CO<sub>2</sub> dissolution in a natural gas reservoir in the North-sea.

## **4.2. Conceptual model and method**

### ***4.2.1. The porous square benchmark: problem description***

The numerical model developed in this work is adaptable for large-scale problems with complex geometries. However, as is common in the literature and theoretical research, we applied it to the problem of saturated porous square, which is widely accepted as a benchmark for several purposes

such as understanding physical processes, comparing numerical codes, and evaluating the effect of aquifer characteristics on trapping process (Farajzadeh et al., 2011; Islam et al., 2014a,b; Islam et al., 2013; Kim et al., 2019). The popularity of this benchmark stems from the regularity of its geometry and the simplicity of the corresponding boundary conditions. Thus, our domain is a square of size  $H$  [m], filled with saturated porous media containing impermeable and adiabatic vertical walls. The boundary conditions for flow, mass, and heat transfer are demonstrated in Figure 4.1. The top wall of the domain is exposed to the constant concentration of solute  $\text{CO}_2$  ( $C_{\text{CO}_2}^s [M.L^{-3}]$ ). No dispersive  $\text{CO}_2$  flux is imposed at the bottom surface. Hot ( $\theta_H [\Theta]$ ) and cold ( $\theta_C [\Theta]$ ) temperatures are applied to the bottom and top boundaries, respectively. These temperatures are representative of a geothermal temperature gradient. Initially, the fluid is at rest with no dissolved  $\text{CO}_2$  in the domain, and the fluid is at a reference temperature ( $\theta_0 [\Theta]$ ). The geochemical reactions of dissolved  $\text{CO}_2$  in the water is considered with calcium carbonate ( $\text{CaCO}_3$ ). The relative non-dimensional concentration of  $\text{CaCO}_3$  is equal to  $C_{\text{CaCO}_3}^s [M.L^{-3}]$  before the dissolution of  $\text{CO}_2$  in the water.

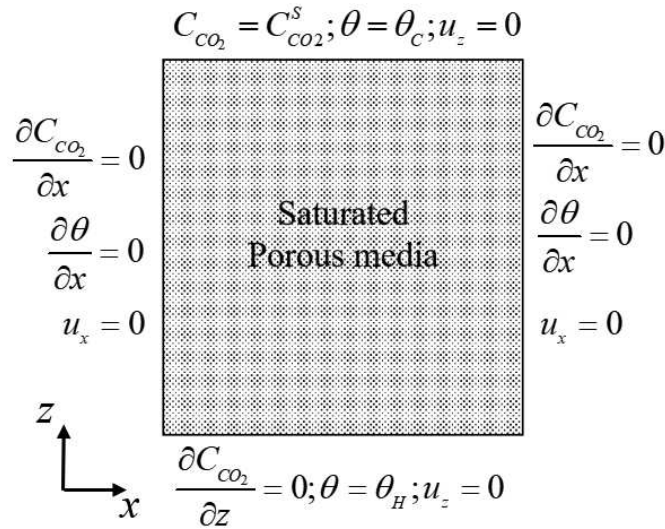


**Figure 4.1.** Illustration of the conceptual model for GCS as a RTHC problem in a porous box.

#### 4.2.2. The mathematical model

The governing equations describing the flow, mass and heat transfer and geochemical reactions processes are as follows:

- continuity equation with Boussinesq approximation:

$$\nabla \cdot \mathbf{u} = 0 \quad (4.1)$$

where,  $\mathbf{u} [L.T^{-1}]$  is the Darcy's velocity field.

- Darcy's law:

$$u_x = -\frac{k}{\mu} \frac{\partial p}{\partial x}; u_z = -\frac{k}{\mu} \left( \frac{\partial p}{\partial z} - (\rho - \rho_0) g \right) \quad (4.2)$$

where,  $u_x [L.T^{-1}]$  and  $u_z [L.T^{-1}]$  are the horizontal and vertical components of Darcy's velocity field, respectively.  $k [L^2]$  is the permeability of the porous media,  $\mu [M.L^{-1}.T^{-1}]$  is the fluid viscosity,  $p [M.L^{-1}.T^{-2}]$  is the fluid pressure,  $\rho [M.L^{-3}]$  is the fluid density, and  $g [L.T^{-2}]$  is the gravity acceleration.

- Mass transport for  $CO_2$  and  $CaCO_3$ :

$$\phi \frac{\partial C_{CO_2}}{\partial t} + u_x \frac{\partial C_{CO_2}}{\partial x} + u_z \frac{\partial C_{CO_2}}{\partial z} = D \cdot \phi \left( \frac{\partial^2 C_{CO_2}}{\partial x^2} + \frac{\partial^2 C_{CO_2}}{\partial z^2} \right) - K_r C_{CO_2} \cdot C_{CaCO_3} \quad (4.3)$$

$$\phi \frac{\partial C_{CaCO_3}}{\partial t} = -K_r C_{CO_2} \cdot C_{CaCO_3} \quad (4.4)$$

where,  $\phi [-]$  is the porosity,  $C_{CO_2} [M.L^{-3}]$  is the concentration of  $CO_2$ ,  $C_{CaCO_3} [M.L^{-3}]$  is the mass fraction of  $CaCO_3$  to the mass of rocks,  $t [T]$  is the time,  $D [L^2.T^{-1}]$  is the molecular diffusion coefficient,  $n$  is the reaction order, and  $K_r [M^{-1}.L^3.T^{-1}]$  is the reaction rate.

- Energy balance:

$$\sigma \frac{\partial \theta}{\partial t} + u_x \frac{\partial \theta}{\partial x} + u_z \frac{\partial \theta}{\partial z} = \alpha \left( \frac{\partial^2 \theta}{\partial x^2} + \frac{\partial^2 \theta}{\partial z^2} \right) \quad (4.5)$$

- where,  $\sigma[-]$  is the ratio of heat capacity of the saturated porous domain to the fluid,  $\theta[\Theta]$  is the temperature and  $\alpha[L^2.T^{-1}]$  is the thermal diffusivity of the saturated porous domain.
- Temperature and concentration dependence on density (Tabrizinejadas et al., 2020):

$$\rho = \rho_0(1 + \beta_c.C_{CO_2} + \beta_T(\theta - \theta_0)) \quad (4.6)$$

where,  $\rho_0[M.L^{-3}]$  is the density of native water at the reference temperature,  $\beta_c[M^{-1}.L^3]$  and  $\beta_T[\Theta^{-1}]$  are, respectively, the solute and thermal expansions, and  $\theta_0[\Theta]$  is the reference water temperature.

- The temperature dependence of the reaction rate (Petrou, 2012):

$$K_r = A \exp\left(-\frac{E_a}{R.\theta}\right) \quad (4.7)$$

where  $A[M^{-1}.L^3.T^{-1}]$  is the pre-exponential factor,  $E_a[M.L^2.T^{-2}]$  is the activation energy,  $R[M.L^2.T^{-2}.\Theta^{-1}]$  is the ideal gas constant.

- The temperature dependence of the viscosity:

$$\mu(\theta) = C_0 + C_1 \times \theta + C_2 \times \theta^2 + C_3 \times \theta^3 + C_4 \times \theta^4 + C_5 \times \theta^5 + C_6 \times \theta^6 \quad (4.8)$$

The coefficients in equation (4.8) are given as follows:  $C_0 = 1.37995$ ,  $C_1 = -0.021224$ ,  $C_2 = 1.360456 \times 10^{-4}$ ,  $C_3 = -4.645409 \times 10^{-7}$ ,  $C_4 = 8.9042735 \times 10^{-10}$ ,  $C_5 = -9.0790692 \times 10^{-13}$  and  $C_6 = 3.8457331 \times 10^{-16}$ .

#### 4.2.3. Dimensionless analysis

We perform our analysis based on the non-dimensional form of the governing equations. The following dimensionless variables are used:

$$X = \frac{x}{H}; Z = \frac{z}{H}; \mathbf{U} = \frac{\mathbf{u}.H}{\phi D}; P = \frac{p.k}{\mu.\phi.D}; \tau = \frac{t.D}{H^2}; CO_2 = \frac{C_{CO_2}}{C_{CO_2}^S};$$

$$CaCO_3 = \frac{C_{CaCO_3}}{C_{CaCO_3}^S}; \eta = \frac{\theta - \theta_c}{\theta_H - \theta_c}$$
(4.9)

By assuming that the reference temperature is  $\theta_c$  ( $\theta_0 = \theta_c$ ) and  $C_{CaCO_3}^S = C_{CO_2}^S$ , the non-dimensional governing equations become as follow:

$$\nabla \cdot \mathbf{U} = 0 \quad (4.10)$$

$$U_x = -\frac{\partial P}{\partial X}; U_z = -\frac{\partial P}{\partial Z} + Ra_s \cdot CO_2 + Ra_T \cdot Le \cdot \eta \quad (4.11)$$

$$\frac{\partial CO_2}{\partial \tau} + U_x \frac{\partial CO_2}{\partial X} + U_y \frac{\partial CO_2}{\partial Y} = \frac{\partial^2 CO_2}{\partial X^2} + \frac{\partial^2 CO_2}{\partial Z^2} - Da \cdot CO_2 \cdot CaCO_3 \quad (4.12)$$

$$\frac{\partial CaCO_3}{\partial \tau} = -Da \cdot CO_2 \cdot CaCO_3 \quad (4.13)$$

$$\sigma \frac{\partial \eta}{\partial \tau} + \phi \cdot U_x \frac{\partial \eta}{\partial X} + \phi \cdot U_z \frac{\partial \eta}{\partial Z} = \phi \cdot Le \left( \frac{\partial^2 \eta}{\partial X^2} + \frac{\partial^2 \eta}{\partial Z^2} \right) \quad (4.14)$$

In equations (4.10)-(4.14), the dimensionless parameters are defined as follows:

- The local solute Rayleigh number expressing the ratio of solute buoyancy to solute diffusivity:

$$Ra_s = \frac{g.k.H.\rho_0.\beta_c.\Delta C_{CO_2}}{\phi.\mu.D} \quad (4.15)$$

where  $\Delta C_{CO_2}$  is the difference between the highest and lowest concentration of  $C_{CO_2}$  in the domain.  $\Delta C_{CO_2}$  is equal to  $C_{CO_2}^S$  because the lowest  $C_{CO_2}$  concentration is assumed to be zero.

- The local thermal Rayleigh number, which is the ratio of thermal buoyancy to thermal diffusivity

$$Ra_T = \frac{g.k.H.\rho_0.\beta_T.\Delta \theta}{\mu.\alpha} \quad (4.16)$$

$\Delta \theta (= \theta_H - \theta_c)$  is the difference between the highest and lowest temperature.

- The Lewis number, expressing the ratio of thermal diffusivity to solute diffusivity, is

$$Le = \frac{\alpha}{\phi \cdot D} \quad (4.17)$$

- The local Damköhler number giving the ratio of geochemical reaction rate to diffusion rate is given by

$$Da = \frac{K_r \cdot C_{CO_2}^s \cdot H^2}{\phi \cdot D} \quad (4.18)$$

- The local Damköhler number is expressed as a function of temperature using the Arrhenius law):

$$Da = Da_0 \exp\left(-\frac{1}{R_1 \eta + R_2}\right) \quad (4.19)$$

In equation (4.19), the parameters  $Da_0$ ,  $R_1$  and  $R_2$  are defined as follows:

$$Da_0 = \frac{A \cdot C_{CO_2}^s \cdot H^2}{\phi \cdot D} \quad (4.20)$$

$$R_1 = \frac{R \Delta \theta}{E_a} \quad (4.21)$$

$$R_2 = \frac{R \theta_c}{E_a} \quad (4.22)$$

#### 4.2.4. A new numerical model for RTHC

A new numerical model is developed to solve the governing equations (equations (4.10)-(4.14)). The new model is based on advanced formulations of the FE method. Appropriate formulations are used to treat the different mathematical operators. The main goal behind selecting these advanced formulations is to reduce CPU time, while maintaining high accuracy. The new model is based on the in-house code TRACES (Transport of RadioActive Elements in Subsurface) (Shao et al., 2018; Younes et al., 2009). TRACES is extended in this study to deal with RTHC simulations. In TRACES, the flow is discretized with the MHFE method, which is more accurate than the standard FE method in simulating fluid flow in heterogeneous porous domains (Younes et al., 2010). The advection operators in the mass transport and energy conservations are treated with the DGFE

method (Miller et al., 2013; Raeisi Isa-Abadi et al., 2020). This method leads to high accuracy solutions as it reduces numerical diffusion and unphysical oscillations (Miller et al., 2013). The dispersion operators for mass and heat transfer are discretized using the MPFA method (Younes et al., 2013) Advantages of this combination of FE formulations have been discussed in (Fahs et al., 2016; Shao et al., 2018; Tabrizinejadas et al., 2020). The equations of flow, mass transfer and energy balance, under variable density, are solved sequentially. The reactive operator is also coupled to the flow and transfer processes with the sequential non-iterative approach. However, it is known that this approach introduces operator splitting errors proportional to the time step (Fahs et al., 2008). To control this error, we implement an adaptive time-stepping based on error estimation. The time step is adapted during the simulation based on error estimation to maintain the prescribed accuracy (Hirthe and Graf, 2012; Younes et al., 2010).

### 4.3. Comparaison TRACES vs. COMSOL

#### 4.3.1. Verification

A new code (TRACES) has been developed to simulate RTHC of  $\text{CO}_2$ . This section aims at verifying the correctness of the new developed code. Thus, TRACES is compared to a FE solution obtained using COMSOL Multiphysics. The COMSOL model is developed by coupling the modules of ‘Darcy’s Law  $-dl$ ’, ‘Heat Transfer in Porous Media  $-ht$ ’ and ‘Transport of Diluted Species in Porous media  $-tds$ ’. The reaction term is defined as a function of temperature and it is included in ‘ $tds$ ’ module as in equation (4.7). This equation is implemented in COMSOL as ‘variables’ in “component definition”. The density is assumed to be a function of temperature and concentration as in equation (4.6). The Boussinesq approximation is implemented in COMSOL by assuming constant density in the three modules (‘ $dl$ ’, ‘ $ht$ ’ and ‘ $tds$ ’) and including variable density in the gravity term. The viscosity is considered as a function of temperature as in equation (4.8).

In our analysis, we use quantitative metrics, which can be helpful for validating and benchmarking numerical codes. As common in the literature, we use the average Nusselt ( $\overline{Nu}$ ) and Sherwood ( $\overline{Sh}$ ) numbers to characterize the rates of heat and mass transfer to the domain, respectively.  $\overline{Nu}$  and  $\overline{Sh}$  are defined as follows (Rajabi et al., 2020):

$$\overline{Nu} = \int_0^1 \frac{\partial \eta}{\partial Z} \Big|_{Z=0} dX \quad (4.23)$$

$$\overline{Sh} = \int_0^1 \frac{\partial CO_2}{\partial Z} \Big|_{Z=1} dX \quad (4.24)$$

For evaluating the capacity of the reservoir in capturing  $\text{CO}_2$ , we use the total diffusive flux at the domain top surface ( $TF^{diff}$ ). This is defined as a time integral of the instantaneous flux. At a dimensionless time  $\tau^*$ ,  $TF^{diff}$  is calculated as follows:

$$TF^{diff} = \int_0^{\tau^*} \overline{Sh} d\tau \quad (4.25)$$

Verification in the case of vertical concentration and temperature gradients is questionable due to the gravitational instability. Therefore, we considered a stable configuration by considering horizontal temperature and concentration gradients. Thus, Dirichlet boundary conditions of temperature and concentration on the vertical walls of the domain and assuming that there is no heat and mass fluxes across the horizontal walls. This case is inspired from (Tabrizinejadas et al., 2020). In order to avoid potential numerical oscillations in the FE solution, the comparison between TRACES and COMSOL is made for a test case with a smooth distribution of concentration and temperature (low convective flow regime and relatively slow reaction rate). This case is denoted by ‘Test case 1-H’, referring to horizontal concentration and temperature gradient. The non-dimensional parameters for this test case are listed in Table 4.1. The corresponding physical parameters used in COMSOL are given in Table 4.2. Parameters in these tables are physically plausible and consistent (Sainz-Garcia et al., 2017). The viscosity is assumed to be independent of temperature (i.e.  $\mu = \mu_0$ ) to ensure constant thermal and solution Rayleigh numbers. To alleviate nonlinearity, we assume a first-order dissolution reaction. Thus, in equation (4.3), the reaction term ( $-K_r C_{\text{CO}_2} \cdot C_{\text{CaCO}_3}$ ) is replaced by  $-K_r C_{\text{CO}_2}$ . In other words, the concentration  $\text{CaCO}_3$  is assumed to be constant (i.e. equal to  $C_{\text{CaCO}_3}^s$ ) in the reaction term. This term is dropped from the equations when  $C_{\text{CaCO}_3}$  becomes null.

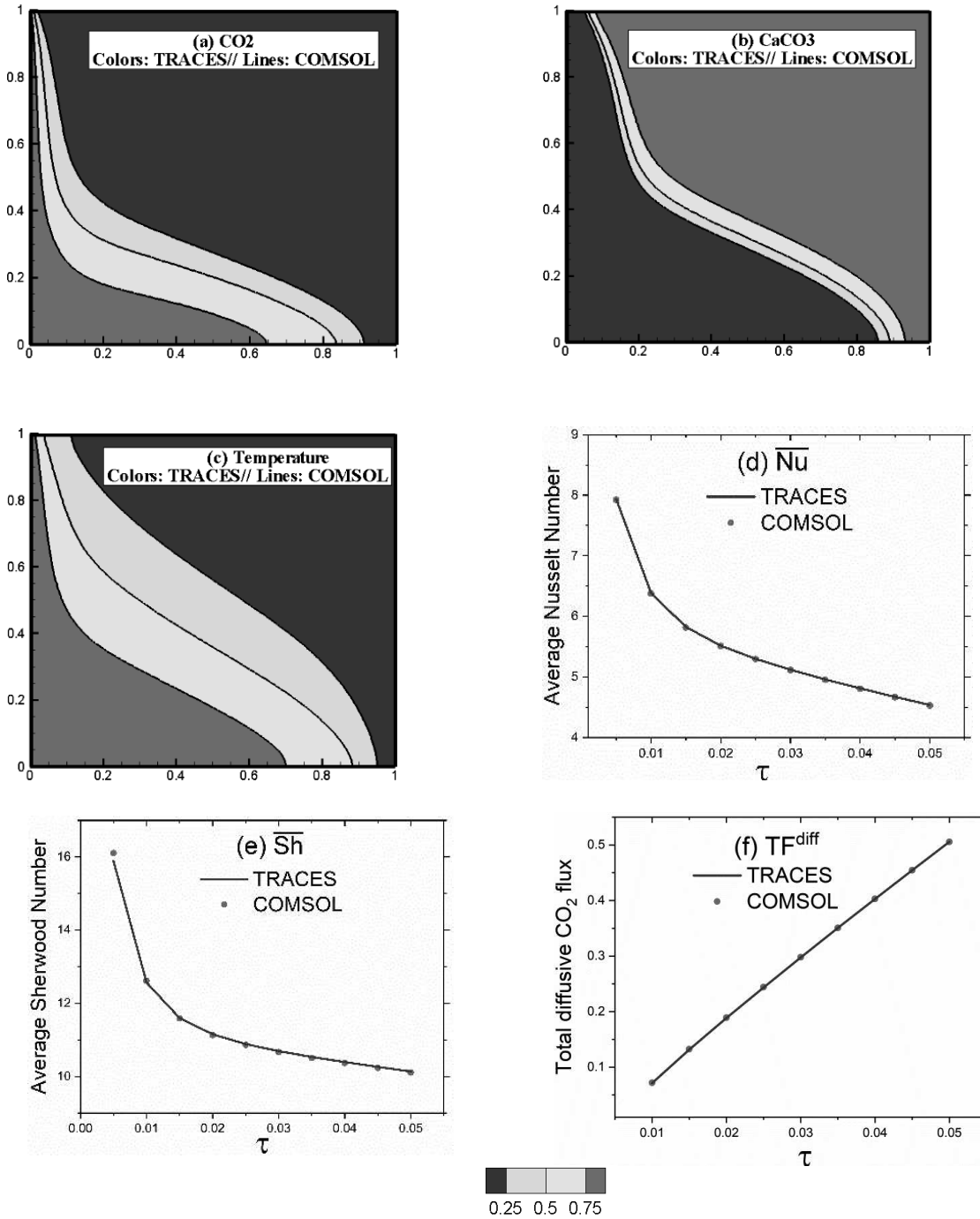
The comparisons between the results of ‘Test case 1-H’ obtained from TRACES and COMSOL are demonstrated in Figure 4.2. The dimensionless concentration and temperature distributions are plotted at a non-dimensional time  $\tau = 0.05$ , and the metrics characterizing mass and heat transport are plotted over time. Both solutions are indistinguishable in terms of concentration ( $\text{CO}_2$  and  $\text{CaCO}_3$ ) and temperature distributions as well as for  $\overline{Nu}$ ,  $\overline{Sh}$  and  $TF^{diff}$ . For the case of horizontal temperature and concentration gradients, these metrics are defined at the left vertical wall. These results confirm not only the correctness of the developed TRACES code, but also the COMSOL model and the post-treatment analysis for the evaluation of metrics used for characterizing the mass and heat transfer processes.

**Table 4.1.** Non-dimensional parameters used for the test cases

	‘Test case 1-V’ and ‘Test case 1-H’	‘Test case 2’	‘Test case 3’
$Ra_s$	300	800	1000
$Ra_T$	30	80	1000
$Le$	2	5	10
$Da_0$	$10^{11}$	$5 \times 10^{11}$	$10^{11}$
$R_1$	$10^{-3}$	$10^{-2}$	$10^{-2}$
$R_2$	$5 \times 10^{-2}$	$7 \times 10^{-2}$	$5 \times 10^{-2}$
$\phi$	0.3	0.3	0.3
$\sigma$	0.46	0.46	0.46

**Table 4.2.** Dimensional parameters used for the test cases

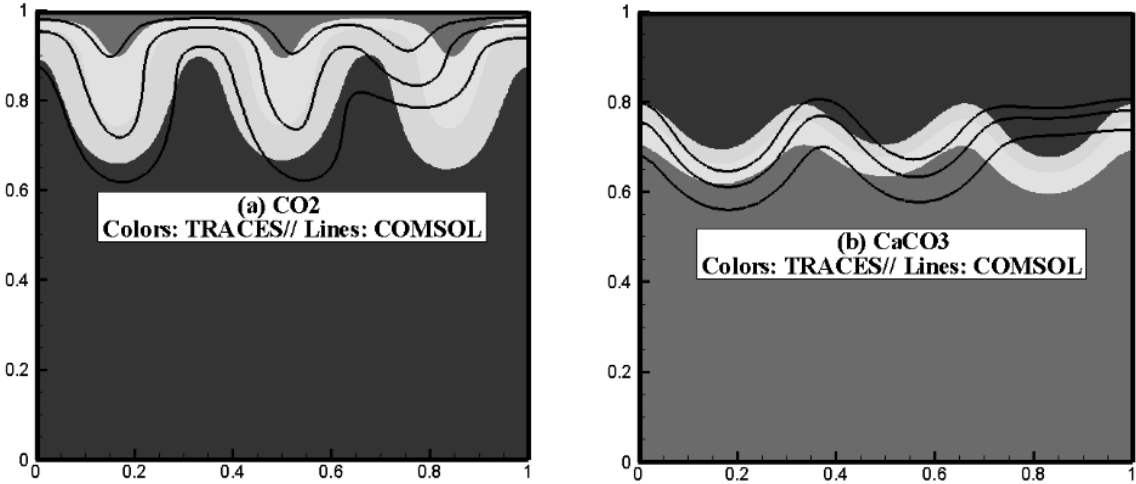
Gas constant	$R = 8.314 \text{ J.mol}^{-1}.\text{K}^{-1}$		
Reference Temperature	$\theta_0 = 277.15 \text{ K}$		
Porous box size	$H = 1 \text{ m}$		
Porosity	0.3		
Concentration of $\text{CO}_2$ at the inlet wall	$C_{\text{CO}_2}^s = 1 \text{ mol.m}^{-3}$		
Initial concentration of $\text{CaCO}_3$	$C_{\text{CaCO}_3}^s = 1 \text{ mol.m}^{-3}$		
Freshwater density	$\rho_0 = 1000 \text{ kg.m}^{-3}$		
Solid phase density	$\rho_s = 2300 \text{ kg.m}^{-3}$		
Gravity	$g = 10 \text{ m.s}^{-2}$		
Viscosity	$\mu_0 = 10^{-3} \text{ kg.m}^{-1}.\text{s}^{-1}$		
Permeability	$k = 10^{-9} \text{ m}^2$		
Cold temperature	$\theta_C = 277.15 \text{ K}$		
Thermal capacity of water	$cp_f = 4200 \text{ J.kg}^{-1}.\text{K}^{-1}$		
Thermal capacity of soil	$cp_s = 418 \text{ J.kg}^{-1}.\text{K}^{-1}$		
Thermal Conductivity of water	$\lambda_f = 0.65 \text{ W.m}^{-1}.\text{K}^{-1}$		
Thermal Conductivity of soil	$\lambda_s = 5.725 \text{ W.m}^{-1}.\text{K}^{-1}$		
	‘test case 1-H and V’	‘test case 2’	‘test case 3’
Thermal expansion coefficient of water	$\beta_T = 5.5 \times 10^{-4} \text{ K}^{-1}$	$\beta_T = 2.05 \times 10^{-4} \text{ K}^{-1}$	$\beta_T = 0.001 \text{ K}^{-1}$
Hot temperature	$\theta_H = 282.61^\circ \text{ K}$	$\theta_H = 316.17^\circ \text{ K}$	$\theta_H = 332.58^\circ \text{ K}$
Mass Expansion	$\beta_C = 0.015 \text{ m}^3.\text{mol}^{-1}$	$\beta_C = 0.016 \text{ m}^3.\text{mol}^{-1}$	$\beta_C = 0.01 \text{ m}^3.\text{mol}^{-1}$
Molecular Diffusion	$D_m = 1.67 \times 10^{-6} \text{ m}^2.\text{s}^{-1}$	$D_m = 6.67 \times 10^{-7} \text{ m}^2.\text{s}^{-1}$	$D_m = 3.33 \times 10^{-7} \text{ m}^2.\text{s}^{-1}$
Activation Energy	$Ea = 45419 \text{ J.mol}^{-1}$	$Ea = 32442 \text{ J.mol}^{-1}$	$Ea = 46085 \text{ J.mol}^{-1}$
Pre-exponential factor in the Arrhenius law	$A = 5 \times 10^4 \text{ s}^{-1}.\text{m}^{-3}.\text{mol}$	$A = 5 \times 10^4 \text{ s}^{-1}.\text{m}^{-3}.\text{mol}$	$A = 10^4 \text{ s}^{-1}.\text{m}^{-3}.\text{mol}$



**Figure 4.2.** ‘Test case 1-H’: Comparison between TRACES and COMSOL for (a) dimensionless CO<sub>2</sub> concentrations, (b) dimensionless CaCO<sub>3</sub> concentration, (c) dimensionless temperature distribution at  $\tau = 0.05$ , (d)  $\overline{Nu}$ , (e)  $\overline{Sh}$  and (f)  $TF^{diff}$ .

We also compared the results of TRACES versus COMSOL in the case of vertical temperature and concentration gradients, involving gravitational instability. This test case is called ‘Test case 1-V’, referring to vertical concentration and temperature gradients (see Figure 4.1). The non-dimensional parameters are kept the same as ‘Test case 1-H’. The same computational mesh and time step, as in ‘Test case 1-H’, is used in the analysis of ‘Test case 1-V’. Thus, numerical artifacts related to space or time discretization can be avoided. The comparison between the results of TRACES and

COMSOL for dimensionless concentrations ( $\text{CO}_2$  and  $\text{CaCO}_3$ ) and temperature (at  $\tau = 0.05$ ) as well as  $\overline{Nu}$ ,  $\overline{Sh}$  and  $TF^{diff}$  (over the time) are shown in Figure 4.3. This figure shows that both models provide equivalent results. Despite the equivalent numerical parameters used for time integration and spatial discretization, both models are not in full agreement. However, this agreement can be seen as satisfactory, knowing that, in the literature, matching results of this unstable configuration in space and time is somewhat unsuccessful (Xie et al., 2012). An important observation is that good agreement between COMSOL and TRACES is obtained for the total flux, which is the most important model output for the evaluation of reservoir capacity in capturing  $\text{CO}_2$ . This means that numerical instability does not materially affect the total flux of  $\text{CO}_2$ .



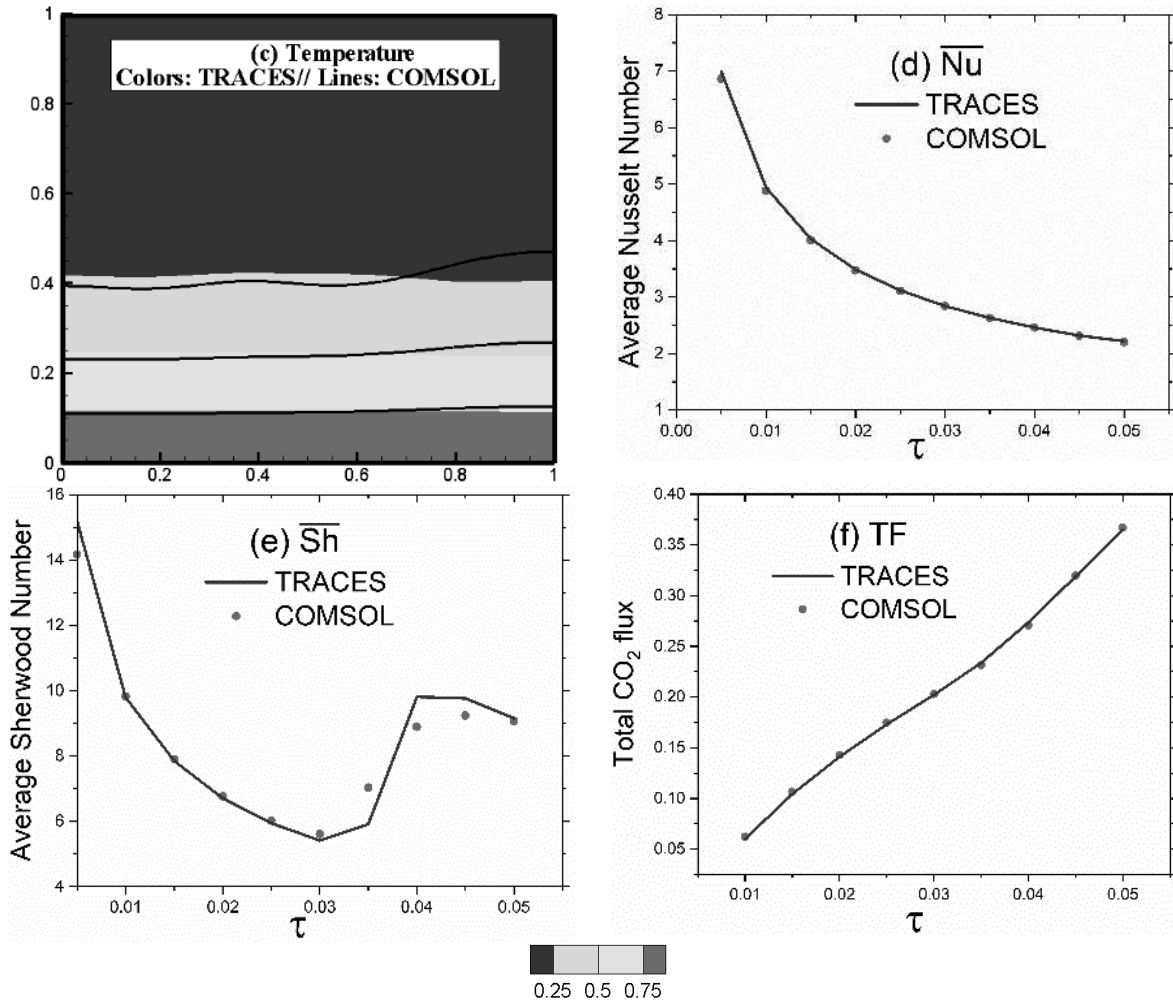


**Figure 4.3.** Comparison between TRACES and COMSOL for ‘Test case 1’V’: (a) dimensionless  $CO_2$  concentrations, (b) dimensionless  $CaCO_3$  concentration, (c) dimensionless temperature, all at  $\tau = 0.05$ . (d) time variation of  $\overline{Nu}$ , (e) time variation of  $\overline{Sh}$  and (f) time variation of  $TF$

#### 4.3.2. Advantages of the newly developed model (TRACES)

One of the objectives of this work is to develop an accurate model for the simulation of RTHC processes, based on advanced FE methods and time integration techniques. This section aims at investigating the advantages of this newly developed model (TRACES), compared to the standard FE method (COMSOL). Thus, we consider a challenging case dealing with sharp temperature and concentration distributions, and high Damköhler number. This test case is challenging because sharp temperature and concentration distributions may lead to unphysical oscillations or introduce numerical diffusion, while fast reaction rate requires small time steps to avoid operator splitting errors. This test case is denoted as ‘Test case 2’. As a mesh independent solution is required to compare the models, we limited this part to the case of horizontal thermal and solute gradients. This reference solution cannot be easily obtained in the case of vertical concentration and temperature

gradients because inherent instability renders the solutions highly sensitive to the mesh. The non-dimensional parameters for ‘Test case 2’ are listed in Table 4.1. The physical parameters used in COMSOL are given in Table 4.2. As for ‘Test case 1’ the viscosity is assumed to be independent on temperature (i.e.  $\mu = \mu_0$ ) and first-order dissolution reaction is considered.

A mesh-independent solution is obtained using TRACES with a mesh consisting of 12K nodes. With the same mesh, the FE solution (i.e., concentrations and temperature distributions) is different (Figures 4.4a-4.4c). The resulting FE solution exhibits spurious/unphysical oscillations. Examples of these oscillations are plotted in Figure 4.5. With the mesh consisting of 12K nodes, low negative concentrations are obtained for CO<sub>2</sub> (maximum negative value is -0.0066) (Figure. 4.5a). Due to the nonlinearity of the reaction term, these small oscillations in CO<sub>2</sub> lead to incoherent results of CaCO<sub>3</sub> with, for instance, negative concentrations (until -1.72) and larger values beyond physics (+1.93) (Figures. 4.5b and 4.5c). The difference between TRACES and FE solutions can be attributed to the unphysical oscillations encountered with the FE method. These solutions are reduced (even avoided) with the numerical scheme used in TRACES.

By refining the mesh progressively, we observed that the FE solution is mesh-dependent. The simulation with 140K nodes is represented in Figures 4.4a-4.4c. The results are plotted for non-dimensional time  $\tau = 0.05$ . It is clear that, by refining the mesh, FE solution is converging towards the TRACES solution. But there is no full agreement between both solutions. A finer mesh should be used to get the same solution obtained with TRACES. But we stopped the mesh refinement at 140K nodes due to CPU time limitations. The oscillations are smoothed out with mesh refining, as can be seen in Figure 4.5. For CO<sub>2</sub>, very small negative values are observed (the maximum negative value is  $-6 \times 10^{-6}$ ) (Figure 4.5d). Oscillations of CaCO<sub>3</sub> have been effectively reduced with mesh refining, but they remain significant (Figures 4.5e and 4.5f). The maximum negative concentration is -0.33, and the largest value beyond 1 is 1.096. These results indicate the agreement between TRACES and the FE solution is improved when the oscillations in the FE method are reduced by mesh refinement. This confirms that the discrepancy between both solutions is related to the oscillations encountered with the FE method. The results of this test case show that simulating RTHC processes at high Rayleigh and Damköhler numbers is challenging for the standard finite element method. This test case can be used as a benchmark for comparing newly developed methods in future studies.

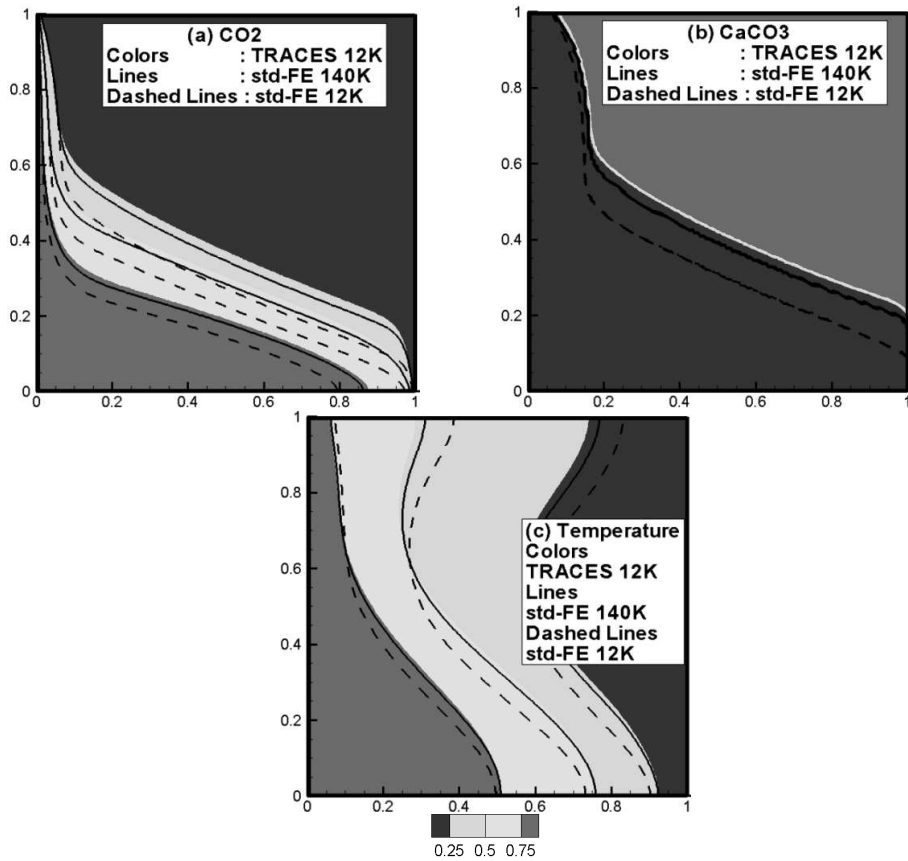


**Figure 4.4.** Comparison between TRACES and std-FE for ‘Test case 2’: (a) dimensionless  $\text{CO}_2$  concentration, (b) dimensionless  $\text{CaCO}_3$  concentration, (c) dimensionless temperature, all at  $\tau = 0.05$ .

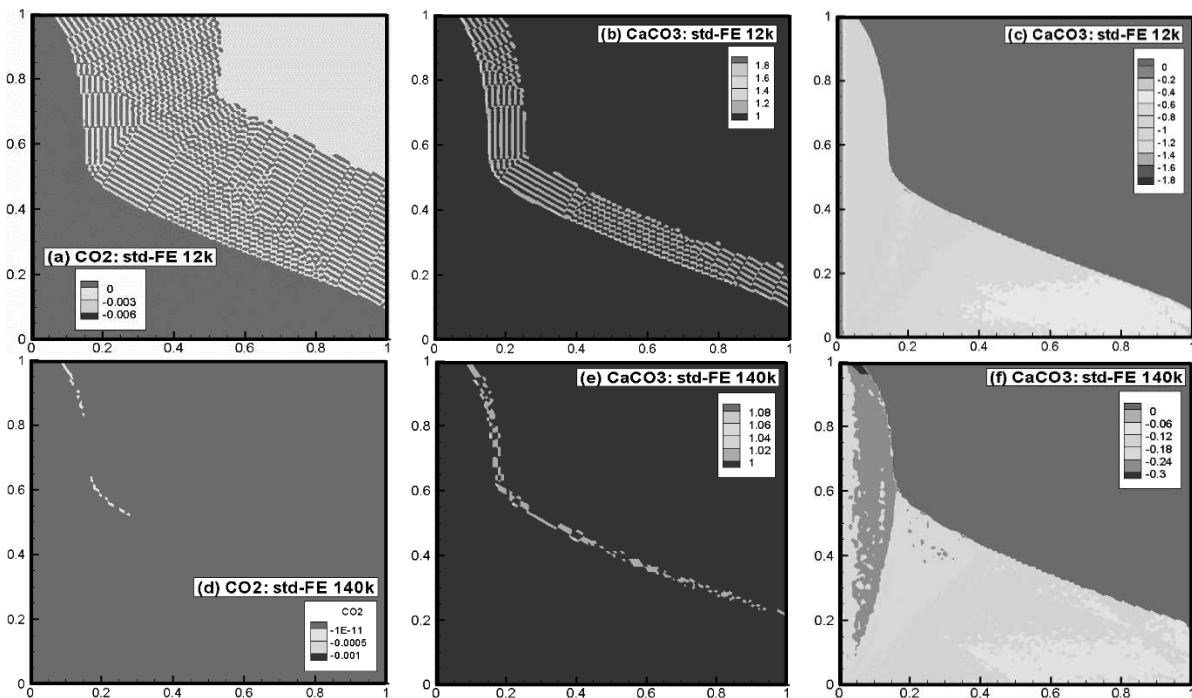


**Figure 4.5.** Oscillations with the std-FE solution for ‘Test case 2’. Negative  $\text{CO}_2$  concentration (a and d),  $\text{CaCO}_3$  concentrations larger than one (b and e) and negative  $\text{CaCO}_3$  concentration (c and f). All the results are presented at  $\tau = 0.05$ .

#### 4.4. Effect of temperature on the processes of convective-reactive CO<sub>2</sub> dissolution

Temperature gradient causes convective flow associated with density and viscosity dependence on temperature. It can also affect the reaction rate of the geochemical dissolution reactions. This section aims at investigating the effects of temperature on the process of convective-reactive CO<sub>2</sub> dissolution. For the first time, this is done based on the hypothetical benchmark of a porous cavity. This allows for understanding the thermal effect under simplified conditions (i.e., small scale and homogenous domain). Then a field case study in an offshore reservoir at the North Sea is investigated for a wider understanding under more realistic conditions such as heterogeneity and large space and time scales.

Our analysis is based on the comparison of three models with increasing levels of complexity and realism. The different simplifications and assumptions of these models are discussed below:

- Model 1 ('Isothermal'): In this model, the isothermal conditions are considered by assuming that the temperature is constant, in space and time. In this model, the density is assumed to be a function of concentration while the reaction rates and the viscosity are constant. The latter is calculated as a function of the constant temperature via equations (4.7) and (4.8), respectively. This model is called 'isothermal'. It imitates models usually used in previous studies, which are based on isothermal assumptions.
- Model 2 ('Linear Temperature'): This model assumes linear distribution of temperature with depth. The temperature is increasing with depth, but it is invariant in time. The viscosity and density are assumed to be independent of temperature, thus thermal convective processes are neglected. But, the reaction rate is assumed to be a function of temperature as in equation (4.7). This model is referred as 'Linear Temperature' in the rest of this paper.
- Model 3 ('RTHC'): in this model, all the RTHC processes are included. Thus, the temperature is assumed to be a function of time and space. It is obtained by solving the heat transfer equation (Equation (4.5)). Density, viscosity, and reaction rate are assumed to be a function of temperature. This model is called 'RTHC'.

The three models are used to simulate both the porous square cavity problem and the field case study. Several metrics such as the temperature and concentration distributions, the cumulative total flux of CO<sub>2</sub> at the top surface, and the total amount of CaCO<sub>3</sub> are used in the analysis. The comparison between models "Isothermal" and "Linear temperature" allows for investigating the effect of the temperature dependence of the reaction rate on these metrics. Comparison between

models “Linear Temperature” and “RTHC” allows for understanding the effect of convective flow on the dissolution processes.

#### **4.4.1. The hypothetical benchmark of porous square cavity**

The dimensionless analysis of this benchmark (see section 2.3) shows that the processes of RTHC are governed by six non-dimensional parameters:  $Ra_s$ ,  $Ra_T$ ,  $Le$ ,  $Da_0$ ,  $R_1$  and  $R_2$ . We first run the three models (“Isothermal”, “Linear Temperature” and “RTHC”) with the parameters used for ‘Test case 1’ dealing with low thermal Rayleigh number (see Tables 4.1 and 4.2). For “Isothermal”,  $Ra_T$  and  $Le$  are set to be 0. The local Damköhler number is calculated as in equation (4.19) with a constant dimensionless temperature  $\eta = 0.5$ . For the model “Linear Temperature”  $Ra_T$  and  $Le$  are also set to be 0, but the local Damköhler number is calculated as in equation (4.19) with a dimensionless temperature that varies linearly between 0 and 1 along the depth. For ‘Test case 1’, the simulations show equivalent results between the three models. These results are not presented for the sake of brevity. This indicates that at low thermal Rayleigh number, at a small scale, and under homogenous configuration, the temperature has no effect on CO<sub>2</sub> concentration nor the metrics characterizing CO<sub>2</sub> storage and flux. We further investigate this benchmark at a higher thermal Rayleigh number. Thus, we consider a new test case (‘Test case 3’) dealing with a higher thermal Rayleigh number and higher dependency of the reaction rate to temperature. Second-order dissolution reaction is assumed in this test case, as in equations (4.12) and (4.13). The non-dimensional parameters of this test case are given in Table 4.1 (‘Test case 3’).  $Ra_T$  and  $Le$  in this table are used only in “RTHC” model. For “Isothermal” and “Linear Temperature”, these parameters are set to zero. The physical parameters of ‘Test case 3’ are given in Table 4.2. The dependency of the Damköhler number to the temperature is plotted in Figure 4.6. This figure shows high variability of the Damköhler number with temperature with values ranging from 200 to about 6,000. These values are coherent with the range of variability of the Damköhler number considered in (Sainz-Garcia et al., 2017).

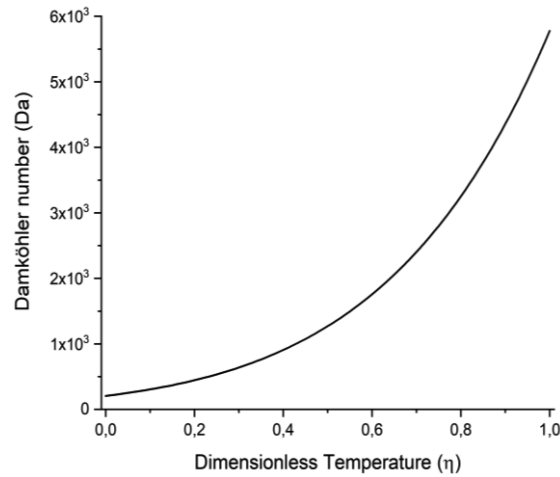


**Figure 4.6.** Variation of the Damköhler number as a function of dimensionless temperature in ‘test case 3’.

Figure 4.7 shows the contour maps of normalized concentration of  $\text{CO}_2$ ,  $\text{CaCO}_3$ , and temperature at  $\tau = 0.01$  (equivalent to  $30000s$ ) for ‘Test case 3’, simulated with three models. Density-driven fingering processes are observed with the three models. Equivalent results have been obtained with “Isothermal” and “Linear Temperature”. However, the growth and depth development of fingers seem to be under-predicted with ‘Isothermal’ (Figures 4.7a and 4.7d). This can be related to the fact that, near the domain top surface, the temperature with “Isothermal” is higher than that with “Linear temperature” (see Figures 4.7c and 4.7f). Thus, in this zone, the local reaction rate is higher with “Isothermal” than with “Linear temperature”. Faster dissolution of  $\text{CO}_2$  leads to less penetration of fingers in the domain. To confirm this conclusion, we further simulate ‘Test case 3’ with “Isothermal” by assuming lower constant temperature ( $\eta = 0.25$ ). The results (not shown for the sake of brevity) indicate more penetrated fingers with a reduced constant temperature. Figures 4.7b and 4.7e show a wider layer of  $\text{CaCO}_3$  dissolution with “Linear temperature”. This is coherent with the results of  $\text{CO}_2$  showing rapid fingers penetration with this model. However, at the top surface of the domain, lower concentration of  $\text{CaCO}_3$  can be observed with “Isothermal”, indicating more local dissolution with this model. This is related to the fact that “Isothermal” over-predicts the reaction rate in this zone. With RTHC, unlike “Isothermal” and “Linear temperature”, due to opposite thermal (upward) and solute (downward) gradients, the convective  $\text{CO}_2$  fingers are irregular and not uniformly distributed. Temperature distribution is also affected by both thermal and solute buoyancy effects (Figure 4.7i). Due to thermal convective processes (Figure 4.7i),  $\text{CO}_2$  reaches the bottom surface of the domain (Figure 4.7g). Dissolution of  $\text{CaCO}_3$  takes place almost overall the domain. In the bottom surface, despite low concentrations of  $\text{CO}_2$ , significant dissolution processes can be observed (Figure 4.7h). The  $\text{CaCO}_3$  concentration in this zone is almost zero. The

high temperature at the bottom surface leads to a high reaction rate and enhances the dissolution processes.

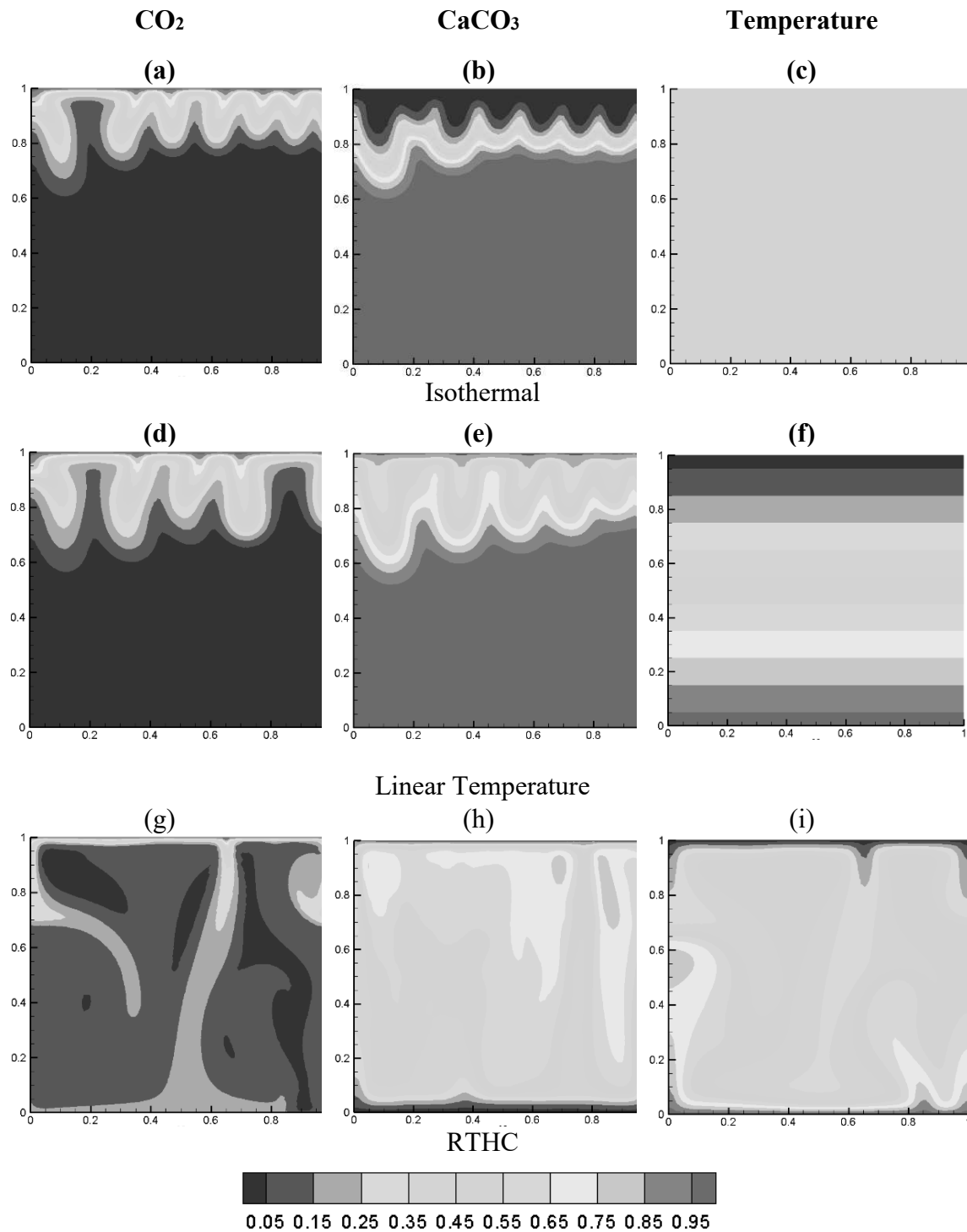


**Figure 4.7.** Dimensionless concentration of  $\text{CO}_2$  (left) and  $\text{CaCO}_3$  (middle) and dimensionless temperature (right) for 'test case 3' with the three models at  $\tau = 0.01$ .

The non-dimensional metric giving the total amount of  $\text{CaCO}_3$  available in the domain is given by:

$$T_{\text{CaCO}_3} = \int_0^1 \int_0^1 \text{CaCO}_3 dXdZ \quad (4.26)$$

Three metrics are used to investigate the  $\text{CO}_2$  flux at the top surface:

- The instantaneous total flux of  $\text{CO}_2$  at the top surface:

$$TF_{\text{CO}_2} = \int_0^1 \left( U_z \text{CO}_2 - \frac{\partial \text{CO}_2}{\partial Z} \right) dX \quad (4.27)$$

- The cumulative total flux of  $\text{CO}_2$  at the dimensionless time  $\tau$  :

$$TF_{\text{CO}_2}^{\text{Cum}} = \int_0^{\tau} TF_{\text{CO}_2} d\tau \quad (4.28)$$

These metrics are investigated for a non-dimensional duration ( $\tau_{\text{max}}$ ) of 0.01, which is equivalent to 30000s. Figure 4.8a plots the variation of the total amount of  $\text{CaCO}_3$  available in the domain with time, with the three models. Due to the dissolution processes, the three models show that the total amount of  $\text{CaCO}_3$  is decreasing with time. “Linear temperature” leads to larger  $T_{\text{CaCO}_3}$  than “Isothermal”, during all the simulated periods. This is coherent with the results of the previous section showing fast dissolution of  $\text{CaCO}_3$  with “Isothermal”. During the first period of simulation ( $\tau < 0.0025$ ), both models “Linear temperature” and “RTHC” give similar results. This is related to the fact that, at this stage, the convection flow is still not affecting the temperature distribution. Thus, this distribution is linear, and in consequence “Linear Temperature” and “RTHC” are equivalent. For  $\tau > 0.0025$ , with “RTHC” the initial linear temperature distribution is disturbed by the convective flow. Due to convection processes, high temperatures can be found in the domain, which can be associated to higher reaction rates. In consequence, fast dissolution processes occur. This explains the faster decrease of  $T_{\text{CaCO}_3}$  with “RTHC” than “Linear Temperature”.

Figure 4.8b illustrates the time variation of the instantaneous total flux of  $\text{CO}_2$  at the domain top surface ( $TF_{\text{CO}_2}$ ). Similar behaviors can be observed with the three models, with a period of decreasing variation at the beginning of the simulation, followed by a period of increasing variation until becoming almost constant. This figure shows equivalent results between models “Isothermal” and “Linear temperature”. During a short time at the beginning of the simulation, the convective

processes are absent. The CO<sub>2</sub> flux is induced by the mass diffusion between the zones of high concentration at the top surface and low concentration within the domain. When CO<sub>2</sub> infiltrates into the domain by diffusion, the concentration gradient at the top surface decreases, and in consequence, the CO<sub>2</sub> flux decreases. After this short period of purely diffusion transport, convective flow starts due to solute buoyancy effects in “Isothermal” and “Linear temperature” models and both thermal and solute buoyancy effects in “RTHC”. Convective processes enhance the CO<sub>2</sub> flux at the domain top surface. This explains this regime of increased CO<sub>2</sub> flux after the first period of decreased variation. Once the convective flow is well-established, the CO<sub>2</sub> flux becomes stable, as it can be seen in Figure 4.8b. From this figure, it is clear that “RTHC” leads to higher CO<sub>2</sub> flux than “Isothermal” and “Linear temperature”. These latter two models under-predict the CO<sub>2</sub> flux because they do not take into account the thermal convective processes. The time variations of cumulative CO<sub>2</sub> flux obtained with the three models are given in Figure 4.8c. Equivalent results can be observed with “Isothermal” and “Linear temperature” models. These models, by considering simplified assumptions of the temperature field, under-predict the total CO<sub>2</sub> flux. The discrepancy between the results of “RTHC” and other models is increasing with time.

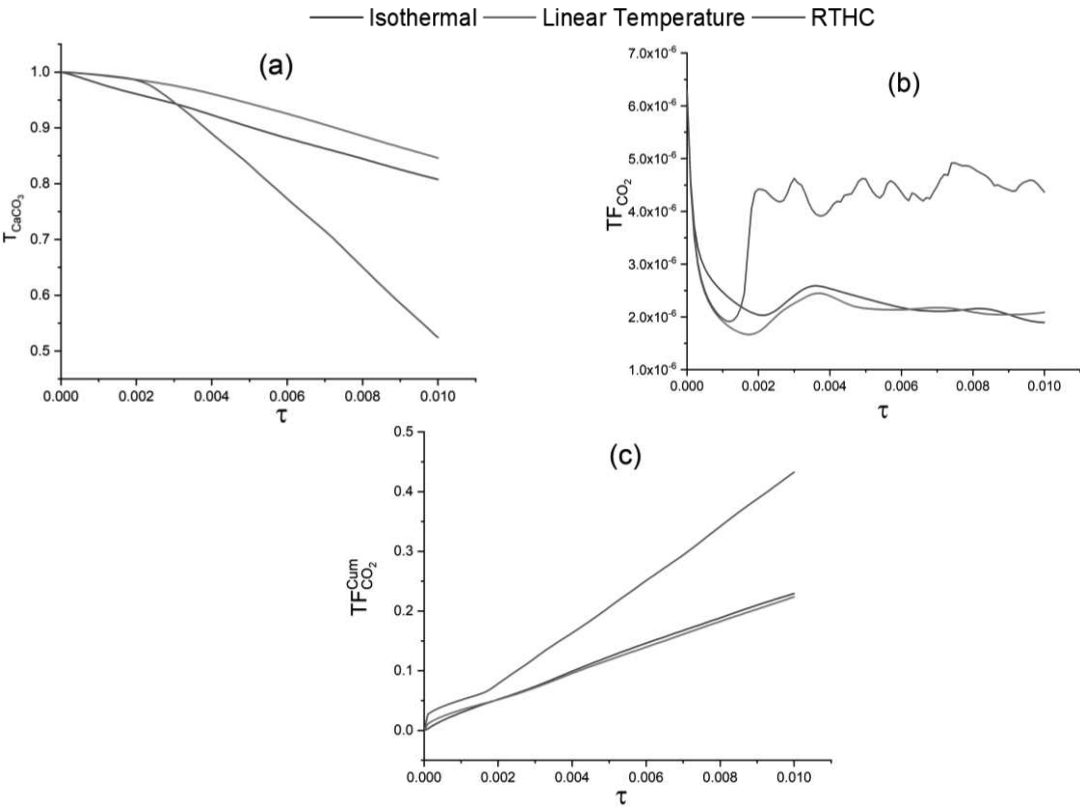


**Figure 4.8.** Time variations of the metrics characterizing CaCO<sub>3</sub> and CO<sub>2</sub> with the three models “Isothermal”, “Linear temperature” and “RTHC”: (a) the total amount of CaCO<sub>3</sub> available in the domain ( $T_{CaCO_3}$ ), (b) the instantaneous total flux of CO<sub>2</sub> at the top surface ( $TF_{CO_2}$ ) and (c) The cumulative total flux of CO<sub>2</sub> ( $TF_{CO_2}^{Cum}$ ).

#### 4.4.2. Field study: The Viking field in the North Sea

Previous studies on the effect of temperature on the processes of convective-reactive CO<sub>2</sub> dissolution are limited to hypothetical problems (A. Islam et al., 2014; A. W. Islam et al., 2014; Islam et al., 2013c). To the best of our knowledge, this topic has never been investigated for a real field application. The effect of heat on convective flow and geochemical reaction of CO<sub>2</sub> at large scale and under real geologic configuration is still not well understood. To address this gap, we investigate RTHC processes of CO<sub>2</sub> in a natural gas reservoir at the Viking field in the North Sea in England, which is under consideration for CO<sub>2</sub> storage (Hoteit et al., 2019; Omar et al., 2021).

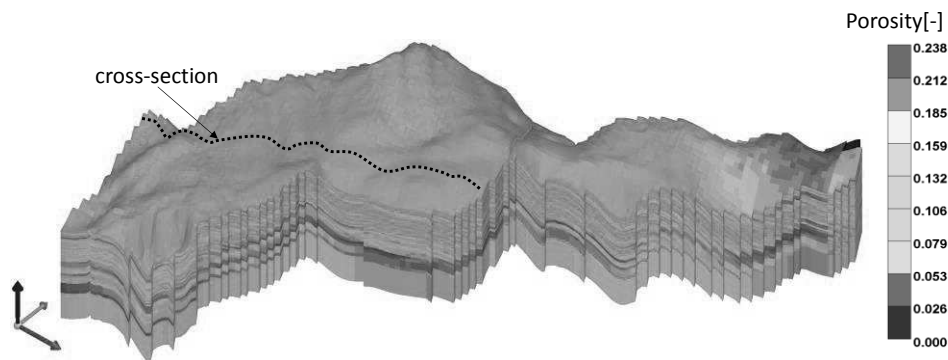


**Figure 4.9.** Geological structure of the Viking field, showing the porosity distribution and the location of a vertical cross-section.

The Viking field is an offshore field located within the coast of Lincolnshire in the North Sea, at a depth of approximately 2780m subsea. The reservoir consists of a heterogeneous sandstone formation with an average porosity of about 15% and permeability ranging from  $10^{-12}$  to  $10^{-14}$  m<sup>2</sup> (see Figure 4.9). The reservoir includes several normal faults with hanging wall blocks.

A vertical cross-section of the reservoir is considered in this study, as shown in Figure 4.10a. The location of this cross-section, which intercepts a normal fault, is also shown in Figure 4.9. Impermeable flow condition is used for all the boundaries. We consider supercritical CO<sub>2</sub>, which has been injected outside our modeling area, to be trapped under the cap rock within a layer of about 100m thickness (Figure 4.10a). In this layer, the concentration of CO<sub>2</sub> is considered to be constant ( $6$  [mol/m<sup>3</sup>]). The initial concentration of CO<sub>2</sub> in the bottom layer is assumed to be zero ( $(C_{CO_2})_0 = 0$ ). No mass transport boundary condition is imposed at the interface between the top and bottom layers. Instead, the full advection-diffusion-reaction equation is applied in the bottom layer, while in the top layer; zero-time derivative of the CO<sub>2</sub> concentration is applied. Zero CO<sub>2</sub> flux is imposed at the vertical boundaries and at the bottom surface. The carbonic acid resulting from the dissolution of CO<sub>2</sub> in the host water reacts with Calcium carbonate minerals of the site.

Dissolution reaction processes are modeled with the second-order kinetic model, as in equations (4.12) and (4.13). The corresponding parameters are given in Table 4.3 (Sainz-Garcia et al., 2017; Sanjuan and Girard, 1996; Sjöberg and Rickard, 1984). No chemical reaction is considered in the top layer. The initial concentration of  $\text{CaCO}_3$  in the bottom layer is assumed to be  $6 \text{ [mol/m}^3\text{]}$ . The reservoir is simulated for a duration of 100 years.

The reservoir is simulated with the three models described in the previous section (“Isothermal”, “Linear temperature” and ‘RTHC”). For “Isothermal” the temperature is assumed to be constant ( $365^\circ\text{[K]}$ ). For “Linear temperature” the temperature is invariable in time. It increases linearly with depth. The geothermal gradient is  $30^\circ \text{ [K/km]}$ . The lowest temperature at the higher point of the vertical cross-section is  $357.15^\circ \text{ [K]}$ . This linear temperature distribution is used as an initial condition in the RTHC model. In this model, the temperature of the injected  $\text{CO}_2$  is assumed to be  $303.15^\circ \text{ [K]}$ . This temperature is applied to the top boundary while the constant geothermal temperature is imposed at the bottom surface. The vertical boundaries are assumed to be adiabatic.

The porosity and permeability maps of the domain are shown in Figures 4.10b and 4.10c, respectively (Omar et al., 2021). Temperature-dependent viscosity is considered as in equation (4.8). All physical properties of rocks and fluid are summarized in Table 4.3.

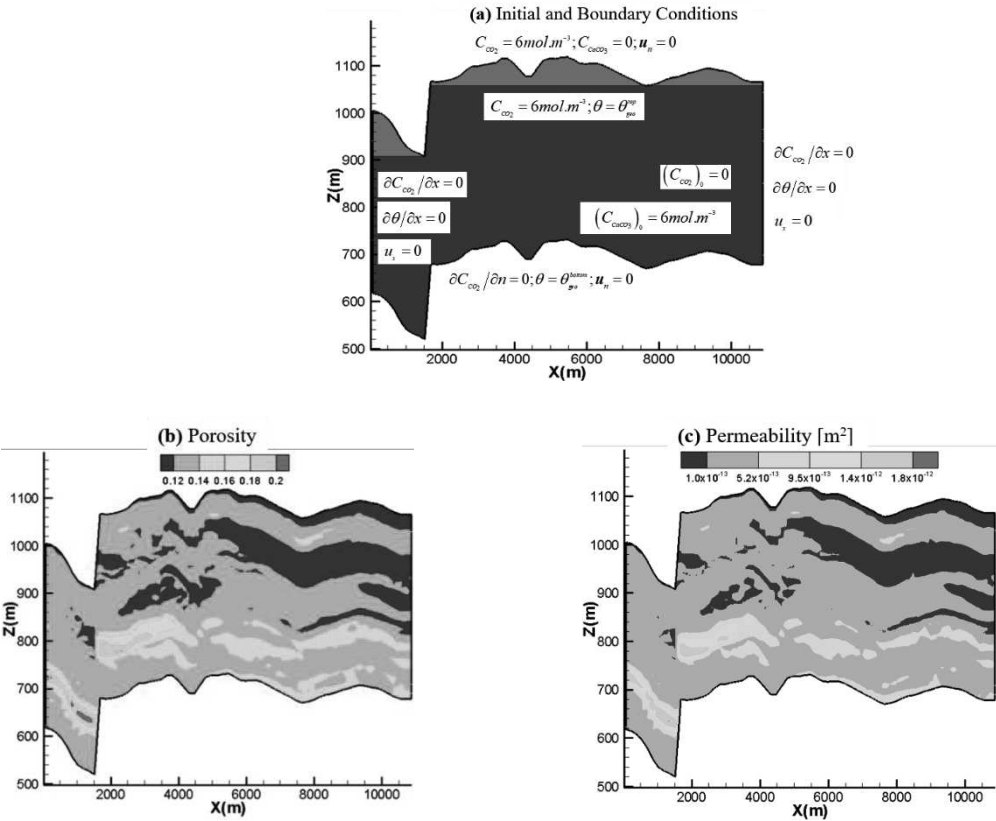


**Figure 4.10.** Description of the site: (a) initial and boundary conditions (b) Porosity map, (c) permeability map

**Table 4.3.** Physical parameters used for the simulations of the real case

<i>Parameter</i>	<i>Value</i>
Gas constant	$R = 8.314 \text{ J.mol}^{-1}.\text{K}^{-1}$
Reference Temperature	$T_{\text{Ref}} = 277.15^\circ \text{ K}$
Freshwater density	$\rho_0 = 1000 \text{ kg.m}^{-3}$
Density of rock	$\rho_R = 2600 \text{ kg.m}^{-3}$
Thermal capacity of water	$CP_f = 4200 \text{ J.kg}^{-1}.\text{K}^{-1}$
Thermal capacity of rock	$CP_R = 880 \text{ J.kg}^{-1}.\text{K}^{-1}$
Thermal Conductivity of water	$\lambda_f = 0.65 \text{ W.m}^{-1}.\text{K}^{-1}$
Thermal Conductivity of rock	$\lambda_R = 3.63 \text{ W.m}^{-1}.\text{K}^{-1}$
Thermal expansion coefficient of water	$\beta_T = 0.001 \text{ K}^{-1}$
Mass Expansion	$\beta_C = 0.00833 \text{ m}^3.\text{mol}^{-1}$
Diffusion coefficient of dissolved $\text{CO}_2$	$D_{\text{CO}_2} = 5.32 \times 10^{-9} \text{ m}^2.\text{s}^{-1}$
Longitudinal dispersivity	$\alpha_L = 5 \text{ m}$
Transversal dispersivity	$\alpha_T = 0.5 \text{ m}$
Activation energy	$E_a = 20 \text{ kJ.mol}^{-1}$
Pre-exponential factor	$A = 10^{-8} \text{ m}^3.\text{mol}^{-1}.\text{s}^{-1}$

The results of the three models are plotted in Figure 4.11. This figure depicts the spatial distribution for  $\text{CO}_2$  and  $\text{CaCO}_3$  concentrations and temperature at the end of the simulation (after 100 years). Figure 4.11 shows that, in contrast to the previous hypothetical benchmark, almost equivalent results are obtained with “Isothermal” and “Linear temperature” models. Figures 4.11a and 4.11d show that, with “Isothermal” and “Linear” models, there are almost no fingers in the right part of the domain. Some fingers can be seen in the left part, where high permeability is observed. “RTHC” leads to different results. A fingering phenomenon can be observed everywhere in the domain with the “RTHC” model (Figure 4.11g). Deeper and more developed fingers can be observed in the left part of the domain, where permeability is relatively high. In general, everywhere in the domain, the fingering phenomenon is more intensive with the “RTHC” than other models. This result gives first evidence that temperature can intensity the fingering phenomenon. This is important for GCS because the fingering phenomenon can affect the processes of  $\text{CO}_2$  dissolution. However, these results should be considered with caution, and further simulations should be developed to better understand this behavior. Indeed, in the simulation with the “RTHC” model, the temperature at the top surface is lower than that used in the “Linear temperature” model. This latter is equivalent to the geothermal temperature. Thus, the temperature gradient between the top and bottom surfaces is higher in “RTHC” than in “Linear temperature”. This means that the difference between the fingering intensities observed with “RTHC” and “Linear temperature” could not be related to the

heat transfer processes that are neglected in “Linear temperature”, but rather to the different temperature gradients used in these models. To verify this point, we developed a further simulation with the “RTHC” model, in which we assume that the temperature of CO<sub>2</sub> trapped at the top surface of the reservoir is equivalent to the geothermal temperature in this zone. The results (not shown for the sake of brevity) of this simulation show intensive fingers, which confirms clearly that the intensified fingers with the “RTHC” model are related to the effect of temperature created but the geothermal temperature gradient.

As in the previous example, the total amount of CaCO<sub>3</sub> per unit of width ( $\Sigma C_{CaCO_3} [mol / m]$ ), available in the domain, is also investigated. It is given by:

$$\Sigma C_{CaCO_3} = \iint C_{CO_2} d\Omega \quad (4.29)$$

The cumulative total flux of CO<sub>2</sub> at the top surface is also investigated. It is given by:

$$TFC_{CO_2}^{Cum} = \int_0^t TFC_{CO_2} dt \quad (4.30)$$

where  $t$  is the time and  $TFC_{CO_2}$  is the instantaneous total flux at the top surface.  $TFC_{CO_2}$  is given by:

$$TFC_{CO_2} = \oint_{\text{top surface}} \left( u_z C_{CO_2} - \frac{\partial C_{CO_2}}{\partial z} \right) dl \quad (4.31)$$

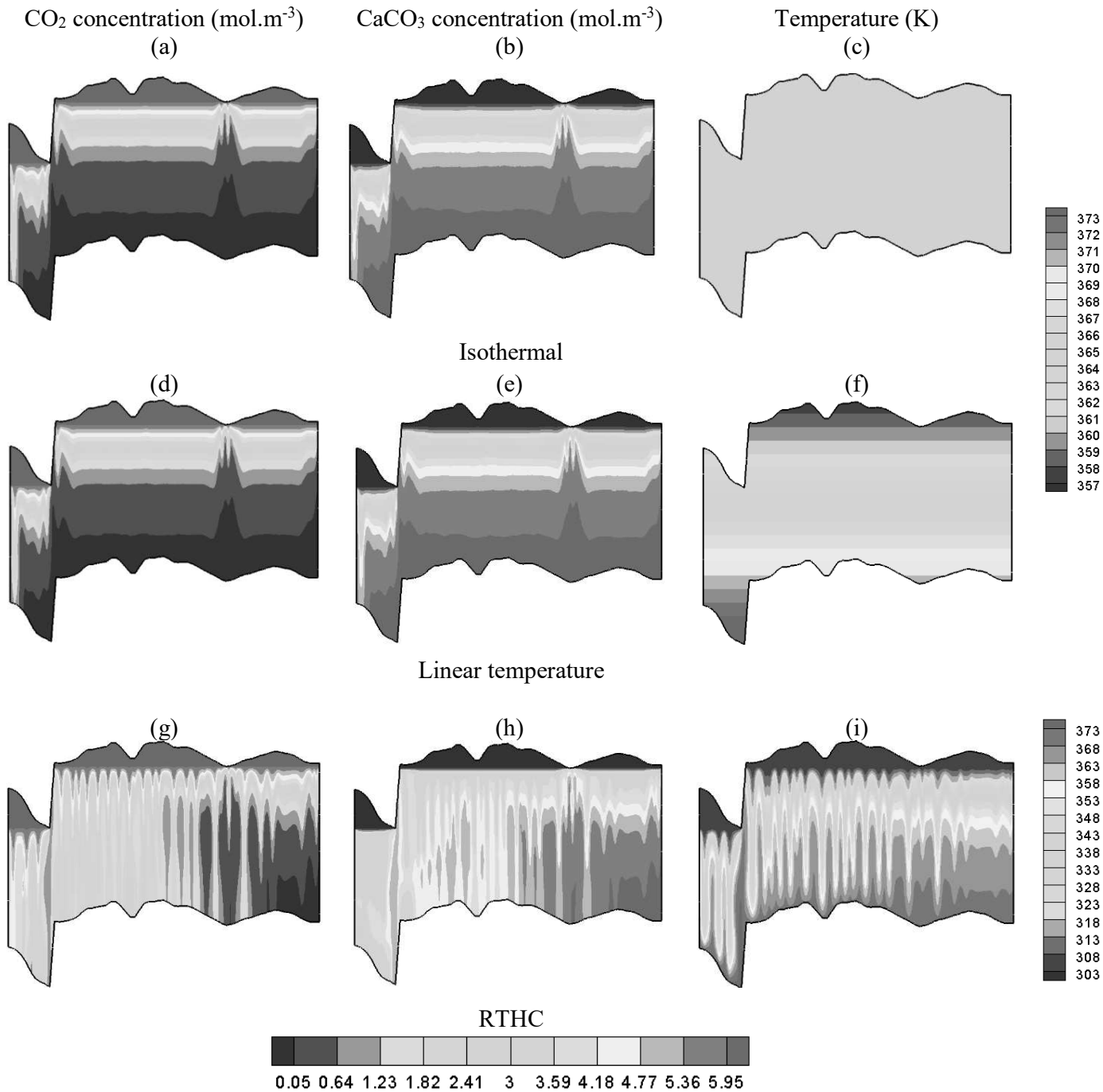


**Figure 4.11.** Results of the three models “Isothermal”, “Linear temperature” and “RTHC”: Spatial distributions of CO<sub>2</sub> (left), CaCO<sub>3</sub> (middle), and temperature (right) after 100 years.

The results of the three models regarding the total amount of CaCO<sub>3</sub> and cumulative CO<sub>2</sub> flux are given in Figure 4.12. Equivalent results are obtained with “Isothermal” and “Linear temperature” models, as for the spatial distributions of CO<sub>2</sub>, CaCO<sub>3</sub>, and temperature in Figure 4.11. Figures 4.11 and 12 confirm that, when the heat transfer processes are not considered, the effect of temperature variability on the processes of convective-reactive CO<sub>2</sub> dissolution is limited. Figure 4.12 shows different results with the “RTHC” model and indicates that heat transfer processes have a significant

impact on the dissolution of CO<sub>2</sub> and in consequence, on the total CO<sub>2</sub> flux and the total amount of CaCO<sub>3</sub>. For the first 20 years, the cumulative total flux of CO<sub>2</sub> is over-predicted with the models “Isothermal” and “Linear temperature” (Figure 4.12a). This is related to the low temperature of CO<sub>2</sub> trapped below the caprock that can slow down the dissolution processes at the top surface of the reservoir. This is clear in Figure 4.12b, which shows more dissolution with “Isothermal” and “Linear temperature” models than “RTHC” model. After this first period of 20 years, the heat transfer processes occur due to convection. They increase the temperature in the reservoir and enhance the dissolution processes. The total amount of available CaCO<sub>3</sub> becomes over-predicted with the “Isothermal” and “Linear temperature” models. More dissolution leads to more infiltration of trapped CO<sub>2</sub> to the reservoir as it can be observed in Figure 4.12a. This figure shows that the “Isothermal” and “Linear temperature” models under-predict the cumulative CO<sub>2</sub> flux after 20 years of simulation.

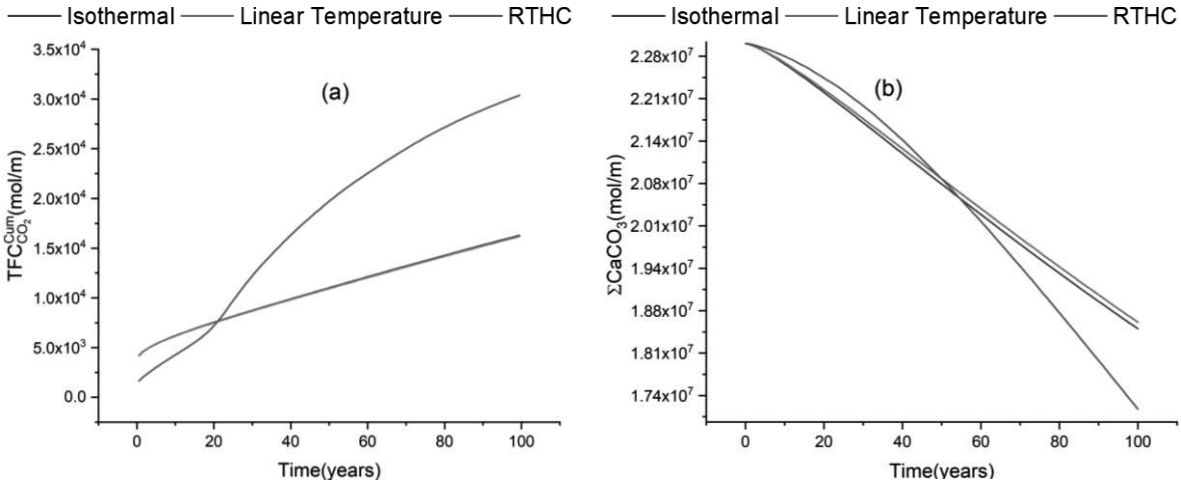


**Figure 4.12.** Comparison between models “Isothermal”, “Linear temperature” and “RTHC”: (a) cumulative CO<sub>2</sub> flux and (b) total amount of CaCO<sub>3</sub> available in the domain.

The results in the previous analysis are based on deterministic values of parameters. However, several parameters could be uncertain. Thus, it is important to investigate the sensitivity of the results to uncertain parameters. A full sensitivity analysis can be performed in this context. However, as the main goal of this study is to investigate the effect of temperature of dissolution processes on CO<sub>2</sub>, we limited the sensitivity analysis to the parameters governing the rate of the dissolution, namely the activation energy ( $Ea$ ) and the pre-exponential factor ( $A$ ) in the Arrhenius law. We developed 9 further simulations with the “RTHC” model by considering all combinations of low, moderate and high values of  $Ea$  and  $A$ . For  $Ea$  the low, moderate and high values are

considered to be 20, 40 and 60 ( $\text{kJ.mol}^{-1}$ ) while these values for  $A$  are assumed to be  $10^{-6}$ ,  $10^{-7}$  and  $10^{-8}$  ( $\text{m}^3.\text{mol}^{-1}.\text{s}^{-1}$ ).

Figure 4.13 shows the  $\text{CO}_2$  concentration maps resulting from 9 simulations with the RTHC model. It can be observed that increasing the pre-exponential factor intensifies the fingering processes and leads to more  $\text{CO}_2$  dissolution. This is also observed when the value of the activation energy is increased from 20 to 40  $\text{kJ.mol}^{-1}$ . However, almost equivalent results are observed when  $E_a$  is increased from 40 to 60  $\text{kJ.mol}^{-1}$ . Sensitivity of the  $\text{CO}_2$  concentration to  $E_a$  is less pronounced at a high pre-exponential factor.

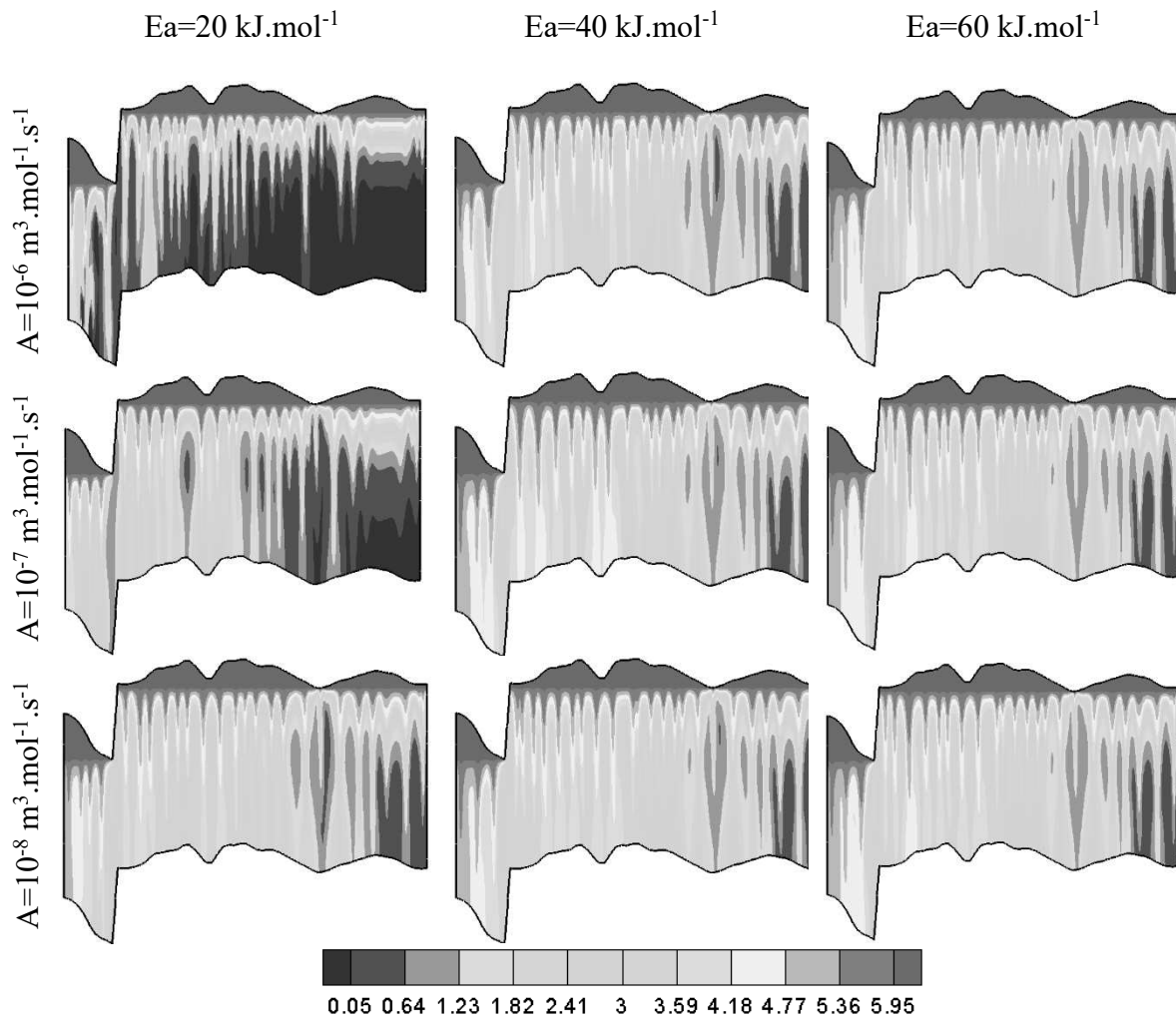


**Figure 4.13.** Results of reaction parameters sensitivity analysis with “RTHC” model: Spatial distributions of  $\text{CO}_2$

The results of reaction parameters sensitivity analysis regarding the cumulative  $\text{CO}_2$  flux ( $\text{TFC}_{\text{CO}_2}^{\text{Cum}}$ ) are given in Figure 4.14. Figures 4.14a and 4.14c show that the cumulative  $\text{CO}_2$  flux is more sensitive to the activation energy at lower pre-exponential factor. Whatever the value of  $A$ , there

is no monotonic variation of  $TFC_{CO_2}^{Cum}$  with respect to  $Ea$ .  $TFC_{CO_2}^{Cum}$  is augmenting when  $Ea$  is increased from 20 to 40  $kJ.mol^{-1}$ , and then it is dropping when  $Ea$  is increased from 40 to 60  $kJ.mol^{-1}$ . At high value of the pre-exponential factor, equivalent results are obtained for the high and low values of  $Ea$ . However, at low values of the pre-exponential factor, the results become different at after 70 years of simulation. Figures 4.14b and 4.14d show that the cumulative CO<sub>2</sub> flux is more sensitive to  $A$  at high activation energy. No monotonic sensitivity to  $A$  can be observed.  $TFC_{CO_2}^{Cum}$  is augmenting when  $A$  increases from  $10^{-6}$  to  $10^{-7}$   $m^3.mol^{-1}.s^{-1}$  and is weakening when  $A$  increases from  $10^{-7}$  to  $10^{-8}$ . Results obtained with  $A$  equal to  $10^{-6}$  and  $10^{-7}$   $m^3.mol^{-1}.s^{-1}$  are almost equivalent with the lowest value of activation energy. For the highest value of activation energy, these results become different, and the discrepancy between them increases with time.

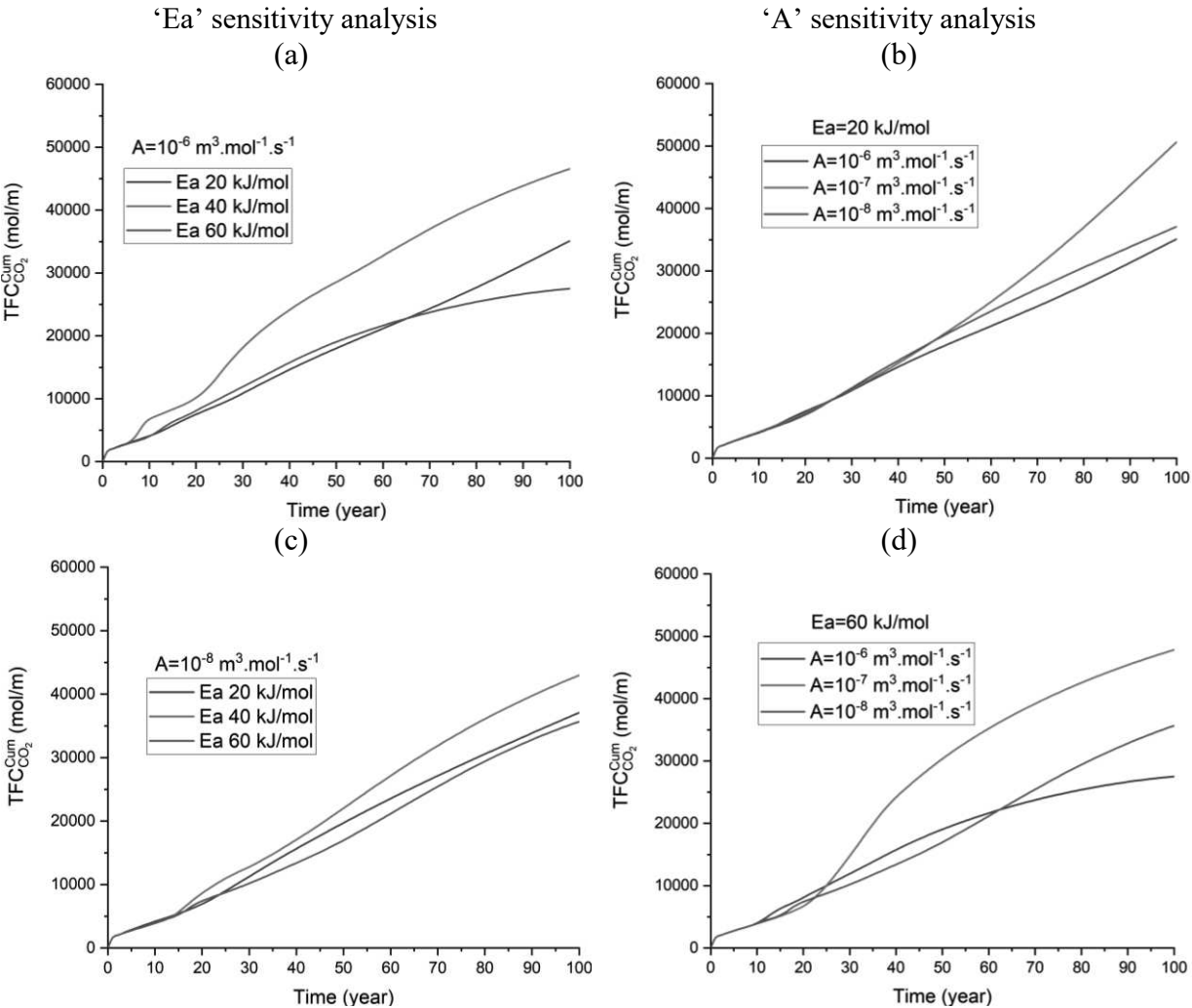


**Figure 4.14.** Comparison between the results of cumulative CO<sub>2</sub> flux with low, moderate and high values of activation energy and pre-exponential factor in the Arrhenius law: (a) and (c): Activation energy sensitivity analysis, (b) and (d): pre-exponential factor sensitivity analysis.

## 4.5. Conclusion

Most of previous modeling-based studies on the convective-reactive transport of CO<sub>2</sub> in geological formations are limited to isothermal conditions and deal with small spatial scale problems. The main goal of this work is to investigate the effect of temperature on convective-reactive transport of CO<sub>2</sub> at large field scale. Thus, an advanced numerical model (TRACES) is developed for the simulation of RTHC process in the application of GCS. Appropriate numerical techniques are implemented in TRACES for the discretization of the spatial derivatives (MHFE and DGFE methods) and time integration (error control time stepping). The new model is verified against a standard finite element solution obtained with COMSOL Multiphysics. Good agreement has been obtained for low Rayleigh numbers. The advantages of TRACES are compared with the standard Finite Element solutions, based on the common benchmark of porous box. Results demonstrated that TRACES solutions are less mesh-dependent than the standard Finite element method, especially at high Rayleigh numbers. The DGFE allows for reducing spurious oscillations and for controlling numerical diffusion that can have significant impact on the model accuracy and performance. We provided quantitative data that can be used as reference solutions for benchmarking RTHC models in further studies.

The effects of temperature on the convective-reactive transport of CO<sub>2</sub> are investigated by using three different models with increasing level of complexity: Isothermal, Linear Temperature and RTHC. In “Isothermal” model the temperature is constant while in “Linear Temperature” model the temperature increases linearly with depth. The results of the porous box benchmark indicate that fingering phenomenon is under-predicted when the RTHC processes are neglected. The effect of temperature on CO<sub>2</sub> transport is also investigated for a field case in the Viking reservoir in the North Sea. The results confirm that, at large scale and under realistic conditions of heterogeneity, neglecting the RTHC processes leads to an underestimation of the fingering phenomenon. The results show also that the intensified fingering phenomenon improves the dissolution processes and increase the total flux of CO<sub>2</sub> to the domain.

The parameters controlling the effect of temperature on the reaction rate, namely the activation energy and the pre-exponential factor in the Arrhenius law, are uncertain. A sensitivity analysis is performed to investigate how the uncertainties related to these parameters can affect the results. This analysis shows that the increase of the pre-exponential factor intensifies the fingering processes and leads to more CO<sub>2</sub> dissolution. Sensitivity of the CO<sub>2</sub> concentration to the activation energy is less pronounced at a high pre-exponential factor. The cumulative CO<sub>2</sub> flux is highly sensitive to the activation energy at lower pre-exponential factor. There is no monotonic variation of the total flux

with respect to the activation energy. The cumulative CO<sub>2</sub> flux is highly sensitive to the pre-exponential at high activation energy.

## **Chapter V: Modelling dissolution processes in discrete fracture networks: an advanced numerical scheme**

### **5.1. Introduction**

Water flow in carbonate rocks is usually associated with the dissolution process and the transport of dissolved species (Liu et al., 2020). Naturally existing networks of fractures as well as dissolution-induced fractures can significantly affect the domain transmissivity that, in turn, affect flow, transport and dissolution processes. When the porosity and permeability of the rocks are low, such as in carbonate rocks (Mukhametdinova et al., 2020), the fractures act as preferential fluid pathways. Therefore, the fluid flow in the rock matrix can be neglected and the domain can be represented as a discrete fracture network (DFN) (Medici et al., 2016). Dissolution processes in DFNs is relevant in several environmental and engineering applications. In karstic systems, dissolution is the key process in karstification (Lopes et al., 2022; Aliouache et al., 2019). Dissolution processes in DFNs are also observed in heat extraction in geothermal reservoirs (Kim et al., 2015), recovery in oil reservoirs (Medekenova and Jones, 2014), radioactive and nuclear waste disposal (Natarajan and Suresh Kumar, 2010) and carbon sequestration (Tran and Jha, 2021).

Despite the wide range of applications, dissolution processes in DFNs are still poorly understood (Lopes et al., 2022; Aliouache et al., 2019). Most of the existing related studies investigate dissolution processes in unfractured domains and study how these processes create preferential flow pathways (Hanna and Rajaram, 1998; Dijk et al., 2002; Detwiler et al., 2003; Detwiler and Rajaram, 2007; Deng and Spycher, 2019). In this context, experimental investigations have shown variety of behaviors because of differences in experimental conditions, which presents challenges for interpreting the effects of controlling parameters (Detwiler and Rajaram, 2007). Modeling has been also used to understand fractures initiation and propagation in unfractured domains due to dissolution processes (Detwiler and Rajaram, 2007; Ameli et al., 2014; Deng and Spycher, 2019). However, modeling-based studies on dissolution processes in well-developed discrete fracture networks are not common (Deng and Spycher, 2019) and the effect of the reaction rate on the dissolution of connected fractures is still poorly understood. Modeling dissolution processes in DFNs reveals specific challenges that are not present in unfractured media (Viswanathan et al., 2022). This challenge arises from the dynamic evolution of the fractured domain due to the geochemical dissolution (Tenthorey and Fitzgerald, 2006). The enlargement of fractures as a result of dissolution process continuously affects the fluid flow field. Flow, in turn, is affecting the dissolution process and the transport of dissolved species. Therefore, the processes are coupled and nonlinear. Furthermore, in DFNs, the whole flow is assigned to the fractures and the storage is

ignored in the matrix, thus, the transport of dissolved species is an advection-dominant process. In such cases, standard numerical methods, such as standard finite element (FE) or finite volume (FV) methods can generate numerical diffusion that may underestimate the dissolution processes. Standard numerical methods can also introduce non-physical oscillations that lead to convergence issues and limit the applicability of the models.

It is known that Discontinuous Galerkin finite element (DG) method is well-adapted to capture the sharp moving fronts in the case of an advection-dominant transport (Younes and Ackerer, 2008). The employment of DG scheme for discretization of the hyperbolic term of the transport equation has been largely reported in the literature. For instance, (Younes et al., 2014) developed an efficient model combining advanced numerical methods including DG in a buoyancy-driven flow problem in a homogeneous domain. In a fractured domain, (Zidane and Firoozabadi, 2014) developed an efficient numerical model for multicomponent compressible flow in a 2D domain and (Moortgat et al., 2016) employed this scheme in modeling multicomponent flow in unstructured 3D fractured domain. However, to the best of our knowledge, DG method has been never applied to dissolution processes in DFNs. Yet, there is a significant potential of such an application, as DG method can, on the one hand, reduce numerical diffusion and better predict the dissolution processes, and on the other hand, improve the stability of the solution and enhance convergence of nonlinear solvers.

In order to fill the aforementioned gaps in the literature, the objective of this paper is to develop an advanced numerical model for the simulation of dissolution processes in DFNs and to investigate the effects of geochemical dissolution on fracture evolution, flow and transport processes, taking advantages of the newly developed model. The numerical model is developed based on an upwind DG scheme for transport. This scheme has been developed for unfractured domains in Younes et al., 2009. In a DFN, within the fractures, the transport equation is similar to unfractured domains. Thus, the DG scheme developed by Younes et al., 2009 can be directly applied inside the fractures. The main challenge for this scheme is the application for intersecting fractures. In fact, the main idea of the DG scheme suggested by Younes et al., 2009 is to use the average value of the concentration over a computational cell as well as the components of the concentration gradient as primary variables. The Riemann solver is then used to evaluate the concentration at the nodes. A new formulation is developed in this work for the nodes where several fractures are intersecting. The upwind approximation in the intersections of fractures is obtained based on an averaging method with the weight of the upwind velocities. The chemical processes are coupled with the advection-dispersion processes and solved simultaneously in order to avoid operator-splitting errors. The flow is simulated with the Richards' equations. This allows for handling both saturated and unsaturated flows. The flow equation is discretized with the Mixed Finite Element (MFE)

method. The mass lumping technique developed by Koohbor et al., 2020 is employed for the discretization of the flow to avoid over and undershoots observed in transient simulations with small time steps.

For the temporal discretization, a higher-order method is used through the method of lines (MOL). MOL has been proven to be very efficient in solving highly nonlinear systems of equations, such as flow in unsaturated porous media with Richard's equation (Fahs et al., 2009; Farthing et al., 2003; Miller et al., 2006) and density driven flow. With MOL, the spatial derivatives are discretized while the time derivatives are kept in their continuous form. This allows for converting the partial derivative equations to a system of Ordinary differential equations. This system is solved using the adaptive, high order implicit solver DASPK (Brown et al., 1994). The advantages of DASPK solver in efficiently and accurately solving systems with large number of unknowns are discussed in Younes et al., 2011.

The newly developed DG scheme is compared to a standard FE solution obtained using COMSOL Multiphysics and a FV solution obtained using an in-house code. The new DG scheme is then used to understand the effects of the reaction rate on dissolutions, flow and transport characteristics based on different physical processes controlling the dissolution rate. The effect of dissolution processes on flow and transport processes is investigated using different dissolution models depending on the regimes of the reaction rate and flow (Agrawal et al., 2021; 2020)

## 5.2. The Mathematical model

The flow in fractures is simulated with the Richards's equation. However, in this work the application are limited to saturated domains. With this assumption, the flow model is based on the continuity and the Darcy's law. The permeability in the fractures is estimated using the well-known Poiseuille equation (Hanna and Rajaram, 1998). The system of equations for the flow becomes as follows:

$$S_s \frac{\partial H}{\partial t} + \nabla \cdot \mathbf{q} = 0 \quad (5.1)$$

$$\mathbf{q} = -\frac{b^2 g}{12\nu} \nabla H \quad (5.2)$$

where,  $S_s [L^{-1}]$  is the specific mass storativity of the fractures,  $H [L]$  is the freshwater head,  $t [T]$  is the time and  $\mathbf{q} [L.T^{-1}]$  is the fluid velocity field which is obtained through equation (5.2), where

$b[L]$  is the fracture aperture,  $g[L.T^{-2}]$  is the gravity acceleration and  $\nu[L^2.T^{-1}]$  is the kinematic viscosity of the fluid.

The mass transport accompanied with the dissolution process is also based on the depth-averaged mass conservation as advection-dispersion-reaction equation (Detwiler and Rajaram, 2007):

$$\frac{\partial(bC)}{\partial t} + \nabla \cdot (b\mathbf{q}C) - \nabla \cdot (b\mathbf{D}\nabla C) = R(C) \quad (5.3)$$

where,  $C[M.L^{-3}]$  is the depth-averaged concentration of the dissolved species,  $R(C)[M.L^{-2}.T^{-1}]$  is the dissolution term and  $\mathbf{D}[L^2.T^{-1}]$  is the velocity-dependent dispersion tensor. In one dimensional transport,  $D$  is given by equation (5.4):

$$D = \alpha_L \times |\mathbf{q}| + D_m \quad (5.4)$$

where,  $\alpha_L[L]$  is the longitudinal dispersivity of the fractures,  $D_m[L^2.T^{-1}]$  is the diffusion coefficient of the dissolved species. The evolution of fractures aperture is obtained via equation (5.5):

$$\rho_r \times \delta \times \frac{\partial b}{\partial t} - R(C) = 0 \quad (5.5)$$

where,  $\rho_r[M.L^{-3}]$  is the density of the rock and  $\delta[-]$  is a stoichiometric coefficient that represents the mass of mineral entering solution for a unit mass of dissolved rock.

In order to obtain the dissolution flux  $R(C)$ , two models are proposed depending on the velocity of the flow. In a relatively fast fluid flow the reaction rate is constant (Reaction control) and the reaction term is obtained via equation (5.6).

$$R(C) = K_C (C - C_s) \quad (5.6)$$

where,  $K_C[L.T^{-1}]$  is the constant reaction rate and  $C_s[M.L^{-3}]$  is the concentration of dissolving species at saturation. With the slower fluid flow movements, the reaction rate is controlled by transport (Yu, 2019) and the reaction flux is obtained as follows (Detwiler and Rajaram, 2007):

$$R(C) = \frac{Sh \times D_m}{2b} (C - C_s) \quad (5.7)$$

where,  $Sh$  is the non-dimensional Sherwood number. In the literature, a range of constant values for the Sherwood number is considered when the mass transfer between parallel plates is taking place with an equilibrium between the dissolved concentrations and the reacting surfaces (Hanna and Rajaram, 1998; Detwiler and Rajaram, 2007).

### 5.3. The Numerical model

To solve the set of equations for flow and reactive transport, we use numerical methods which allow obtaining accurate and consistent results. The spatial discretization is based on the combination of the MFE method for the flow equations, the upwind DG method for advection part of the transport equation and the FV method for dispersion and reaction terms. In the following, we summarize the main steps of the spatial discretization that allows for obtaining the system of ordinary differential equations. This system is solved with the DASPK time integration solver. The notations used for the spatial discretization of the flow and transport are shown in Figure 5.1. In this figure NC (resp. NH) represents the concentration (resp. freshwater head) on a node. TC (resp. TH) represents the value of the concentration (resp. head) at an element.  $q$  is the water flux at a node.

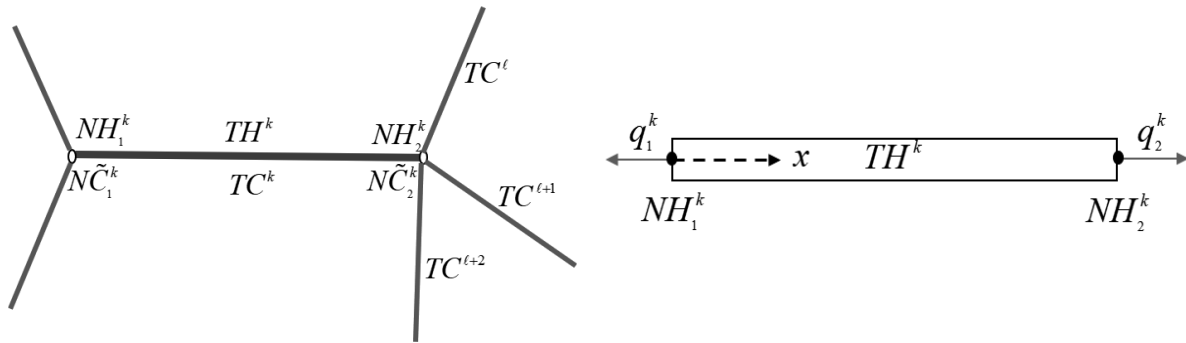


**Figure 5.1.** Flow and transport notations in a fracture  $k$

#### 5.3.1. Spatial discretization of the flow

One-dimensional flow is considered inside the fractures. The linear test functions of the MFE are used for the discretization of the velocity field. Thus, for a fracture  $k$  with the length of  $\ell^k$  and the width of  $b^k$  the velocity is approximated as follows:

$$q^k = \sum_{j=1}^2 q_j^k w_j^k \quad (5.8)$$

where,  $q^k$  is the velocity inside fracture k,  $w_1^k = \frac{x - \ell^k}{b^k \ell^k}$  and  $w_2^k = \frac{x}{b^k \ell^k}$  are the linear interpolation functions and  $q_j^k$  is the flux leaving node j of the fracture k. This consideration leads to the following equation for spatial discretization of mass continuity equation:

$$b^k \ell^k S_S^k \frac{dTH^k}{dt} + q_1^k + q_2^k = 0 \quad (5.9)$$

With  $TH^k [L]$  as the freshwater head in the fracture and  $S_S^k [L^{-1}]$  as the specific mass storativity related to head changes. Finite Element (FE) discretization on equation (5.2) writes:

$$q^k = \sum_{j=1}^2 q_j^k \int_0^{\ell^k} \theta_i^k w_j^k = -\frac{(b^k)^2 g}{12\nu} \times \int_0^{\ell^k} (\nabla H) \theta_i^k \quad (5.10)$$

where,  $\theta_i^k; i=1,2$  is the FE weighting function. Integration by part leads to:

$$\sum_{j=1}^2 q_j^k \int_0^{\ell^k} \theta_i^k w_j^k = \frac{(b^k)^2 g}{12\nu} \left( \int_0^{\ell^k} H (\nabla \theta_i^k) - [H \theta_i^k]_{x=0}^{x=\ell^k} \right) \quad (5.11)$$

Using the trapezoidal rule (the mass lumping technique) in the left term integral yields to:

$$q_i^k = \frac{(b^k)^2 g}{12\nu} \times \frac{2b^k}{\ell^k} (TH^k - NH_i^k) \quad (5.12)$$

Equation (5.12) is substituted into equation (5.9) to obtain  $q_1^k$  and  $q_2^k$  and it forms the final system as follows:

$$-b^k \ell^k S_S^k \frac{dTH_i^k}{dt} + \frac{(b^k)^3 g}{6\ell^k \nu} \times (NH_1^k + NH_2^k - 2TH_i^k) = 0 \quad (5.13)$$

To close the system (5.13), mass conservation is written at each intersection of fractures. At the node i surrounded by n fractures, we have:

$$\sum_n q_i^n = 0 \quad (5.14)$$

Which yields:

$$\sum_n \frac{(b^n)^3}{6\ell^n \nu} \times (TH^n - NH_i^n) = 0 \quad (5.15)$$

The final system is formed by writing equation (5.13) for all the fractures and equation (5.15) for all the nodes not imposed to the Dirichelet boundary condition.

### 5.3.2. Spatial discretization of the transport

The advection term is discretized with the DG scheme. With this scheme the test functions are discontinuous. It is well suited for solutions with sharp interface. Inside each fracture k, we assume:

$$C^k(x, t)|_k = \phi_1^k(x) \times TC^k + \phi_2^k(x) \times C_x^k \quad (5.16)$$

$C^k$  is the concentration at the fracture k which is calculated based on two degrees of freedom:  $TC^k$  and  $C_x^k$ .  $TC^k$  is the average value of concentration on the cell and  $C_x^k$  is the concentration deviation along the fracture direction with the corresponding interpolation functions:

$$\phi_1^k(x) = 1, \quad \phi_2^k(x) = x - \bar{x}_k \quad (5.17)$$

$\bar{x}_k$  is the center of the fracture. Thus, the transport equation (equation (5.3)) will be discretized as follows:

$$\int_k \frac{\partial(bC)}{\partial t} \phi_i + \int_k \nabla \cdot (bCq\phi_i) - \int_k bC\phi_i(\nabla \cdot q) - \int_k bCq\nabla \phi_i + \int_k \nabla \cdot (bD\nabla \cdot C)\phi_i = \int_k R(C)\phi_i \quad (5.18)$$

The first integral writes:

$$\int_k \frac{\partial(bC)}{\partial t} \phi_i = b^k \underbrace{\begin{bmatrix} \ell^k & 0 \\ 0 & \frac{(\ell^k)^3}{12} \end{bmatrix}}_{M_1} \begin{bmatrix} \frac{\partial TC^k}{\partial t} \\ \frac{\partial C_x^k}{\partial t} \end{bmatrix} \quad (5.19)$$

The second integral writes:

$$\int_k \nabla \cdot (bqC\phi_i) = b^k \left( q_1^k C_1^{k,*} \phi_i|_{x=0} + q_2^k C_2^{k,*} \phi_i|_{x=\ell^k} \right) \quad (5.20)$$

With  $C^*$  as the upwind concentration and it is obtained as follows:

$$\begin{aligned}
C_1^{k,*} \Big|_{x=0} &= \lambda_1^k NC_{1,in}^k + (1 - \lambda_1^k) NC_{1,out}^k \Big|_{x=0} \\
C_2^{k,*} \Big|_{x=\ell_k} &= \lambda_2^k NC_{2,in}^k + (1 - \lambda_2^k) NC_{2,out}^k \Big|_{x=\ell_k}
\end{aligned} \tag{5.21}$$

where,  $NC_{j,in}^k$  and  $NC_{j,out}^k$  are the interior and outer concentrations at the node  $j$  of the fracture  $k$ , respectively.  $\lambda_j^k$  is the coefficient which determines if the node  $j$  of the fracture  $k$  is calculated as an upwind node ( $\lambda_j^k = 1$ ) or a downwind node ( $\lambda_j^k = 0$ ).

$$(\lambda_j^k)_{j=1,2} = \begin{cases} 1 & \text{if } q_j^k \geq 0 \\ 0 & \text{if } q_j^k < 0 \end{cases} \tag{5.22}$$

For obtaining  $NC_{j,in}^k$  we can write:

$$NC_{j,in}^k = TC^k + \tau_j^k C_x^k \tag{5.23}$$

With  $\tau_1^k = -\frac{\ell^k}{2}$  and  $\tau_2^k = \frac{\ell^k}{2}$ , the corresponding interpolation functions in equation (5.17) are

satisfied for the first node  $\left(x - \bar{x}_k = -\frac{\ell^k}{2}\right)$  and the second node  $\left(x - \bar{x}_k = \frac{\ell^k}{2}\right)$  of the a fracture  $k$ .

$NC_{j,out}^k$  is calculated using the interior concentration ( $NC_{j,in}^n$ ) of  $n_{max}$  fractures sharing the node  $j$  with the fracture  $k$ , having the upwind flux checked by  $\lambda_j^n$  as in equation (5.22).  $NC_{j,out}^k$  is written as follows:

$$NC_{j,out}^k = \frac{1}{\sum_{n=1}^{n_{max}} \lambda_j^n q_j^n} \sum_{n=1}^{n_{max}} \lambda_j^n q_j^n NC_{j,in}^n \tag{5.24}$$

With the aforementioned considerations, the second integral is formulated as follows:

$$\begin{aligned}
\int_k \nabla \cdot (b \mathbf{q} C \phi_i) &= b^k \times \underbrace{\begin{bmatrix} \lambda_1^k q_1^k + \lambda_2^k q_2^k & \tau_1^k \lambda_1^k q_1^k + \tau_2^k \lambda_2^k q_2^k \\ \tau_1^k \lambda_1^k q_1^k + \tau_2^k \lambda_2^k q_2^k & (\tau_1^k)^2 \lambda_1^k q_1^k + (\tau_2^k)^2 \lambda_2^k q_2^k \end{bmatrix}}_{M_{2,1}} \begin{bmatrix} TC^k \\ C_x^k \end{bmatrix} \\
&+ b^k \times \underbrace{(1 - \lambda_1^k) q_1^k}_{V_1} \begin{bmatrix} 1 \\ \tau_1^k \end{bmatrix} NC_{1,out}^k + b^k \times \underbrace{(1 - \lambda_2^k) q_2^k}_{V_2} \begin{bmatrix} 1 \\ \tau_2^k \end{bmatrix} NC_{2,out}^k
\end{aligned} \tag{5.25}$$

The third integral writes:

$$-\int_k b C \phi_i (\nabla \cdot \mathbf{q}) = -\frac{q_1^k + q_2^k}{\ell^k} \int_k C \phi_i = -\underbrace{(q_1^k + q_2^k)}_{M_3} \begin{bmatrix} 1 & 0 \\ 0 & \frac{(\ell^k)^2}{12} \end{bmatrix} \begin{bmatrix} TC^k \\ C_x^k \end{bmatrix} \tag{5.26}$$

The fourth integral becomes:

$$-\int_k b C \mathbf{q} \nabla \phi_i = -\underbrace{\begin{bmatrix} 0 & 0 \\ \frac{\ell^k}{2} (q_2^k - q_1^k) & \frac{(\ell^k)^2}{12} (q_1^k + q_2^k) \end{bmatrix}}_{M_4} \begin{bmatrix} TC^k \\ C_x^k \end{bmatrix} \tag{5.27}$$

The integral related to the dispersive flux writes:

$$\int_k \nabla \cdot (b \mathbf{D} \nabla \cdot C) \phi_i = \int_k (\nabla \cdot \tilde{\mathbf{q}}) \phi_i = \frac{\tilde{q}_1^k + \tilde{q}_2^k}{\ell^k} \int_k \phi_i = \begin{bmatrix} \tilde{q}_1^k + \tilde{q}_2^k \\ 0 \end{bmatrix} \tag{5.28}$$

where,  $\tilde{\mathbf{q}}$  is the dispersive flux. For discretization of the dispersive flux, the second interpolation function ( $\phi_2(x)$ ) is set to be zero. The dispersive flux inside fracture k is obtain as follows:

$$\tilde{q}_j^k = b^k D_k \frac{TC^k - \tilde{N}C_j}{\ell^k/2} \tag{5.29}$$

where  $\tilde{N}C_j$  is the concentration at the node j which is obtained by satisfying the continuity condition of dispersive fluxes arriving from all the fractures (including k) sharing node j. For instance, if node j shares overall n fractures,  $\tilde{N}C_j$  is obtained as follows:

$$\sum_n 2b^n D_n \frac{TC^n - N\tilde{C}_j}{\ell^n} = 0 \quad (5.30)$$

Which yield:

$$N\tilde{C}_j = \frac{\sum_n \frac{b^n}{\ell^n} D_n TC^n}{\sum_n \frac{b^n}{\ell^n} D_n} \quad (5.31)$$

$N\tilde{C}_j$  is then substituted into equation (5.29):

$$\tilde{q}_j = 2 \frac{b^k}{\ell^k} D_k \left( TC^k - \frac{\sum_n \frac{b^n}{\ell^n} D_n TC^n}{\sum_n \frac{b^n}{\ell^n} D_n} \right) \quad (5.32)$$

The dispersion coefficient in a 1D fracture k is approximated by:

$$D_k = \alpha_L^k |\bar{q}_k| + D_m \quad (5.33)$$

where,  $\alpha_L^k$  is the longitudinal dispersivity through the fracture k and  $\bar{q}_k = \frac{(q_2^k - q_1^k)}{2e_k}$  is the mean velocity in the fracture.

Finally, the last integral which is related to the reactive flux writes:

$$\int_k R(C) \phi_i = \begin{bmatrix} R(C) \times \ell^k \\ 0 \end{bmatrix} \quad (5.34)$$

For the discretization of the reactive fluxes also the terms in associate with  $\phi_2(x)$  are not considered. Therefore, the calculation of the integral related to the reactive term is reduced to equation (5.34). The final system related to the transport equation becomes:

$$-[M_1] \begin{bmatrix} \frac{\partial TC^k}{\partial t} \\ \frac{\partial C_x^k}{\partial t} \end{bmatrix} - [M_{234}] \begin{bmatrix} TC^k \\ C_x^k \end{bmatrix} - [V_1] NC_{1,out}^k - [V_2] NC_{2,out}^k + \begin{bmatrix} -\tilde{q}_1 - \tilde{q}_2 \\ 0 \end{bmatrix} = \begin{bmatrix} R(C) \times \ell^k \\ 0 \end{bmatrix} \quad (5.35)$$

$$M_{234} = M_{2l} + M_3 + M_4$$

The final system to solve for the transport given by equation (5.35) has the mean and gradient of concentration at fractures as unknowns.

Flow and transport systems are coupled with equation (5.5) which describes the fracture aperture evolution. This equation is also discretized via a FV approach which is not presented here for the sake of brevity.

For the temporal discretization, a high-order method based on MOL is employed to improve the accuracy and efficiency. For employment of MOL, we first provide the spatial discretization of the system and then we integrate the semi-discrete problem as an ODE in time. The employment of MOL on the implicit solver DASPK is explained in details in the previous works (Younes et al., 2011; 2022).

#### **5.4. Numerical experiments**

A new code has been developed to simulate dissolution processes in DFNs. This section aims at verifying the correctness of the new developed code and evaluating its performance for the simulation of advective dominant solute transport in the fractures. To do so, we compare the results of the newly developed code (denoted by DG) with the results of COMSOL Multiphysics which is based on the standard FE method. Furthermore, the advantage of employment of DG scheme is demonstrated in the comparison with FV scheme in a challenging example with sharp advective fronts. Three following examples are developed for fulfilling the aforementioned goals.

##### ***5.4.1. Verification: Tracer transport in a DFN with constant aperture (example 1)***

For the verification of numerical codes analytical solutions are of great interest. For coupled flow, transport and dissolution process some analytical and reference solutions were developed under simplified conditions (Hayek et al., 2012; Suk, 2016). However, these solutions cannot deal with fractured domain. Verification in fractured domain cannot be performed against analytical solution. Therefore, to verify our newly developed code under these conditions, we have used another numerical model developed in COMSOL Multiphysics software based on standard Finite element scheme. There is no specific interface for the simulation of flow and transport in DFNs in COMSOL. Thus, to simulate flow and transport in DFNs in COMSOL we have developed a model based of the interfaces ‘Darcy’s Law –dl’ for flow and ‘Transport of Diluted Species in Porous media –tds’ for transport. The modules “Fracture flow” and “Fracture”, are respectively used with the interfaces ‘Darcy’s Law –dl’ and ‘Transport of Diluted Species in Porous media –tds to simulate flow and transport in fractures. These modules are based on the hybrid approach that assumes fractures as 1D lines in the 2D matrix domain. Intrinsically, this approach does not neglect flow and transport in matrix and consider the water and mass exchange between both continuums, which is not the case in DFN. To neglect flow and transport in matrix and to neglect the interaction of fracture and matrix in COMSOL model, negligible values are considered for permeability, porosity of the matrix. Also, negligible value is used for the diffusion coefficient in the matrix. Example 1 is

defined for the verification purpose. Therefore, high values are used for the dispersion and diffusion coefficient to avoid unphysical oscillations. In COMSOL, there is no available interface that considers the dissolution process merely in the fractures. Also changing the fracture aperture due to dissolution processes does not exist in COMSOL. Thus, in Example 1, as the first step of verification we ignored the dissolution process. For the generation of the stochastic network, we used Discrete Fracture Network Add-In which is available in the recent versions of COMSOL. This Add-In creates randomized distribution of position, size, orientation and aperture for the fracture network. We used power law stochastic rule to create the network (Barton and Zoback, 1992; Hooker et al., 2009). The network of fractures under investigation for Example 1 is shown in Figure 5.2a. The network is located on a horizontal plane and a constant head gradient is imposed to the plane from left to right. The domain initially contains freshwater. The left boundary of the domain is subjected to the saltwater and an outflow boundary condition is considered for the right side of the domain. No flow and no flux boundary conditions are considered for the top and bottom boundaries. The parameters for Example 1 are shown in Table 5.1. The comparison between the results are also made on two observation points ( $O_1$  and  $O_2$ ) and one monitoring fracture ( $F_1$ ) which are highlighted in Figure 5.2b.

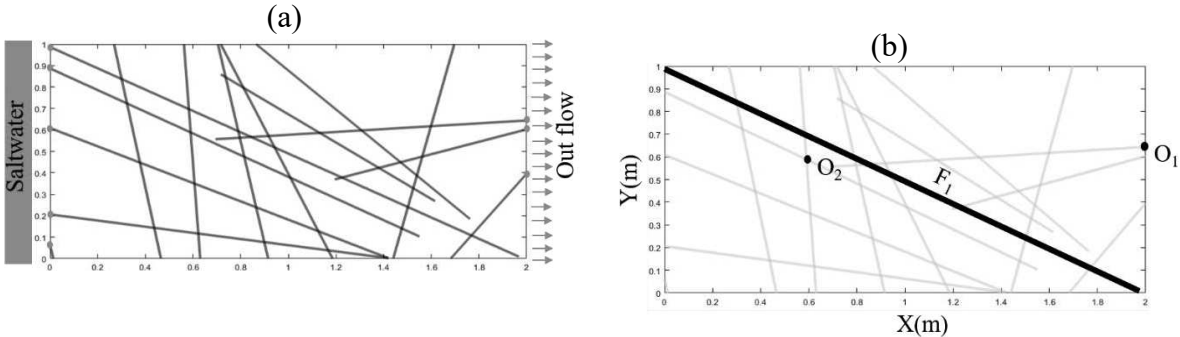


**Figure 5.2.** Problem description: (a) network of fractures and boundary conditions, (b) Highlighted observation points ( $O_1$ ,  $O_2$ ) and fracture ( $F_1$ )

**Table 5.1**, Input Parameters for Example 1, Example 2 and Example 3

Freshwater density	$\rho_0 = 1000 \text{ kg.m}^{-3}$		
Porosity	1.0		
Viscosity	$\mu = 0.001 \text{ Pa.s}$		
	Example 1	Example 2	Example 3
Diffusion	$D_m = 10^{-6} \text{ m}^2.\text{s}^{-1}$	$D_m = 10^{-7} \text{ m}^2.\text{s}^{-1}$	$D_m = 10^{-9} \text{ m}^2.\text{s}^{-1}$
Dispersivity	$\alpha = 0.2 \text{ m}$	$\alpha = 0$	$\alpha = 0$
Initial Thickness	$e = e_0 = 1\text{cm}$	$e_0 = 1\text{mm}$	$e = e_0 = 1\text{cm}$
Permeability	$k = 10^{-11} \text{ m}^2$	$k = \frac{e^2}{12}$	$k = 10^{-9} \text{ m}^2$
Head at the upstream	$H_1 = 1\text{m}$	$H_1 = 0.01\text{m}$	$H_1 = 1\text{m}$
Head at the downstream	$H_0 = 0$	$H_0 = 0$	$H_0 = 0$
Reaction rate	(-)	$K_C = 10^{-5} \text{ m.s}^{-1}$	(-)
Initial concentration	$C^0 = 0$	$C^0 = 0.1768 \text{ mol.m}^{-3}$	$C^0 = 0$
Concentration at the Inlet ports	$C^{Inj} = 1\text{mol.m}^{-3}$	$C^{Inj} = 0$	$C^{Inj} = 1\text{mol.m}^{-3}$

The results of the DG scheme are compared with the COMSOL results in Figure 5.3. The COMSOL model is denoted by FE. The distribution of dimensionless concentration in the fracture network after 14 hours with DG and FE are shown in Figure 5.3a and 5.3b, respectively. Identical concentration distribution is observed between DG and FE solutions. For a more profound comparison, we plotted the variation of concentration with time with both schemes at two observation points  $O_1$  and  $O_2$  in Figures 5.3c and 5.3d, respectively. The concentration with DG and FE solutions after 14 hours are also plotted along  $F_1$  in Figure 5.3e. Excellent agreement is observed between the results of DG and FE solutions in Figures 5.3c-5.3e. These figures allow for verifying the correctness of both the newly developed code based on the DG and the COMSOL model based on the FE method.

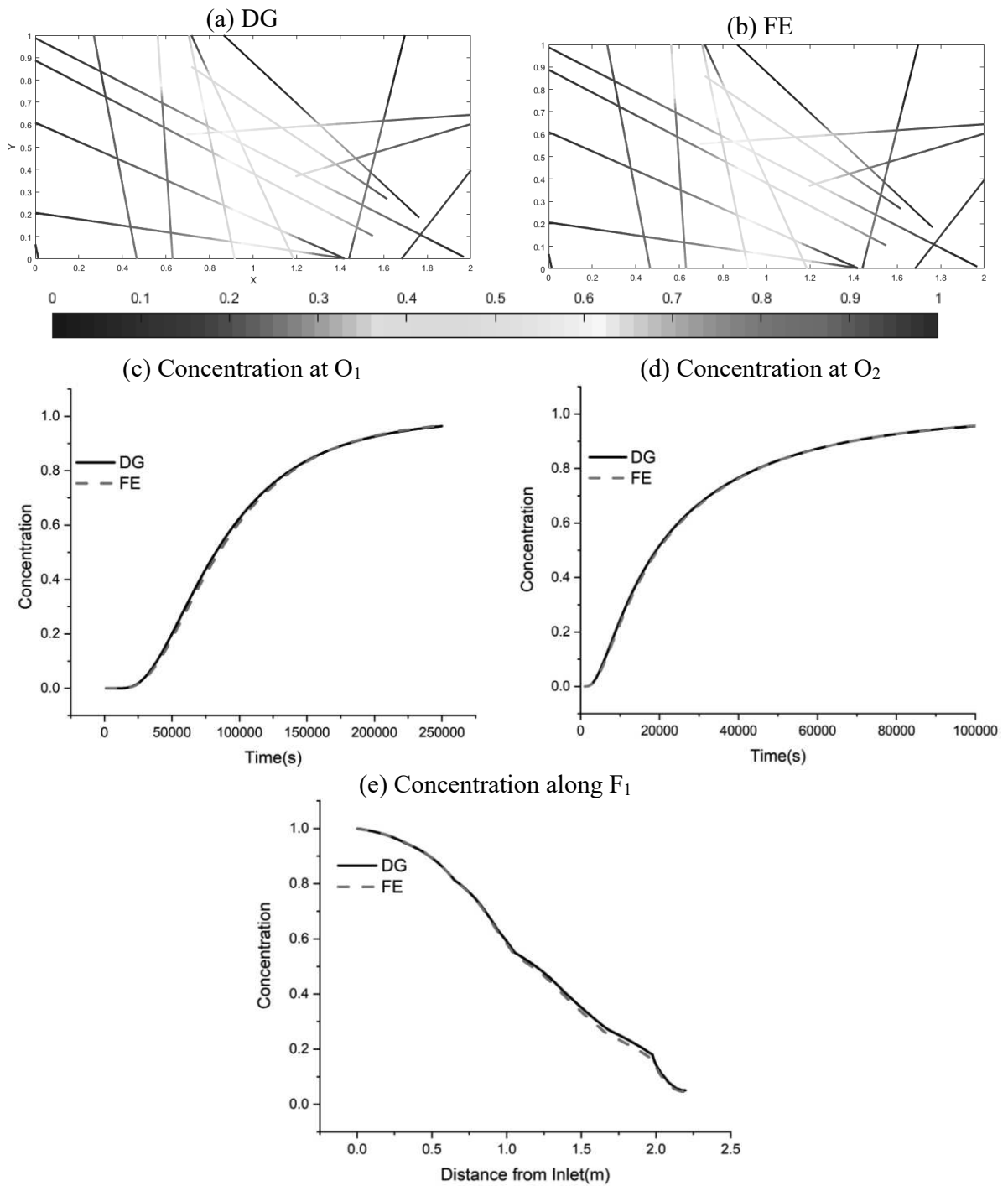


**Figure 5.3.** ‘Example 1’: Dimensionless concentration contours with (a): DG, (b): FE and comparison between DG and FE for dimensionless concentration (c): at  $O_1$ , (d): at  $O_2$  and (e): along fracture  $F_1$

**5.4.2. Verification: Coupled flow, transport and dissolution in variable aperture fracture (example 2)**

Example 1 allows for verifying the correctness of the DG scheme in the case of non-reactive transport in a constant aperture DFN. However, one of the challenges of the newly developed DG scheme is the accurate simulation of the dissolution processes and the effect of dissolution on fractures. Considering these processes in a DFN is not possible with COMSOL. In this example, we consider the dissolution process associated with the flow and transport in a variable aperture single fracture. In the case of single fracture, coupled flow, transport and dissolution processes can be simulated with COMSOL, as well as the effect of dissolution on the fracture aperture. The COMSOL model has been developed by using 1D geometry and coupling the interfaces ‘Darcy’s Law –dl’ for flow and ‘Transport of Diluted Species in Porous media –tds’ for transport. Reaction term has been included in the transport with the module “Reaction”. Equation (5.5) describing the evaluation of the fracture aperture due to dissolution processes is considered in COMSOL using the interface “Domain ODEs and DAEs” with the module “Distributed ODE”. All the equations are solved simultaneously in COMSOL with the fully coupled approach.

The domain under investigation is shown in Figure 5.4. The fracture receives freshwater upstream and is initially saturated with respect to the dissolving species. Freshwater enters the domain from the left boundary and there is an outflow condition on the right boundary. The input parameters for the Example 2 are shown in Table 5.1. To increase the numerical complexity of the problem, the diffusion coefficient has been reduced, compare to example 1, and the dispersion coefficient has been neglected.

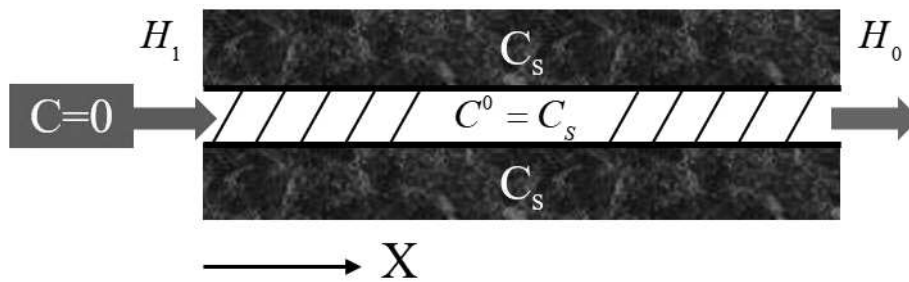


**Figure 5.4.** Conceptual model for dissolution in a single fracture

Beside the FE solution, an FV solution is used to investigate the correctness and performance of the newly developed DG scheme. The FV solution is obtained using an in-house code. This code can be easily obtained as a variant of the code developed with the DG scheme by reducing the spatial order of the test function from piecewise linear to constant approximation.

Thus, three numerical schemes (FE, FV and DG) are employed to calculate the concentration of dissolving species in the domain as well as the evolution of the thickness of fracture due to the dissolution process. The temporal and spatial distribution of concentration and thickness calculated with three schemes are plotted in Figure 5.5.

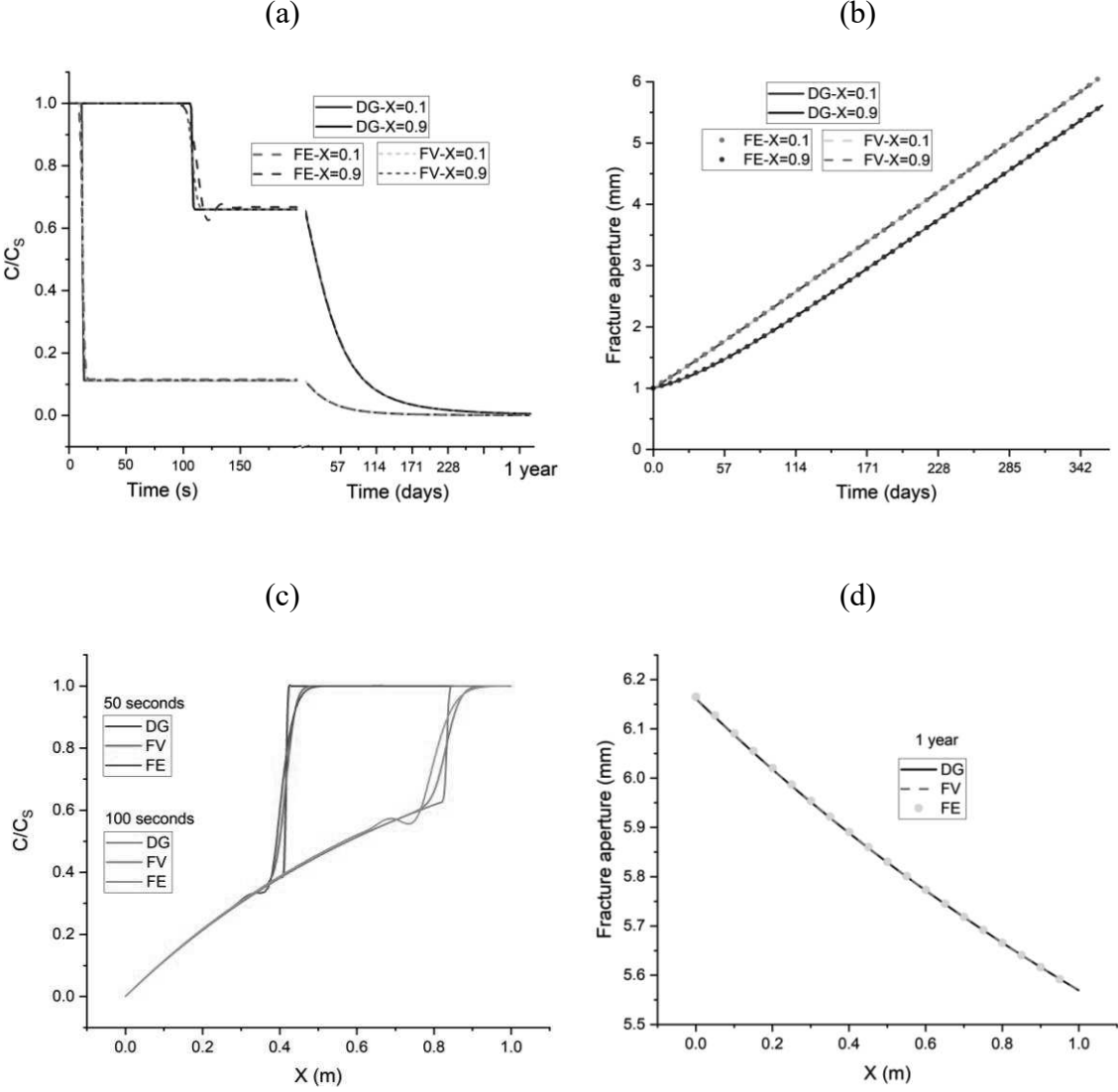


**Figure 5.5.** Example 2: Comparison between the three numerical schemes for dissolution on a single fracture, (a) and (b): time variation of concentration and fracture aperture, (c): concentration along the fracture after 50 and 100 seconds and (d) opening through the fracture and 1 year

Figures 5.5a and 5.5b show the time variation of dimensionless concentration and the thickness at two different points of the domain ( $X=0.1$  and  $0.9$ ). The dimensionless concentration at  $t=50$  seconds and 100 seconds and the thickness after 1 year are also plotted along the fracture in Figures 5.5c and 5.5d, respectively. It is observed that there are small numerical oscillations in FE results

of short-term concentration, especially near the outlet (Figures 5.5a and 5.5c). These oscillations are removed in the long-term results. In short times the dominant process that derive the freshwater towards the outlet is advection and after it reaches the outlet, dissolution and diffusion are the deriving processes for thickness and concentration evolution. That is the reason for observing numerical discrepancy in short-term concentration results. Despite the differences revealed between the short-term concentration of three schemes the long-term results for the thickness and concentration are similar between the three schemes and the three numerical models are physically equivalent.

#### ***5.4.3. Advantages of developed DG model: numerical diffusion (example 3)***

Example 3 aims at investigating the advantages of the DG scheme in the case of flow and transport in a DFN, where the transport processes are advection dominated. Thus, we consider an example similar to example 1 but we assume reduced diffusion coefficient and no dispersion. The input parameters for Example 3 are given in Table 5.1. The comparison between DG and FV scheme for Example 3 is shown in Figure 5.6. A mesh sensitivity analysis has been performed with both DG and FV schemes. The time variation of concentration at two observation points  $O_1$  and  $O_2$  are shown in Figures 5.6a and 5.6b, respectively. It is observed that with the DG scheme a mesh-independent solution is obtained with a relatively coarse mesh (272 nodes). However, the results of FV model with the same mesh show a smooth front because of the numerical diffusion. By refining the mesh in FV model till 1145 nodes, the numerical diffusion with the FV scheme can be reduced and the FV results converge toward the DG results. The convergence of FV results toward DG results by refining the mesh is also observed in concentration along Line  $F_1$  which is plotted at the time  $t=200$  seconds in Figure 5.6c. This figure shows that the development of concentration along the line  $F_1$  is slowed down with 272 nodes in FV due to the dampening effects of numerical diffusion. The discrepancy between DG and FV schemes in Example 3 are coherent with that observed between these schemes FV and DG in short-term concentration in Example 2. With the dominance of advection in Example 3, the discrepancy between DG and FV schemes become more significant since in such cases the presence of numerical diffusion are more affecting the sharp advective fronts. This result confirms the accuracy and efficiency of the DG scheme in an advection dominant problem where the FV scheme fails to obtain accurate results.

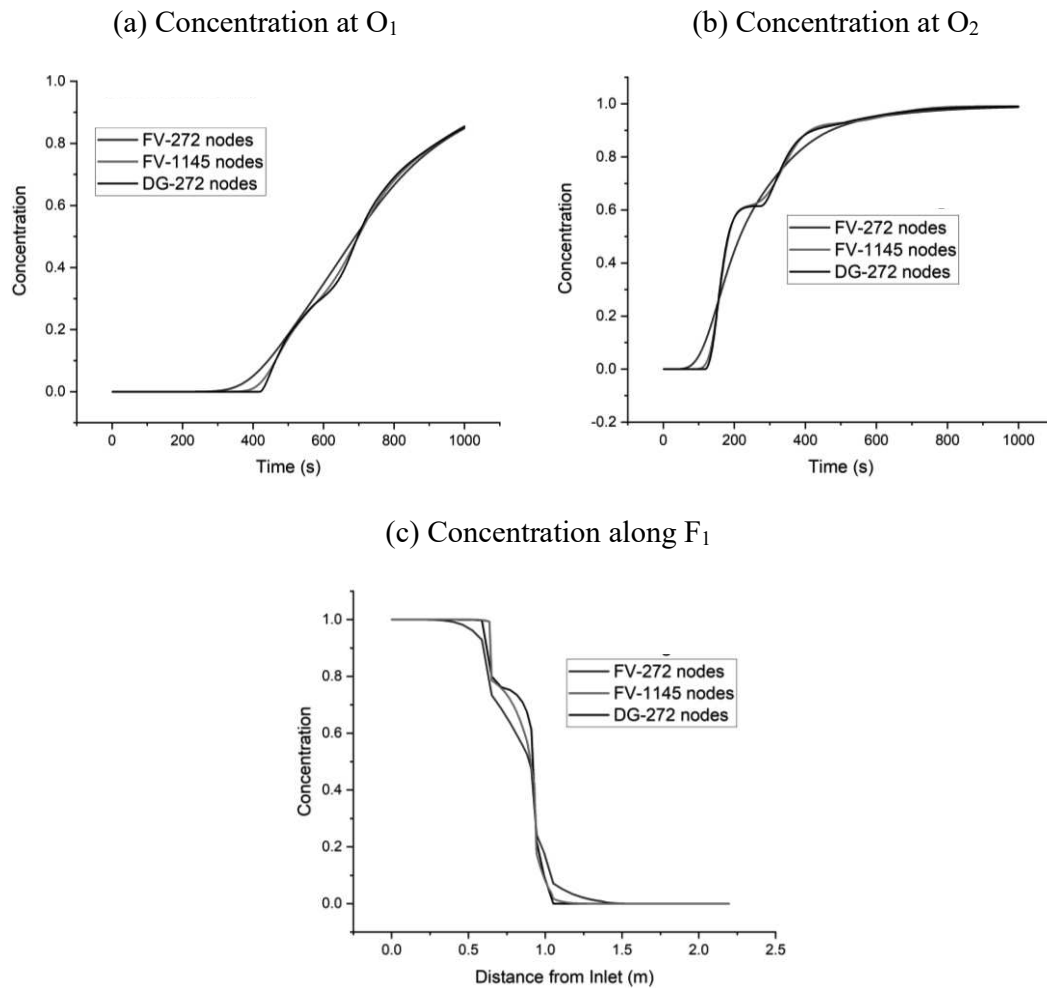


**Figure 5.6.** ‘Example 3’: Comparison between DG and FV schemes for dimensionless concentrations (a) at  $O_1$ , (b) at  $O_2$  and (c) along line  $F_1$  at  $t=200s$

### 5.5. Effects of geochemical dissolutions

This section aims at providing insights into the underlying physical processes of dissolution in a DFN and the related fracture evolution. The controlling factors in the dissolution processes lies into the velocity of the fluid flow and reaction rate. We investigate two configurations dealing with reaction controlled (RC) and transport controlled (TC) processes. In the case of fast fluid flow, the dissolution rate will be dependent upon the mineral surface. This configuration is called reaction controlled dissolution. However, in the case of slow fluid flow, the dependence of the dissolution rate on the velocity increases. This configuration is called TC dissolution. More details about this classification can be found in Ameli et al., (2014) and Yu, (2019). The equations describing the dissolution processes in both configurations are given in equations (5.6) and (5.7).

Dissolution processes for both configurations are investigated, firstly, in a single fracture with a constant head gradient (similar to Example 2) and then, in a DFN incorporating connected horizontal and vertical fractures, as it can be found in karst systems.

### **5.5.1. Dissolution processes in a single fracture**

We consider exactly the same physical problem as in Example 2 (input parameters are provided in Table 5.1). The upstream head,  $H_1 = 0.01\text{m}$  is kept for the case of RC dissolution. This leads to an initial velocity equal to  $0.00833 \text{ m.s}^{-1}$  ( $720 \text{ m.day}^{-1}$ ). Such a fluid velocity in groundwater is categorized as a fast fluid flow (Abdullah et al. 2020). Therefore, the RC model is employed to obtain the dissolution rate in this case. This model assigns a constant reaction rate ( $K_C$ ) to the dissolution rate (see equation (5.6)). We investigate the effect of the constant reaction rate on dissolution processes by assuming two values for  $K_C$   $5 \times 10^{-6} \text{ m.s}^{-1}$  and  $10^{-5} \text{ m.s}^{-1}$ , respectively.

For the TC dissolution, the initial velocity is reduced by assuming the upstream head to be  $0.005\text{m}$ . In the case of TC dissolution, the reaction rate is calculated based on the molecular diffusion coefficient, the fracture aperture and the non-dimensional Sherwood number (Sh). For mass transfer associated with laminar flow between parallel plates, a constant value of Sh is considered. Two values of Sh based on the literature (4.86 and 8.24) (Hanna and Rajaram 1998) are employed in this study.

Figure 5.7, shows the results of the simulation with a simulated time of 1 year with RC and TC models. The initial fracture is plotted in Figure 5.7a. Figures 5.7b and 5.7c show the fracture geometry with small values of  $K_C$  and Sh, respectively. A uniform increase in the fracture aperture is observed with the RC model since in this case, the velocity is high and freshwater is available all through the domain and the dissolution process is taking place in the same way, everywhere in the domain. However, with the TC model, a conic shape is observed for the fracture as a result of localized dissolution near the freshwater inlet. In this case, while an intense opening of the fracture is observed near the inlet, the downstream areas, away from the inlet, experience no increase, and the fracture aperture remains insensitive to the dissolution processes because the transport of freshwater is limited to these areas. The fracture geometry is plotted with higher values of  $K_C$  and Sh in Figures 5.7d and 5.7e. The increase of the fracture aperture has been augmented homogeneously with the RC model since the transport of the freshwater is still not a limiting factor for the increase in the thickness of the fracture. However, with the TC model, the localization of the increase in the fracture aperture is intensified at the domain inlet, as a result of increasing Sh. This is due to the fact that with the increase in the dissolution rate, higher increase in the fracture aperture is observed with the accessibility of freshwater. This intense increase in the fracture aperture leads

to an increase in the cross section of the fracture which reduces the velocity of freshwater and limits the transport of freshwater to the domain further and therefore, smaller regions are experiencing the increase in the fracture aperture with higher  $Sh$ . The water flow velocity after 1 year, along the fracture, calculated with RC and TC models are plotted in Figures 5.7f and 5.7g, respectively. The results show that with RC model, the velocity is uniformly increasing from the inlet to the outlet. This is due to the small reduction of the fracture aperture when going from the inlet to the outlet. The higher  $K_C$  value leads to higher water flow velocity. This is due to the larger fracture aperture, that increases the fracture permeability, which is calculated with the cubic law as a function of fracture aperture. With the TC model, the water flow velocity is reduced in the parts of the fracture experiencing the aperture increase. In these areas, the increase in the fracture aperture is intense and even though the permeability is increased, the increase in the cross section has the dominant effect on the water flow and it reduces the water flow velocity. The concentration after 1 year along the fracture obtained with the RC and TC models are also plotted in Figures 5.7h and 5.7i, respectively. For the case of RC model, small values of concentration are remaining in the domain after 1 year since the significant amount of transport of freshwater had happened during this time in compare with the dissolution process. With the increase in  $K_C$ , the value of concentration has decreased despite the higher value of dissolution rate. This is because of the higher velocity in the case of higher  $K_C$  which leads to more transport of freshwater to the domain and reduces the concentration value. For the TC model, the effect of entrance of freshwater to the domain after 1 year is only observed on the areas close to the entrance of freshwater. This effected area is larger for the case of smaller  $Sh$  since the dissolution rate is lower and allows for more transport to the domain. These plots are coherent with the plots related to the fracture geometry since merely the affected areas with the entrance of freshwater are experiencing the increase in the fracture aperture.

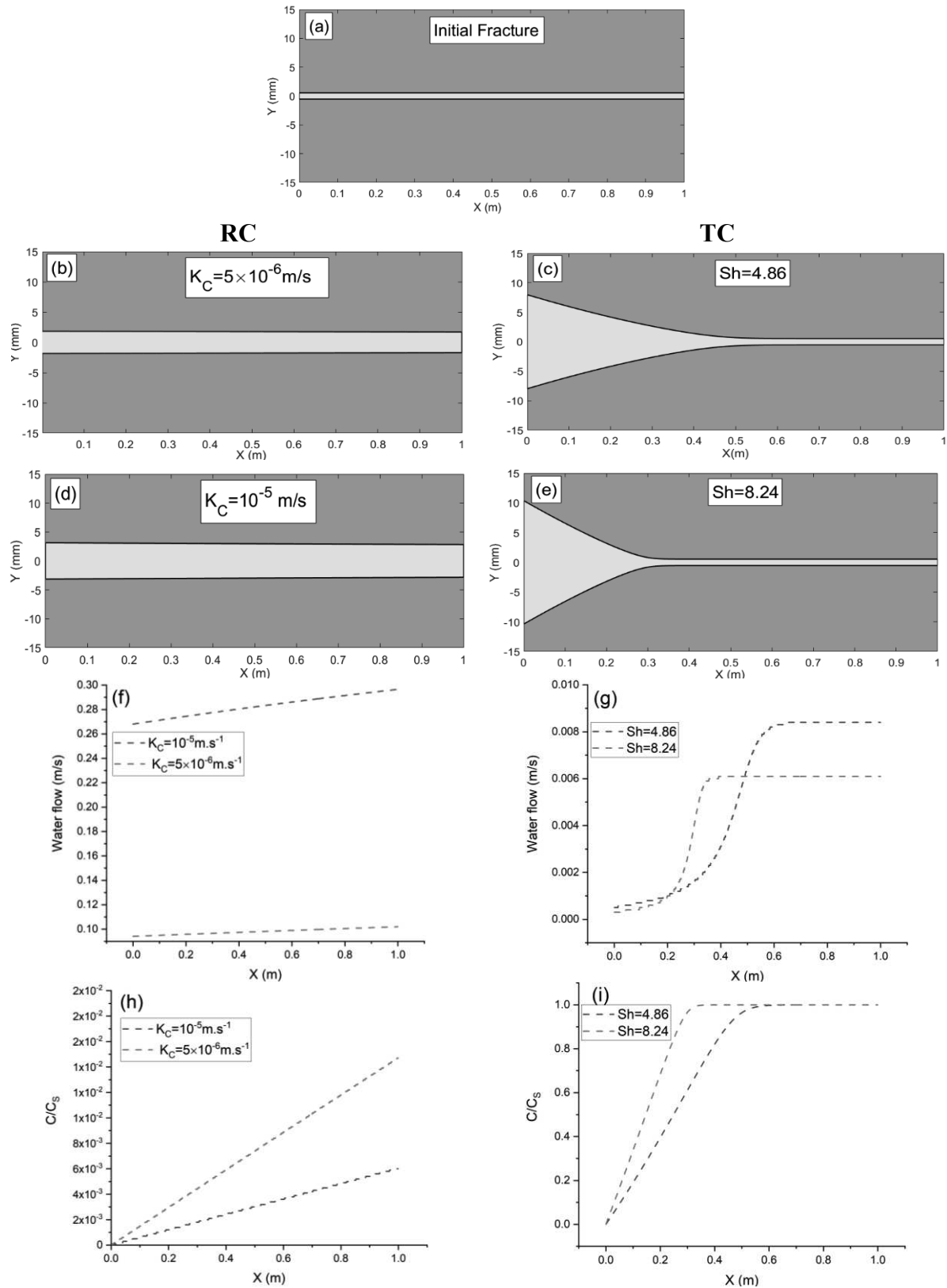


**Figure 5.7.** Spatial distributions of fracture aperture (a-e) concentration (f,g) and flow velocity (h,i) after 1 year with the RC and TC models. High and low values of constant reaction rate and Sherwood number are used for RC and TC models, respectively.

The effects of RC and TC dissolution on the time evolution of fractures, water velocity and concentration are plotted in Figure 5.8. This figure shows the time variation of the outputs at an

observation point near the inlet ( $X=0.1$ ). For the evolution of concentration with the RC model (Figure 5.8a), we observe three steps. The first one is the initial concentration and after a short time (roughly 10 seconds), the concentration drops due to the relatively fast effects of advection. After that, the concentration gets to a semi-steady value due to the interactive effects of transport of freshwater to the domain and the dissolution process. This semi-steady value is smaller for the case of lower  $K_C$  which is reasonable since smaller  $K_C$  calculates lower dissolution. The quasi-steady state values for the concentration are maintained until about two months and eventually the dominant effects of freshwater transport to the domain makes the concentration values converge to zero. The time variation of concentration with TC model (Figure 5.8-b) shows no drop in the concentration in the short-term (the first 50 seconds). The drop in the concentration is delayed about two months after the entrance of freshwater to the domain and it is delayed further with higher value of  $Sh$ . This proves the further limitation of the transport with employing higher constant values of  $Sh$  since the drop in the concentration is merely linked to the transport process. The time variation of the fracture aperture for the case of RC model (Figure 5.8c) shows a linear increase in the fracture aperture with time and higher values of the fracture aperture are calculated with the higher  $K_C$  which calculates more dissolution. The variations of fracture aperture in the case of TC model (Figure 5.8c), is showing a nonlinear behavior since there is a delay in the increase of the fracture aperture and this delay is longer for the case with higher value of  $Sh$  which is coherent with the time lag observed in the drops of concentration in the case of TC model. The effects of higher limitation of transport in the case of higher  $Sh$  is also observed in the evolution of fracture aperture since for the first 200 days of simulation the case with higher  $Sh$  calculates less fracture aperture despite its higher dissolution rate. This is due to the less availability of reacting species in the case of higher  $Sh$  with more limitation of transport. In larger time scales, the transport of freshwater to the domain provides enough reacting species and the dissolution rate becomes a controlling factor in the increase of fracture aperture. Therefore, after 200 days, the case with higher  $Sh$  calculates higher fracture aperture. The plots of the variation of water flow with time with RC and TC models are shown in Figure 5.8e and 5.8f, respectively. With the RC model, the water flow increases with time due to the increase in the permeability and the opening all through the fracture. Since there is more opening in the fracture in the case of higher  $K_C$ , the increase in the water flow is more in this case. The evolution of water flow in the case of TC model shows a different trend. In this case, the water flow increases only for a short time before intensive increases take part in the fracture opening. Small variations of fracture aperture in the beginning of the simulation time increase the permeability and consequently, the water flow. However, after intensive increases in the fracture aperture, the increase of the cross section obtains the dominant effect on the water flow and the water flow starts decreasing. This decrease is reasonable since a closed wormhole is created in the

domain and an intense increase in the cross section has been appeared without an opening all through the domain. The short increase of the beginning and the final decrease in the water flow is more pronounced in the case with high Sh as the conical wormhole effects are more intense in this case.

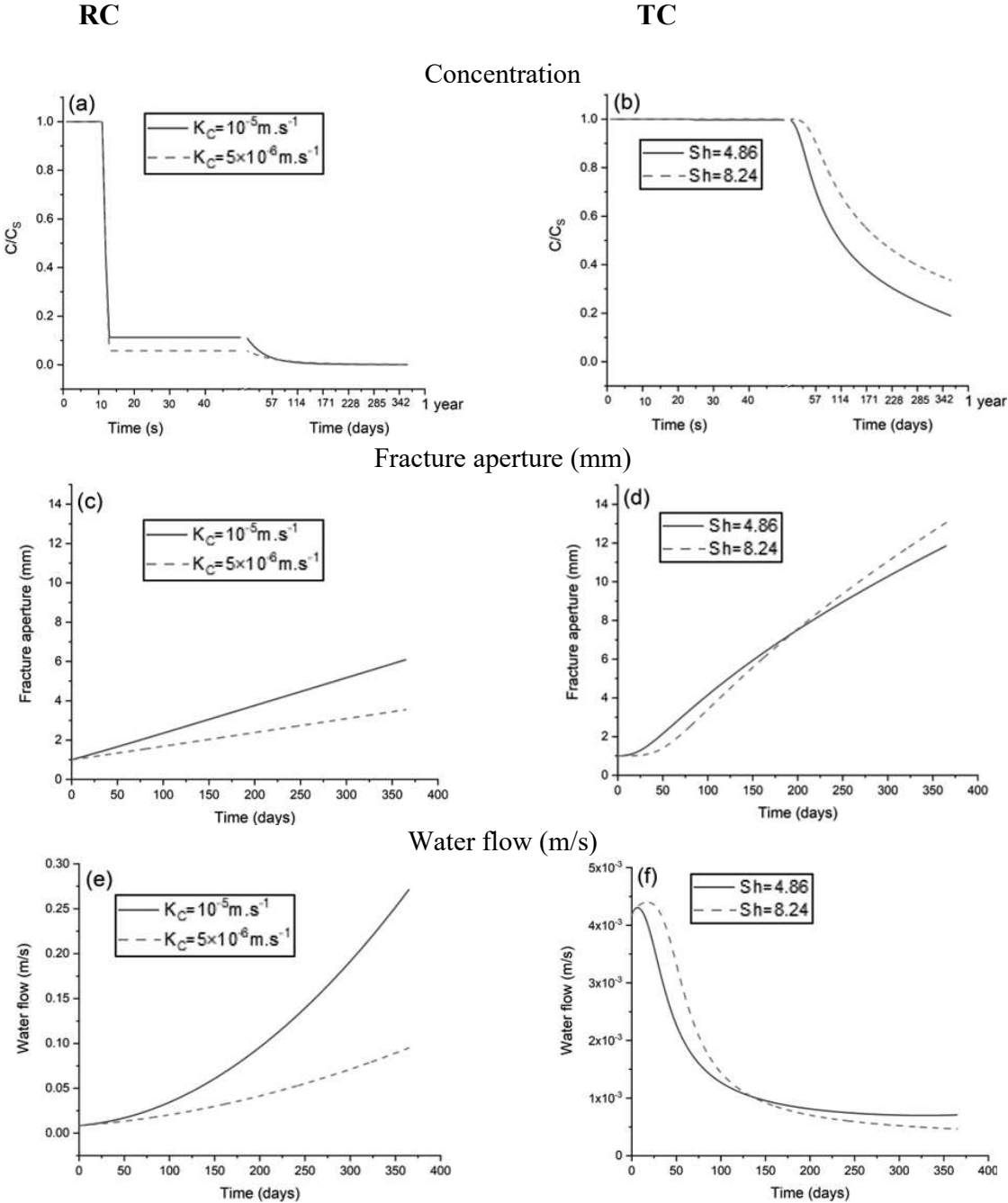


**Figure 5.8.** Time evolution of concentration (a,b), fracture aperture (c,d) and water flow (e,f) obtained with the RC and TC models with high and low values of constant reaction rate ( $K_C$ ) and the Sherwood number ( $Sh$ ), respectively. The results correspond to the case of single fracture and they are plotted near the inlet at  $X=0.1$

### 5.5.2. Dissolution processes in a DFN

This section extends the discussion of the previous section to DFNs. We consider a network of connected horizontal and vertical fractures as in Figure 5.9. This figure shows also an observation point ( $P_1$ ) that is used in our analysis here.

The domain is a horizontal plane, initially saturated with dissolving species and as shown in Figure 5.9, the freshwater is injected at the left-bottom corner and the water containing dissolved species are pumped out at the right-top corner. The values of the injection and production rates are identical and for the RC and TC models their values is considered as  $10^{-4} m^2 / s$  and  $5 \times 10^{-5} m^2 / s$ , respectively. For the rest of the input parameters, the same values are considered as in the case of the single fracture (see Table 5.1). For the sake of brevity, in this example we only consider one value for  $K_C$  ( $10^{-5} m \cdot s^{-1}$ ) and  $Sh$  (4.86) for RC and TC models, respectively.

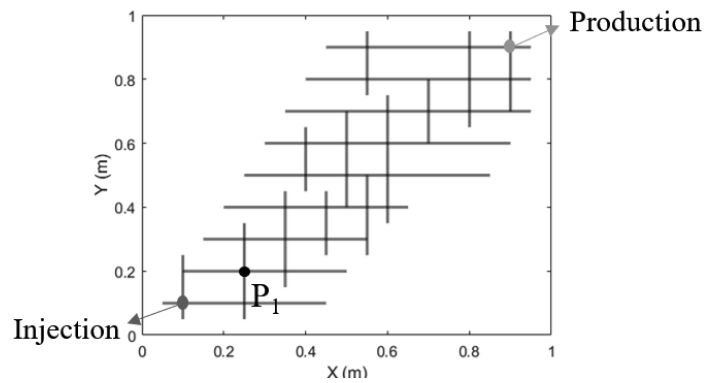


**Figure 5.9.** Conceptual model for dissolution process in a DFN

The results of fracture aperture, water flow and concentration in the fracture network after 1 year are plotted in Figure 5.10. The plots for the fracture aperture for both RC and TC models (Figures 5.10a and 5.10b) show that the aperture of the branches of fractures which are not connected to the main diagonal stream between the injection and production corners remain constant. This makes sense, as no dissolution is expected if no velocity is occurring in the fracture. The apertures of the branches connected to the main stream are increasing uniformly in RC model. With the TC model, more increase of the fracture aperture is observed near the injection well, which is coherent with the results of fracture geometry in a single fracture (see Figures 5.7b-5.7e). Since the network provides different possible fluid pathways, in the TC model, despite the limitation of transport, the effects of injecting freshwater after 1 year is pronounced in the regions far from the injection point. However, there is still a strong heterogeneity in the opening of fractures in the network with this model. The distribution of water flow in the fracture network with RC and TC models are plotted in Figures 5.10c and 5.10d, respectively. For both models as expected the value of the water flow

in the branches of fractures that are not connected to the main stream is not noticeable. Among the fractures connected to the main diagonal stream, a roughly uniform distribution of water flow is observed for the RC model with a slight increase from the injection corner towards the production corner. In the TC model, however, the water flow distribution is highly heterogeneous. In this case, the water flow is higher in the branches that are not experiencing big changes in their apertures. This is due to the heterogeneity in the spatial distribution of the fracture aperture in the network. In an intersection of several branches of fractures, higher flows (velocities) are assigned to the branches with smaller aperture. This is proved by the obtaining same regions with higher water flow and smaller apertures in the adjacency of the regions with lower water flow and higher aperture in the network with the TC model. These regions are also highlighted in the concentration plot of the TC model (Figure 5.10f) with being almost saturated with respect to the dissolving species. We can conclude that with the TC model in a network, regions with higher water flow receive more dissolving species from the surrounding and the concentration is kept near the saturation level which leads to very small increase in the aperture of the fracture and it will in turn increase the water flow in these regions. This is then reasonable to observe that in the concentration plot of RC model (Figure 5.10e) most of the dissolving species are depleted all through the domain since there is freshwater available for providing a more or less uniform change in the fracture aperture and water flow plots. The small heterogeneity in the RC model plots is near the outlet where the concentration is higher as a result of high velocity with Higher concentration is observed near the outlet with higher velocity and smaller aperture of the fractures which is coherent with the explanations of the TC model.

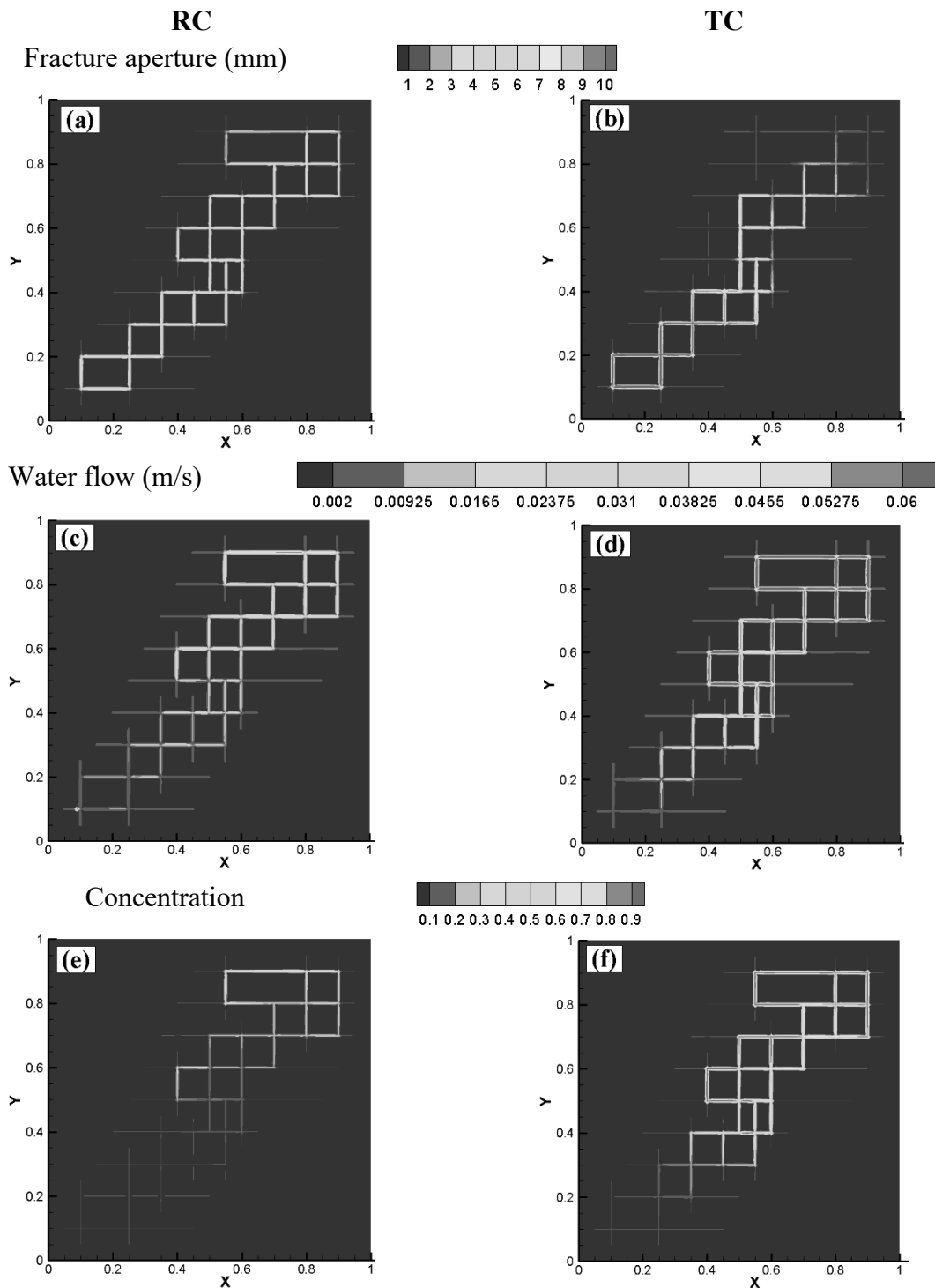


**Figure 5.10.** Comparison of spatial distributions of fracture aperture (a,b), water flow (c,d) and concentration (e,f) after 1 year between reaction and transport control formulations in a network of fractures

The evolutions of concentration, fracture aperture and water flow during 1 year in the fracture network at the observation point ( $P_1$ ) are plotted in Figure 5.11. In the concentration plot with RC model (Figure 5.11a) there is an early stage drop, similar to the case of a single fracture, due to advection. This drop reduces the concentration to a very small value which is the steady state value.

The concentration variation in the TC model shows different stages (Figure 5.11b). There is also an early stage drop in concentration of TC model due to advection. However, a relatively high semi-steady state value is maintained for the concentration due to the dominant effects of dissolution and in long-term with continuous injection of freshwater to the domain, the concentration keeps reducing. The plot of fracture aperture with time in RC model (Figure 5.11c) shows linear increase of the fracture aperture with time. However, the increase of fracture aperture with time in TC model (Figure 5.11d) is showing a parabolic behavior. It means that while RC model is calculating a constant rate for the increase in the fracture opening, this rate is not constant with TC model. In the beginning of the simulation this rate is very small due to the initial saturation of the domain with respect to the dissolving species. In a short time, with the arrival of fresh water, the rate of increase in the fracture aperture increases and we obtain a high opening in the fracture. After 200 days, the rate of fracture aperture opening starts reducing. This is due to the dependence of the dissolution rate on the fracture aperture in TC model. In this formulation, as the fracture aperture increases, the dissolution rate decreases and this explains the final stage reduce in the fracture opening rate. The evolution of water flow with time for both RC and TC model (Figures 5.11e and 5.11f, respectively) shows hyperbolic behaviors with drop in both models. This is due to imposing constant flux to the domain which causes a drop in water flow with an increase in the fracture opening. The drop in the water flow is smoother for RC model than TC model. This is understandable with the constant rate in the increase of fracture opening in RC model. However, fast increase in the fracture opening in TC model which increases the cross section and consequently, reduces the velocity causes the sharp drop in the water flow of TC model.

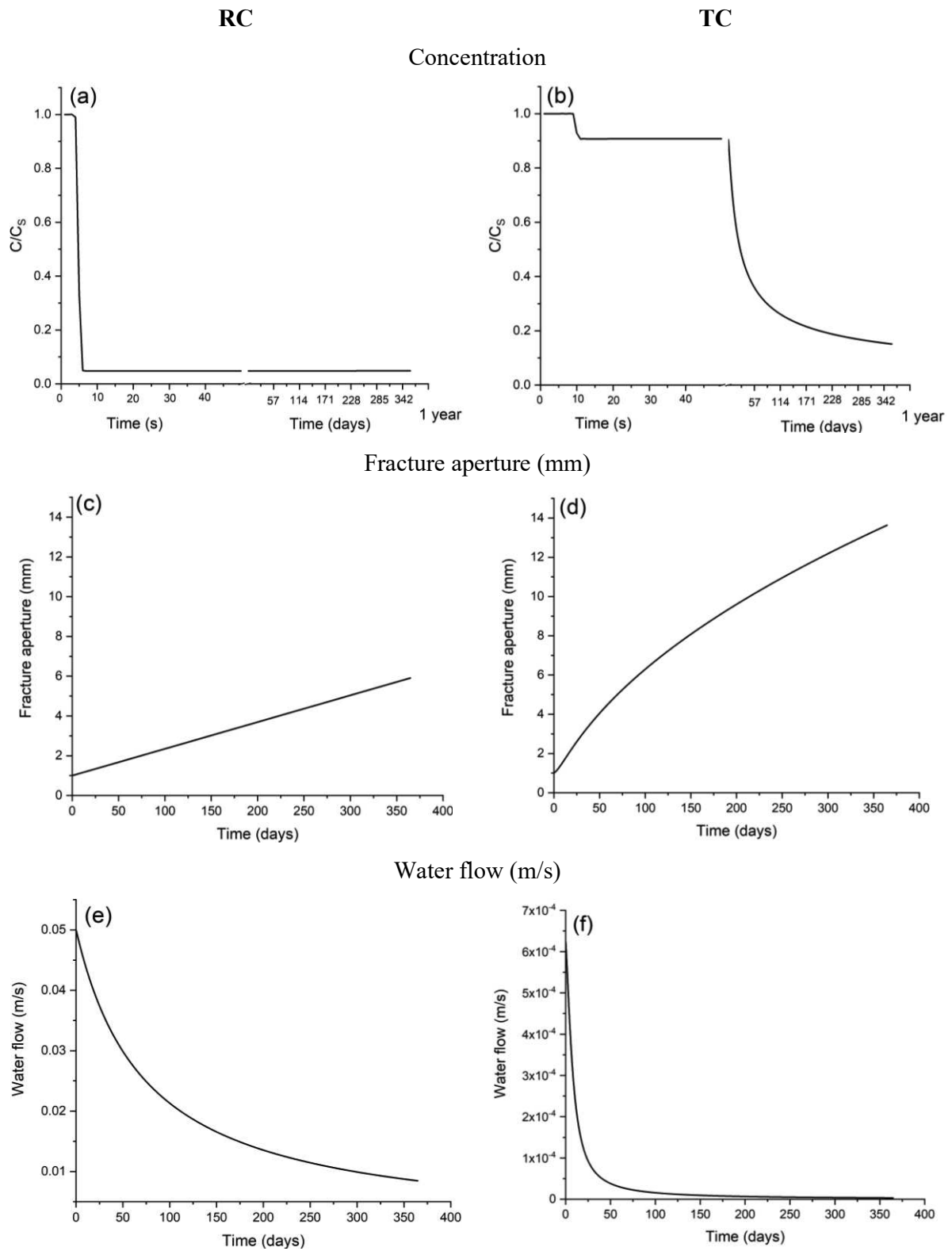


**Figure 5.11.** Comparison of the temporal evolutions of concentration (a,b), fracture aperture (c,d) and water flow (e,f) between RC and TC models in a network of fractures near the inlet at the point  $P_1$

## 5.6. Conclusion

Most of the previous studies on dissolution process in porous media are limited to unfractured domains and investigate how these processes create fractures and preferential flow pathways. The dissolution processes in naturally existing DFN and the impact of dissolution on fracture evolution and flow and transport mechanisms are still poorly understood. Modeling dissolution processes in a DFN is a computationally challenging problem because of the nonlinear coupling between the flow, transport and reactive processes, introduced by the impact of dissolution on fracture aperture. More challenge is also related to the fact that in the fractures the transport is advection dominated. In such a case, standard finite element formulation can introduce numerical diffusion that over estimates the dissolution processes. Standard finite element formulations can also introduce unphysical oscillations that may leads to converge issues. We developed a new model based on advanced numerical schemes to simulate dissolution processes in DFNs. The model is based on coupling the MFE method for flow with the DG scheme for transport. DG scheme is known to be suitable for advection dominated problems, as it can reduce numerical diffusion and unphysical oscillations. We suggest a new formulation of the DG scheme to deal with the Riemann solver at intersection of connecting fractures. The newly developed scheme is based on an averaging method with the weight of the upwind velocities. The time integration is improved by using an advanced solver of ODEs via the MOL.

The newly developed DG scheme is verified against a standard FE solution obtained with COMSOL Multiphysics. Great agreement has been obtained in examples dealing with high diffusion coefficients. The advantages of DG model in capturing the sharp moving fronts in an advection dominant transport is highlighted by comparing it to the results of the FV method. The results show that the DG scheme allows for capturing the sharp advective fronts with relatively coarse mesh, while the FV method fails to capture those fronts because of the dampening effects of the numerical diffusion. By refining the mesh with the FV model, the results converge toward the DG results. Based on the DG method, we provide quantitative data that can be used as reference solutions for benchmarking flow and transport in DFNs.

The effect of dissolution of fracture evolution and flow and transport processes is investigated, taking advantages the accuracy and efficiency of the newly developed DG scheme, Dissolution processes are investigated under reaction or transport-controlled configurations associated to the fast and slow flow rates, respectively. The results in both cases of a single fracture and a DFN show that the reaction-controlled dissolution leads to uniform dissolution through the fractures. However, the dissolution and its associated processes are localized around the flow inlet in the case of transport-controlled dissolution.

A parameter sensitivity analysis is performed to understand the effect of reaction rate on dissolution, flow and transport processes. In the case of reaction-controlled dissolution, the results show that the increase of the reaction rate leads to more opening in the fracture and therefore, higher flow rates and transport. However, in the case of transport-controlled dissolution, the increase of the reaction rate, represented by higher Sherwood number, lead to more localized dissolution at the flow inlet and the more pronounced worm hole effects. The increase of Sherwood number increases the fracture aperture and in consequence the fracture permeability. However, despite the increase in fracture permeability, it is observed that the flow velocity decreases. This is related to the fact that the increase of fracture section reduces the velocity, as by the mass conservation law, and the reduction of velocity related to fracture opening is more significant than the velocity augmentation related to the increase of permeability.

## Chapter VI: Conclusion and perspectives

### 6.1. General conclusion

This work is focused on modeling flow, reactive transport and heat transfer in porous media with focusing on three main applications: (i) multi-component reactive transport in the electro-diffusion process, (ii) Thermohaline convection in saturated porous media and (iii) Flow, dissolution and transport in fractured rocks. The main objective of this work is to improve the efficiency and accuracy of the numerical models and provide a deep understanding of the underlying physical processes. The first part has been devoted to assessing the common and simplifying assumptions in multicomponent reactive transport in porous media. A significant effort has been devoted to modeling and profoundly understanding the thermohaline convection process. The first attempts were assigned to the development of a semi-analytical solution for thermohaline convection that can be used for the evaluation of the newly developed numerical codes. We also developed a robust and efficient numerical model for reactive thermohaline convection with the application of CO<sub>2</sub> sequestration. The investigations on the CO<sub>2</sub> sequestration process have been expanded to field-scale analysis. We were also interested in modeling the key processes taking part in karstification in fractured rocks. Therefore, we developed an accurate numerical model for simulating flow, dissolution and transport in fractured rocks.

A common assumption in studying the electro-diffusion process in a multi-component reactive transport model is the null current assumption. This assumption is very popular since it improves the CPU time by reducing the non-linearity of the problem and it brings more convenience in code implementations. However, the validity of this assumption in a general reactive transport problem has been never studied in the literature. We have developed the numerical models based on two approaches: the null current assumption and the general Nernst-Planck-Poisson system of equations and we validated the models on the well-known benchmarks in the literature. We showed that both approaches lead to similar results when the electrical charge is only considered for the water phase. However, we observed that important differences appear between both approaches when both non-dissolved and dissolved parts are contributing to the creation of the electric flow. The differences between the results come from the fact that the null current assumption calculates the electric potential merely based on the dissolved concentration of the species. However, in a general case of reactive transport such as the cases involving the sorption process, this assumption is not validated and for these cases, the Nernst-Planck-Poisson system of equations has to be used which contains advective, diffusive and reactive fluxes accompanied with an electro diffusion flux that considers

an electric potential term. This electric potential is linked to the total ionic concentration in the Poisson equation and these two equations are solved together.

In the next part of the thesis, we have worked on the development of a semi-analytical solution for the thermohaline convection process in saturated porous media. Analytical solutions are helpful for understanding the physical processes. However, existing analytical models for thermohaline convection are limited to 2D under steady-state conditions. We developed the first semi-analytical solution for thermohaline convection with crossed-horizontal temperature and concentration gradients for which the 2D assumption is not valid. Accurate 3D simulations of THC are computationally expensive as they require dense computational grids. We develop a meshless semi-analytical solution based on the Fourier series method, applied to the vector potential form of the governing equations. The extension to transient solutions represents an important technical feature of this work, as the applications of the FS method to density-driven problems have been limited to steady-state conditions. Numerical experiments show the worthiness of the developed semi-analytical solution as a benchmark because it clearly allows for making a distinction between different numerical techniques.

The newly developed semi-analytical code has been used to perform a detailed parameter sensitivity analysis to understand the effects of controlling parameters on 3D thermohaline convection. A vortex convective flow is observed and the orientation and intensity of the flow are found sensitive to the gravity number. In the thermally-dominated cases, the transient behavior of the heat and mass fluxes can be affected by the Lewis number, in contrast to the steady-state regime which is insensitive to this parameter. We have also evaluated the effect of temperature gradient on salinity flux. This is important in the applications involving heat gradient in salinized aquifers. We showed that the increase of the temperature gradient reduces the salinity flux.

We were also interested in studying reactive transport associated with thermohaline convection. We performed our study with the application of CO<sub>2</sub> sequestration since understating the fate of CO<sub>2</sub> behavior is crucial for securing its containment in the reservoir and predicting the impact of dissolved CO<sub>2</sub> on the environment. For studying the convective-reactive transport in the CO<sub>2</sub> sequestration process, the common assumption in the literature is the isothermal conditions. Therefore, the effect of temperature on the convection and reaction in the CO<sub>2</sub> sequestration process is still poorly understood, particularly at the field scale. We developed a robust and efficient numerical model to study CO<sub>2</sub> sequestration with temperature-dependent viscosity, density and reaction rate. Appropriate numerical techniques are implemented in the model for the discretization of the spatial derivatives (mixed hybrid finite element for flow, Discontinuous Galerkin finite element for convective terms and multipoint flux approximation for diffusive terms). The

combination of these methods has shown several advantages in generating accurate and efficient numerical solutions to variable-density flow problems. However, it has never been applied to reactive thermohaline convection processes. Flow, mass transport, heat transfer, and chemical dissolution are solved sequentially. An adaptive time-stepping procedure, based on error control, is implemented to avoid operator splitting errors.

We also used the advanced numerical model to understand the effect of temperature gradient on the convective-reactive CO<sub>2</sub> dissolution. We considered three different models with increasing levels of complexity: Isothermal, Linear Temperature and Reactive thermohaline convection. In “Isothermal” model the temperature is constant while in “Linear Temperature” model the temperature increases linearly with depth. The results of the porous box benchmark indicate that the fingering phenomenon is under-predicted when the temperature-dependent convective processes are neglected. The effect of temperature on CO<sub>2</sub> transport is also investigated for a field case in the Viking reservoir in the North Sea. The results confirm that, at large scale and under realistic conditions of heterogeneity and geometric complexity, neglecting the temperature-dependent convective processes leads to an underestimation of the fingering phenomenon. The results show also that the intensified fingering phenomenon improves the dissolution processes and increases the total flux of CO<sub>2</sub> to the domain.

The parameters controlling the effect of temperature on the reaction rate, namely the activation energy and the pre-exponential factor in the Arrhenius law, are uncertain. A sensitivity analysis is performed to investigate how the uncertainties related to these parameters can affect the results. This analysis shows that the increase of the pre-exponential factor intensifies the fingering processes and leads to more CO<sub>2</sub> dissolution. Sensitivity of the CO<sub>2</sub> concentration to the activation energy is less pronounced at a high pre-exponential factor. The cumulative CO<sub>2</sub> flux is highly sensitive to the activation energy at a lower pre-exponential factor. There is no monotonic variation of the total flux with respect to the activation energy. The cumulative CO<sub>2</sub> flux is highly sensitive to the pre-exponential at high activation energy.

In the last part of the thesis, we devoted our efforts to modeling the dissolution processes in fractured rocks. Modeling dissolution processes in a Discrete Fracture Network domain is a computationally challenging problem because of the nonlinear coupling between the flow, transport and reactive processes, introduced by the impact of dissolution on fracture aperture. More challenge is also related to the fact that in the fractures the transport is advection dominated. In such a case, standard finite element formulation can introduce numerical diffusion that over estimates the dissolution processes. Standard finite element formulations can also introduce unphysical oscillations that may lead to converge issues. We developed a new model based on advanced numerical schemes to

simulate dissolution processes in DFNs. The model is based on coupling the MFE method for flow with the DG scheme for transport. DG scheme is known to be suitable for advection dominated problems, as it can reduce numerical diffusion and unphysical oscillations. We suggest a new formulation of the DG scheme to deal with the Riemann solver at intersection of connecting fractures. The newly developed scheme is based on an averaging method with the weight of the upwind velocities. The time integration is improved by using an advanced solver of ODEs via the MOL.

The advantages of DG model in capturing the sharp moving fronts in an advection dominant transport is highlighted by comparing it to the results of the FV method. The results show that the DG scheme allows for capturing the sharp advective fronts with relatively coarse mesh, while the FV method fails to capture those fronts because of the dampening effects of the numerical diffusion. The newly developed model is then used to provide physical insights into the dissolution process on fracture evolution and flow and transport. Dissolution processes are investigated under reaction or transport-controlled configurations associated to the fast and slow flow rates, respectively. The results in both cases of a single fracture and a DFN show that the reaction-controlled dissolution leads to uniform dissolution through the fractures. However, the dissolution and its associated processes are localized around the flow inlet in the case of transport-controlled dissolution.

A parameter sensitivity analysis is performed to understand the effect of reaction rate on dissolution, flow and transport processes. In the case of reaction-controlled dissolution, the results show that the increase of the reaction rate leads to more opening in the fracture and therefore, higher flow rates and transport. However, in the case of transport-controlled dissolution, the increase of the reaction rate, represented by higher Sherwood number, lead to more localized dissolution at the flow inlet and the more pronounced worm hole effects. The increase of Sherwood number increases the fracture aperture and in consequence the fracture permeability. However, despite the increase in fracture permeability, it is observed that the flow velocity decreases. This is related to the fact that the increase of fracture section reduces the velocity, as by the mass conservation law, and the reduction of velocity related to fracture opening is more significant than the velocity augmentation related to the increase of permeability.

## **6.2. Perspective**

The concepts discussed in this work reveal the potential spots for future research topics. We shortly listed these topics. However, future research works are not limited to the following list:

1. Experimental studies are required in the case of multicomponent reactive transport in the studies of electro-diffusion to approve the validity of the Nernst-Planck-Poisson equation with sorption.
2. Semi-analytical solutions for thermohaline convection are limited to the problems with a series of simplifications. For instance, there is a spot to work on the reactive thermohaline convection with the semi-analytical approach for providing reference solutions in this case.
3. The advanced numerical model developed for the reactive-thermohaline convection with the application of CO<sub>2</sub> sequestration deals with the single-phase flow problem. Further research works are required to expand the model to study the multiphase flow with the existence of CO<sub>2</sub> gas phase in the domain. Also, the model can be expanded to deal with the fractured domain with Discrete Fracture Matrix approach. Furthermore, more sophisticated and realistic processes can be considered in the system as they are applicable to the process of CO<sub>2</sub> sequestration.
4. The developed DFN model for the fracture dissolution in 1D, can be expanded to a 2D model since the increase in the fracture aperture due to the dissolution process makes the 2D modeling in the fractures more realistic. Also, the effects of other factors on the fracture deformations such as geochemical precipitation in fracture clogging or mechanical forces in the increase of the fracture aperture could be considered in DFN modeling.

## Chapitre VI: Conclusion et perspectives

### 6.1. Conclusion générale

Ce travail se concentre sur la modélisation de l'écoulement, du transport réactif et du transfert de chaleur dans les milieux poreux, en mettant l'accent sur trois applications principales : (i) le transport réactif multi-composants dans le processus d'électro-diffusion, (ii) la convection thermohaline dans les milieux poreux saturés et (iii) l'écoulement, la dissolution et le transport dans les roches fracturées. L'objectif principal de ce travail est d'améliorer l'efficacité et la précision des modèles numériques et de fournir une compréhension approfondie des processus physiques sous-jacents. La première partie a été consacrée à l'évaluation des hypothèses communes et simplificatrices dans le transport réactif multicomposant dans les milieux poreux. Un effort significatif a été consacré à la modélisation et à la compréhension profonde du processus de convection thermohaline. Les premières tentatives ont été consacrées au développement d'une solution semi-analytique pour la convection thermohaline qui peut être utilisée pour l'évaluation des codes numériques nouvellement développés. Nous avons également développé un modèle numérique robuste et efficace pour la convection thermohaline réactive avec l'application de la séquestration du CO<sub>2</sub>. Les recherches sur le processus de séquestration du CO<sub>2</sub> ont été étendues à l'analyse à l'échelle du terrain. Nous nous sommes également intéressés à la modélisation des processus clés qui participent à la karstification dans les roches fracturées. Nous avons donc développé un modèle numérique précis pour simuler l'écoulement, la dissolution et le transport dans les roches fracturées.

Une hypothèse courante dans l'étude du processus d'électro-diffusion dans un modèle de transport réactif multi-composants est l'hypothèse de courant nul. Cette hypothèse est très populaire car elle améliore le temps de calcul de l'unité centrale en réduisant la non-linéarité du problème et apporte plus de commodité dans l'implémentation des codes. Cependant, la validité de cette hypothèse dans un problème général de transport réactif n'a jamais été étudiée dans la littérature. Nous avons développé des modèles numériques basés sur deux approches : l'hypothèse du courant nul et le système général d'équations de Nernst-Planck-Poisson, et nous avons validé les modèles sur des références bien connues dans la littérature. Nous avons montré que les deux approches conduisent à des résultats similaires lorsque la charge électrique n'est prise en compte que pour la phase aqueuse. Cependant, nous avons observé que des différences importantes apparaissent entre les deux approches lorsque les parties non dissoutes et dissoutes contribuent à la création du flux électrique. Les différences entre les résultats proviennent du

fait que l'hypothèse du courant nul calcule le potentiel électrique uniquement sur la base de la concentration dissoute de l'espèce. Cependant, dans un cas général de transport réactif tel que les cas impliquant le processus de sorption, cette hypothèse n'est pas validée et pour ces cas, le système d'équations de Nernst-Planck-Poisson doit être utilisé qui contient des flux advectifs, diffusifs et réactifs accompagnés d'un flux d'électrodifusion qui prend en compte un terme de potentiel électrique. Ce potentiel électrique est lié à la concentration ionique totale dans l'équation de Poisson et ces deux équations sont résolues ensemble.

Dans la partie suivante de la thèse, nous avons travaillé sur le développement d'une solution semi-analytique pour le processus de convection thermohaline dans les milieux poreux saturés. Les solutions analytiques sont utiles pour comprendre les processus physiques. Cependant, les modèles analytiques existants pour la convection thermohaline sont limités à la 2D dans des conditions d'équilibre. Nous avons développé la première solution semi-analytique pour la convection thermohaline avec des gradients de température et de concentration horizontaux croisés pour lesquels l'hypothèse 2D n'est pas valide. Les simulations 3D précises de la convection thermohaline sont coûteuses en termes de calcul car elles nécessitent des grilles de calcul denses. Nous développons une solution semi-analytique sans maillage basée sur la méthode des séries de Fourier, appliquée à la forme du potentiel vectoriel des équations gouvernantes. L'extension aux solutions transitoires représente une caractéristique technique importante de ce travail, étant donné que les applications de la méthode des séries de Fourier aux problèmes liés à la densité ont été limitées aux conditions d'équilibre. Les expériences numériques montrent la valeur de la solution semi-analytique développée en tant que référence, car elle permet clairement de faire la distinction entre les différentes techniques numériques.

Le code semi-analytique nouvellement développé a été utilisé pour effectuer une analyse détaillée de la sensibilité des paramètres afin de comprendre les effets des paramètres de contrôle sur la convection thermohaline en 3D. Un écoulement convectif tourbillonnaire est observé et l'orientation et l'intensité de l'écoulement sont sensibles au nombre de gravité. Dans les cas à dominante thermique, le comportement transitoire des flux de chaleur et de masse peut être affecté par le nombre de Lewis, contrairement au régime permanent qui est insensible à ce paramètre. Nous avons également évalué l'effet du gradient de température sur le flux de salinité. Cet aspect est important pour les applications impliquant un gradient de chaleur dans les aquifères salinisés. Nous avons montré que l'augmentation du gradient de température réduit le flux de salinité.

Nous nous sommes également intéressés à l'étude du transport réactif associé à la convection thermohaline. Nous avons réalisé notre étude dans le cadre de la séquestration du CO<sub>2</sub>, car il est essentiel de comprendre le comportement du CO<sub>2</sub> pour assurer son confinement dans le réservoir et prévoir l'impact du CO<sub>2</sub> dissous sur l'environnement. Pour étudier le transport convectif-réactif dans le processus de séquestration du CO<sub>2</sub>, l'hypothèse commune dans la littérature est l'isothermie. Par conséquent, l'effet de la température sur la convection et la réaction dans le processus de séquestration du CO<sub>2</sub> est encore mal compris, en particulier à l'échelle du terrain. Nous avons développé un modèle numérique robuste et efficace pour étudier la séquestration du CO<sub>2</sub> avec une viscosité, une densité et un taux de réaction dépendant de la température. Des techniques numériques appropriées sont mises en œuvre dans le modèle pour la discrétisation des dérivés spatiaux (éléments finis hybrides mixtes pour l'écoulement, éléments finis de Galerkin discontinu pour les termes convectifs et approximation de flux multipoints pour les termes diffusifs). La combinaison de ces méthodes a montré plusieurs avantages dans la génération de solutions numériques précises et efficaces pour les problèmes d'écoulement à densité variable. Cependant, elle n'a jamais été appliquée aux processus de convection thermohaline réactive. L'écoulement, le transport de masse, le transfert de chaleur et la dissolution chimique sont résolus de manière séquentielle. Une procédure adaptative de pas de temps, basée sur le contrôle des erreurs, est mise en œuvre pour éviter les erreurs de division des opérateurs.

Nous avons également utilisé le modèle numérique avancé pour comprendre l'effet du gradient de température sur la dissolution convective-réactive du CO<sub>2</sub>. Nous avons considéré trois modèles différents avec des niveaux de complexité croissants : isotherme, température linéaire et convection thermohaline réactive. Dans le modèle "isotherme", la température est constante tandis que dans le modèle "température linéaire", la température augmente linéairement avec la profondeur. Les résultats du benchmark de la boîte poreuse indiquent que le phénomène de fingering est sous-prévu lorsque les processus convectifs dépendant de la température sont négligés. L'effet de la température sur le transport du CO<sub>2</sub> est également étudié pour un cas de terrain dans le réservoir Viking en mer du Nord. Les résultats confirment qu'à grande échelle et dans des conditions réalistes d'hétérogénéité et de complexité géométrique, la négligence des processus convectifs dépendant de la température conduit à une sous-estimation du phénomène de fingering. Les résultats montrent également que l'intensification du phénomène de fingering améliore les processus de dissolution et augmente le flux total de CO<sub>2</sub> dans le domaine.

Les paramètres contrôlant l'effet de la température sur la vitesse de réaction, à savoir l'énergie d'activation et le facteur pré-exponentiel dans la loi d'Arrhenius, sont incertains. Une analyse de sensibilité est réalisée pour étudier comment les incertitudes liées à ces paramètres peuvent affecter les résultats. Cette analyse montre que l'augmentation du facteur pré-exponentiel intensifie les processus de doigté et conduit à une plus grande dissolution du CO<sub>2</sub>. La sensibilité de la concentration de CO<sub>2</sub> à l'énergie d'activation est moins prononcée lorsque le facteur pré-exponentiel est élevé. Le flux cumulé de CO<sub>2</sub> est très sensible à l'énergie d'activation lorsque le facteur pré-exponentiel est faible. Il n'y a pas de variation monotone du flux total en fonction de l'énergie d'activation. Le flux cumulé de CO<sub>2</sub> est très sensible au facteur préexponentiel à une énergie d'activation élevée.

Dans la dernière partie de la thèse, nous avons consacré nos efforts à la modélisation des processus de dissolution dans les roches fracturées. La modélisation des processus de dissolution dans un domaine de réseau de fractures discrètes est un problème de calcul difficile en raison du couplage non linéaire entre les processus d'écoulement, de transport et de réaction, introduit par l'impact de la dissolution sur l'ouverture des fractures. Un autre défi est lié au fait que dans les fractures, le transport est dominé par l'advection. Dans ce cas, la formulation standard des éléments finis peut introduire une diffusion numérique qui surestime les processus de dissolution. Les formulations d'éléments finis standard peuvent également introduire des oscillations non physiques qui peuvent conduire à des problèmes de convergence. Nous avons développé un nouveau modèle basé sur des schémas numériques avancés pour simuler les processus de dissolution dans les DFN. Le modèle est basé sur le couplage de la méthode MFE pour l'écoulement avec le schéma DG pour le transport. Le schéma DG est connu pour être adapté aux problèmes dominés par l'advection, car il peut réduire la diffusion numérique et les oscillations non physiques. Nous proposons une nouvelle formulation du schéma DG pour traiter le solveur de Riemann à l'intersection de fractures communicantes. Le nouveau schéma développé est basé sur une méthode de calcul de la moyenne avec le poids des vitesses au vent. L'intégration temporelle est améliorée par l'utilisation d'un solveur avancé d'EDO via le MOL.

Les avantages du modèle DG dans la capture des fronts mobiles aigus dans un transport dominant l'advection sont mis en évidence en le comparant aux résultats de la méthode FV. Les résultats montrent que le schéma DG permet de capturer les fronts advectifs aigus avec un maillage relativement grossier, alors que la méthode FV ne parvient pas à capturer ces fronts en raison des effets d'amortissement de la diffusion numérique. Le modèle nouvellement développé est ensuite utilisé pour donner un aperçu physique du processus de dissolution sur

l'évolution des fractures et l'écoulement et le transport. Les processus de dissolution sont étudiés dans des configurations contrôlées par la réaction ou le transport, associées à des débits rapides et lents, respectivement. Les résultats dans les deux cas d'une fracture unique et d'un DFN montrent que la dissolution contrôlée par la réaction conduit à une dissolution uniforme à travers les fractures. Cependant, la dissolution et ses processus associés sont localisés autour de l'entrée de l'écoulement dans le cas de la dissolution contrôlée par le transport.

Une analyse de sensibilité des paramètres est effectuée pour comprendre l'effet du taux de réaction sur les processus de dissolution, d'écoulement et de transport. Dans le cas de la dissolution contrôlée par la réaction, les résultats montrent que l'augmentation de la vitesse de réaction entraîne une plus grande ouverture de la fracture et, par conséquent, des débits et un transport plus élevés. Cependant, dans le cas de la dissolution contrôlée par le transport, l'augmentation du taux de réaction, représentée par un nombre de Sherwood plus élevé, conduit à une dissolution plus localisée à l'entrée du flux et à des effets de ver plus prononcés. L'augmentation du nombre de Sherwood accroît l'ouverture de la fracture et, par conséquent, la perméabilité de la fracture. Cependant, malgré l'augmentation de la perméabilité des fractures, on observe que la vitesse d'écoulement diminue. Ceci est lié au fait que l'augmentation de la section des fractures réduit la vitesse, conformément à la loi de conservation de la masse, et que la réduction de la vitesse liée à l'ouverture des fractures est plus importante que l'augmentation de la vitesse liée à l'augmentation de la perméabilité.

## **6.2. Perspectives**

Les concepts discutés dans ce travail révèlent les points potentiels des futurs sujets de recherche. Nous avons brièvement énuméré ces sujets. Toutefois, les travaux de recherche futurs ne se limitent pas à la liste suivante :

1. Des études expérimentales sont nécessaires dans le cas du transport réactif multicomposant dans les études d'électro-diffusion pour approuver la validité de l'équation de Nernst-Planck-Poisson avec sorption.
2. Les solutions semi-analytiques pour la convection thermohaline sont limitées aux problèmes comportant une série de simplifications. Par exemple, il y a un point à travailler sur la convection thermohaline réactive avec l'approche semi-analytique pour fournir des solutions de référence dans ce cas.
3. Le modèle numérique avancé développé pour la convection thermohaline réactive avec l'application de la séquestration du CO<sub>2</sub> traite le problème de l'écoulement monophasique.

D'autres travaux de recherche sont nécessaires pour étendre le modèle à l'étude de l'écoulement multiphasique avec l'existence de la phase gazeuse du CO<sub>2</sub> dans le domaine. Le modèle peut également être étendu pour traiter le domaine fracturé avec l'approche de la matrice de fractures discrètes. En outre, des processus plus sophistiqués et plus réalistes peuvent être pris en compte dans le système car ils sont applicables au processus de séquestration du CO<sub>2</sub>.

4. Le modèle DFN développé pour la dissolution des fractures en 1D peut être étendu à un modèle 2D car l'augmentation de l'ouverture des fractures due au processus de dissolution rend la modélisation 2D des fractures plus réaliste. En outre, les effets d'autres facteurs sur les déformations des fractures, tels que les précipitations géochimiques dans le colmatage des fractures ou les forces mécaniques dans l'augmentation de l'ouverture des fractures, pourraient être pris en compte dans la modélisation DFN.

## References

### Chapter I: Introduction

- Abd, Abdul Salam, and Ahmad Abushaikha. "A Review of Numerical Modelling Techniques for Reactive Transport in Subsurface Reservoirs and Application in Mimetic Finite Difference Discretization Schemes." In *Day 2 Tue, June 04, 2019, D021S001R012*. London, England, UK: SPE, 2019. <https://doi.org/10.2118/195558-MS>.
- Abd, Abdul Salam, and Ahmad S. Abushaikha. "Reactive Transport in Porous Media: A Review of Recent Mathematical Efforts in Modeling Geochemical Reactions in Petroleum Subsurface Reservoirs." *SN Applied Sciences* 3, no. 4 (April 2021): 401. <https://doi.org/10.1007/s42452-021-04396-9>.
- Al-Khoury, Rafid. *Computational Modeling of Shallow Geothermal Systems*. 0 ed. CRC Press, 2011. <https://doi.org/10.1201/b11462>.
- Chen, Zhangxin. "Reservoir Simulation - Mathematical Techniques in Oil Recovery." In *CBMS-NSF Regional Conference Series in Applied Mathematics*, 2007.
- Class, Holger, Anozie Ebigbo, Rainer Helmig, Helge K. Dahle, Jan M. Nordbotten, Michael A. Celia, Pascal Audigane, et al. "A Benchmark Study on Problems Related to CO<sub>2</sub> Storage in Geologic Formations: Summary and Discussion of the Results." *Computational Geosciences* 13, no. 4 (December 2009): 409–34. <https://doi.org/10.1007/s10596-009-9146-x>.
- Diaz Viera, Martin A., Pratap Sahay, Manuel Coronado, and Arturo Ortiz Tapia, eds. *Mathematical and Numerical Modeling in Porous Media: Applications in Geosciences*. 0 ed. CRC Press, 2012. <https://doi.org/10.1201/b12080>.
- Erfani, Hamidreza, Vahid Joekar-Niasar, and Rouhi Farajzadeh. "Impact of Microheterogeneity on Upscaling Reactive Transport in Geothermal Energy." *ACS Earth and Space Chemistry* 3, no. 9 (September 19, 2019): 2045–57. <https://doi.org/10.1021/acsearthspacechem.9b00056>.
- Firoozabadi, Abbas, and Philip C. Myint. "Prospects for Subsurface CO<sub>2</sub> Sequestration." *AIChE Journal* 56, no. 6 (June 2010): 1398–1405. <https://doi.org/10.1002/aic.12287>.
- Helmig R. (2015) Numerical Models for Evaluating the Competitive Use of the Subsurface: The Influence of Energy Storage and Production in Groundwater, Darcy lecture, University of Bergen
- Juanes, Ruben, and Holger Class. "Special Issue on Computational Methods in Geologic CO<sub>2</sub> Sequestration." *Advances in Water Resources* 62 (December 2013): 353–55. <https://doi.org/10.1016/j.advwatres.2013.10.012>.
- Kalla, L., P. Vasseur, R. Benacer, H. Beji, and R. Duval. "Double Diffusive Convection within a Horizontal Porous Layer Salted from the Bottom and Heated Horizontally." *International Communications in Heat and Mass Transfer* 28, no. 1 (January 2001): 1–10. [https://doi.org/10.1016/S0735-1933\(01\)00207-X](https://doi.org/10.1016/S0735-1933(01)00207-X).
- Khalili, N., A.R. Russell, and A. Khoshghalb, eds. *Unsaturated Soils: Research & Applications*. 1st ed. CRC Press, 2020. <https://doi.org/10.1201/9781003070580>.
- Kim, Jihoon, Eric L. Sonnenthal, and Jonny Rutqvist. "Formulation and Sequential Numerical Algorithms of Coupled Fluid/Heat Flow and Geomechanics for Multiple Porosity Materials: FORMULATION AND SEQUENTIAL NUMERICAL ALGORITHMS OF COUPLED FLUID/HEAT." *International Journal for Numerical Methods in Engineering* 92, no. 5 (November 2, 2012): 425–56. <https://doi.org/10.1002/nme.4340>.

- Koohbor, Behshad, Marwan Fahs, Hussein Hoteit, Joanna Doummar, Anis Younes, and Benjamin Belfort. "An Advanced Discrete Fracture Model for Variably Saturated Flow in Fractured Porous Media." *Advances in Water Resources* 140 (June 2020): 103602. <https://doi.org/10.1016/j.advwatres.2020.103602>.
- Ladd, Anthony J.C., and Piotr Szymczak. "Reactive Flows in Porous Media: Challenges in Theoretical and Numerical Methods." *Annual Review of Chemical and Biomolecular Engineering* 12, no. 1 (June 7, 2021): 543–71. <https://doi.org/10.1146/annurev-chembioeng-092920-102703>.
- Lee, Jan van der, Laurent De Windt, Vincent Lagneau, and Patrick Goblet. "Module-Oriented Modeling of Reactive Transport with HYTEC." *Computers & Geosciences* 29, no. 3 (April 2003): 265–75. [https://doi.org/10.1016/S0098-3004\(03\)00004-9](https://doi.org/10.1016/S0098-3004(03)00004-9).
- MASUDA, Yoshio, Michio YONEYA, and Shigeo KIMURA. "Multiple Solutions of Double-Diffusive Convection in Porous Media Due to Opposing Heat and Mass Fluxes on Vertical Walls." *Journal of Thermal Science and Technology* 8, no. 3 (2013): 533–42. <https://doi.org/10.1299/jtst.8.533>.
- May D.A. (2014) Numerical Modelling in Geosciences, Short-course on Numerical Modelling, National Observatory of Athens.
- Miller, Cass T., Clint N. Dawson, Matthew W. Farthing, Thomas Y. Hou, Jingfang Huang, Christopher E. Kees, C.T. Kelley, and Hans Petter Langtangen. "Numerical Simulation of Water Resources Problems: Models, Methods, and Trends." *Advances in Water Resources* 51 (January 2013): 405–37. <https://doi.org/10.1016/j.advwatres.2012.05.008>.
- Nield, Donald A., and Adrian Bejan. *Convection in Porous Media*. New York, NY: Springer New York, 2013. <https://doi.org/10.1007/978-1-4614-5541-7>.
- Shao, Qian, Marwan Fahs, Anis Younes, Ahmed Makradi, and Thierry Mara. "A New Benchmark Reference Solution for Double-Diffusive Convection in a Heterogeneous Porous Medium." *Numerical Heat Transfer, Part B: Fundamentals* 70, no. 5 (November 2016): 373–92. <https://doi.org/10.1080/10407790.2016.1215718>.
- Singh, Ajay. "Groundwater Resources Management through the Applications of Simulation Modeling: A Review." *Science of The Total Environment* 499 (November 2014): 414–23. <https://doi.org/10.1016/j.scitotenv.2014.05.048>.
- Tabrizinejadas, Sara, Jerome Carrayrou, Maarten W. Saaltink, Husam Musa Baalousha, and Marwan Fahs. "On the Validity of the Null Current Assumption for Modeling Sorptive Reactive Transport and Electro-Diffusion in Porous Media." *Water* 13, no. 16 (August 15, 2021): 2221. <https://doi.org/10.3390/w13162221>.
- Tabrizinejadas, Sara, Marwan Fahs, Behzad Ataie-Ashtiani, Craig T. Simmons, Raphaël Chiara Roupert, and Anis Younes. "A Fourier Series Solution for Transient Three-Dimensional Thermohaline Convection in Porous Enclosures." *Water Resources Research* 56, no. 11 (November 2020). <https://doi.org/10.1029/2020WR028111>.
- Trevisan, Osvaldo V., and Adrian Bejan. "Mass and Heat Transfer by Natural Convection in a Vertical Slot Filled with Porous Medium." *International Journal of Heat and Mass Transfer* 29, no. 3 (March 1, 1986): 403–15. [https://doi.org/10.1016/0017-9310\(86\)90210-3](https://doi.org/10.1016/0017-9310(86)90210-3).
- UNFCCC, Decision. "1/CP. 21, Adoption of the Paris Agreement. UN Doc." FCCC/CP/2015/10/Add. 1, 2015.

- Vilarrasa, Victor, and Jesus Carrera. “Geologic Carbon Storage Is Unlikely to Trigger Large Earthquakes and Reactivate Faults through Which CO<sub>2</sub> Could Leak.” *Proceedings of the National Academy of Sciences* 112, no. 19 (May 12, 2015): 5938–43. <https://doi.org/10.1073/pnas.1413284112>.
- Werner, Adrian D., Mark Bakker, Vincent E.A. Post, Alexander Vandenbohede, Chunhui Lu, Behzad Ataie-Ashtiani, Craig T. Simmons, and D.A. Barry. “Seawater Intrusion Processes, Investigation and Management: Recent Advances and Future Challenges.” *Advances in Water Resources* 51 (January 2013): 3–26. <https://doi.org/10.1016/j.advwatres.2012.03.004>.
- Whitley, Shelagh. *G7 Fossil Fuel Subsidy Scorecard: Tracking the Phase-out of Fiscal Support and Public Finance for Oil, Gas and Coal*. International Institute for Sustainable Development, 2018.
- Younes, Anis, and Philippe Ackerer. “Solving the Advection–Dispersion Equation with Discontinuous Galerkin and Multipoint Flux Approximation Methods on Unstructured Meshes.” *International Journal for Numerical Methods in Fluids* 58, no. 6 (2008): 687–708.
- Younes, Anis, Marwan Fahs, and Selim Ahmed. “Solving Density Driven Flow Problems with Efficient Spatial Discretizations and Higher-Order Time Integration Methods.” *Advances in Water Resources* 32, no. 3 (March 2009): 340–52. <https://doi.org/10.1016/j.advwatres.2008.11.003>.
- Zhang, Hubao, and Franklin W. Schwartz. “Multispecies Contaminant Plumes in Variable Density Flow Systems.” *Water Resources Research* 31, no. 4 (April 1995): 837–47. <https://doi.org/10.1029/94WR02567>.
- Zhao, Chongbin. “Computational Methods for Simulating Some Typical Problems in Computational Geosciences.” *International Journal of Computational Methods* 13, no. 02 (March 2016): 1640016. <https://doi.org/10.1142/S0219876216400168>.
- Zhao, Chongbin, Bruce E Hobbs, and Alison Ord. *Fundamentals of Computational Geoscience: Numerical Methods and Algorithms*. Vol. 122. Springer Science & Business Media, 2009.
- Chapter II: On the Validity of the Null Current Assumption for Modeling Sorptive Reactive Transport and Electro-Diffusion in Porous Media**
- Babaei, Masoud, and Akand Islam. “Convective-Reactive CO<sub>2</sub> Dissolution in Aquifers With Mass Transfer With Immobile Water.” *Water Resources Research* 54, no. 11 (November 2018): 9585–9604. <https://doi.org/10.1029/2018WR023150>.
- Ben-Yaakov, S. “Diffusion of Sea Water Ions—I. Diffusion of Sea Water into a Dilute Solution.” *Geochimica et Cosmochimica Acta* 36, no. 12 (December 1972): 1395–1406. [https://doi.org/10.1016/0016-7037\(72\)90069-5](https://doi.org/10.1016/0016-7037(72)90069-5).
- Birgersson, Martin, and Ola Karnland. “Ion Equilibrium between Montmorillonite Interlayer Space and an External Solution—Consequences for Diffusional Transport.” *Geochimica et Cosmochimica Acta* 73, no. 7 (April 2009): 1908–23. <https://doi.org/10.1016/j.gca.2008.11.027>.
- Boudreau, Bernard P., Filip J.R. Meysman, and Jack J. Middelburg. “Multicomponent Ionic Diffusion in Porewaters: Coulombic Effects Revisited.” *Earth and Planetary Science Letters* 222, no. 2 (May 2004): 653–66. <https://doi.org/10.1016/j.epsl.2004.02.034>.
- Brovelli, Alessandro, and Giorgio Cassiani. “Effective Permittivity of Porous Media: A Critical Analysis of the Complex Refractive Index Model.” *Geophysical Prospecting* 56, no. 5 (September 2008): 715–27. <https://doi.org/10.1111/j.1365-2478.2008.00724.x>.

- Charlton, Scott R., and David L. Parkhurst. "Modules Based on the Geochemical Model PHREEQC for Use in Scripting and Programming Languages." *Computers & Geosciences* 37, no. 10 (October 2011): 1653–63. <https://doi.org/10.1016/j.cageo.2011.02.005>.
- Cussler, Edward Lansing, and Edward Lansing Cussler. *Diffusion: Mass Transfer in Fluid Systems*. Cambridge university press, 2009.
- Erfani, Hamidreza, Vahid Joekar-Niasar, and Rouhi Farajzadeh. "Impact of Microheterogeneity on Upscaling Reactive Transport in Geothermal Energy." *ACS Earth and Space Chemistry* 3, no. 9 (2019): 2045–57.
- Frizon, F, S Lorente, J.P Ollivier, and P Thouvenot. "Transport Model for the Nuclear Decontamination of Cementitious Materials." *Computational Materials Science* 27, no. 4 (June 2003): 507–16. [https://doi.org/10.1016/S0927-0256\(03\)00051-X](https://doi.org/10.1016/S0927-0256(03)00051-X).
- Islam, Akand, Aboulghasem Kazemi Nia Korrani, Kamy Sepehrnoori, and Tad Patzek. "Effects of Geochemical Reaction on Double Diffusive Natural Convection of CO<sub>2</sub> in Brine Saturated Geothermal Reservoir." *International Journal of Heat and Mass Transfer* 77 (October 2014): 519–28. <https://doi.org/10.1016/j.ijheatmasstransfer.2014.05.040>.
- Katz, Amitai, and Sam Ben-Yaakov. "Diffusion of Seawater Ions. Part II. The Role of Activity Coefficients and Ion Pairing." *Marine Chemistry* 8, no. 4 (February 1980): 263–80. [https://doi.org/10.1016/0304-4203\(80\)90016-X](https://doi.org/10.1016/0304-4203(80)90016-X).
- Kazemi Nia Korrani, Aboulghasem, Kamy Sepehrnoori, and Mojdeh Delshad. "A Novel Mechanistic Approach for Modeling Low Salinity Water Injection." In *Day 2 Tue, October 01, 2013*, D021S021R007. New Orleans, Louisiana, USA: SPE, 2013. <https://doi.org/10.2118/166523-MS>.
- Kim, Jihoon, Eric Sonnenthal, and Jonny Rutqvist. "A Sequential Implicit Algorithm of Chemo-Thermo-Poro-Mechanics for Fractured Geothermal Reservoirs." *Computers & Geosciences* 76 (March 2015): 59–71. <https://doi.org/10.1016/j.cageo.2014.11.009>.
- Lasaga, Antonio C. "Multicomponent Exchange and Diffusion in Silicates." *Geochimica et Cosmochimica Acta* 43, no. 4 (April 1979): 455–69. [https://doi.org/10.1016/0016-7037\(79\)90158-3](https://doi.org/10.1016/0016-7037(79)90158-3).
- Maineult, Alexis, Yves Bernabé, and Philippe Ackerer. "Detection of Advected Concentration and PH Fronts from Self-Potential Measurements: DETECTION OF CONCENTRATION OR PH FRONTS." *Journal of Geophysical Research: Solid Earth* 110, no. B11 (November 2005). <https://doi.org/10.1029/2005JB003824>.
- Mayer, K. Ulrich, Emil O. Frind, and David W. Blowes. "Multicomponent Reactive Transport Modeling in Variably Saturated Porous Media Using a Generalized Formulation for Kinetically Controlled Reactions: REACTIVE TRANSPORT MODELING IN VARIABLY SATURATED MEDIA." *Water Resources Research* 38, no. 9 (September 2002): 13-1-13–21. <https://doi.org/10.1029/2001WR000862>.
- Muniruzzaman, Muhammad, and Massimo Rolle. "Modeling Multicomponent Ionic Transport in Groundwater with IPhreeqc Coupling: Electrostatic Interactions and Geochemical Reactions in Homogeneous and Heterogeneous Domains." *Advances in Water Resources* 98 (December 2016): 1–15. <https://doi.org/10.1016/j.advwatres.2016.10.013>.
- Parkhurst, David L, Kenneth L Kipp, Peter Engesgaard, and Scott R Charlton. "Phast, a Program for Simulating Ground-Waterflow, Solute Transport, and Multicomponent Geochemical Reactions." *US Geological Survey Techniques and Methods* 6 (2004): A8.

- Parkhurst, David L., and Laurin Wissmeier. "PhreeqcRM: A Reaction Module for Transport Simulators Based on the Geochemical Model PHREEQC." *Advances in Water Resources* 83 (September 2015): 176–89. <https://doi.org/10.1016/j.advwatres.2015.06.001>.
- Post, V. E. A., and H. Prommer. "Multicomponent Reactive Transport Simulation of the Elder Problem: Effects of Chemical Reactions on Salt Plume Development: REACTIVE ELDER PROBLEM." *Water Resources Research* 43, no. 10 (October 2007). <https://doi.org/10.1029/2006WR005630>.
- Prommer, H., D.A. Barry, and C. Zheng. "MODFLOW/MT3DMS-Based Reactive Multicomponent Transport Modeling." *Ground Water* 41, no. 2 (March 2003): 247–57. <https://doi.org/10.1111/j.1745-6584.2003.tb02588.x>.
- Rasouli, Pejman, Carl I. Steefel, K. Ulrich Mayer, and Massimo Rolle. "Benchmarks for Multicomponent Diffusion and Electrochemical Migration." *Computational Geosciences* 19, no. 3 (June 2015): 523–33. <https://doi.org/10.1007/s10596-015-9481-z>.
- Rolle, Massimo, Riccardo Sprocati, Matteo Masi, Biao Jin, and Muhammad Muniruzzaman. "Nernst-Planck-Based Description of Transport, Coulombic Interactions, and Geochemical Reactions in Porous Media: Modeling Approach and Benchmark Experiments." *Water Resources Research* 54, no. 4 (April 2018): 3176–95. <https://doi.org/10.1002/2017WR022344>.
- Rubinstein, Isaak. *Electro-Diffusion of Ions*. SIAM, 1990.
- Spycher, N.F., E.L. Sonnenthal, and J.A. Apps. "Fluid Flow and Reactive Transport around Potential Nuclear Waste Emplacement Tunnels at Yucca Mountain, Nevada." *Journal of Contaminant Hydrology* 62–63 (April 2003): 653–73. [https://doi.org/10.1016/S0169-7722\(02\)00183-3](https://doi.org/10.1016/S0169-7722(02)00183-3).
- Steefel, C. I., and A. C. Lasaga. "A Coupled Model for Transport of Multiple Chemical Species and Kinetic Precipitation/Dissolution Reactions with Application to Reactive Flow in Single Phase Hydrothermal Systems." *American Journal of Science* 294, no. 5 (May 1, 1994): 529–92. <https://doi.org/10.2475/ajs.294.5.529>.
- "User's Guide to PHREEQC (Version 2): A Computer Program for Speciation, Batch-Reaction, One-Dimensional Transport, and Inverse Geochemical Calculations," 1999. <https://doi.org/10.3133/wri994259>.
- Xu, Tianfu, Eric Sonnenthal, Nicolas Spycher, and Karsten Pruess. "TOUGHREACT User's Guide: A Simulation Program for Non-Isothermal Multiphase Reactive Geochemical Transport in Variable Saturated Geologic Media," May 24, 2004. <https://doi.org/10.2172/834237>.

### **Chapter III: A Fourier series solution for transient three-dimensional thermohaline convection in porous enclosures**

- Alavyoon, F. (1993). On natural convection in vertical porous enclosures due to prescribed fluxes of heat and mass at the vertical boundaries. *International Journal of Heat and Mass Transfer*, 36(10), 2479–2498. [https://doi.org/10.1016/S0017-9310\(05\)80188-7](https://doi.org/10.1016/S0017-9310(05)80188-7)
- Babaei, M., & Islam, A. (2018). Convective-Reactive CO<sub>2</sub> Dissolution in Aquifers With Mass Transfer With Immobile Water. *Water Resources Research*, 54(11), 9585–9604. <https://doi.org/10.1029/2018WR023150>
- Bao, T., & Liu, Z. (Leo). (2019). Thermohaline stratification modeling in mine water via double-diffusive convection for geothermal energy recovery from flooded mines. *Applied Energy*, 237, 566–580. <https://doi.org/10.1016/j.apenergy.2019.01.049>
- Bennacer, R., Tobbal, A., Beji, H., & Vasseur, P. (2001). Double diffusive convection in a vertical enclosure filled with anisotropic porous media. *International Journal of Thermal Sciences*, 40(1), 30–41. [https://doi.org/10.1016/S1290-0729\(00\)01185-6](https://doi.org/10.1016/S1290-0729(00)01185-6)
- Bera, P., Pippal, S., & Sharma, A. K. (2014). A thermal non-equilibrium approach on double-diffusive

- natural convection in a square porous-medium cavity. *International Journal of Heat and Mass Transfer*, 78, 1080–1094. <https://doi.org/10.1016/j.ijheatmasstransfer.2014.07.041>
- Brown, P. N., Hindmarsh, A. C., & Petzold, L. R. (1994). Using Krylov Methods in the Solution of Large-Scale Differential-Algebraic Systems. *SIAM Journal on Scientific Computing*, 15(6), 1467–1488. <https://doi.org/10.1137/0915088>
- Cabeza, L. F., Martorell, I., Miró, L., Fernández, A. I., & Barreneche, C. (2015). Introduction to thermal energy storage (TES) systems. In *Advances in Thermal Energy Storage Systems* (pp. 1–28). Elsevier. <https://doi.org/10.1533/9781782420965.1>
- Chamkha, A. J. (2002). Double-diffusive convection in a porous enclosure with cooperating temperature and concentration gradients and heat generation or absorption effects. *Numerical Heat Transfer, Part A: Applications*, 41(1), 65–87. <https://doi.org/10.1080/104077802317221447>
- Cooper, C. A., Glass, R. J., & Tyler, S. W. (2001). Effect of buoyancy ratio on the development of double-diffusive finger convection in a Hele-Shaw Cell. *Water Resources Research*, 37(9), 2323–2332. <https://doi.org/10.1029/2001WR000343>
- De Giorgio, G., Chieco, M., Zuffianò, L., Limoni, P., Sottani, A., Pedron, R., et al. (2018). The Compatibility of Geothermal Power Plants with Groundwater Dependent Ecosystems: The Case of the Cesine Wetland (Southern Italy). *Sustainability*, 10(2), 303. <https://doi.org/10.3390/su10020303>
- Evans, D. G., Nunn, J. A., & Hanor, J. S. (1991). Mechanisms driving groundwater flow near salt domes. *Geophysical Research Letters*, 18(5), 927–930. <https://doi.org/10.1029/91GL00908>
- Fahs, M., Younes, A., & Mara, T. A. (2014). A new benchmark semi-analytical solution for density-driven flow in porous media. *Advances in Water Resources*, 70, 24–35. <https://doi.org/10.1016/j.advwatres.2014.04.013>
- Fahs, M., Younes, A., & Makradi, A. (2015). A Reference Benchmark Solution for Free Convection in A Square Cavity Filled with A Heterogeneous Porous Medium. *Numerical Heat Transfer, Part B: Fundamentals*, 67(5), 437–462. <https://doi.org/10.1080/10407790.2014.977183>
- Fahs, M., Ataie-Ashtiani, B., Younes, A., Simmons, C. T., & Ackerer, P. (2016). The Henry problem: New semianalytical solution for velocity-dependent dispersion. *Water Resources Research*, 52(9), 7382–7407. <https://doi.org/10.1002/2016WR019288>
- Guerrero-Martínez, F. J., Younger, P. L., Karimi, N., & Kyriakis, S. (2017). Three-dimensional numerical simulations of free convection in a layered porous enclosure. *International Journal of Heat and Mass Transfer*, 106, 1005–1013. <https://doi.org/10.1016/j.ijheatmasstransfer.2016.10.072>
- Hadidi, N., & Bennacer, R. (2018a). Heat and mass transfer by natural convection in a bi-layered cubic enclosure with opposing temperature and concentration gradients. *International Journal of Thermal Sciences*, 132, 534–551. <https://doi.org/10.1016/j.ijthermalsci.2018.06.013>
- Hadidi, N., & Bennacer, R. (2018b). Heat and mass transfer by natural convection in a bi-layered cubic enclosure with opposing temperature and concentration gradients. *International Journal of Thermal Sciences*, 132, 534–551. <https://doi.org/10.1016/j.ijthermalsci.2018.06.013>
- Henry, H. R. (1964). Effects of dispersion on salt encroachment in coastal aquifers, 1613–C, 70–84.
- Hughes, J. D., Sanford, W. E., & Vacher, H. L. (2005). Numerical simulation of double-diffusive finger convection. *Water Resources Research*, 41(1). <https://doi.org/10.1029/2003WR002777>
- Islam, A. W., Sharif, M. A. R., & Carlson, E. S. (2013). Numerical investigation of double diffusive natural convection of CO<sub>2</sub> in a brine saturated geothermal reservoir. *Geothermics*, 48, 101–111. <https://doi.org/10.1016/j.geothermics.2013.07.001>
- Islam, A. W., Lashgari, H. R., & Sefernoori, K. (2014). Double diffusive natural convection of CO<sub>2</sub> in a brine saturated geothermal reservoir: Study of non-modal growth of perturbations and heterogeneity effects. *Geothermics*, 51, 325–336. <https://doi.org/10.1016/j.geothermics.2014.03.001>
- Jafari Raad, S. M., Hassanzadeh, H., & Ennis-King, J. (2019). On the Dynamics of Two-Component Convective Dissolution in Porous Media. *Water Resources Research*, 2018WR024572. <https://doi.org/10.1029/2018WR024572>
- Jamshidzadeh, Z., Tsai, F. T.-C., Mirbagheri, S. A., & Ghasemzadeh, H. (2013). Fluid dispersion effects on density-driven thermohaline flow and transport in porous media. *Advances in Water Resources*, 61, 12–28. <https://doi.org/10.1016/j.advwatres.2013.08.006>

- Jamshidzadeh, Z., Tsai, F. T.-C., Ghasemzadeh, H., Mirbagheri, S. A., Barzi, M. T., & Hanor, J. S. (2015). Dispersive thermohaline convection near salt domes: a case at Napoleonville Dome, southeast Louisiana, USA. *Hydrogeology Journal*, 23(5), 983–998. <https://doi.org/10.1007/s10040-015-1251-4>
- Javaheri, M., Abedi, J., & Hassanzadeh, H. (2010). Linear Stability Analysis of Double-Diffusive Convection in Porous Media, with Application to Geological Storage of CO<sub>2</sub>. *Transport in Porous Media*, 84(2), 441–456. <https://doi.org/10.1007/s11242-009-9513-z>
- Kalla, L., Vasseur, P., Benacer, R., Beji, H., & Duval, R. (2001). Double diffusive convection within a horizontal porous layer salted from the bottom and heated horizontally. *International Communications in Heat and Mass Transfer*, 28(1), 1–10. [https://doi.org/10.1016/S0735-1933\(01\)00207-X](https://doi.org/10.1016/S0735-1933(01)00207-X)
- Khadiri, A., Amahmid, A., Hasnaoui, M., & Rtibi, A. (2010). Soret Effect on Double-Diffusive Convection in a Square Porous Cavity Heated and Salted from Below. *Numerical Heat Transfer, Part A: Applications*, 57(11), 848–868. <https://doi.org/10.1080/10407782.2010.489487>
- Koohbor, B., Fahs, M., Ataie-Ashtiani, B., Simmons, C. T., & Younes, A. (2018). Semianalytical solutions for contaminant transport under variable velocity field in a coastal aquifer. *Journal of Hydrology*, 560, 434–450. <https://doi.org/10.1016/j.jhydrol.2018.03.048>
- Langevin, C. D., Dausman, A. M., & Sukop, M. C. (2010). Solute and Heat Transport Model of the Henry and Hilleke Laboratory Experiment. *Ground Water*, 48(5), 757–770. <https://doi.org/10.1111/j.1745-6584.2009.00596.x>
- Le Lous, M., Larroque, F., Dupuy, A., & Moignard, A. (2015). Thermal performance of a deep borehole heat exchanger: Insights from a synthetic coupled heat and flow model. *Geothermics*, 57, 157–172. <https://doi.org/10.1016/j.geothermics.2015.06.014>
- Li, S., & Petzold, L. (1999). *Design of new DASPCK for sensitivity analysis* (Handbook of Systemic Autoimmune Diseases). Retrieved from [https://www.researchgate.net/publication/2626137\\_Design\\_of\\_new\\_DASPCK\\_for\\_sensitivity\\_analysis/citations](https://www.researchgate.net/publication/2626137_Design_of_new_DASPCK_for_sensitivity_analysis/citations)
- van Lopik, J. H., Hartog, N., Zaadnoordijk, W. J., Cirkel, D. G., & Raouf, A. (2015). Salinization in a stratified aquifer induced by heat transfer from well casings. *Advances in Water Resources*, 86, 32–45. <https://doi.org/10.1016/j.advwatres.2015.09.025>
- Love, A. J., Simmons, C. T., & Nield, D. A. (2007). Double-diffusive convection in groundwater wells. *Water Resources Research*, 43(8). <https://doi.org/10.1029/2007WR006001>
- Magri, F., Akar, T., Gemici, U., & Pekdeger, A. (2012). Numerical investigations of fault-induced seawater circulation in the Seferihisar-Balçova Geothermal system, western Turkey. *Hydrogeology Journal*, 20(1), 103–118. <https://doi.org/10.1007/s10040-011-0797-z>
- Mansour, A., Amahmid, A., Hasnaoui, M., & Bourich, M. (2006). Multiplicity of Solutions Induced by Thermosolutal Convection in a Square Porous Cavity Heated from Below and Submitted to Horizontal Concentration Gradient in the Presence of Soret Effect. *Numerical Heat Transfer, Part A: Applications*, 49(1), 69–94. <https://doi.org/10.1080/10407780500302166>
- Masuda, Y., Yoneya, M., & Kimura, S. (2013). Multiple Solutions of Double-Diffusive Convection in Porous Media due to Opposing Heat and Mass Fluxes on Vertical Walls. *Journal of Thermal Science and Technology*, 8(3), 533–542. <https://doi.org/10.1299/jtst.8.533>
- Mchirgui, A., Hidouri, N., Magherbi, M., & Brahim, A. B. (2012). Entropy Generation in Double-Diffusive Convection in a Square Porous Cavity using Darcy–Brinkman Formulation. *Transport in Porous Media*, 93(1), 223–240. <https://doi.org/10.1007/s11242-012-9954-7>
- Mohamad, A.A., & Bennacer, R. (2002). Double diffusion, natural convection in an enclosure filled with saturated porous medium subjected to cross gradients; stably stratified fluid. *International Journal of Heat and Mass Transfer*, 45(18), 3725–3740. [https://doi.org/10.1016/S0017-9310\(02\)00093-5](https://doi.org/10.1016/S0017-9310(02)00093-5)
- Mohamad, Abdulmajeed A., & Bennacer, R. (2001). Natural convection in a confined saturated porous medium with horizontal temperature and vertical solutal gradients. *International Journal of Thermal Sciences*, 40(1), 82–93. [https://doi.org/10.1016/S1290-0729\(00\)01182-0](https://doi.org/10.1016/S1290-0729(00)01182-0)
- Musuuza, J. L., Radu, F. A., & Attinger, S. (2012). Predicting predominant thermal convection in thermohaline flows in saturated porous media. *Advances in Water Resources*, 49, 23–36. <https://doi.org/10.1016/j.advwatres.2012.07.020>

- Navelot, V., Géraud, Y., Favier, A., Diraison, M., Corsini, M., Lardeaux, J.-M., et al. (2018). Petrophysical properties of volcanic rocks and impacts of hydrothermal alteration in the Guadeloupe Archipelago (West Indies). *Journal of Volcanology and Geothermal Research*, 360, 1–21. <https://doi.org/10.1016/j.jvolgeores.2018.07.004>
- Nield, D. A., & Kuznetsov, A. V. (2013). The Effect of Heterogeneity on the Onset of Double-Diffusive Convection Induced by Internal Heating in a Porous Medium: A Layered Model. *Transport in Porous Media*, 100(1), 83–99. <https://doi.org/10.1007/s11242-013-0206-2>
- Nield, D. A., Simmons, C. T., Kuznetsov, A. V., & Ward, J. D. (2008). On the evolution of salt lakes: Episodic convection beneath an evaporating salt lake. *Water Resources Research*, 44(2). <https://doi.org/10.1029/2007WR006161>
- Peyret, R. (2013). *Spectral Methods for Incompressible Viscous Flow*. New York, NY: Springer.
- Post, V., & Abarca, E. (2010). Preface: Saltwater and freshwater interactions in coastal aquifers. *Hydrogeology Journal*, 18(1), 1–4. <https://doi.org/10.1007/s10040-009-0561-9>
- van Reeuwijk, M., Mathias, S. A., Simmons, C. T., & Ward, J. D. (2009). Insights from a pseudospectral approach to the Elder problem: PSEUDOSPECTRAL APPROACH TO THE ELDER PROBLEM. *Water Resources Research*, 45(4). <https://doi.org/10.1029/2008WR007421>
- Schilling, O., Sheldon, H. A., Reid, L. B., & Corbel, S. (2013). Hydrothermal models of the Perth metropolitan area, Western Australia: implications for geothermal energy. *Hydrogeology Journal*, 21(3), 605–621. <https://doi.org/10.1007/s10040-012-0945-0>
- Segol, G. (1994). *Classic groundwater simulations: proving and improving numerical models*. Englewood Cliffs, N.J: PTR Prentice Hall.
- Sezai, I., & Mohamad, A. A. (1999). Three-dimensional double-diffusive convection in a porous cubic enclosure due to opposing gradients of temperature and concentration. *Journal of Fluid Mechanics*, 400, 333–353. <https://doi.org/10.1017/S0022112099006540>
- Shao, Q., Fahs, M., Younes, A., & Makradi, A. (2016). A high-accurate solution for Darcy-Brinkman double-diffusive convection in saturated porous media. *Numerical Heat Transfer, Part B: Fundamentals*, 69(1), 26–47. <https://doi.org/10.1080/10407790.2015.1081044>
- Shao, Q., Fahs, M., Younes, A., Makradi, A., & Mara, T. (2016). A new benchmark reference solution for double-diffusive convection in a heterogeneous porous medium. *Numerical Heat Transfer, Part B: Fundamentals*, 70(5), 373–392. <https://doi.org/10.1080/10407790.2016.1215718>
- Shao, Q., Fahs, M., Hoteit, H., Carrera, J., Ackerer, P., & Younes, A. (2018). A 3-D Semianalytical Solution for Density-Driven Flow in Porous Media. *Water Resources Research*, 54(12). <https://doi.org/10.1029/2018WR023583>
- Sheldon, H. A., Florio, B., Trefry, M. G., Reid, L. B., Ricard, L. P., & Ghori, K. A. R. (2012). The potential for convection and implications for geothermal energy in the Perth Basin, Western Australia. *Hydrogeology Journal*, 20(7), 1251–1268. <https://doi.org/10.1007/s10040-012-0886-7>
- Simpson, Matthew J., & Clement, T. P. (2004). Improving the worthiness of the Henry problem as a benchmark for density-dependent groundwater flow models: IMPROVING THE HENRY PROBLEM. *Water Resources Research*, 40(1). <https://doi.org/10.1029/2003WR002199>
- Simpson, M.J., & Clement, T. P. (2003). Theoretical analysis of the worthiness of Henry and Elder problems as benchmarks of density-dependent groundwater flow models. *Advances in Water Resources*, 26(1), 17–31. [https://doi.org/10.1016/S0309-1708\(02\)00085-4](https://doi.org/10.1016/S0309-1708(02)00085-4)
- Sivasankaran, S., Kandaswamy, P., & Ng, C. O. (2008). Double diffusive convection of anomalous density fluids in a porous cavity. *Transport in Porous Media*, 71(2), 133–145. <https://doi.org/10.1007/s11242-007-9114-7>
- Stajniko, J. K., Ravník, J., & Jecl, R. (2017). Numerical simulation of three-dimensional double-diffusive natural convection in porous media by boundary element method. *Engineering Analysis with Boundary Elements*, 76, 69–79. <https://doi.org/10.1016/j.enganabound.2016.12.007>
- Thorne, D., Langevin, C. D., & Sukop, M. C. (2006). Addition of simultaneous heat and solute transport and variable fluid viscosity to SEAWAT. *Computers & Geosciences*, 32(10), 1758–1768. <https://doi.org/10.1016/j.cageo.2006.04.005>
- Trevisan, O. V., & Bejan, A. (1986). Mass and heat transfer by natural convection in a vertical slot filled with porous medium. *International Journal of Heat and Mass Transfer*, 29(3), 403–415. [https://doi.org/10.1016/0017-9310\(86\)90210-3](https://doi.org/10.1016/0017-9310(86)90210-3)

- Vafai, K. (Ed.). (2015). Handbook of porous media (Third edition). Boca Raton: CRC Press, Taylor & Francis Group.
- Voss, C. I., Simmons, C. T., & Robinson, N. I. (2010). Three-dimensional benchmark for variable-density flow and transport simulation: matching semi-analytic stability modes for steady unstable convection in an inclined porous box. *Hydrogeology Journal*, 18(1), 5–23. <https://doi.org/10.1007/s10040-009-0556-6>
- Yilmaz Turali, E., & Simsek, S. (2017). Conceptual and 3D simulation modeling of the Sorgun hydrothermal reservoir (Yozgat,Turkey). *Geothermics*, 66, 85–100. <https://doi.org/10.1016/j.geothermics.2016.11.012>
- Younes, A., Fahs, M., & Ackerer, P. (2007). A new approach to avoid excessive numerical diffusion in Eulerian-Lagrangian methods. *Communications in Numerical Methods in Engineering*, 24(11), 897–910. <https://doi.org/10.1002/cnm.996>
- Younes, A., & Fahs, M. (2014). A semi-analytical solution for saltwater intrusion with a very narrow transition zone. *Hydrogeology Journal*, 22(2), 501–506. <https://doi.org/10.1007/s10040-014-1102-8>
- Younes, A., & Fahs, M. (2015). Extension of the Henry semi-analytical solution for saltwater intrusion in stratified domains. *Computational Geosciences*, 19(6), 1207–1217. <https://doi.org/10.1007/s10596-015-9534-3>
- Zechner, E., Dresmann, H., Mocuța, M., Danchiv, A., Huggenberger, P., Scheidler, S., et al. (2019). Salt dissolution potential estimated from two-dimensional vertical thermohaline flow and transport modeling along a Transylvanian salt diapir, Romania. *Hydrogeology Journal*, 27(4), 1245–1256. <https://doi.org/10.1007/s10040-018-1912-1>
- Zhu, Q. Y., Zhuang, Y. J., & Yu, H. Z. (2017). Entropy generation due to three-dimensional double-diffusive convection of power-law fluids in heterogeneous porous media. *International Journal of Heat and Mass Transfer*, 106, 61–82. <https://doi.org/10.1016/j.ijheatmasstransfer.2016.10.050>
- Zidane, A., Younes, A., Huggenberger, P., & Zechner, E. (2012). The Henry semianalytical solution for saltwater intrusion with reduced dispersion. *Water Resources Research*, 48(6). <https://doi.org/10.1029/2011WR011157>

#### **Chapter IV: Robust numerical model for reactive-thermohaline convection of CO<sub>2</sub> in brine saturated reservoir**

- Ahmadinia, M., Shariatipour, S.M., Andersen, O., Nobakht, B., 2020. Quantitative evaluation of the joint effect of uncertain parameters in CO<sub>2</sub> storage in the Sleipner project, using data-driven models. *International Journal of Greenhouse Gas Control* 103, 103180. <https://doi.org/10.1016/j.ijggc.2020.103180>
- Andres, J.T.H., Cardoso, S.S.S., 2011. Onset of convection in a porous medium in the presence of chemical reaction. *Phys. Rev. E* 83, 046312. <https://doi.org/10.1103/PhysRevE.83.046312>
- Babaei, M., Islam, A., 2018. Convective-Reactive CO<sub>2</sub> Dissolution in Aquifers With Mass Transfer With Immobile Water. *Water Resour. Res.* 54, 9585–9604. <https://doi.org/10.1029/2018WR023150>
- Battle, F., Carrera, J., Ayora, C., 2002. A comparison of lagrangian and eulerian formulations for reactive transport modelling, in: *Developments in Water Science*. Elsevier, pp. 571–578. [https://doi.org/10.1016/S0167-5648\(02\)80110-1](https://doi.org/10.1016/S0167-5648(02)80110-1)

- Boudreau, B.P., Sulpis, O., Mucci, A., 2020. Control of CaCO<sub>3</sub> dissolution at the deep seafloor and its consequences. *Geochimica et Cosmochimica Acta* 268, 90–106. <https://doi.org/10.1016/j.gca.2019.09.037>
- Chen, Z., Wu, Y.-P., Feng, G.-L., Qian, Z.-H., Sun, G.-Q., 2021. Effects of global warming on pattern dynamics of vegetation: Wuwei in China as a case. *Applied Mathematics and Computation* 390, 125666. <https://doi.org/10.1016/j.amc.2020.125666>
- Collins, M., Knutti, R., Arblaster, J., Dufresne, J.-L., Fichet, T., Friedlingstein, P., Gao, X., Gutowski, W.J., Johns, T., Krinner, G., 2013. Long-term climate change: projections, commitments and irreversibility, in: *Climate Change 2013-The Physical Science Basis: Contribution of Working Group I to the Fifth Assessment Report of the Intergovernmental Panel on Climate Change*. Cambridge University Press, pp. 1029–1136.
- Emami-Meybodi, H., Hassanzadeh, H., Green, C.P., Ennis-King, J., 2015. Convective dissolution of CO<sub>2</sub> in saline aquifers: Progress in modeling and experiments. *International Journal of Greenhouse Gas Control* 40, 238–266. <https://doi.org/10.1016/j.ijggc.2015.04.003>
- Erfani, H., Babaei, M., Niasar, V., 2020. Signature of Geochemistry on Density-Driven CO<sub>2</sub> Mixing in Sandstone Aquifers. *Water Resour. Res.* 56. <https://doi.org/10.1029/2019WR026060>
- Fahs, M., Ataie-Ashtiani, B., Younes, A., Simmons, C.T., Ackerer, P., 2016. The Henry problem: New semianalytical solution for velocity-dependent dispersion: NEW SEMIANALYTICAL SOLUTION FOR HENRY PROBLEM. *Water Resour. Res.* 52, 7382–7407. <https://doi.org/10.1002/2016WR019288>
- Fahs, M., Carrayrou, J., Younes, A., Ackerer, P., 2008. On the Efficiency of the Direct Substitution Approach for Reactive Transport Problems in Porous Media. *Water Air Soil Pollut* 193, 299–308. <https://doi.org/10.1007/s11270-008-9691-2>
- Fahs, M., Younes, A., Delay, F., 2009. On the use of large time steps with ELLAM for transport with kinetic reactions over heterogeneous domains. *AIChE J.* 55, 1121–1126. <https://doi.org/10.1002/aic.11727>
- Farajzadeh, R., Ranganathan, P., Zitha, P.L.J., Bruining, J., 2011. The effect of heterogeneity on the character of density-driven natural convection of CO<sub>2</sub> overlying a brine layer. *Advances in Water Resources* 34, 327–339. <https://doi.org/10.1016/j.advwatres.2010.12.012>
- Ghesmat, K., Hassanzadeh, H., Abedi, J., 2011. The impact of geochemistry on convective mixing in a gravitationally unstable diffusive boundary layer in porous media: CO<sub>2</sub> storage in saline aquifers. *J. Fluid Mech.* 673, 480–512. <https://doi.org/10.1017/S0022112010006282>

- Ghoshal, P., Kim, M.C., Cardoso, S.S.S., 2017. Reactive–convective dissolution in a porous medium: the storage of carbon dioxide in saline aquifers. *Phys. Chem. Chem. Phys.* 19, 644–655. <https://doi.org/10.1039/C6CP06010B>
- Hamann, E., Post, V., Kohfahl, C., Prommer, H., Simmons, C.T., 2015. Numerical investigation of coupled density-driven flow and hydrogeochemical processes below playas. *Water Resour. Res.* 51, 9338–9352. <https://doi.org/10.1002/2015WR017833>
- Hewitt, D.R., Neufeld, J.A., Lister, J.R., 2014. High Rayleigh number convection in a three-dimensional porous medium. *J. Fluid Mech.* 748, 879–895. <https://doi.org/10.1017/jfm.2014.216>
- Hidalgo, J.J., Carrera, J., 2009. Effect of dispersion on the onset of convection during CO<sub>2</sub> sequestration. *J. Fluid Mech.* 640, 441–452. <https://doi.org/10.1017/S0022112009991480>
- Hidalgo, J.J., Dentz, M., Cabeza, Y., Carrera, J., 2015. Dissolution patterns and mixing dynamics in unstable reactive flow: MIXING IN UNSTABLE REACTIVE FLOW. *Geophys. Res. Lett.* 42, 6357–6364. <https://doi.org/10.1002/2015GL065036>
- Hirthe, E.M., Graf, T., 2012. Non-iterative adaptive time-stepping scheme with temporal truncation error control for simulating variable-density flow. *Advances in Water Resources* 49, 46–55. <https://doi.org/10.1016/j.advwatres.2012.07.021>
- Hoteit, H., Fahs, M., Soltanian, M.R., 2019. Assessment of CO<sub>2</sub> Injectivity During Sequestration in Depleted Gas Reservoirs. *Geosciences* 9, 199. <https://doi.org/10.3390/geosciences9050199>
- Hoteit, H., Firoozabadi, A., 2018. Modeling of multicomponent diffusions and natural convection in unfractured and fractured media by discontinuous Galerkin and mixed methods: Modeling of multicomponent diffusions and natural convection. *Int J Numer Methods Eng* 114, 535–556. <https://doi.org/10.1002/nme.5753>
- Hoteit, H., Firoozabadi, A., 2008. Numerical modeling of two-phase flow in heterogeneous permeable media with different capillarity pressures. *Advances in Water Resources* 31, 56–73. <https://doi.org/10.1016/j.advwatres.2007.06.006>
- IPCC. (2019)., n.d.
- Islam, A.W., Lashgari, H.R., Sephernoori, K., 2014a. Double diffusive natural convection of CO<sub>2</sub> in a brine saturated geothermal reservoir: Study of non-modal growth of perturbations and heterogeneity effects. *Geothermics* 51, 325–336. <https://doi.org/10.1016/j.geothermics.2014.03.001>
- Islam, A., Korrani, A.K.N., Sephernoori, K., Patzek, T., 2014b. Effects of geochemical reaction on double diffusive natural convection of CO<sub>2</sub> in brine saturated geothermal reservoir. *International Journal of Heat and Mass Transfer* 77, 519–528. <https://doi.org/10.1016/j.ijheatmasstransfer.2014.05.040>

- Islam, A.W., Sharif, M.A.R., Carlson, E.S., 2013. Numerical investigation of double diffusive natural convection of CO<sub>2</sub> in a brine saturated geothermal reservoir. *Geothermics* 48, 101–111. <https://doi.org/10.1016/j.geothermics.2013.07.001>
- Jiang, X., 2011. A review of physical modelling and numerical simulation of long-term geological storage of CO<sub>2</sub>. *Applied Energy* 88, 3557–3566. <https://doi.org/10.1016/j.apenergy.2011.05.004>
- Kim, M., Kim, K., Han, W.S., Oh, J., Park, E., 2019. Density-Driven Convection in a Fractured Porous Media: Implications for Geological CO<sub>2</sub> Storage. *Water Resour. Res.* 55, 5852–5870. <https://doi.org/10.1029/2019WR024822>
- Koohbor, B., Fahs, M., Hoteit, H., Doummar, J., Younes, A., Belfort, B., 2020. An advanced discrete fracture model for variably saturated flow in fractured porous media. *Advances in Water Resources* 140, 103602. <https://doi.org/10.1016/j.advwatres.2020.103602>
- Lu, C., Han, W.S., Lee, S.-Y., McPherson, B.J., Lichtner, P.C., 2009. Effects of density and mutual solubility of a –brine system on storage in geological formations: “Warm” vs. “cold” formations. *Advances in Water Resources* 32, 1685–1702. <https://doi.org/10.1016/j.advwatres.2009.07.008>
- Masson-Delmotte, V., Zhai, P., Pörtner, H.-O., Roberts, D., Skea, J., Shukla, P.R., Pirani, A., Moufouma-Okia, W., Péan, C., Pidcock, R., 2018. Global warming of 1.5 C. An IPCC Special Report on the impacts of global warming of 1.
- Miller, C.T., Dawson, C.N., Farthing, M.W., Hou, T.Y., Huang, J., Kees, C.E., Kelley, C.T., Langtangen, H.P., 2013. Numerical simulation of water resources problems: Models, methods, and trends. *Advances in Water Resources* 51, 405–437. <https://doi.org/10.1016/j.advwatres.2012.05.008>
- Moortgat, J., 2017. Adaptive implicit finite element methods for multicomponent compressible flow in heterogeneous and fractured porous media: AIM FOR HETEROGENEOUS FRACTURED MEDIA. *Water Resour. Res.* 53, 73–92. <https://doi.org/10.1002/2016WR019644>
- Moortgat, J., Amooie, M.A., Soltanian, M.R., 2016. Implicit finite volume and discontinuous Galerkin methods for multicomponent flow in unstructured 3D fractured porous media. *Advances in Water Resources* 96, 389–404. <https://doi.org/10.1016/j.advwatres.2016.08.007>
- Nordbotten, J.M., Celia, M.A., 2011. *Geological Storage of CO<sub>2</sub>: Modeling Approaches for Large-Scale Simulation*. John Wiley & Sons, Inc., Hoboken, NJ, USA. <https://doi.org/10.1002/9781118137086>
- Omar, A., Addassi, M., Vahrenkamp, V., Hoteit, H., 2021. Co-Optimization of CO<sub>2</sub> Storage and Enhanced Gas Recovery Using Carbonated Water and Supercritical CO<sub>2</sub>. *Energies* 14, 7495. <https://doi.org/10.3390/en14227495>

- Petrou, A.L., 2012. The Free Energy of Activation as the critical factor in geochemical processes. *Chemical Geology* 308–309, 50–59. <https://doi.org/10.1016/j.chemgeo.2012.03.015>
- Prasad, A., Simmons, C.T., 2005. Using quantitative indicators to evaluate results from variable-density groundwater flow models. *Hydrogeol J* 13, 905–914. <https://doi.org/10.1007/s10040-004-0338-0>
- Raeisi Isa-Abadi, A., Fontaine, V., Ghafouri, H.-R., Younes, A., Fahs, M., 2020. A fully interior penalty discontinuous Galerkin method for variable density groundwater flow problems. *Computers & Fluids* 213, 104744. <https://doi.org/10.1016/j.compfluid.2020.104744>
- Rajabi, M.M., Fahs, M., Panjehfouladgaran, A., Ataie-Ashtiani, B., Simmons, C.T., Belfort, B., 2020. Uncertainty quantification and global sensitivity analysis of double-diffusive natural convection in a porous enclosure. *International Journal of Heat and Mass Transfer* 162, 120291. <https://doi.org/10.1016/j.ijheatmasstransfer.2020.120291>
- Riaz, A., Hesse, M., Tchelepi, H.A., Orr, F.M., 2006. Onset of convection in a gravitationally unstable diffusive boundary layer in porous media. *J. Fluid Mech.* 548, 87. <https://doi.org/10.1017/S0022112005007494>
- Sainz-Garcia, A., Abarca, E., Nardi, A., Grandia, F., Oelkers, E.H., 2017. Convective mixing fingers and chemistry interaction in carbon storage. *International Journal of Greenhouse Gas Control* 58, 52–61. <https://doi.org/10.1016/j.ijggc.2016.12.005>
- Sanjuan, B., Girard, J., 1996. Review of Kinetic Data on Carbonate Mineral Precipitation: BRGM Report R39062. Orléans: BRGM.
- Sathaye, K.J., Hesse, M.A., Cassidy, M., Stockli, D.F., 2014. Constraints on the magnitude and rate of CO<sub>2</sub> dissolution at Bravo Dome natural gas field. *Proceedings of the National Academy of Sciences* 111, 15332–15337. <https://doi.org/10.1073/pnas.1406076111>
- Shafabakhsh, P., Ataie-Ashtiani, B., Simmons, C.T., Younes, A., Fahs, M., 2021. Convective-reactive transport of dissolved CO<sub>2</sub> in fractured-geological formations. *International Journal of Greenhouse Gas Control* 109, 103365. <https://doi.org/10.1016/j.ijggc.2021.103365>
- Shao, Q., Fahs, M., Hoteit, H., Carrera, J., Ackerer, P., Younes, A., 2018. A 3-D Semianalytical Solution for Density-Driven Flow in Porous Media. *Water Resour. Res.* 54. <https://doi.org/10.1029/2018WR023583>
- Shi, X., Chen, J., Gu, L., Xu, C.-Y., Chen, H., Zhang, L., 2020. Impacts and socioeconomic exposures of global extreme precipitation events in 1.5 and 2.0 °C warmer climates. *Science of The Total Environment* 142665. <https://doi.org/10.1016/j.scitotenv.2020.142665>

- Sigfusson, B., Gislason, S.R., Matter, J.M., Stute, M., Gunnlaugsson, E., Gunnarsson, I., Aradottir, E.S., Sigurdardottir, H., Mesfin, K., Alfredsson, H.A., 2015. Solving the carbon-dioxide buoyancy challenge: The design and field testing of a dissolved CO<sub>2</sub> injection system. *International Journal of Greenhouse Gas Control* 37, 213–219.
- Singh, H., Islam, A., 2018. Enhanced safety of geologic CO<sub>2</sub> storage with nanoparticles. *International Journal of Heat and Mass Transfer* 121, 463–476. <https://doi.org/10.1016/j.ijheatmasstransfer.2017.12.152>
- Sjöberg, E.L., Rickard, D.T., 1984. Temperature dependence of calcite dissolution kinetics between 1 and 62°C at pH 2.7 to 8.4 in aqueous solutions. *Geochimica et Cosmochimica Acta* 48, 485–493. [https://doi.org/10.1016/0016-7037\(84\)90276-X](https://doi.org/10.1016/0016-7037(84)90276-X)
- Soltanian, M.R., Amooie, M.A., Gershenson, N., Dai, Z., Ritzi, R., Xiong, F., Cole, D., Moortgat, J., 2017. Dissolution Trapping of Carbon Dioxide in Heterogeneous Aquifers. *Environ. Sci. Technol.* 51, 7732–7741. <https://doi.org/10.1021/acs.est.7b01540>
- Soltanian, M.R., Hajirezaie, S., Hosseini, S.A., Dashtian, H., Amooie, M.A., Meyal, A., Ershadnia, R., Ampomah, W., Islam, A., Zhang, X., 2019. Multicomponent reactive transport of carbon dioxide in fluvial heterogeneous aquifers. *Journal of Natural Gas Science and Engineering* 65, 212–223. <https://doi.org/10.1016/j.jngse.2019.03.011>
- Tabrizinejadas, S., Fahs, M., Ataie-Ashtiani, B., Simmons, C.T., Chiara Roupert, R., Younes, A., 2020. A Fourier Series Solution for Transient Three-Dimensional Thermohaline Convection in Porous Enclosures. *Water Resour. Res.* 56. <https://doi.org/10.1029/2020WR028111>
- UNFCCC, D., 2015. 1/CP. 21, Adoption of the Paris Agreement. UN Doc. FCCC/CP/2015/10/Add. 1.
- van Reeuwijk, M., Mathias, S.A., Simmons, C.T., Ward, J.D., 2009. Insights from a pseudospectral approach to the Elder problem: PSEUDOSPECTRAL APPROACH TO THE ELDER PROBLEM. *Water Resour. Res.* 45. <https://doi.org/10.1029/2008WR007421>
- Voss, C.I., Simmons, C.T., Robinson, N.I., 2010. Three-dimensional benchmark for variable-density flow and transport simulation: matching semi-analytic stability modes for steady unstable convection in an inclined porous box. *Hydrogeol J* 18, 5–23. <https://doi.org/10.1007/s10040-009-0556-6>
- Wang, X., Yang, Y., Dong, Z., Zhang, C., 2009. Responses of dune activity and desertification in China to global warming in the twenty-first century. *Global and Planetary Change* 67, 167–185. <https://doi.org/10.1016/j.gloplacha.2009.02.004>
- Whitley, S., 2018. G7 fossil fuel subsidy scorecard: Tracking the phase-out of fiscal support and public finance for oil, gas and coal. International Institute for Sustainable Development.

Wu, Y., Li, P., 2020. The potential of coupled carbon storage and geothermal extraction in a CO<sub>2</sub>-enhanced geothermal system: a review. *Geotherm Energy* 8, 19. <https://doi.org/10.1186/s40517-020-00173-w>

Xie, Y., Simmons, C.T., Werner, A.D., Diersch, H.-J.G., 2012. Prediction and uncertainty of free convection phenomena in porous media: PREDICTION OF FREE CONVECTION PHENOMENA IN POROUS MEDIA. *Water Resour. Res.* 48. <https://doi.org/10.1029/2011WR011346>

Xu, R., Li, R., Ma, J., He, D., Jiang, P., 2017. Effect of mineral dissolution/precipitation and CO<sub>2</sub> exsolution on CO<sub>2</sub> transport in geological carbon storage. *Accounts of chemical research* 50, 2056–2066.

Younes, A., Ackerer, P., 2010. Empirical versus time stepping with embedded error control for density-driven flow in porous media: TIME STEP MANAGEMENT FOR DENSITY-DRIVEN FLOW. *Water Resour. Res.* 46. <https://doi.org/10.1029/2009WR008229>

Younes, A., Ackerer, P., Delay, F., 2010. Mixed finite elements for solving 2-D diffusion-type equations. *Rev. Geophys.* 48, RG1004. <https://doi.org/10.1029/2008RG000277>

Younes, A., Fahs, M., Ahmed, S., 2009. Solving density driven flow problems with efficient spatial discretizations and higher-order time integration methods. *Advances in Water Resources* 32, 340–352. <https://doi.org/10.1016/j.advwatres.2008.11.003>

Younes, A., Fahs, M., Belfort, B., 2013. Monotonicity of the cell-centred triangular MPFA method for saturated and unsaturated flow in heterogeneous porous media. *Journal of Hydrology* 504, 132–141. <https://doi.org/10.1016/j.jhydrol.2013.09.041>

Zhang, D., Song, J., 2014. Mechanisms for Geological Carbon Sequestration. *Procedia IUTAM* 10, 319–327. <https://doi.org/10.1016/j.piutam.2014.01.027>

Zhang, Z., Huisingsh, D., 2017. Carbon dioxide storage schemes: technology, assessment and deployment. *Journal of Cleaner Production* 142, 1055–1064.

## **Chapter V: Modelling dissolution processes in discrete fracture networks: an advanced numerical scheme**

Abdullah, Twana O., Salahalddin S. Ali, Nadhir A. Al-Ansari, Sven Knutsson, and Jan Laue. “Magnitude and Direction of Groundwater Seepage Velocity in Different Soil and Rock Materials.” *Engineering* 12, no. 04 (2020): 242–53. <https://doi.org/10.4236/eng.2020.124020>.

Agrawal, Priyanka, Arjen Mascini, Tom Bultreys, Hamed Aslannejad, Mariëtte Wolthers, Veerle Cnudde, Ian B. Butler, and Amir Raoof. “The Impact of Pore-Throat Shape Evolution during Dissolution on

- Carbonate Rock Permeability: Pore Network Modeling and Experiments.” *Advances in Water Resources* 155 (September 2021): 103991. <https://doi.org/10.1016/j.advwatres.2021.103991>.
- Agrawal, Priyanka, Amir Raouf, Oleg Iliev, and Mariëtte Wolthers. “Evolution of Pore-Shape and Its Impact on Pore Conductivity during CO<sub>2</sub> Injection in Calcite: Single Pore Simulations and Microfluidic Experiments.” *Advances in Water Resources* 136 (February 2020): 103480. <https://doi.org/10.1016/j.advwatres.2019.103480>.
- Aliouache, Mohammed, Xiaoguang Wang, Hervé Jourde, Zhaoqin Huang, and Jun Yao. “Incipient Karst Formation in Carbonate Rocks: Influence of Fracture Network Topology.” *Journal of Hydrology* 575 (August 2019): 824–37. <https://doi.org/10.1016/j.jhydrol.2019.05.082>.
- Ameli, Pasha, Jean E. Elkhoury, Joseph P. Morris, and Russell L. Detwiler. “Fracture Permeability Alteration Due to Chemical and Mechanical Processes: A Coupled High-Resolution Model.” *Rock Mechanics and Rock Engineering* 47, no. 5 (September 2014): 1563–73. <https://doi.org/10.1007/s00603-014-0575-z>.
- Barton, Colleen A., and Mark D. Zoback. “Self-Similar Distribution and Properties of Macroscopic Fractures at Depth in Crystalline Rock in the Cajon Pass Scientific Drill Hole.” *Journal of Geophysical Research* 97, no. B4 (1992): 5181. <https://doi.org/10.1029/91JB01674>.
- Brown, Peter N., Alan C. Hindmarsh, and Linda R. Petzold. “Using Krylov Methods in the Solution of Large-Scale Differential-Algebraic Systems.” *SIAM Journal on Scientific Computing* 15, no. 6 (November 1994): 1467–88. <https://doi.org/10.1137/0915088>.
- Deng, Hang, and Nicolas Spycher. “Modeling Reactive Transport Processes in Fractures.” *Reviews in Mineralogy and Geochemistry* 85, no. 1 (September 1, 2019): 49–74. <https://doi.org/10.2138/rmg.2019.85.3>.
- Detwiler, Russell L., Robert J. Glass, and William L. Bourcier. “Experimental Observations of Fracture Dissolution: The Role of Peclet Number on Evolving Aperture Variability: FRACTURE DISSOLUTION.” *Geophysical Research Letters* 30, no. 12 (June 2003). <https://doi.org/10.1029/2003GL017396>.
- Detwiler, Russell L., and Harihar Rajaram. “Predicting Dissolution Patterns in Variable Aperture Fractures: Evaluation of an Enhanced Depth-Averaged Computational Model: PREDICTING DISSOLUTION PATTERNS.” *Water Resources Research* 43, no. 4 (April 2007). <https://doi.org/10.1029/2006WR005147>.
- Dijk, Peter Erik, Brian Berkowitz, and Yoseph Yechieli. “Measurement and Analysis of Dissolution Patterns in Rock Fractures: MEASUREMENT AND ANALYSIS OF DISSOLUTION IN ROCK FRACTURES.” *Water Resources Research* 38, no. 2 (February 2002): 5-1-5–12. <https://doi.org/10.1029/2001WR000246>.

- Fahs, Marwan, Anis Younes, and François Lehmann. “An Easy and Efficient Combination of the Mixed Finite Element Method and the Method of Lines for the Resolution of Richards’ Equation.” *Environmental Modelling & Software* 24, no. 9 (September 2009): 1122–26. <https://doi.org/10.1016/j.envsoft.2009.02.010>.
- Farthing, Matthew W, Christopher E Kees, and Cass T Miller. “Mixed Finite Element Methods and Higher Order Temporal Approximations for Variably Saturated Groundwater Flow.” *Advances in Water Resources* 26, no. 4 (2003): 373–94.
- Hanna, R. Blair, and Harihar Rajaram. “Influence of Aperture Variability on Dissolutional Growth of Fissures in Karst Formations.” *Water Resources Research* 34, no. 11 (November 1998): 2843–53. <https://doi.org/10.1029/98WR01528>.
- Hayek, Mohamed, Georg Kosakowski, Andreas Jakob, and Sergey V. Churakov. “A Class of Analytical Solutions for Multidimensional Multispecies Diffusive Transport Coupled with Precipitation-Dissolution Reactions and Porosity Changes: ANALYTICAL SOLUTIONS FOR DIFFUSIVE TRANSPORT.” *Water Resources Research* 48, no. 3 (March 2012). <https://doi.org/10.1029/2011WR011663>.
- Hooker, J.N., J.F.W. Gale, L.A. Gomez, S.E. Laubach, R. Marrett, and R.M. Reed. “Aperture-Size Scaling Variations in a Low-Strain Opening-Mode Fracture Set, Cozzette Sandstone, Colorado.” *Journal of Structural Geology* 31, no. 7 (July 1, 2009): 707–18. <https://doi.org/10.1016/j.jsg.2009.04.001>.
- Kim, Jihoon, Eric Sonnenthal, and Jonny Rutqvist. “A Sequential Implicit Algorithm of Chemo-Thermo-Poro-Mechanics for Fractured Geothermal Reservoirs.” *Computers & Geosciences* 76 (March 2015): 59–71. <https://doi.org/10.1016/j.cageo.2014.11.009>.
- Koohbor, Behshad, Marwan Fahs, Hussein Hoteit, Joanna Doummar, Anis Younes, and Benjamin Belfort. “An Advanced Discrete Fracture Model for Variably Saturated Flow in Fractured Porous Media.” *Advances in Water Resources* 140 (June 2020): 103602. <https://doi.org/10.1016/j.advwatres.2020.103602>.
- Liu, Min, Vitalii Starchenko, Lawrence M. Anovitz, and Andrew G. Stack. “Grain Detachment and Transport Clogging during Mineral Dissolution in Carbonate Rocks with Permeable Grain Boundaries.” *Geochimica et Cosmochimica Acta* 280 (July 2020): 202–20. <https://doi.org/10.1016/j.gca.2020.04.022>.
- Lopes, Juliana A.G., Walter E. Medeiros, Vincenzo La Bruna, Alexandre de Lima, Francisco H.R. Bezerra, and Denis José Schiozer. “Advancements towards DFKN Modelling: Incorporating Fracture Enlargement Resulting from Karstic Dissolution in Discrete Fracture Networks.” *Journal of Petroleum Science and Engineering* 209 (February 2022): 109944. <https://doi.org/10.1016/j.petrol.2021.109944>.

- Medekenova, Alfiya, and Gareth D. Jones. “Characterization and Modeling Challenges Associated with Fracture and Karst (Non-Matrix) in the Margin Area of a Carbonate Reservoir.” In *All Days*, SPE-172275-MS. Astana, Kazakhstan: SPE, 2014. <https://doi.org/10.2118/172275-MS>.
- Medici, G., L.J. West, and N.P. Mountney. “Characterizing Flow Pathways in a Sandstone Aquifer: Tectonic vs Sedimentary Heterogeneities.” *Journal of Contaminant Hydrology* 194 (November 2016): 36–58. <https://doi.org/10.1016/j.jconhyd.2016.09.008>.
- Miller, Cass T, Chandra Abhishek, and Matthew W Farthing. “A Spatially and Temporally Adaptive Solution of Richards’ Equation.” *Advances in Water Resources* 29, no. 4 (2006): 525–45.
- Moortgat, Joachim, Mohammad Amin Amooie, and Mohamad Reza Soltanian. “Implicit Finite Volume and Discontinuous Galerkin Methods for Multicomponent Flow in Unstructured 3D Fractured Porous Media.” *Advances in Water Resources* 96 (October 2016): 389–404. <https://doi.org/10.1016/j.advwatres.2016.08.007>.
- Mukhametdinova, Aliya, Andrey Kazak, Tagir Karamov, Natalia Bogdanovich, Maksim Serkin, Sergey Melekhin, and Alexey Cheremisn. “Reservoir Properties of Low-Permeable Carbonate Rocks: Experimental Features.” *Energies* 13, no. 9 (May 3, 2020): 2233. <https://doi.org/10.3390/en13092233>.
- Natarajan, N, and G Suresh Kumar. “Solute Transport in a Coupled Fracture-Matrix System with Sinusoidal Fracture Geometry.” *International Journal of Engineering Science and Technology* 2, no. 6 (2010): 1886–1992.
- Suk, Heejun. “Generalized Semi-Analytical Solutions to Multispecies Transport Equation Coupled with Sequential First-Order Reaction Network with Spatially or Temporally Variable Transport and Decay Coefficients.” *Advances in Water Resources* 94 (August 2016): 412–23. <https://doi.org/10.1016/j.advwatres.2016.06.004>.
- Tenthorey, E, and J Fitzgerald. “Feedbacks between Deformation, Hydrothermal Reaction and Permeability Evolution in the Crust: Experimental Insights.” *Earth and Planetary Science Letters* 247, no. 1–2 (July 15, 2006): 117–29. <https://doi.org/10.1016/j.epsl.2006.05.005>.
- Tran, Minh, and Birendra Jha. “Effect of Poroelastic Coupling and Fracture Dynamics on Solute Transport and Geomechanical Stability.” *Water Resources Research* 57, no. 10 (October 2021). <https://doi.org/10.1029/2021WR029584>.
- Viswanathan, H. S., J. Ajo-Franklin, J. T. Birkholzer, J. W. Carey, Y. Guglielmi, J. D. Hyman, S. Karra, et al. “From Fluid Flow to Coupled Processes in Fractured Rock: Recent Advances and New Frontiers.” *Reviews of Geophysics* 60, no. 1 (March 2022). <https://doi.org/10.1029/2021RG000744>.
- Younes, A., M. Konz, M. Fahs, A. Zidane, and P. Huggenberger. “Modelling Variable Density Flow Problems in Heterogeneous Porous Media Using the Method of Lines and Advanced Spatial Discretization

Methods.” *Mathematics and Computers in Simulation* 81, no. 10 (June 2011): 2346–55.  
<https://doi.org/10.1016/j.matcom.2011.02.010>.

Younes, Anis, and Philippe Ackerer. “Solving the Advection-Dispersion Equation with Discontinuous Galerkin and Multipoint Flux Approximation Methods on Unstructured Meshes.” *International Journal for Numerical Methods in Fluids* 58, no. 6 (October 30, 2008): 687–708.  
<https://doi.org/10.1002/flid.1783>.

Younes, Anis, Marwan Fahs, and Selim Ahmed. “Solving Density Driven Flow Problems with Efficient Spatial Discretizations and Higher-Order Time Integration Methods.” *Advances in Water Resources* 32, no. 3 (March 2009): 340–52. <https://doi.org/10.1016/j.advwatres.2008.11.003>.

Younes, Anis, Behshad Koohbor, Benjamin Belfort, Philippe Ackerer, Joanna Doummar, and Marwan Fahs. “Modeling Variable-Density Flow in Saturated-Unsaturated Porous Media: An Advanced Numerical Model.” *Advances in Water Resources* 159 (January 2022): 104077.  
<https://doi.org/10.1016/j.advwatres.2021.104077>.

Younes, Anis, Ahmed Makradi, Ali Zidane, Qian Shao, and Lyazid Bouhala. “A Combination of Crouzeix-Raviart, Discontinuous Galerkin and MPFA Methods for Buoyancy-Driven Flows.” *International Journal of Numerical Methods for Heat & Fluid Flow* 24, no. 3 (April 1, 2014): 735–59.  
<https://doi.org/10.1108/HFF-07-2012-0156>.

Yu, Cheng. “Modeling of Fracture Geometry Alteration and Fracture Flow Evolution under Geostress and Water-Rock Interaction,” 2019. <https://doi.org/10.48550/ARXIV.1904.05659>.

Zidane, Ali, and Abbas Firoozabadi. “An Efficient Numerical Model for Multicomponent Compressible Flow in Fractured Porous Media.” *Advances in Water Resources* 74 (December 2014): 127–47.  
<https://doi.org/10.1016/j.advwatres.2014.08.010>.

## Appendices

### Appendix A: Explanations of benchmarks in Chapter II

#### 1. Benchmark 1



**Figure A1.** Configuration of benchmark 1

**Table A1.** Boundary conditions, initial conditions, and parameters for benchmark 1

Species	Left boundary condition (mM)	Initial Condition (mM)
$H^+$	0.001	0.1
$Na^+$	0.1	0.1
$Cl^-$	0.1	0.1
$NO_3^-$	0.001	0.1
Parameters		
Permittivity [ $F/m$ ]	$7.08 \times 10^{-10}$	
Molecular diffusion coefficients [ $m^2/s$ ]	$Na^+ : 1.33 \times 10^{-9}$ $Cl^- : 2.03 \times 10^{-9}$ $NO_3^- : 1.9 \times 10^{-9}$ $H^+ : 9.31 \times 10^{-9}$	

#### 2. Benchmark 2



**Figure A2.** Configuration of benchmark 2

Table A2. Boundary conditions, initial conditions, and parameters for benchmark 2

Species	Left boundary condition (mM) (Initial condition in the left half of the domain)	Right boundary condition (mM) (Initial condition in the right half of the domain)
$H^+$	$10^{-4}$	$10^{-4}$
$Na^+$	0.5	0.1
$^{22}Na^+$	$10^{-6}$	$10^{-6}$
$Cl^-$	0.5	0.1
$OH^-$	$10^{-4}$	$10^{-4}$
Parameters		
Permittivity [ $F/m$ ]	$5.85 \times 10^{-10}$	
Molecular diffusion coefficients [ $m^2/s$ ]	$H^+ : 9.31 \times 10^{-9}$ , $OH^- : 5.27 \times 10^{-9}$ $Na^+, ^{22}Na^+ : 1.33 \times 10^{-9}$ $Cl^- : 2.03 \times 10^{-9}$	

## 2. Benchmark 3

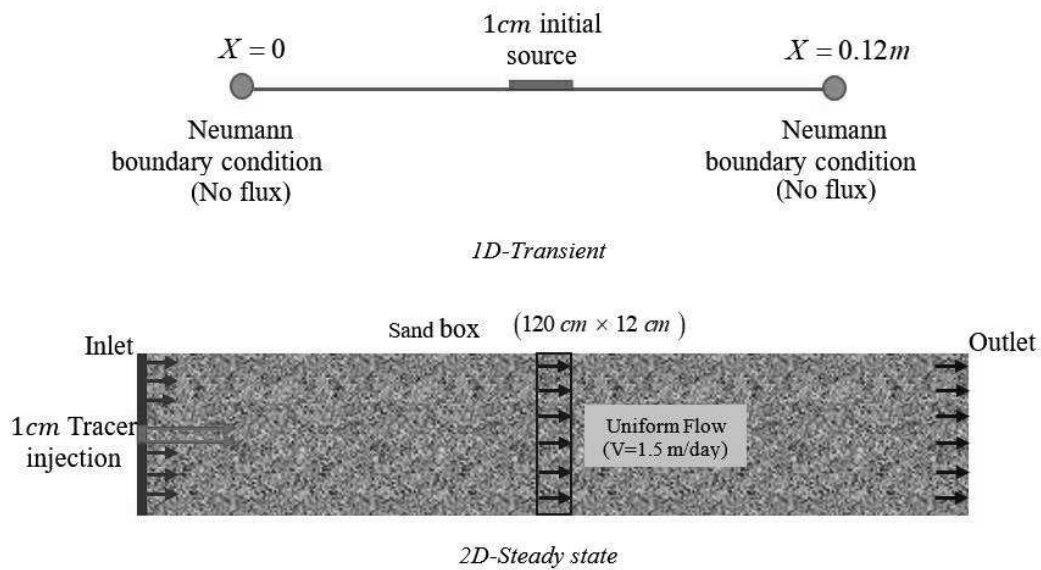


Figure A3. Configuration of benchmark 3

Table A3. Boundary conditions, initial conditions, and parameters for benchmark 3

Species	Initial source (1D) and the tracer injection ports (mM)	Initial condition (1D) and remaining injection ports (2D) (mM)
$K^+$	0.29	$1 \times 10^{-6}$
$Mg^{2+}$	0.29	$1 \times 10^{-6}$
$Cl^-$	0.87	$3 \times 10^{-6}$
Parameters		
Permittivity $[F/m]$	$5.85 \times 10^{-10}$	
Molecular diffusion coefficients $[m^2/s]$	$K^+ : 1.77 \times 10^{-9}$ $Mg^{2+} : 6.26 \times 10^{-10}$ $Cl^- : 2.03 \times 10^{-9}$	
Transverse dispersion coefficients $[m^2/s]$	$K^+ : 2.405 \times 10^{-9}$ $Mg^{2+} : 1.745 \times 10^{-9}$ $Cl^- : 2.425 \times 10^{-9}$	

### Appendix B: Coefficients of the spectral system in Chapter III

$$\delta_i = \begin{cases} 1 & \text{if } i = 0 \\ 0 & \text{if } i \neq 0 \end{cases} \quad (B1)$$

$$\alpha_I = \begin{cases} 2 & \text{if } I = 0 \\ 1 & \text{if } I \neq 0 \end{cases} \quad (B2)$$

$$\Gamma_{G,r} = \begin{cases} \frac{1 - (-1)^{G+r}}{G+r} + \frac{1 - (-1)^{G-r}}{G-r} & \text{if } G \neq r \\ 0 & \text{if } G = r \end{cases} \quad (B3)$$

$$A'_{i,j,k} = \begin{cases} A_{i,j,k} & \text{if } i \leq Ni, j \leq Nj \text{ and } k \leq Nk \\ 0 & \text{else} \end{cases} \quad (B4)$$

$$B'_{i,j,k} = \begin{cases} B_{i,j,k} & \text{if } i \leq Nl, j \leq Nm \text{ and } k \leq Nn \\ 0 & \text{else} \end{cases} \quad (B5)$$

$$E'_{i,j,k} = \begin{cases} E_{i,j,k} & \text{if } i \leq Nu, j \leq Nv \text{ and } k \leq Nw \\ 0 & \text{else} \end{cases} \quad (B6)$$

$$G'_{i,j,k} = \begin{cases} G_{i,j,k} & \text{if } i \leq Ns, j \leq Np \text{ and } k \leq Nt \\ 0 & \text{else} \end{cases} \quad (\text{B7})$$

$$\xi_{G,r,o} = \delta_{G,r+o} + \delta_{G,r-o} + \delta_{G,-r+o} + \delta_{G,-r-o} \quad (\text{B8})$$

$$\eta_{G,r,o} = \delta_{G,r+o} + \delta_{G,r-o} + \delta_{G,-r+o} \quad (\text{B9})$$

$$\gamma_{G,r,o} = \delta_{G,r+o} + \delta_{G,r-o} - \delta_{G,-r+o} \quad (\text{B10})$$

$$\kappa_{G,r,o} = \delta_{G,r+o} - \delta_{G,r-o} + \delta_{G,-r+o} \quad (\text{B11})$$

$$\zeta_{G,r,o} = -\delta_{G,r+o} + \delta_{G,r-o} + \delta_{G,-r+o} \quad (\text{B12})$$

where  $\delta_{i,j}$  is the Kronecker delta function

### Appendix C: Converting the spectral equations to a system of ordinary differential equations in Chapter III

$$A_{I,J,K} = \Upsilon_{I,J,K} \frac{N_g Ra_T \alpha_I}{\pi} \sum_{v=1}^{N_v} \sum_{w=0}^{N_w} v E'_{I,v,w} \Gamma_{J,v} \Gamma_{K,w} \quad (\text{C1})$$

$$- \Upsilon_{I,J,K} \frac{2N_g Ra_T}{\pi^2} \Gamma_{J,0} \Gamma_{K,0} \delta_{I,0} + \Upsilon_{I,J,K} \frac{Ra_T J}{\pi} \sum_{s=1}^{N_s} \sum_{t=0}^{N_t} G'_{s,J,t} \Gamma_{s,I} \Gamma_{K,t}$$

$$B_{L,M,N} = \Upsilon_{M,L,N} \frac{LN_g Ra_T}{\pi} \sum_{v=1}^{N_v} \sum_{w=0}^{N_w} E'_{L,v,w} \Gamma_{v,M} \Gamma_{N,w} \quad (\text{C2})$$

$$+ \Upsilon_{M,L,N} \frac{Ra_T \alpha_M}{\pi} \sum_{s=1}^{N_s} \sum_{t=0}^{N_t} s G'_{s,M,t} \Gamma_{L,s} \Gamma_{N,t} - \Upsilon_{M,L,N} \frac{2Ra_T}{\pi^2} \Gamma_{L,0} \Gamma_{N,0} \delta_{M,0}$$

where  $\Upsilon_{I,J,K} = \frac{-1}{\pi^2 (I^2 + \alpha_I J^2 + \alpha_I K^2)}$

## Modeling water flow, reactive transport and heat transfer in porous media

### Résumé

Ce travail traite de la modélisation de l'écoulement, du transport réactif et du transfert de chaleur dans les milieux poreux en se concentrant sur trois applications principales : (i) le transport réactif multicomposant dans le processus d'électrodifusion, (ii) la convection thermohaline dans les milieux poreux saturés et (iii) l'écoulement, la dissolution et le transport dans les roches fracturées. L'objectif principal de ce travail est d'améliorer l'efficacité et la précision des modèles numériques et de fournir une compréhension approfondie des processus physiques sous-jacents. Les premiers efforts sont consacrés à l'évaluation des hypothèses communes sur la formulation des études de transport réactif multicomposant pour l'électrodifusion. Une partie importante est consacrée aux études de la convection thermohaline dans les milieux poreux saturés. Une solution semi-analytique est développée pour le cas de la convection thermohaline 3D et un modèle numérique avancé est développé pour la convection thermohaline réactive avec l'application de la séquestration du CO<sub>2</sub>. La dernière partie de la thèse est consacrée à l'étude de l'écoulement, de la dissolution et du transport dans les roches fracturées, basée sur une technique numérique avancée.

**Mots clés:** modélisation numérique ; modélisation semi-analytique ; électro-diffusion ; transport réactif ; transfert de chaleur ; convection thermohaline ; karstification.

### Abstract

This work addresses the modeling of flow, reactive transport and heat transfer in porous media with focusing on three main applications: (i) multicomponent reactive transport in the electro-diffusion process, (ii) Thermohaline convection in saturated porous media and (iii) Flow, dissolution and transport in fractured rocks. The main objective of this work is to improve the efficiency and accuracy of the numerical models and provide a deep understanding of the underlying physical processes. The first efforts are devoted to the evaluation of common assumptions on the formulation of multicomponent reactive transport studies for electro-diffusion. A significant part is dedicated to studies of thermohaline convection in saturated porous media. A semi-analytical solution is developed for the case of the 3D thermohaline convection and an advanced numerical model is developed for the reactive thermohaline convection with the application of CO<sub>2</sub> sequestration. The last part of the thesis is devoted to the studies of flow, dissolution and transport in fractured rocks based on an advanced numerical technique.

**Keywords:** numerical modeling; semi-analytical modeling; electro-diffusion; reactive transport; heat transfer; thermohaline convection; karstification

